TURBULENCE MODELS FOR NON-CIRCULAR DUCTS AND CHANNELS

Davor P. Cokljat
(B.Eng.)

Thesis submitted for the degree of
Doctor of Philosophy
in the School of Engineering,
City University

Hydraulics Division
Department of Civil Engineering
City University
Northampton Square
London EC1V 0HB

March 1993

Abstract

This thesis describes the development and application of numerical predictive procedures for flows in which turbulence-driven secondary motion plays an important role. The focus is on fully-developed flows in closed ducts and open channels of various cross-sectional geometries.

Two different turbulence models were evaluated: a complete Reynolds-stress-transport model and a two-equation k-ϵ model used in conjunction with a nonlinear stress-strain relationship. Detailed consideration was given to the various approximations utilized in closing the Reynolds-stress equations, particularly to the difficult pressure-strain-correlation term which proved crucial for the accurate prediction of the turbulence-driven secondary motion. The thesis also considers the validity of such models to flows influenced by the presence of a free surface.

Appropriate numerical procedures were developed to handle the variety of geometries likely to be encountered in engineering practice. Particular attention was placed on the development of the numerical procedure which utilizes the nonlinear k-ϵ model in conjunction with body fitted coordinates.

The performance of each model was assessed through detailed comparisons with published data from a very wide range of flows in non-circular ducts and channels. Both models succeeded in predicting the secondary flow and its effects on the mean-velocity field in rectangular and compound ducts.

For flows in rectangular channels, the Reynolds-stress model proved capable of accurately predicting the strength and location of secondary-flow cells and their role in displacing the position of the mean-velocity maximum to below the free surface. In contrast, the nonlinear model failed to reproduce this result for reasons discussed in some detail in the thesis. Both models predicted equally well the shear stress over wetted perimeter indicating that the defect of the nonlinear model encountered near to the free surface was rather localized. The Reynolds-stress model also proved to be particularly accurate in the prediction of flows in compound channels. The nonlinear k-ϵ model was found to be less accurate there but, due to its economy and robustness, this model seems to be an acceptable alternative to Reynolds-stress models for the practical prediction of flows in simple and compound open channels.

Acknowledgements

I am very grateful to my Supervisor, Dr B.A. Younis, for his active interest, criticism and guidance throughout the course of this study. I would like to thank Dr I. Demirdzic who introduced me to Dr B.A. Younis and made arrangement for my study at City University. I am grateful to Dr M. Peric for his generous help with prediction of the flows using body-fitted coordinates. I wish also to thank Mr B. Basara with whom I had occasional but helpful discussions.

This research was funded by the SERC under Grant: GR/F/61172.

Contents

Nomenclature

Symbol	Meaning
a	Coefficient in discretized equation
A	Area
a_{ij}	Anisotropy tensor
a_{lj}^{mi}	Fourth-order tensor
B	Half width of duct or channel
b	Half width of main part of duct or channel
C_D, C_E	Coefficients in nonlinear stress-strain relationship
C_f	Coefficient in free-surface-damping function
C_S	Coefficient in model for triple correlation
C_ϵ	Coefficient in model for diffusion of ϵ
$C_{\epsilon 1}, C_{\epsilon 2}$	Coefficient in model for sources of ϵ
C_μ	Coefficient in formulation for eddy-viscosity
C_1	Coefficient in model for $\Phi_{ij,1}$
C_2	Coefficient in model for $\Phi_{ij,2}$
C_1', C_2'	Coefficients in model for $\Phi_{ij,w}$
D	Diffusion
D_{ij}	Tensor in model for $\Phi_{ij,2}$ term
$\overline{D_{ij}}$	Main rate of strain tensor
$\overset{\circ}{\overline{D_{ij}}}$	Oldroyd derivative
E	Logarithmic law constant
f	Damping functions
F	Mass flux
g	Earth acceleration
h	Height of flood plain
h^*	Ratio between depths of main-channel and flood-plain flows
H	Depth of open channel
J	Jacobian of coordinate transformation
k	Turbulence kinetic energy
L	Length scale of turbulence
$\dot{m}$	Mass flow rate
n_i	Unit vector normal to the surface

p	Time-averaged value of pressure
p'	Fluctuating value of pressure and also pressure correction
$\hat{p}$	Instantaneous value of pressure
P_{ij}	Rate of production $\overline{u_i u_j}$
P_{Ω_z}	Production of vorticity
P_k	Production of turbulent kinetic energy
q	Total transport
R	Residual
Re	Reynolds number
t	Time
U_i, u_i	Time-averaged and fluctuating velocity
$\hat{U}_i$	Instantaneous value of velocity
$\overline{u_i u_j}$	Reynolds-stress tensor
$\overline{u_i u_j u_k}$	Triple velocity correlation
V	Volume
u, v, w	Fluctuating velocity components in x, y and z directions
U, V, W	Time-averaged velocity components in x, y and z directions
W_τ	Mean shear velocity
$\overline{u^2}, \overline{v^2}, \overline{w^2}$	Normal-stress components in x, y and z directions
$\overline{uv}, \overline{uw}, \overline{vw}$	Shear-stress components
x^+	Non-dimensional distance from wall
x, y, z	Cartesian coordinates
x^1, x^2, x^3	Cartesian coordinates
y^1, y^2, y^3	Coordinates of general system

Greek Symbols

$\alpha, \beta, \eta, \nu_1$	Coefficients in expression for a_{lj}^{mi}
β_i^j	Coordinate transformation factor
Γ_Φ	Diffusivity coefficient
δ_{ij}	Kronecker delta
ϵ	Dissipation of turbulent kinetic energy
ϵ_{ij}	Dissipation rate of $\overline{u_i u_j}$
θ	Slope of the channel bed and also wall inclination angle
κ	von Karman constant
λ	Longitudinal spacing between rough elements

μ	Molecular viscosity
μ_t	Turbulent viscosity
ν	Molecular kinematic viscosity
ν_t	Turbulent kinematic viscosity
ρ, ρ'	Time-averaged and fluctuating value of density
$\hat{\rho}$	Instantaneous density
σ_k, σ_ϵ	Coefficients of turbulent diffusion of k and ϵ
$\overline{\tau}$	Average shear stress
τ_{ij}	Shear-stress tensor
$\Phi_{ij,1}$, $\Phi_{ij,2}$, $\Phi_{ij,w}$	Terms in modelled pressure-strain correlation
Φ	Symbol which denotes any variable
χ	Roughness parameter
Ψ	Streamline
Ω	Vorticity

Subscripts

b	Bed
c	Channel
f	Free surface and also flood plain
l	Left
r	Right and also roughness
w	Wall
x, y	Relating to x and y directions

Abbreviations

AR	Aspect ratio
ASM	Algebraic stress model
CL	Centre line
NKE	Nonlinear k-ϵ model
RSM0	Starting version of Reynolds-stress model
RSM	Final version of Reynolds-stress model
SL	Channel slope

List of Figures

Chapter 1

INTRODUCTION

1.1 Background

Turbulence is both the most complicated and the most common kind of fluid motion and the motivation for the understanding and practical prediction of turbulent flows stems from their frequent occurrence in engineering practice. There are instances when the effects of turbulence are undesirable (e.g. energy dissipation in fluid-transport systems) but, equally, there are many instances where turbulence plays a very positive role such as in the dispersion of contaminants in the environment. In all cases, the turbulence phenomenon is closely connected with the well-being of the society and this justifies the theoretical and experimental research into its nature.

One interesting turbulent phenomenon is the turbulence-driven secondary motion observed in non-circular ducts and channels. This is usually referred to as Prandtl's second kind of secondary motion to distinguish it from Prandtl's first kind of secondary motion which is driven by the pressure gradients in the flow field. The turbulence-driven motion (which is obviously absent from laminar flows) is only of the order of $1 - 3$ % of

the streamwise bulk velocity and arises from the anisotropy of the turbulence field as will be discussed in Section 1.2. Yet, despite its modest strength, that motion exerts a profound influence on the main flow as was first observed by Nikuradze (1926) who identified it as the cause of the bulging of the axial velocity contours towards the corners of a square duct under fully-developed flow conditions. Such distortions of the mean-velocity contours cause a reduction in the wall-shear-stress in the centre portion of the duct with important consequences to the rates of heat or mass transport there. A prerequisite to the prediction of turbulence-driven secondary motion is the understanding of its origin, and this is the subject of the next section.

1.2 The Origin of the Turbulence-Driven Secondary Motion

Prandtl (1926) attributed the origin of that motion to the turbulent fluctuations along the isovels which produce the secondary flow normal to the isovels wherever a variation in curvature occurs. This remined unverified due to the lack of measurements for the secondary velocities at that time.

In the past thirty years several researchers have analysed the streamwise vorticity equation in order to examine the importance of each term in that equation.

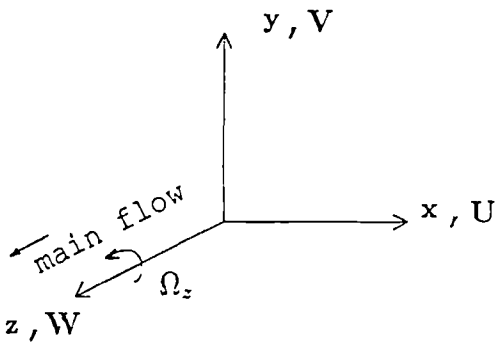

Fig. 1.1 The coordinate system for streamwise vorticity equation

The general vorticity equation in tensor notation can be written as follows:

$$U_j \frac{\partial \Omega_k}{\partial x_j} - \Omega_j \frac{\partial U_k}{\partial x_j} = \epsilon_{ijk} \frac{\partial^2(-\overline{u_l u_j})}{\partial x_i \partial x_l} + \nu \frac{\partial^2 \Omega_k}{\partial x_j \partial x_j} \tag{1.1}$$

where

ϵ_{ijk} - alternating third-order tensor

$\Omega_k = \epsilon_{ijk}(\partial U_j / \partial x_i)$ - turbulent vorticity

Using the notation of Fig. 1.1, the streamwise vorticity equation for the three-dimensional fully developed flow can be written in the following form:

$$\overbrace{U\frac{\partial \Omega_z}{\partial x} + V\frac{\partial \Omega_z}{\partial y}}^{A1} = \overbrace{\frac{\partial^2}{\partial x \partial y}(\overline{u^2} - \overline{v^2})}^{A2} - \overbrace{(\frac{\partial^2}{\partial x^2} - \frac{\partial^2}{\partial y^2})\overline{uv}}^{A3} + \overbrace{\nu(\frac{\partial^2 \Omega_z}{\partial x^2} + \frac{\partial^2 \Omega_z}{\partial y^2})}^{A4} \tag{1.2}$$

were

$$\Omega_z = (\partial V / \partial x - \partial U / \partial y)$$

Brundrett and Baines (1964) measured all three velocity components and all six Reynolds stresses and used their measurements to examine the magnitude of the terms in equation (1.2). Term A1 represents the convection of streamwise vorticity by the secondary flow itself. Term A4 represents the diffusion of vorticity by molecular viscosity. Terms A2 and A3 represent the rates of production of streamwise vorticity. They found that the term involving the difference in normal stresses $(\overline{u^2} - \overline{v^2})$ is an order of magnitude greater than the shear-stress term $(\overline{uv})$ and therefore they concluded that the main contribution to the production of vorticity is due to term A2.

Gessner and Jones (1965) used X-array hot-wire probes to measure the terms in the momentum equation for a velocity component along a secondary flow streamline. They found that the convective and viscous terms were approximately two orders of magnitude less than the pressure and turbulence terms in the momentum equation. They also found

that the terms containing the normal and shear stresses were of the same order of magnitude. The findings of Gessner and Jones contradict those of Brundrett and Baines in so far as the former found that the strength of the normal- and shear-stress terms appeared to be balanced.

Perkins (1970) used his data to investigate the mechanism for generating the streamwise vorticity in developing corner flow. He arrived at similar conclusions as Gessner and Jones (1965) suggesting that terms A2 and A3 are of equal order of magnitude, contrary to previous findings of Brundrett and Baines. The experimental results for the shear stress $\overline{uv}$ of Brundrett and Baines were criticized by Perkins (1970) on the following ground: the turbulent stresses $\overline{uv}$ and $\overline{u^2} - \overline{v^2}$ were obtained from 4 measured r.m.s. voltages, using a rotating single-wire sensor to eight different orientations at each point in the flow, so that an error of only $\pm$ 1 % in each r.m.s. voltage would introduce an error of $\pm$ 100 % in the shear stress $\overline{uv}$.

The experimental findings on the generation of turbulence-driven secondary motion may be used to draw a following conclusion: the terms A2 and A3 both contribute to the production of streamwise vorticity in three-dimensional fully-developed flows and hence both the turbulence anisotropy together with the secondary shear-stress must be modelled accurately in order to realistically predict the secondary flow.

1.3 Previous Predictions

1.3.1 Algebraic-Stress Models

Algebraic-stress models are based on explicit algebraic relationships for the Reynolds stresses, obtained by simplifying the modelled transport equations for the turbulent stresses. Launder and Ying (1973) were the first to apply such a model for predicting the secondary flow in non-circular ducts. They simplified the modelled transport equations for tur-

bulent stresses proposed by Hanjalic and Launder (1972,b), using the assumption that the turbulence is in a state of a local equilibrium and this allowed them to neglect the convection and the diffusion terms from those equations. They also neglected all the secondary velocity gradients in the expressions for the Reynolds stresses. Turbulence kinetic energy (k) was obtained from solution of a differential transport equation while the turbulence length scale (L) was determined using Buleev's (1963) algebraic formula. Application of this model to the square-duct flow produced fairly good results for the main-flow isolines and secondary-flow profiles which is surprising considering that the same model underestimated the turbulence anisotropy by at least one order of magnitude (Kacker, 1973). The authors also had to reduce the value of a certain coefficient in the algebraic equations in order to avoid too large secondary motions; their model then differed from the one originally proposed by Hanjalic and Launder (1972,b) by a factor of 3.6.

Tatchell (1975) adopted a different approach to that of Launder and Ying in that he calculated the dissipation of turbulence kinetic energy (ϵ) from its own transport equation. Gosman and Rapley (1980) applied Tatchell's model to flows in rectangular ducts and to some non-orthogonal geometries using a curvilinear mesh system. They obtained satisfactory results for the main flow though the model's performance for the turbulence anisotropy was not reported.

Naot and Rodi (1981,1982) were the first to apply the ASM to open-channel flows. The expressions for the normal stresses $\overline{u^2}$, $\overline{v^2}$ and the shear stress $\overline{uv}$ were similar to those proposed by Launder and Ying but contained additional terms arising from the use of a surface-proximity correction to the pressure strain model. Moreover, the authors used the eddy-viscosity terms from k-ϵ model in the expressions for the $\overline{u^2}$, $\overline{v^2}$ and the shear stress $\overline{uv}$. The primary shear stresses $\overline{uw}$ and $\overline{vw}$ were calculated using an eddy-viscosity model in which the turbulent viscosity was assumed to be anisotropic (i.e. different for the x- and y-directions) an approach which, at best, can only be regarded as highly empirical.

Another application of the ASM is that of Nakayama et al. (1983) who applied it to rectangular and trapezoidal ducts. They obtained satisfactory results for the the mean-velocity field but again underestimated the turbulence anisotropy and the secondary-shear stress by one order of magnitude.

Demuren and Rodi (1984) argued that the underprediction of turbulence anisotropy obtained by Launder and Ying's model is due to two reasons. Firstly, because the model is developed from the stress-equation model of Hanjalic and Launder (1972,b) which does not account for the influence of the wall on the turbulence field and, secondly, because of the neglect of all the secondary-velocity gradients from the stress expressions. Demuren and Rodi then re-introduced the secondary-velocity gradients in their ASM model which was developed from the stress-equation model of Launder et al. (1975) and found that the model was able to realistically simulate many important features of the secondary flow. The strength of the secondary motions was, however, underestimated and hence the authors concluded:
... further work is necessary in order to develop a model for simulating accurately the secondary velocities without any tuning of constants.

Krishnappan and Lau (1986) applied the ASM to flows in open compound channels. Their work was primarily aimed at the prediction of the bulk quantities in those flows (e.g. the total discharge) which, on the whole, were in good agreement with the data.

1.3.2 Reynolds-Stress-Transport Models

To our knowledge there have been only two attempts to apply the Reynolds-stress model for predicting the secondary motion in three-dimensional flows. Naot, Shavit and Wolfshtein (1972) applied this model to flows in square duct. They specified the turbulent length scale from geometric considerations (along the lines proposed by Prandtl, 1925) and this limits

the applicability of their method to simple ducts. Their predictions for the main-velocity isolines were reasonably good. The predicted turbulence anisotropy was of the same order as that measured.

Reece (1977) applied the model of Launder et al. (1975) to flows in square ducts (both developed and developing) and, also, to an open channel flow. Demuren and Rodi (1984) claimed that Reece probably accounted for the influence of the secondary velocity gradients by using an eddy-viscosity expression (as Naot and Rodi 1982) built into the computer program but this cannot be confirmed from Reece's thesis. At any rate, his predictions of the both the velocity and the turbulence for the square-duct flow were in good agreement with the data. This was also the case for the mean-velocity contours for the narrow open-channel flow (aspect ratio 0.6).

1.3.3 Nonlinear k-ϵ (k-l) Model

Speziale (1987) presented a novel non-linear stress-strain relationship which, together with the standard k-ϵ and k-l equations, proved capable of predicting the turbulence-driven secondary motion in non-circular ducts. Younis and Abdellatif (1989) used this model to calculate flows in rectangular ducts with various aspect ratios and they obtained fairly good results for all measured parameters. Hur, Thangam and Speziale (1989) calculated flow in a square duct using the nonlinear k-l model and their predictions were in satisfactory agreement with the experimental results.

1.4 Motivation and Objectives of the Present Work

The need for a predictive procedure for turbulent flows in ducts and channels of non-circular cross-section arises from the frequent occurrence

of such flows in all branches of engineering. Examples include the air-conditioning ducts, heat exchangers, intake ducts of jet engines, open channels, river flood relief schemes, sewers and estuarine flows. In all those flows the mean-flow field is significantly affected by the turbulence-driven secondary motion.

The focus of previous research has been on the development and application of Algebraic-Stress Models to flows in non-circular geometries. It is now clear that such models are not entirely satisfactory, not, at any rate, when applied in their standard forms and cannot thus be relied upon to form the basis of a genuinely predictive procedure. Reynolds-stress-transport model overcome many of the limitations inherent in the algebraic approach, but those are not well tested for the flows of interest here. Indeed, there are only two previous uses of such models for flows in square duct but, as mentioned in the previous section, neither one can be considered as a comprehensive test of the validity and limitations of such models. One reason for the shortage of RSM applications is that the implementation of those models in practical numerical schemes, and the procurement of stable solutions, are not trivial tasks. The real potential of Reynolds-stress models for predicting turbulence-driven secondary motion remains unknown. The same can be said for the non-linear stress-strain relationship proposed by Speziale (1987): it looks promising but its real potential is not fully determined.

The objectives of this work are as follows:

1. To conduct a critical review of the various closure approximations for the turbulent diffusion, dissipation and pressure-strain correlation in the Reynolds-stress model. This task is treated in Chapter 2.

2. To implement a complete Reynolds-stress-transport model and a nonlinear k-ϵ model of turbulence into appropriate numerical solution procedures and to adapt those to handle all the flows considered in the present study (Fig. 1.2). This task is treated in Chapter 3.

3. To conduct a preliminary assessment of the two models for square-duct flows in order to identify the merits and deficiencies of each

model and to advance alternative closure assumptions, if necessary. This task is treated in Section 4.2 of Chapter 4.

4. To conduct a detailed models assessment against experimental data for closed ducts and to explore the models performance for the widest possible range of geometries giving rise to turbulence-driven secondary motion. The results obtained for non-circular ducts are reported in Sections 4.3 – 4.5 of Chapter 4.

5. To identify the physical processes that are dominant in the region adjacent to the free surface and to investigate their modelling in conjunction with the present closure assumptions. This aspect of the work is presented in Sections 5.1 – 5.3 of Chapter 5.

6. To assess the accuracy of the models and to determine their validity and limitations for practical applications. This will be done by comparing their results with well-documented experimental data for various open-channel flows with particular attention to two-stage (compound) channels. The results obtained for non-circular channels are reported in Sections 5.3 and 5.4 of Chapter 5.

Conclusions and fulfillment of the stated objectives are to be critically reviewed in Chapter 6 where recommendations for future work will also be made.

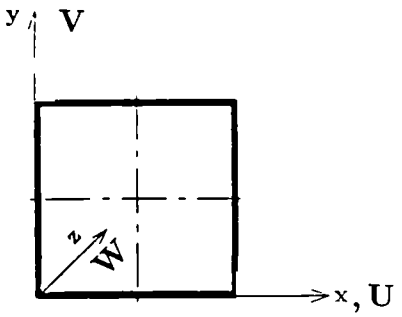

rectangular duct-flow

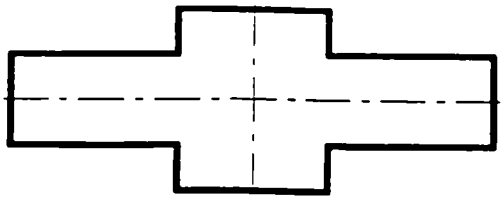

compound-symmetric duct-flow

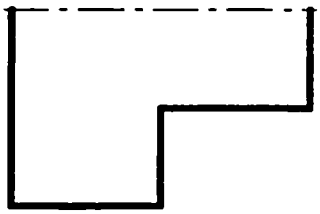

compound-asymmetric duct-flow

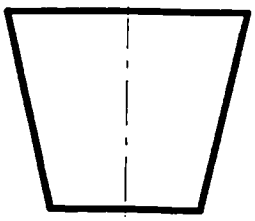

trapezoidal duct-flow

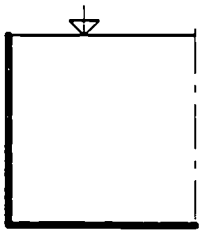

rectangular open-channel-flow

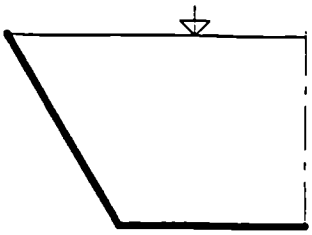

trapezoidal open-channel-flow

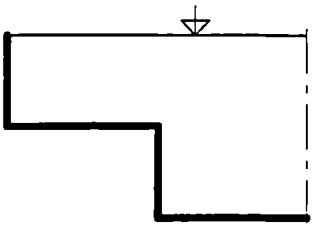

compound-symmetric open-channel-flow

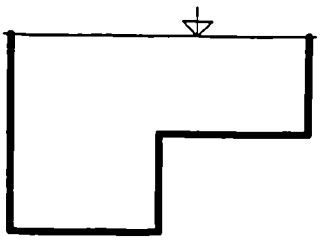

compound-asymmetric open-channel-flow

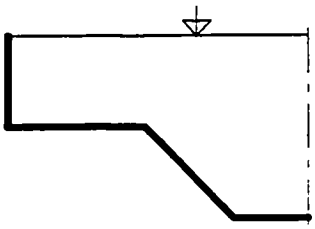

compound-symmetric open-channel-flow with trapezoidal main channel

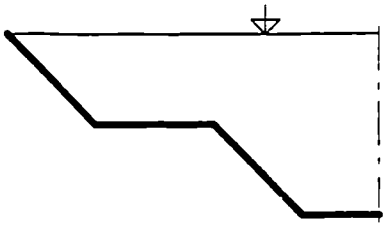

compound-symmetric open-channel-flow with trapezoidal main channel and flood plain

Fig. 1.2 The flows predicted in the present work

Chapter 2

TURBULENCE MODELLING

2.1 Introduction

Application of the principle of conservation of momentum for a continuum fluid yields the Navier-Stokes equations. Those equations, together with the equation for mass conservation (continuity), describe all practical types of fluid flow.

The continuity equation for constant-density, steady flow reads:

$$\frac{\partial \hat{U}_i}{\partial x_i} = 0. \tag{2.1}$$

where $\hat{U}_i$ represents the instantaneous velocity. Tensor notation is used wherein repeated indices imply summation. The Navier-Stokes equations for a Newtonian fluids of viscosity μ and in the absence of body forces reads:

$$\hat{\rho}\,\hat{U}_j \frac{\partial \hat{U}_i}{\partial x_j} = -\frac{\partial \hat{p}}{\partial x_i} + \frac{\partial}{\partial x_j}(\,\hat{\tau_{ij}}\,) \tag{2.2}$$

where $\hat{\rho}$ and $\hat{p}$ represent the instantaneous density and pressure. The

shear-stress tensor $\hat{\tau}_{ij}$ in equation (2.2) is given by:

$$\hat{\tau}_{ij} = \mu \left(\frac{\partial \hat{U}_i}{\partial x_j} + \frac{\partial \hat{U}_j}{\partial x_i} \right) \tag{2.3}$$

The above equations can be applied to all flows irrespective of whether or not turbulent. The rapid development of computers in last two decades provided an opportunity to obtain numerical solutions to the Navier-Stokes equations. This has lead to significant advances in the prediction of laminar flows but the complicated nature of turbulence prevented the direct solution of equation (2.2) for practically-relevant flows. The reasons for this can be understood by taking, for example, the process describing the dissipation of energy, which is one of the basic processes occurring in turbulent flows. Dissipation is governed by the small-scale motions which have a length-scale typically as small as 0.1 mm in air. Any numerical attempt to solve such flows through direct numerical simulations would require a computational mesh of dimensions smaller than the smallest vortices. This means that a vast number of cells would be required, even for small flow domains. Moreover, the time dependent nature of turbulence would require the solution of the unsteady forms of the equations, through the use of a large number of time steps. The direct numerical solution of equations (2.2) is clearly not a practical proposition.

In engineering practice, interest is confined to the averaged, rather than the instantaneous, characteristics of turbulent flows. This enables significant simplification of the Navier-Stokes equations through the time-averaging of the terms in those equations.

Reynolds (1895) suggested that each instantaneous variable in the Navier-Stokes equations may be decomposed into a mean and a fluctuating part, thus:

$$\hat{U}_i = U_i + u_i, \qquad \hat{\rho} = \rho + \rho' \qquad \text{and} \qquad \hat{p} = p + p'$$

where the mean parts are obtained through statistical averaging, defined

by:

$$U_i = \lim_{\Delta t \to \infty} \frac{1}{\Delta t} \int_{t_0}^{t_0+\Delta t} \hat{U}_i dt \tag{2.4}$$

By substituting the instantaneous variables in equations (2.1) and (2.2) with the mean and fluctuating parts and averaging with respect to time there yields, for a constant-density steady flow, the following set of equations:

$$\frac{\partial U_i}{\partial x_i} = 0. \tag{2.5}$$

$$\rho U_j \frac{\partial U_i}{\partial x_j} = -\frac{\partial p}{\partial x_i} + \frac{\partial}{\partial x_j}\left(\tau_{ij} - \rho \overline{u_i u_j}\right) \tag{2.6}$$

Reynolds was the first to give equation (2.6) in this form and so this equation is usually called the Reynolds-Averaged Navier-Stokes Equation. The turbulent stresses $\overline{u_i u_j}$ are known as the Reynolds stresses. Unfortunately, the appearance of the Reynolds stresses means that equations (2.5) and (2.6) are no longer closed: all six components of the Reynolds-stress tensor need first to be determined. Since the turbulence and Prandtl's second kind of secondary motion are linked, an appropriate definition for those stresses is of essential importance for the prediction of flows in three-dimensional fully-developed ducts and channels. The manner of approximation of the turbulent stresses is the main subject of this work and will be treated in the following sections.

2.2 The k-ϵ Model of Turbulence

The k-ϵ model of turbulence is the most popular model in current computational fluid dynamic practice. Boussinesq's (1877) relationship forms the basis of this model. By analogy with laminar flow, the turbulent

stresses are taken to be proportional to the mean rate of strain. This defines a coefficient of proportionality, called the turbulent (or eddy) viscosity μ_t thus:

$$-\rho\,\overline{u_i u_j} = \mu_t \left(\frac{\partial U_i}{\partial x_j} + \frac{\partial U_j}{\partial x_i} \right) - \frac{2}{3}\rho\,\delta_{ij}\,k \tag{2.7}$$

The isotropic part in equation (2.7) was added to ensure that $\sum \overline{u_i^2} = 2k$. It must be mentioned that μ_t is not a property of the fluid but, rather, of the flow: it must first be defined to close equation (2.7). Dimensional analysis gives:

$$\mu_t = \rho\, C_\mu \frac{k^2}{\epsilon} \tag{2.8}$$

The constant C_μ turns out to be the square of the structure parameter $\overline{uv}/k$. The generally-accepted value for C_μ is 0.09.

The kinetic energy of turbulence (k) and the dissipation rate of turbulent kinetic energy (ϵ) are determined by solving transport equations of the form:

$$\overbrace{\rho U_j \frac{\partial \Phi}{\partial x_j}}^{\text{convection}} = \overbrace{\frac{\partial}{\partial x_j}\left(\Gamma_\Phi \frac{\partial \Phi}{\partial x_j} \right)}^{\text{diffusion}} + \overbrace{S_\Phi}^{\text{source}} \tag{2.9}$$

where Φ can stand for k or ϵ, Γ_Φ is the turbulent exchange (diffusivity) coefficient and S_Φ is the source term for the scalar quantity Φ, thus:

Φ	Γ_Φ	S_Φ
k	$\frac{\mu_t}{\sigma_k}$	$\rho\,(P_k - \epsilon)$
ϵ	$\frac{\mu_t}{\sigma_\epsilon}$	$\rho\,\frac{\epsilon}{k}\,(\,C_{\epsilon 1}\,P_k - C_{\epsilon 2}\,\epsilon\,)$

Table 2.1 Determination of terms for k and ϵ transport equations.

The values for empirical constants $\sigma_k, \sigma_\epsilon$, $C_{\epsilon 1}$ and $C_{\epsilon 2}$ are given in Table 2.2. The production of turbulent kinetic energy is formulated as:

$$P_k = -\overline{u_i u_j} \frac{\partial U_i}{\partial x_j} \tag{2.10}$$

Although widely used, two-equation models of turbulence, such as the k-ϵ, do not satisfactorily predict many kinds of turbulent flows. By assuming Boussinesq's concept of linear stress-strain relationship, all transport effects on the turbulent stresses are neglected and this introduces unacceptable errors in flows where history effects are important such as in a wall jet where the turbulent viscosity concept would wrongly result in the coincidence of the points of zero shear stress and zero strain rate. Another severe defect of k-ϵ model appears when the model is used to predict fully-developed flows in three-dimensional non-circular ducts where it erroneously predicts isotropy of the normal stresses ($\overline{u^2} = \overline{v^2} = 2/3$ k). The shear stress $\overline{uv}$ is also erroneously predicted as zero. Consequently, the terms A2 and A3 in streamwise-vorticity equation (1.2) vanish and hence the model is not able to produce any turbulence-driven secondary motion. The prediction of turbulence-driven secondary motion using the k-ϵ model is therefore only possible after suitable replacement of equation (2.7), as will be discussed below.

2.2.1 The Nonlinear Stress-strain Relationship

Rivlin (1957) suggested an analogy between the turbulent Newtonian fluid and the laminar flow of non-Newtonian fluid. He developed a relationship which expressed the stress components as polynomials in the gradients of velocity, acceleration etc. The idea of viscoelastic behaviour of turbulence was further developed by Lumley (1970) who indicated that turbulence undergoing homogeneous deformation behaves like a classical nonlinear non-Newtonian medium. But it was not until recently that

Speziale (1987) embodied such ideas into a practical relationship between the turbulent stresses and mean rate of strain which is potentially suited to flows in non-circular ducts.

In order to develop the nonlinear stress-strain relationship, Speziale restricted development to the next higher level of approximation to the linear form (equation 2.7). He assumed the functional form for the Reynolds stresses which was developed to the final shape by applying several constraints such as general coordinate and dimensional invariance, realizability and material frame-indifference in the limit of two-dimensional turbulence. The final nonlinear stress-strain relationship takes the form:

$$
\begin{aligned}
-\rho\,\overline{u_i u_j} = & -\frac{2}{3}\rho\, k\,\delta_{ij} + 2\,\mu_t\,\overline{D_{ij}} + C_D\,L_1\,(\overline{D_{im}}\,\overline{D_{mj}} - \frac{1}{3}\,\overline{D_{mn}}\,\overline{D_{mn}}\,\delta_{ij}) \\
& + C_E\,L_1\,(\overset{\circ}{\overline{D_{ij}}} - \frac{1}{3}\,\overset{\circ}{\overline{D_{mm}}}\,\delta_{ij})
\end{aligned}
\tag{2.11}
$$

where

$L_1 = 4\,\rho\,C_\mu^2\,\frac{k^3}{\epsilon^2}$

C_D, C_E - empirical constants (Table 2.2)

The main rate of strain tensor can be expressed as:

$$
\overline{D_{ij}} = \frac{1}{2}\left(\frac{\partial U_i}{\partial x_j} + \frac{\partial U_j}{\partial x_i}\right) \tag{2.12}
$$

while the Oldroyd derivative of the main rate of strain tensor takes form:

$$
\overset{\circ}{\overline{D_{ij}}} = \frac{\partial \overline{D_{ij}}}{\partial t} + U_m\frac{\partial \overline{D_{ij}}}{\partial x_m} - \frac{\partial U_i}{\partial x_m}\,\overline{D_{mj}} - \frac{\partial U_j}{\partial x_m}\,\overline{D_{mi}} \tag{2.13}
$$

The nonlinear stress-strain relationship (2.11), together with the definition of μ_t and transport equations for k and ϵ, identical to those of the

standard k-ϵ model form the nonlinear k-ϵ model which is denoted hereafter as NKE. The empirical constants are given in the table below:

C_μ	σ_k	σ_ϵ	$C_{\epsilon 1}$	$C_{\epsilon 2}$	C_D	C_E
0.09	1.0	1.22	1.44	1.92	1.68	1.68

Table 2.2 The constants for the nonlinear k-ϵ model

To see the implications of the nonlinear terms on the turbulence anisotropy, the full explicit relations for three-dimensional, fully-developed, flows are presented below:

$$
\begin{aligned}
-\rho\,\overline{u^2} &= -\frac{2}{3}\rho k + 2\,\mu_t\frac{\partial U}{\partial x} \\
&+ \frac{L_1 C_D}{4}\left\{4\left(\frac{\partial U}{\partial x}\right)^2 + \left(\frac{\partial W}{\partial x}\right)^2 + \left(\frac{\partial U}{\partial y}+\frac{\partial V}{\partial x}\right)^2\right. \\
&\left. - \frac{4}{3}\left[\left(\frac{\partial U}{\partial x}\right)^2 + \left(\frac{\partial V}{\partial y}\right)^2 + \frac{1}{2}\left(\left(\frac{\partial W}{\partial x}\right)^2 + \left(\frac{\partial W}{\partial y}\right)^2 + \left(\frac{\partial U}{\partial y}+\frac{\partial V}{\partial x}\right)^2\right)\right]\right\} \\
&- L_1 C_E\left\{2\left(\frac{\partial U}{\partial x}\right)^2 + \left(\frac{\partial U}{\partial y}\right)^2 - \left(\frac{\partial U}{\partial y}\frac{\partial V}{\partial x}\right) + U\frac{\partial^2 U}{\partial x^2} - V\frac{\partial^2 U}{\partial y \partial x}\right. \\
&\left. - \frac{2}{3}\left[\left(\frac{\partial U}{\partial x}\right)^2 + \left(\frac{\partial V}{\partial y}\right)^2 + \frac{1}{2}\left(\left(\frac{\partial W}{\partial x}\right)^2 + \left(\frac{\partial W}{\partial y}\right)^2 + \left(\frac{\partial U}{\partial y}+\frac{\partial V}{\partial x}\right)^2\right)\right]\right\} \qquad (2.14)
\end{aligned}
$$

$$
\begin{aligned}
-\rho\,\overline{v^2} &= -\frac{2}{3}\rho k + 2\,\mu_t\frac{\partial V}{\partial y} \\
&+ \frac{L_1 C_D}{4}\left\{4\left(\frac{\partial V}{\partial y}\right)^2 + \left(\frac{\partial W}{\partial y}\right)^2 + \left(\frac{\partial U}{\partial y}+\frac{\partial V}{\partial x}\right)^2\right. \\
&\left. - \frac{4}{3}\left[\left(\frac{\partial U}{\partial x}\right)^2 + \left(\frac{\partial V}{\partial y}\right)^2 + \frac{1}{2}\left(\left(\frac{\partial W}{\partial x}\right)^2 + \left(\frac{\partial W}{\partial y}\right)^2 + \left(\frac{\partial U}{\partial y}+\frac{\partial V}{\partial x}\right)^2\right)\right]\right\} \\
&- L_1 C_E\left\{\left(\frac{\partial V}{\partial x}\right)^2 + 2\left(\frac{\partial V}{\partial y}\right)^2 - \left(\frac{\partial U}{\partial y}\frac{\partial V}{\partial x}\right) + U\frac{\partial^2 V}{\partial x \partial y} - V\frac{\partial^2 V}{\partial^2 y}\right. \\
&\left. - \frac{2}{3}\left[\left(\frac{\partial U}{\partial x}\right)^2 + \left(\frac{\partial V}{\partial y}\right)^2 + \frac{1}{2}\left(\left(\frac{\partial W}{\partial x}\right)^2 + \left(\frac{\partial W}{\partial y}\right)^2 + \left(\frac{\partial U}{\partial y}+\frac{\partial V}{\partial x}\right)^2\right)\right]\right\} \qquad (2.15)
\end{aligned}
$$

$$
\begin{aligned}
-\ \rho\ \overline{w^2} &= -\frac{2}{3}\rho k \\
&+\ \frac{L_1 C_D}{4}\left\{\left(\frac{\partial W}{\partial x}\right)^2+\left(\frac{\partial W}{\partial y}\right)^2\right. \\
&-\ \left.\frac{4}{3}\left[\left(\frac{\partial U}{\partial x}\right)^2+\left(\frac{\partial V}{\partial y}\right)^2+\frac{1}{2}\left(\left(\frac{\partial W}{\partial x}\right)^2+\left(\frac{\partial W}{\partial y}\right)^2+\left(\frac{\partial U}{\partial y}+\frac{\partial V}{\partial x}\right)^2\right)\right]\right\} \\
&-\ L_1 C_E\left\{\left(\frac{\partial W}{\partial x}\right)^2+\left(\frac{\partial W}{\partial y}\right)^2\right. \\
&-\ \left.\frac{2}{3}\left[\left(\frac{\partial U}{\partial x}\right)^2+\left(\frac{\partial V}{\partial y}\right)^2+\frac{1}{2}\left(\left(\frac{\partial W}{\partial x}\right)^2+\left(\frac{\partial W}{\partial y}\right)^2+\left(\frac{\partial U}{\partial y}+\frac{\partial V}{\partial x}\right)^2\right)\right]\right\} \qquad (2.16)
\end{aligned}
$$

The expressions for shear stresses are:

$$
\begin{aligned}
-\rho\,\overline{uv} &= \mu_t\left(\frac{\partial U}{\partial y}+\frac{\partial V}{\partial x}\right) \\
&+\ \frac{L_1 C_D}{4}\left(\frac{\partial W}{\partial x}\frac{\partial W}{\partial y}\right)-\frac{L_1 C_E}{2}\left\{3\left(\frac{\partial U}{\partial x}\right)\left(\frac{\partial V}{\partial x}\right)\right. \\
&+\ 3\left(\frac{\partial U}{\partial y}\right)\left(\frac{\partial V}{\partial y}\right)+\left(\frac{\partial U}{\partial x}\right)\left(\frac{\partial U}{\partial y}\right)+\left(\frac{\partial V}{\partial y}\right)\left(\frac{\partial V}{\partial x}\right) \\
&-\ \left.\left[U\frac{\partial}{\partial x}\left(\frac{\partial U}{\partial y}+\frac{\partial V}{\partial x}\right)+V\frac{\partial}{\partial y}\left(\frac{\partial U}{\partial y}+\frac{\partial V}{\partial x}\right)\right]\right\} \qquad (2.17)
\end{aligned}
$$

$$
\begin{aligned}
-\rho\,\overline{uw} &= \mu_t\frac{\partial W}{\partial x} \\
&+\ \frac{L_1 C_D}{4}\left\{2\left(\frac{\partial W}{\partial x}\right)\left(\frac{\partial U}{\partial x}\right)+\left(\frac{\partial W}{\partial y}\right)\left(\frac{\partial U}{\partial y}\right)+\left(\frac{\partial W}{\partial y}\right)\left(\frac{\partial V}{\partial x}\right)\right\} \\
&-\ \frac{L_1 C_E}{2}\left\{3\left(\frac{\partial U}{\partial x}\right)\left(\frac{\partial W}{\partial x}\right)+2\left(\frac{\partial U}{\partial y}\right)\left(\frac{\partial W}{\partial y}\right)+\left(\frac{\partial V}{\partial x}\right)\left(\frac{\partial W}{\partial y}\right)\right. \\
&-\ \left.\left[U\frac{\partial}{\partial x}\left(\frac{\partial W}{\partial x}\right)+V\frac{\partial}{\partial y}\left(\frac{\partial W}{\partial x}\right)\right]\right\} \qquad (2.18)
\end{aligned}
$$

$$
\begin{aligned}
-\rho\,\overline{vw} &= \mu_t\frac{\partial W}{\partial y} \\
&+\ \frac{L_1 C_D}{4}\left\{2\left(\frac{\partial W}{\partial y}\right)\left(\frac{\partial V}{\partial y}\right)+\left(\frac{\partial W}{\partial x}\right)\left(\frac{\partial U}{\partial y}\right)+\left(\frac{\partial W}{\partial x}\right)\left(\frac{\partial V}{\partial x}\right)\right\} \\
&-\ \frac{L_1 C_E}{2}\left\{3\left(\frac{\partial V}{\partial y}\right)\left(\frac{\partial W}{\partial y}\right)+2\left(\frac{\partial V}{\partial x}\right)\left(\frac{\partial W}{\partial x}\right)+\left(\frac{\partial W}{\partial x}\right)\left(\frac{\partial U}{\partial y}\right)\right. \\
&-\ \left.\left[U\frac{\partial}{\partial x}\left(\frac{\partial W}{\partial y}\right)+V\frac{\partial}{\partial y}\left(\frac{\partial W}{\partial y}\right)\right]\right\} \qquad (2.19)
\end{aligned}
$$

In the above equations, the first lines correspond to Boussinesq's relationship while the rest is a consequence of the nonlinear part of equation (2.11). New terms appear, they contain quadratic mean-velocity gradients and remain finite even for fully-developed conditions. Accordingly, the model produces different levels of the normal stresses at every point in the flow field which is the necessary mechanism for generating the turbulence-driven secondary motion. Furthermore, the presence of secondary motion gradients in the main-shear-stress expressions ($\overline{uw}$ and $\overline{vw}$) ensures the feedback influence of the secondary motion on the main flow.

Relations (2.14)–(2.19) and those which arise from the algebraic-stress model are arguably quite similar: both models provide explicit functions for the Reynolds stresses but the similarities end there. By simplifying the modelled equations for $\overline{u_i u_j}$, different stress expressions may be obtained depending on the choice of closure assumptions used, on whether production is assumed equal to dissipation and, also, on whether wall-reflection terms are included. The nonlinear model is simply a constitutive relationship which is one order higher then Boussinesq's. Unlike ASM, it is always coordinate invariant.

2.3 The Reynolds-Stress-Transport Model

Many of the defects associated with the Boussinesq's relationship can be eliminated altogether by determining the Reynolds stresses from their own transport equations. To derive the Reynolds-stress equations, the Navier-Stokes equations for the instantaneous i and j components are multiplied with u_j and u_i respectively and then summed and time-averaged. The resulting differential transport equations for the Reynolds-stress tensor, for stationary constant-density flow in the absence of body forces,

are given as:

$$U_k \frac{\partial \overline{u_i u_j}}{\partial x_k} = - (\overline{u_i u_k}\frac{\partial U_j}{\partial x_k} + \overline{u_j u_k}\frac{\partial U_i}{\partial x_k}) + \overline{\frac{p'}{\rho}\left(\frac{\partial u_i}{\partial x_j} + \frac{\partial u_j}{\partial x_i}\right)} - \frac{\partial}{\partial x_k}(\overline{u_i u_j u_k})$$
$$- \frac{1}{\rho}\left(\frac{\partial}{\partial x_j}\overline{p' u_i} + \frac{\partial}{\partial x_i}\overline{p' u_j}\right) + \nu\left(\overline{u_i \frac{\partial^2 u_j}{\partial x_k^2}} + \overline{u_j \frac{\partial^2 u_i}{\partial x_k^2}}\right) \qquad (2.20)$$

The first term in equation (2.20) represents convection of the turbulent stresses by the mean velocity. The second term represents production due to interaction between the turbulent motion and the mean rates of strain. The third term is called the pressure-strain correlation term. This term tends to equalize the normal stresses by re-distributing the turbulence kinetic energy amongst the three fluctuating components. The fourth term contains triple-velocity correlations: it represents the transport of the $\overline{u_i u_j}$ in the x_k direction by the velocity fluctuations. The fluctuating pressure-velocity correlations also represent a transport term, due to pressure fluctuations. The last term involves mutual interaction between the molecular viscosity and turbulent velocity fluctuations and is usually decomposed into two parts:

$$\nu\left(\overline{u_i \frac{\partial^2 u_j}{\partial x_k^2}} + \overline{u_j \frac{\partial^2 u_i}{\partial x_k^2}}\right) = \frac{\partial}{\partial x_k}\left(\nu \frac{\partial \overline{u_i u_j}}{\partial x_k}\right) - 2\nu\left(\overline{\frac{\partial u_i}{\partial x_k}\frac{\partial u_j}{\partial x_k}}\right) \qquad (2.21)$$

The first part represents the molecular transport of the turbulent stresses. The second term is always negative and represents the dissipation of turbulent energy by viscous action.

Equation (2.20) can now be re-written as:

$$\overbrace{U_k \frac{\partial \overline{u_i u_j}}{\partial x_k}}^{\text{convection}} = \overbrace{- (\overline{u_i u_k}\frac{\partial U_j}{\partial x_k} + \overline{u_j u_k}\frac{\partial U_i}{\partial x_k})}^{\text{production}}$$
$$\overbrace{- \frac{\partial}{\partial x_k}\left[\overline{u_i u_j u_k} + \frac{1}{\rho}(\overline{p' u_i}\delta_{jk} + \overline{p' u_j}\delta_{ik}) - \nu\frac{\partial \overline{u_i u_j}}{\partial x_k}\right]}^{\text{diffusion}}$$
$$\underbrace{- 2\nu\left(\overline{\frac{\partial u_i}{\partial x_k}\frac{\partial u_j}{\partial x_k}}\right)}_{\text{dissipation}} + \underbrace{\overline{\frac{p'}{\rho}\left(\frac{\partial u_i}{\partial x_j} + \frac{\partial u_j}{\partial x_i}\right)}}_{\text{redistribution}} \qquad (2.22)$$

Unfortunately, having obtained the Reynolds-stress equations, the determination of turbulent stresses $\overline{u_i u_j}$ is far from complete. It is obvious from equation (2.22) that only the convection, production and viscous-diffusion terms can be treated in exact form. The task now is to approximate the terms representing diffusion, dissipation and redistribution as functions of known or knowable quantities such as the mean velocity (U_i), turbulent stresses ($\overline{u_i u_j}$) and the dissipation of turbulent kinetic energy (ϵ). This is the subject of the following sections.

2.3.1 Diffusion

The diffusion term in equation (2.22) is comprised of three different parts: diffusion due to viscous effects, diffusion caused by velocity fluctuations and, finally, by pressure fluctuations. The viscous term is usually neglected for high Reynolds-number flows away from walls but, since the numerical incorporation of this term in a computer code is straightforward, it has been retained in the present study.

The term which represents diffusion by pressure fluctuations is difficult to model because the pressure fluctuations cannot be measured directly. Hanjalic and Launder (1972,a) obtained an estimate of the magnitude of this term by measuring all the remaining terms in the equation for the turbulence kinetic energy in an asymmetric plane channel flow. Pressure diffusion was then taken as the out-of-balance term which showed it to be much smaller than all the others. Those workers expressed some caution about drawing general conclusions from that simple experiment but the result is nevertheless quite useful. Some other measurements for various flows (Lawn (1971) for pipe-flow and Irwin (1973) for plane-wall jet) also confirmed that the pressure diffusion term is small and can be neglected, which is what will be done in the present work.

Daly and Harlow (1970) proposed modelling the triple-velocity correla-

tions in the manner suggested by gradient-transport hypothesis, thus:

$$-\overline{u_i u_j u_k} = C_s \frac{k}{\epsilon} \overline{u_k u_l} \frac{\overline{\partial u_i u_j}}{\partial x_l} \tag{2.23}$$

where C_s is an empirical constant.

Hanjalic and Launder (1972,b) derived a transport equation for the triple-velocity correlations and then simplified it by neglecting convective transport and by applying numerous approximations. The outcome was an algebraic expression of the form:

$$-\overline{u_i u_j u_k} = C_s \frac{k}{\epsilon} \left(\overline{u_i u_l} \frac{\overline{\partial u_j u_k}}{\partial x_l} + \overline{u_j u_l} \frac{\overline{\partial u_k u_i}}{\partial x_l} + \overline{u_k u_l} \frac{\overline{\partial u_i u_j}}{\partial x_l} \right) \tag{2.24}$$

The last term in (2.24) represents the model proposed by Daly and Harlow. Unlike Daly and Harlow's model, equation (2.24) satisfies the condition of rotational symmetry (i.e. the same result would be obtained irrespective of the rotation of coordinate system). In order to compare the performance of these two proposals several researchers (see Launder et al. (1975) , Samaraweera (1978) and Gibson and Younis (1982)) applied them to various flows and found that the Daly and Harlow model produced better overall results. Consequently, the Daly and Harlow model for triple-velocity correlations is adopted in the present study.

2.3.2 Dissipation

Dissipation of turbulent kinetic energy occurs in the smallest vortices which, when the local turbulent Reynolds number is high, are assumed

to be isotropic. Rotta (1951) proposed modelling the dissipation term in equation (2.22) as follows:

$$2\nu\left(\overline{\frac{\partial u_i}{\partial x_k}\frac{\partial u_j}{\partial x_k}}\right) = \frac{2}{3}\delta_{ij}\,\epsilon \tag{2.25}$$

where

$$\delta_{ij} = \begin{cases} 1 & \text{for } i = j \\ 0 & \text{for } i \neq j \end{cases}$$

As for the k-ϵ model, the dissipation is obtained from its own transport equation. The transport equation for ϵ, when used in conjunction with the Reynolds-stress model, is of the same general form as equation (2.9) except for the diffusion part which is taken, following Hanjalic and Launder (1972,b), as:

$$\text{diffusion}(\epsilon) = C_\epsilon \frac{\partial}{\partial x_k}\left(\frac{k}{\epsilon}\overline{u_k u_l}\frac{\partial \epsilon}{\partial x_l}\right) \tag{2.26}$$

2.3.3 Redistribution

The redistributive nature of the pressure-strain term can be seen from consideration of the turbulent-kinetic-energy equation which is obtained from equation (2.22) by contraction of the indices and by summation. The absence of the pressure-strain term from that equation means that this term has no influence on the total energy balance: its role is simply to re-distribute the total energy among the various components. With this in mind, it seems that the redistribution term is very influential in determining the turbulence anisotropy and hence the success of a particular Reynolds-stress model in predicting the turbulence-driven secondary motion will depend on the correct modelling of this term.

A Poisson equation for fluctuating pressure can be obtained by taking the divergence of the equation for fluctuating motion which, after multiplication with $(\partial u_i/\partial x_j + \partial u_j/\partial x_i)$, averaging and integration yields (Chou, 1945):

$$\overline{\frac{p'}{\rho}\left(\frac{\partial u_i}{\partial x_j}+\frac{\partial u_j}{\partial x_i}\right)} = \frac{1}{4\pi}\int_V \overbrace{\left[\overline{\left(\frac{\partial^2 u_l u_m}{\partial x_l \partial x_m}\right)'\left(\frac{\partial u_i}{\partial x_j}+\frac{\partial u_j}{\partial x_i}\right)'}\right]}^{\Phi_{ij,1}}$$

$$+ \underbrace{2\left(\frac{\partial U_l}{\partial x_m}\right)'\left[\overline{\left(\frac{\partial u_m}{\partial x_l}\right)'\left(\frac{\partial u_i}{\partial x_j}+\frac{\partial u_j}{\partial x_i}\right)'}\right]}_{\Phi_{ij,2}} \frac{dV(x')}{r}$$

$$+ \underbrace{\frac{1}{4\rho\pi}\int_{A'}\left[\frac{1}{r}\frac{\partial}{\partial n'}\overline{p'\left(\frac{\partial u_i}{\partial x_j}+\frac{\partial u_j}{\partial x_i}\right)'} - \overline{p'\left(\frac{\partial u_i}{\partial x_j}+\frac{\partial u_j}{\partial x_i}\right)'}\frac{\partial}{\partial n'}\left(\frac{1}{r}\right)\right]}_{\Phi_{ij,w}} dA' \quad (2.27)$$

All primed terms in (2.27) denote position x′ which is removed from the position x by distance r. dV(x′) is a volume element, dA′ is a surface element and $\partial/\partial n'$ denotes the normal derivative of the surface.

This term can now be expressed as a sum of three terms $\Phi_{ij,1}$, $\Phi_{ij,2}$ and $\Phi_{ij,w}$. $\Phi_{ij,1}$ is a consequence of interactions among different fluctuating velocity components. $\Phi_{ij,2}$ represents interaction between the mean rates of strain and fluctuating velocities. The surface integral, denoted as $\Phi_{ij,w}$, is important only in regions adjacent to a wall. The modelling of these three terms is presented in the following sections.

2.3.3.1 A Model for $\Phi_{ij,1}$

The $\Phi_{ij,1}$ term is the only part of pressure-strain correlation which remains in anisotropic homogeneous turbulence with zero mean strain. Turbulence will evolve into an isotropic state under these conditions

and hence this term is usually called the return-to-isotropy term. Rotta (1951) proposed $\Phi_{ij,1}$ to be linear function of the anisotropy tensor a_{ij}, as follows:

$$\Phi_{ij,1} = -C_1 \epsilon a_{ij} = -C_1 \epsilon \left(\frac{\overline{u_i u_j}}{k} - \frac{2}{3}\delta_{ij} \right) \tag{2.28}$$

Many researchers tried to formulate nonlinear expression for $\Phi_{ij,1}$: either as nonlinear combination of a_{ij} (Lumley and Khajeh Nouri,1974) or to introduce nonlinearity through the definition of variable coefficient C_1 (Lumley and Newman,1977).

Hanjalic (1984) argued that although the nonlinear nature of redistribution was not in doubt, the use of nonlinear expressions had not shown any particular improvement as was shown by Vasic (1982) for some flows where $\Phi_{ij,1}$ is dominant. For this reason, and because of the considerable complexity of nonlinear models for $\Phi_{ij,1}$, expression (2.28) is adopted in the present study. The value for the empirical constant C_1 depends on the overall model and so its value is presented in Section 2.4.

2.3.3.2 A Model for $\Phi_{ij,2}$

The second term in the pressure-strain correlation contains the rate of mean-flow deformation as well as the components of the fluctuating velocities. By assuming that mean flow is homogeneous in the vicinity of observed point, Rotta (1951) proposed the following approximation for $\Phi_{ij,2}$:

$$\Phi_{ij,2} = \frac{\partial U_l}{\partial x_m} \left(a_{lj}^{mi} + a_{li}^{mj} \right) \tag{2.29}$$

where the fourth-order tensor reads:

$$a_{lj}^{mi} = -\frac{1}{2\pi}\int_V \frac{\partial^2 \overline{u'_m u_i}}{\partial r_l \partial r_j}\,\frac{dV(x')}{r} \tag{2.30}$$

where r_l and r_j are the Cartesian components of r.

The integration in equation (2.30) seems to be the logical way to obtain the values for a_{lj}^{mi} but in situation of inhomogeneous turbulence the turbulent correlation $\overline{u'_m u_i}$ is unknown. For that reason Hanjalic (1970) and Hanjalic and Launder (1972,b) proposed modelling of a_{lj}^{mi} as a nonlinear combination of second-order tensors. By abandoning the nonlinear terms from that equation, Launder, Reece and Rodi (1975) proposed the form which satisfies the symmetry constraints ($a_{lj}^{mi} = a_{lj}^{im} = a_{jl}^{im}$), as follows:

$$\begin{aligned} a_{lj}^{mi} &= \alpha\,\overline{u_m u_i}\,\delta_{lj} + \beta\,(\,\overline{u_i u_j}\,\delta_{ml} + \overline{u_m u_j}\,\delta_{il} + \overline{u_m u_l}\,\delta_{ij} + \overline{u_i u_l}\,\delta_{mj}\,) \\ &+ C_2\,\overline{u_l u_j}\,\delta_{mi} + [\eta\,\delta_{mi}\,\delta_{lj} + \nu_1(\,\delta_{ml}\,\delta_{ij} + \delta_{mj}\,\delta_{il}\,)]\,k \end{aligned} \tag{2.31}$$

Using the kinematic constraint of continuity $a_{li}^{mi} = 0$ as well as expression $a_{jj}^{mi} = 2\overline{u_m u_i}$ all coefficients (α, β, η and ν_1) in equation (2.31) can be expressed as function of C_2:

$$\left.\begin{aligned} \alpha &= \frac{10+4C_2}{11} \qquad \beta = -\frac{2+3C_2}{11} \\ \eta &= -\frac{4+50C_2}{55} \qquad \nu_1 = \frac{6+20C_2}{55} \end{aligned}\right\} \tag{2.32}$$

Thus only determination of one empirical constant is needed for closing equation (2.31). On combining (2.31), (2.32) and (2.29) term $\Phi_{ij,2}$ takes the form:

$$\begin{aligned} \Phi_{ij,2} = &-\frac{C_2+8}{11}\,(P_{ij} - \frac{2}{3}\,\delta_{ij}\,P_k) - \frac{30C_2-2}{55}\,k\,\left(\frac{\partial U_i}{\partial x_j} + \frac{\partial U_j}{\partial x_i}\right) \\ &- \frac{8C_2-2}{11}\,(D_{ij} - \frac{2}{3}\,\delta_{ij}\,P_k) \end{aligned} \tag{2.33}$$

where

$$P_{ij} = -\left(\overline{u_i u_k}\frac{\partial U_j}{\partial x_k} + \overline{u_j u_k}\frac{\partial U_i}{\partial x_k}\right)$$

$$D_{ij} = -\left(\overline{u_i u_k}\frac{\partial U_k}{\partial x_j} + \overline{u_j u_k}\frac{\partial U_k}{\partial x_i}\right)$$

and P_k denotes production of turbulent kinetic energy.

Launder, Reece and Rodi (1975) recognized the dominant role of the first term in equation (2.33) and therefore proposed a simplified version thus:

$$\Phi_{ij,2} = -C_2\left(P_{ij} - \frac{2}{3}\delta_{ij}P_k\right) \tag{2.34}$$

where the value of empirical constant C_2 when used in simplified approximation (2.34) is clearly different from the value used in the complete expression (2.33). The values for those constants together with all others needed for the Reynolds-stress model are presented in Section 2.4.

Launder, Reece and Rodi applied the complete and the simplified version of $\Phi_{ij,2}$ to two-dimensional inhomogeneous shear flows including the jet, the wake, the mixing layer and plane channel flow. They obtained better overall agreement using the complete version (2.33). The simplified version (2.34) was generally of similar accuracy as (2.33) for free flows but slightly worse for wall flows. This was attributed by the authors to defects in the near-wall corrections rather than in model (2.34).

The complete model for $\Phi_{ij,2}$ was further tested for turbulent shear flows with extra rates of strain by Irwin and Smith (1975) for curved flows and by Launder and Morse (1977) for swirling jets. The model produced good agreement with experimental results for the first group of flows while agreement for the second group was not at all satisfactory. Younis (1984) suggested that the cause for such malprediction of the free swirling jet flows must be attributed to the value of constant C_2 in the model for

$\Phi_{ij,2}$.

In all flows mentioned above, the anisotropy of the normal stresses is not as important as the shear stresses, and hence it is not possible to arrive at an early conclusion regarding the suitability of either model for the prediction of turbulence-driven secondary motion.

Reece (1977) did obtain apparently good results for a square duct using the complete model (2.33) but his predictions cannot be used as a basis for eliminating the simple version (2.34) from further consideration. In fact, the choice between the two models for $\Phi_{ij,2}$ will be shown to be of crucial importance for predicting the turbulence-driven secondary motion as will be discussed in Section 2.4.

2.3.3.3 A Model for $\Phi_{ij,w}$

The wall influences the turbulence in its vicinity by modifying the pressure field in such way as to impede the transfer of energy from the streamwise direction to that normal to it. Thus the normal stress component in the direction perpendicular to the wall is damped while, by continuity, the other two stress components are enhanced. Clearly, then, rigid boundaries are very influential in determining the turbulence anisotropy and their effects must be correctly approximated.

Launder et al. (1975) suggested that the wall affects both the mean-strain and the turbulent part of the pressure-strain correlation. Accordingly, they proposed a near-wall correction of the form:

$$\Phi_{ij,w} = \left[C_1' \frac{\epsilon}{k} \left(\overline{u_i u_j} - \frac{2}{3} \delta_{ij} k \right) + \frac{\partial U_l}{\partial x_m} (b_{lj}^{mi} + b_{li}^{mj}) \right] f\left(\frac{l}{x_2}\right) \qquad (2.35)$$

where function $f\left(\frac{l}{x_2}\right)$ depends on the turbulent length scale (l) and on

the normal distance from the wall (x_2). The mean-strain part of equation (2.35) needs further approximation. The fourth-order tensor b_{ij}^{mi} has similar characteristics as the corresponding tensor a_{ij}^{mi} in equation (2.29) and thus can be decomposed in the same way, only with different value of the constants. In order to reduce the number of unknown constants in that equation, Launder et al. (1975) applied the constraint of continuity which reflects the redistributive nature of $\Phi_{ij,w}$ term. Thus they determined a wall correction to the mean-strain term which when applied to equation (2.35) yields:

$$\Phi_{ij,w} = \left[C_1' \frac{\epsilon}{k} \left(\overline{u_i u_j} - \frac{2}{3} \delta_{ij} k \right) + C_2' \left(P_{ij} - D_{ij} \right) \right] f \left(\frac{l}{x_2} \right) \qquad (2.36)$$

where P_{ij} and D_{ij} are determined in the same way as for equation (2.33).

Younis (1982) applied this model to a number of boundary-layer flows and found the model expressed by (2.36) to be very sensitive to the wall boundary conditions imposed on the $\overline{u_i u_j}$ and ϵ equations. He attributed such behaviour to the serious inconsistencies in the model formulation as discovered by Gessner and Epich (1981).

The idea of a separate wall correction for both parts of pressure-strain correlation ($\Phi_{ij,1}$ and $\Phi_{ij,2}$) was adopted by others as well. Shir (1973) proposed a correction for the $\Phi_{ij,1}$ term as follows:

$$\Phi_{ij,1}' = C_1' \frac{\epsilon}{k} \left(\overline{u_k u_m} n_k n_m \delta_{ij} - \frac{3}{2} \overline{u_k u_i} n_k n_j - \frac{3}{2} \overline{u_k u_j} n_k n_i \right) f \left(\frac{l}{n_i r_i} \right) \qquad (2.37)$$

where

r - the position vector,

n_i - the unit vector normal to the surface

Gibson and Launder (1978), following Shir, proposed the following addition :

$$\Phi'_{ij,2} = C'_2 \left(\Phi_{km,2}\, n_k n_m\, \delta_{ij} - \frac{3}{2}\Phi_{ki,2}\, n_k n_j - \frac{3}{2}\Phi_{kj,2}\, n_k n_i \right) f\left(\frac{l}{n_i r_i}\right) \quad (2.38)$$

Combination of equations (2.37) and (2.38) provides a complete near-wall correction to the pressure-strain correlation (2.27):

$$\Phi_{ij,w} = \Phi'_{ij,1} + \Phi'_{ij,2} \quad (2.39)$$

This model was successfully applied in various calculations (Gibson and Launder (1978), Gibson et al. (1981) and Younis (1982)) and is therefore adopted in the present study. The values for the empirical constants C'_1 and C'_2 are given in Section 2.4.

So far, the definition of $f\left(\frac{l}{n_i r_i}\right)$ has not been considered but it is obvious that this function controls the influence of the wall, as discussed below.

2.3.4 Wall-Damping Function

The main role of the function f in expressions (2.37) and (2.38) is to decrease the wall influence on the pressure-strain correlation with increasing the distance from it. It is therefore logical to assume that the wall function f is inversely proportional to the distance from the nearest wall. Launder et al. (1975) assumed a linear function (e.g. $f_y = L_y/y$). Gibson and Rodi (1989) found that a more rapid variation for the f produced better results for various boundary layer flows and therefore it was adopted for their channel flow calculations. The linear and nonlinear definitions of f represent different physical behaviour in the sense that the linear approach extends the wall influence deeper inside the flow while

a quadratic approach, for example, would confine the wall effects more closely to the wall. In the present work, a quadratic definition of the wall-damping function was found to be the more appropriate one (Section 4.2.1).

The presence of two walls in three-dimensional duct flows further complicates the determination of f. Here, we assume that the bottom wall damps only the vertical fluctuations and the side wall damps only the horizontal fluctuations. The following separate wall functions are proposed:

$$f_x = \frac{L_x^2}{< x >^2} \quad ; \; f_y = \frac{L_y^2}{< y >^2} \tag{2.40}$$

where L_x and L_y represent corresponding turbulent length scales.

In order to account for the interaction of several surfaces, Naot and Rodi's (1981) proposal for the definition of the average distance from the wall is adopted :

$$\frac{1}{< y >^2} = \frac{2}{\pi} \int_0^{2\pi} \frac{d\Phi}{s^2} \tag{2.41}$$

The solution of integral (2.41) for a single flat plate of finite length l (Fig. 2.1) is

$$\frac{1}{< y >^2} = \frac{1}{\pi y^2} \left[\arctan\left(\frac{l-x}{y}\right) + \arctan\left(\frac{x}{y}\right) + \frac{1}{\frac{y}{l-x} + \frac{l-x}{y}} + \frac{1}{\frac{y}{x} + \frac{x}{y}} \right] \tag{2.42}$$

An analogous solution for $\frac{1}{<x>^2}$ can be obtained.

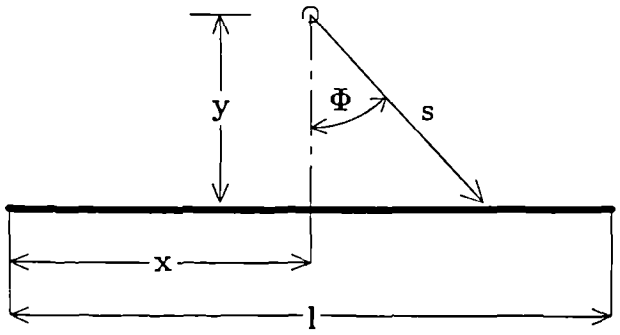

Fig. 2.1 Nomenclature for calculation of average wall distance

The turbulent length scale is usually accepted to be proportional to

$$L \propto \frac{k^{3/2}}{\epsilon} \tag{2.43}$$

while the dimensionless coefficient of proportionality is taken as

$$\frac{C_\mu^{3/4}}{\kappa} \tag{2.44}$$

where κ is the von Karman constant.

A three-dimensional square-duct flow can be imagined as two separate two-dimensional boundary layers interacting in the corner. Bearing in mind that the constant C_μ in two-dimensional boundary layer represents a structural parameter of the turbulence, for three-dimensional flows the following forms of the function L are proposed:

$$L_x = \frac{1}{\kappa} \left| \frac{\overline{uw}}{k} \right|_{wall}^{3/2} \frac{k^{3/2}}{\epsilon} \tag{2.45}$$

$$L_y = \frac{1}{\kappa} \left| \frac{\overline{vw}}{k} \right|_{wall}^{3/2} \frac{k^{3/2}}{\epsilon} \tag{2.46}$$

2.3.5 Free-Surface-Damping Function

The measurements in an open channel flow by Komori et al. (1982) showed that the vertical turbulent fluctuations are damped in the vicinity of the free surface and the turbulence anisotropy is therefore increased there. Thus, the free-surface exerts a similar influence as that observed in the near-wall region which suggests that similar treatments may be appropriate. A damping function is therefore introduced, following Naot and Rodi (1982), thus:

$$f_f = \left[\frac{L}{< \frac{1}{y_f^2} >^{-1/2} + C_f L} \right]^2 \tag{2.47}$$

where

C_f - an empirical constant.

The turbulent length scale for the free-surface-damping function is determined as:

$$L = \frac{C_\mu^{3/4}}{\kappa} \frac{k^{3/2}}{\epsilon} \tag{2.48}$$

It can be seen from equation (2.47) that without $C_f L$ term, the formulation of f_f is the same as for the wall. However, Naot and Rodi argued that length scale of turbulence has a finite value at the surface and therefore the actual distance from the surface was replaced by the distance from a point above the surface. Thus, equation (2.47) at the surface becomes $1/C_f^2$. The empirical constant C_f was adjusted with the aid of experimental results for developed open-channel flow to the value of 0.16.

2.4 The Reynolds-Stress-Model Development

From reviewing various theoretical and calculated results, appropriate models were adopted for the processes of diffusion (equation 2.23), dissipation (equation 2.25) and pressure-strain redistribution (return-to-isotropy term: equation 2.28) in the Reynolds-stress equations. This work was started using the simplified $\Phi_{ij,2}$ model (equation 2.34) in conjunction with Shir's (1973) and Gibson and Launder's (1978) proposals for $\Phi_{ij,w}$ term (equations 2.37, 2.38 and 2.39). The linear form of the wall-damping function was assumed. This model combination (denoted as the RSM0) has produced very good results for a wide range of complex flows (see Younis (1982) ; Gibson, Jones and Younis (1981) ; Kebede, Launder and Younis (1985) ; Launder, Tselepidakis and Younis (1987) etc.). The constants appearing in the RSM0 are assigned the following values recommended by the originators:

Constant	C_1	C_2	C_1'	C_2'	C_s	C_ϵ	$C_{\epsilon 1}$	$C_{\epsilon 2}$
RSM0	1.8	0.6	0.5	0.3	0.22	0.18	1.45	1.90

Table 2.3 Model constants for RSM0

Unfortunately, it soon became clear that this model was not producing secondary motion of sufficient strength and hence the distortion to the mean-velocity field was less than expected. This behaviour in three-dimensional fully-developed duct flows can be related to a known defect in this model which is apparent even in simple free shear flows, namely that the simplified model for $\Phi_{ij,2}$, when used in conjunction with Daly and Harlow's proposal for the diffusion term, produces equal normal stresses in the plane normal to the main flow direction. This defect did not matter too much in the simpler applications mentioned above because turbulence anisotropy was not as important as the level of shear stress.

The difference between $\overline{u^2}$ and $\overline{v^2}$ in the RSM0, when applied to the flows in non-circular ducts, is entirely due to $\Phi_{ij,w}$ and can therefore be increased by prescribing a more rapid decay of the wall function there. It was indeed found that the model's behaviour was improved by the quadratic definition of that function. However, this was still resulting in mild mean-velocity distortions and this suggested that different model combinations were needed to ensure a greater turbulence anisotropy. The most logical step to follow then was to abandon the simplified $\Phi_{ij,2}$ model in favour of the complete one of Launder, Reece and Rodi (equation 2.33). However, the $\Phi_{ij,w}$ model of Launder, Reece and Rodi (equation 2.36) was known to be fundamentally defective and was therefore replaced with the wall-reflections models of Shir and Gibson and Launder, presented earlier in this chapter. This model combination will be referred to from now on as RSM.

The new combination of $\Phi_{ij,2}$ and $\Phi_{ij,w}$ requires re-optimization of model constants in order to obtain approximately correct levels of relative turbulent stresses in the vicinity of the wall. This is usually done by simplifying equation (2.22) and by assuming that turbulence near a wall is in local equilibrium (i.e. production of turbulent kinetic energy, P_k, equals its dissipation rate, ϵ). The transport terms in equation (2.22) can then be neglected and algebraic expressions for the stress levels are obtained as:

$$\frac{\overline{u_i u_j}}{k} = \frac{2}{3}\,\delta_{ij} + \frac{P_{ij} + \Phi_{ij,2} - \frac{2}{3}\delta_{ij}\epsilon + \Phi_{ij,w}}{C_1\,\epsilon} \qquad (2.49)$$

Substitution of P_{ij}, $\Phi_{ij,2}$ and $\Phi_{ij,w}$ into equation (2.49) and setting the wall function f to unity produces the following equations (the streamwise direction is taken as x_1 and x_2 is normal to the horizontal plane surface):

$$\frac{\overline{u_1^2}}{k} = \frac{2}{3} + \frac{8 + 12C_2}{33C_1} + \frac{C_1'}{C_1}\frac{\overline{v^2}}{k} + \frac{2C_2'}{3C_1}(\alpha - 2\gamma)$$

$$\frac{\overline{u_2^2}}{k} = \frac{2}{3} + \frac{2 - 30C_2}{33C_1} - 2\frac{C_1'}{C_1}\frac{\overline{v^2}}{k} + \frac{2C_2'}{3C_1}(-2\alpha + 4\gamma)$$

$$\frac{\overline{u_3^2}}{k} = \frac{2}{3} + \frac{-10 + 18C_2}{33C_1} + \frac{C_1'}{C_1}\frac{\overline{v^2}}{k} + \frac{2C_2'}{3C_1}(\alpha - 2\gamma)$$

$$\left(\frac{\overline{u_1 u_2}}{k}\right)^2 = \frac{1}{C_1 + 3C_1'}\left(\frac{\overline{v^2}}{k} - \alpha\frac{\overline{v^2}}{k} + \beta - \gamma\frac{\overline{u^2}}{k}\right) + \frac{3C_2'}{C_1 + 3C_1'}\left(\frac{\alpha\overline{v^2}}{k} - \beta + \gamma\frac{\overline{u^2}}{k}\right)$$

where

$$\alpha = \frac{C_2 + 8}{11} \quad \beta = \frac{30C_2 - 2}{55} \quad \gamma = \frac{8C_2 - 2}{11}$$

The values of model constants for the RSM, as proposed in Younis (1982), are given in table 2.4.

Constant	C_1	C_2	C_1'	C_2'	C_s	C_ϵ	$C_{\epsilon 1}$	$C_{\epsilon 2}$
RSM	1.5	0.4	0.5	0.1	0.22	0.18	1.45	1.90

Table 2.4 Model constants for RSM

With those constants, the following stress levels are obtained:

Quantity	$\overline{u_1^2}/k$	$\overline{u_2^2}/k$	$\overline{u_3^2}/k$	$\overline{u_1 u_2}/k$
RSM	1.03	0.25	0.72	- 0.234
Data[1]	1.10	0.25	0.65	- 0.26

Table 2.5 Relative stress levels for the near-wall turbulence

[1] A consensus of near-wall turbulence data given in Gibson and Launder (1978)

2.5 Closure to Chapter 2

Two turbulence models chosen for the present applications were presented in this chapter: the complete Reynolds-stress model and the nonlinear variant of k- ϵ model of turbulence. The formulation of the standard k-ϵ model and its inability to produce turbulence-driven secondary motion was discussed in Section 2.2. The benefits of using a nonlinear stress-strain relationship were given in Subsection 2.2.1. Various approximations to the unknown terms in the Reynolds-stress transport equation were considered in Section 2.3. The final version of the Reynolds-stress model used in this work was presented in Section 2.4.

In the next chapter, the numerical procedure employed for the solution of the mean-flow and turbulence-model equations will be presented.

Chapter 3

SOLUTION PROCEDURE

3.1 Introduction

The numerical treatment of the averaged momentum equations is closely linked with the physical nature of the flow under consideration, particularly whether or not such flow contains a recirculating zone. If one does not occur, the flow depends only on upstream conditions and is called parabolic. The numerical solution of those flows does not require an iterative procedure in the main-flow direction. In contrast, if reverse flow does occur in the main-flow direction, the flow is influenced by downstream conditions and is regarded as elliptic requiring an iterative solution procedure. Often a flow is encountered which exhibits both parabolic and elliptic characteristics as, for example, in the case of the three-dimensional flow in non-circular ducts. There, the flow is parabolic in the main direction but elliptical in the cross-stream plains. The implications of this on the choice of the present solution strategy will be discussed in Section 3.4.

The main idea behind the numerical solution of the governing partial differential equations (2.5) and (2.6) is the transformation of those equations into a set of linear algebraic equations which can then be solved. The method of transforming the partial differential equations into algebraic equations is called the discretization procedure. One such method

is the control-volume procedure which involves dividing the calculation domain into a number of control volumes and then integrating the partial differential equations over them to obtain a set of algebraic equations. A grid has first to be constructed, as will be discussed below.

3.2 Grid Arrangements

A finite volume grid consists of a number of control volumes which cover the calculation domain. In the present study, all grid nodes are placed at the centres of the control volumes where the scalar variables are stored. The storage of the velocity components U and V in the center of the control volume, together with the usage of linear interpolation, leads to the well-known checkerboard oscillations in the flow field (Patankar, 1980). One way to avoid this behaviour is to shift the position of velocity components to the cell faces, as will be shown in the following section.

3.2.1 The Staggered Grid Arrangement

The appearance of oscillations in the computed velocity and pressure field was the main reason for adopting the staggered grid arrangement (Fig. 3.1).

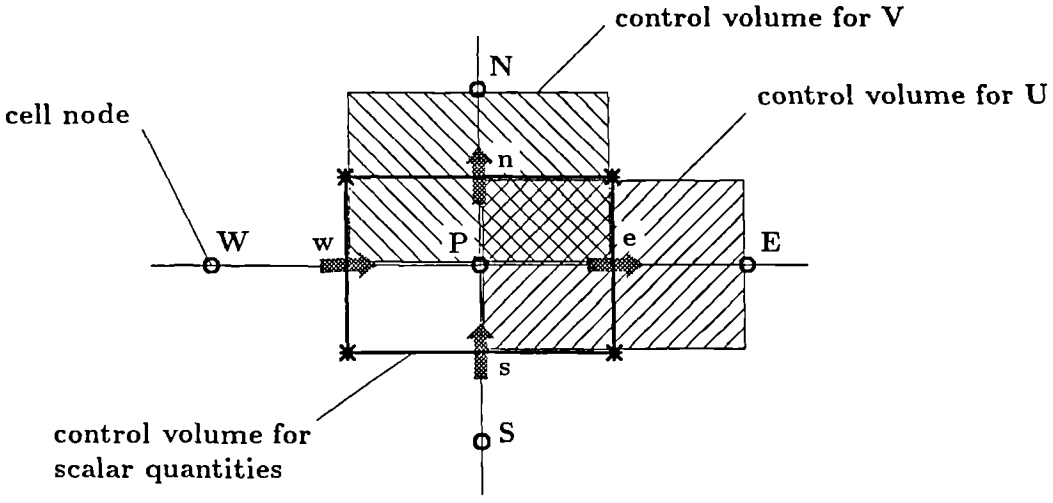

Fig. 3.1 The staggered grid arrangement

Location in Fig. 3.1	Variable	
	NKE	RSM
→	U	U, $\overline{uw}$
↑	V	V, $\overline{vw}$
o	W, p, k, ϵ	W, p, ϵ, $\overline{u^2}$, $\overline{v^2}$, $\overline{w^2}$
*	-	$\overline{uv}$

Table 3.1 The variable locations using staggered grid arrangement

The staggered grid arrangement brings some further advantages. Calculation of cell continuity balance is simplified because the velocities are placed in the positions where fluxes enter the control volume. Also, the momentum equations are strongly coupled with the Reynolds-stress equations and hence locating all the stresses in the centres of the control volumes can cause numerical instabilities. Difficulties associated with interpolation of the shear stresses to the cell faces can be overcome by using the staggered approach for those stresses as well. The locations of all variables using the staggered grid arrangement are shown in Table 3.1.

The staggered grid arrangement is very convenient for the calculation of the fluid flows in three-dimensional ducts, and especially when orthogonal grids are used. In the present work, therefore, all orthogonal geometries are calculated using the staggered grid approach. When non-orthogonal geometries are considered, the staggered grid arrangement is not the most suitable one and an alternative approach is used, as will be discussed in the following section.

3.2.2 The Co-located Grid Arrangement

This grid arrangement (Fig. 3.2) has been preferred by many researchers (Rhie and Chow (1983), Peric (1985), Demirdzic and Peric (1990) etc.) as a more convenient approach when considering non-orthogonal flow

geometries.

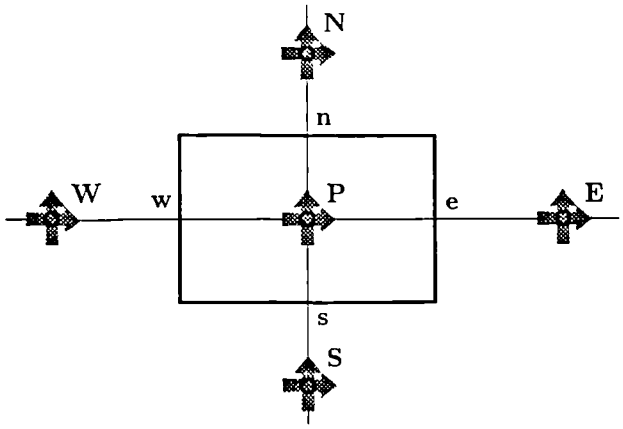

Fig. 3.2 The co-located grid arrangement

The advantages of co-located grid over staggered one were pointed out by Peric (1985) and by Peric et al. (1988), and can be summarized as follows:

- using co-located grid arrangement all variables share the same control volume and therefore there is only need for one set of control volumes,
- the convection contribution to the coefficients in the discretized equations is the same for all variables,
- co-located grid approach enables using the Cartesian velocity components, even for the non-orthogonal geometries, which results in simpler equations than when the grid-oriented velocity components are employed.

In the present study, the co-located grid arrangement was adopted in conjunction with the nonlinear k-ϵ model for the prediction of flows in non-orthogonal ducts and channels.

3.3 Discretization Procedure

Discretization of the governing differential equations can be done by integration of the partial differential equations over each control volume

assuming profiles of the Φ variation between the grid nodes. The technique is well-established for orthogonal grids (Patankar, 1980) and so only its essentials will be presented here. The discretization procedure for the non-orthogonal grids is a more difficult task but that has already been resolved by Peric (1985).

The basic ideas behind control-volume approach are the same for orthogonal and non-orthogonal geometries and will be explained with reference to the scalar equation (2.9) using the orthogonal control volume (Fig. 3.3). The presentation is divided into two parts. The first is concerned with the basic features of the discretization procedure that are common for orthogonal and non-orthogonal grids. The second part presents the discretization for non-orthogonal grids with special emphasis on the discretization of the nonlinear stress-strain relationship.

3.3.1 Control-Volume Approach

The scalar equation (2.9) represents a typical prototype for the governing equations encountered in computational fluid dynamics and will therefore be used to explain the basis of the control-volume approach.

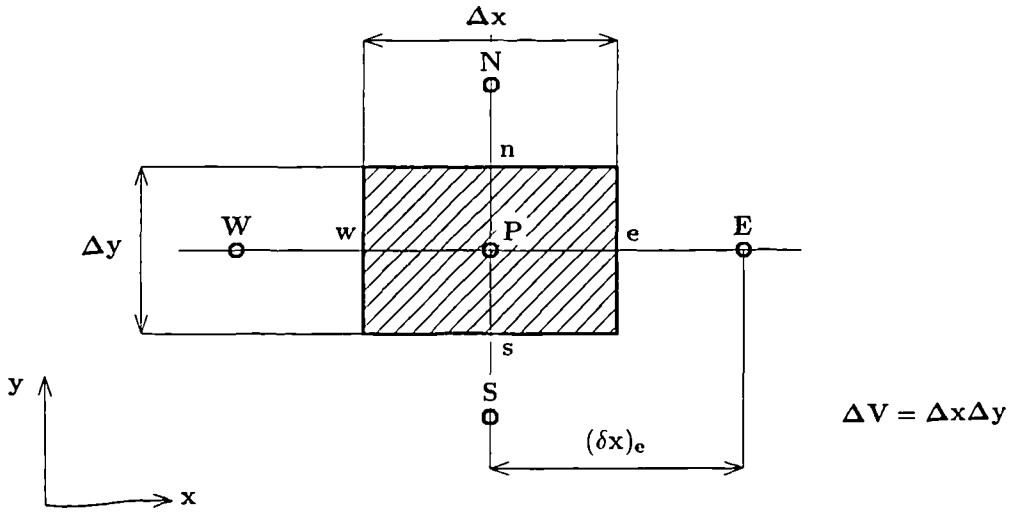

Fig. 3.3 Scalar control volume

It must be noted here that in three-dimensional flows in non-circular ducts, fully-developed conditions imply no change in the main-flow direction, which means that only a two-dimensional method is required. Thus, the discretization is explained using the two-dimensional cell shown in Fig. 3.3. For convenience, the governing equation (2.9) can be re-written as follows:

$$\frac{\partial}{\partial x_j}\overbrace{\left(\rho U_j \Phi - \Gamma_\Phi \frac{\partial \Phi}{\partial x_j}\right)}^{\text{total transport } q_j} = S_\Phi \tag{3.1}$$

Equation (3.1) is integrated over each control volume. In the integration, the volume integral of the transport terms is replaced by corresponding surface integrals using Gauss's theorem:

$$\int_V \frac{\partial f_j}{\partial x_j}\, dV = \int_{A_e} f_e\, dA - \int_{A_w} f_w\, dA + \int_{A_n} f_n\, dA - \int_{A_s} f_s\, dA \tag{3.2}$$

where f_e is component of f_j normal to the east cell face and A_e is the area of that cell face.

Using equation (3.2) for the orthogonal cell shown in Fig. 3.3, equation (3.1) after integration can be written as:

$$q_e A_e - q_w A_w + q_n A_n - q_s A_s = S_\Phi \Delta V \tag{3.3}$$

where

$$q_e A_e = \overbrace{\rho U_e A_e \Phi_e}^{\text{convection of } \Phi} - \overbrace{\Gamma_{\Phi,e}\left(\frac{\partial \Phi}{\partial x}\right)_e A_e}^{\text{diffusion of } \Phi} \tag{3.4}$$

represents the total transport on the east cell face. Similar expressions can be obtained for the remaining cell faces.

Convection term

In order to define the convection term, the mass flux $\rho U_e A_e$ ($\equiv F_e$) and value of Φ_e at the east cell face are to be determined. In the case of staggered grid arrangement the calculation of mass flux is straightforward because U_e exactly coincides with value of U velocity there while when co-located grid arrangement is considered the special interpolation technique need to be employed to obtain velocity value at the cell face (Subsection 3.4.1.2). The value of Φ_e in convection term is directly related to the choice of differencing scheme.

Diffusion term

The gradient of Φ need to be determined on the east cell face in order to calculate the diffusion flux in expression (3.4). For that purpose linear distribution of Φ is assumed thus:

$$\Gamma_{\Phi,e}\left(\frac{\partial\Phi}{\partial x}\right)_e A_e = \Gamma_{\Phi,e}\left(\frac{\Phi_E - \Phi_P}{(\delta x)_e}\right)_e A_e = \overbrace{\frac{\Gamma_{\Phi,e}\,A_e}{(\delta x)_e}}^{D_e}(\Phi_E - \Phi_P) \qquad (3.5)$$

Differencing scheme

The closeness of the power-law scheme to the exact exponential scheme was suggested by Patankar (1980) and therefore that scheme is employed in the present study. Thus, all quantities which multiply the Φ_E are grouped in the following algebraic coefficient:

$$a_E = D_e \max\left[0, \left(1 - \frac{0.1\,|F_e|}{D_e}\right)^5\right] + \max(0, -F_e)$$

An identical procedure is applied for the discretization of the convection

and diffusion terms on the remaining cell faces.

Source term

It is usual to split the source term into two parts as follows:

$$S_\Phi \ \Delta V = S_u + S_P \Phi_P \tag{3.6}$$

where the S_P is added to the coefficient a_P. This improves the stability of the iterative solution procedure, by enhancing diagonal dominance (only if $S_P < 0$).

The final form of discretized equations

After combining all discretized terms, equation (3.3) can be re-arranged for point P (centre of the control volume) thus:

$$a_P \Phi_P = \sum_{nb} a_{nb} \Phi_{nb} + S_u \tag{3.7}$$

where

$$a_P = \sum_{nb} a_{nb} - S_P$$

and a_{nb} - denotes the coefficient which multiplies the values of Φ at the neighbouring nodes (E,W,N,S).

The discretized equation (3.7) is written for each control volume within the flow domain to form a set of linearized algebraic equations which can then be solved using one of several standard techniques.

3.3.2 Treatment of Non-Orthogonal Geometries

Calculations of the flows in ducts with arbitrarily shaped cross sections were performed with a method based on that of Peric (1985). The method solves the governing differential equations for a general coordinate system using Cartesian velocity components. The method was extended here to handle the nonlinear k-ϵ model for ducts and channels with arbitrary shaped cross sections using non-orthogonal meshes represented by cell shown in Fig. 3.4.

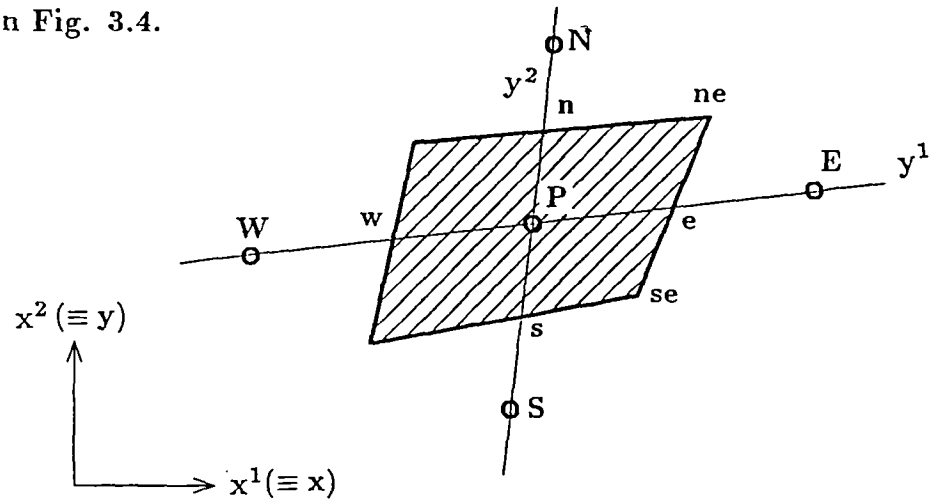

Fig. 3.4 Two-dimensional non-orthogonal control volume

Fig. 3.4 shows arbitrary control volume presented in respect to the general (y^1, y^2) as well as the Cartesian (x^1, x^2) coordinate system. The general (non-orthogonal) coordinate system coincides with lines which connect neighbouring grid nodes. Accordingly, all variations are related to the general coordinate system and hence the governing differential equations need to be presented for that system. The compact form of the continuity and momentum equations (equations 2.5 and 2.6) for the non-orthogonal coordinate system can be written as follows (Demirdzic, 1982 and Peric, 1985):

$$\frac{1}{J} \frac{\partial}{\partial y^j} (\rho \, U_m \, \beta^j_m) = 0 \tag{3.8}$$

$$\frac{1}{J}\ \frac{\partial}{\partial y^j}\left[(\rho U_m U_i - \tau_{mi} + \rho\overline{u_m u_i})\,\beta_m^j\right] = -\frac{1}{J}\ \frac{\partial(p\delta_{mi})}{\partial y^j}\,\beta_m^j \tag{3.9}$$

where

J - the Jacobian of coordinate transformation $x^i = x^i(y^j)$,

β - the coordinate transformation factor,

$$\tau_{mi} = \mu\left(\frac{\partial U_i}{\partial y^n}\,\beta_m^n + \frac{\partial U_m}{\partial y^l}\,\beta_i^l\right)\ \frac{1}{J}\ .$$

The same form of the nonlinear stress-strain relationship, given by equation (2.11), can be used for the definition of the Reynolds stresses $\overline{u_m u_i}$ in equation (3.9). The mean rate of strain and the Oldroyd derivative in expression (2.11) need to be transformed into the general coordinate system, resulting for stationary flow in:

$$\overline{D_{ij}} = \frac{1}{2}\left(\frac{\partial U_i}{\partial y^n}\,\beta_j^n + \frac{\partial U_j}{\partial y^l}\,\beta_i^l\right)\ \frac{1}{J} \tag{3.10}$$

$$\overset{\circ}{\overline{D_{ij}}} = \left(U_m\frac{\partial\overline{D_{ij}}}{\partial y^k}\,\beta_m^k - \overline{D_{mj}}\frac{\partial U_i}{\partial y^n}\,\beta_m^n - \overline{D_{mi}}\frac{\partial U_j}{\partial y^l}\,\beta_m^l\right)\ \frac{1}{J} \tag{3.11}$$

Implementation of the nonlinear stress-strain relationship is not particularly difficult, and follows closely the lines adopted in the orthogonal case. The gradients presented in respect to the Cartesian and the general coordinate systems are related thus:

$$\frac{\partial U_i}{\partial x^j} = \frac{1}{J}\ \frac{\partial U_i}{\partial y^n}\,\beta_j^n \tag{3.12}$$

In two-dimensional case the Jacobian takes form:

$$J = \frac{\partial x^1}{\partial y^1}\frac{\partial x^2}{\partial y^2} - \frac{\partial x^1}{\partial y^2}\frac{\partial x^2}{\partial y^1} \tag{3.13}$$

while the corresponding β_j^n coefficients can be written as :

$$\left.\begin{aligned} \beta_1^1 &= \frac{\partial x^2}{\partial y^2} & \beta_2^1 &= -\frac{\partial x^1}{\partial y^2} \\ \beta_1^2 &= -\frac{\partial x^2}{\partial y^1} & \beta_2^2 &= \frac{\partial x^1}{\partial y^1} \end{aligned}\right\} \tag{3.14}$$

Discretization of the nonlinear part of the stress-strain relationship is straightforward in that every Cartesian velocity gradient in the expanded expressions for individual Reynolds stresses (equations 2.14–2.19) is converted into its non-orthogonal counterpart using equation (3.12). For example, the W-velocity gradient in the $x^1(\equiv x)$ direction on the east cell face reads:

$$\left(\frac{\partial W}{\partial x}\right)_e = \frac{1}{J_e}\left(\frac{\partial W}{\partial y^1}\beta_1^1 + \frac{\partial W}{\partial y^2}\beta_1^2\right)_e \tag{3.15}$$

Using equations (3.14), the previous expression becomes:

$$\left(\frac{\partial W}{\partial x}\right)_e = \frac{1}{J_e}\left(\frac{\partial W}{\partial y^1}\frac{\partial x^2}{\partial y^2} - \frac{\partial W}{\partial y^2}\frac{\partial x^2}{\partial y^1}\right)_e \tag{3.16}$$

With the notation of Fig. 3.4, all gradients needed in expression (3.16) can be obtained from the simple geometrical manipulations as reads:

$$\left(\frac{\partial W}{\partial y^1}\right)_e = \frac{W_E - W_P}{y_E^1 - y_P^1} \qquad \left(\frac{\partial W}{\partial y^2}\right)_e = \frac{W_{ne} - W_{se}}{y_{ne}^2 - y_{se}^2}$$

$$\left(\frac{\partial x^1}{\partial y^1}\right)_e = \frac{x_E^1 - x_P^1}{y_E^1 - y_P^1} \qquad \left(\frac{\partial x^1}{\partial y^2}\right)_e = \frac{x_{ne}^1 - x_{se}^1}{y_{ne}^2 - y_{se}^2}$$

$$\left(\frac{\partial x^2}{\partial y^1}\right)_e = \frac{x_E^2 - x_P^2}{y_E^1 - y_P^1} \qquad \left(\frac{\partial x^2}{\partial y^2}\right)_e = \frac{x_{ne}^2 - x_{se}^2}{y_{ne}^2 - y_{se}^2}$$

On combining above listed expressions with equations (3.13) and (3.16),

the final discretized form can be written as follows:

$$\left(\frac{\partial W}{\partial x}\right)_e = \frac{(W_E - W_P)(x^2_{ne} - x^2_{se}) - (W_{ne} - W_{se})(x^2_E - x^2_P)}{(x^1_E - x^1_P)(x^2_{ne} - x^2_{se}) - (x^1_{ne} - x^1_{se})(x^2_E - x^2_P)}$$

By repeating this procedure for all gradients in equations (2.14) – (2.19), the discretized form for all Reynolds stresses can be obtained on the desired cell faces to be then used to obtain integrated Reynolds-stress gradients over each control volume.

The convection, diffusion and pressure term are also discretized with respect to the general coordinate system. Details of the discretization of remaining terms may be found in Peric (1985) and are therefore not repeated here.

3.4 Calculation of Pressure Field

3.4.1 Cross-Stream Pressure Field

The idea of pressure calculation is to find the pressure field which yields velocities that satisfy the continuity equation. There are many iterative procedures which can serve this purpose and the most popular one is presented in the following section.

3.4.1.1 The SIMPLE Algorithm

The SIMPLE (Semi-Implicit Method for Pressure-Linked Equations) algorithm, proposed by Patankar and Spalding (1972), is adopted for the calculation of cross-stream pressure field. In order to explain this method, the discretized form of the U-momentum equation is used, which for the

staggered grid arrangement (Fig. 3.1) reads:

$$a_e U_e = \sum_{nb} a_{nb} U_{nb} + S_u^- + A_e (p_P - p_E) \tag{3.17}$$

where the pressure part is separated from the mean source S_u resulting in S_u^-.

The starting point in this algorithm is a guessed pressure field (p*). When this field is employed for the calculation of pressure gradient in the U-momentum equation it results in the following algebraic equation:

$$a_e U_e^* = \sum_{nb} a_{nb} U_{nb}^* + S_u^- + A_e (p_P^* - p_E^*) \tag{3.18}$$

The guessed pressure field is usually incorrect and when used in the momentum equations results in a velocity field (U* and V*) which generally does not satisfy the continuity equation. Thus, the guessed pressure field need to be corrected using the relation:

$$p = p^* + p' \tag{3.19}$$

where p' denotes pressure correction.

The velocity field is corrected in a similar manner:

$$\left.\begin{aligned} U &= U^* + U' \\ V &= V^* + V' \end{aligned}\right\} \tag{3.20}$$

The task now is to determine the pressure and velocity corrections. The velocity-correction equation is obtained by subtracting equation (3.18)

from (3.17), resulting in:

$$a_e U'_e = \sum_{nb} a_{nb} U'_{nb} + A_e \, (p'_P - p'_E) \tag{3.21}$$

If the first term on the right hand side of equation (3.21) is neglected, the velocity correction reads:

$$U'_e = d_e \, (p'_P - p'_E) \tag{3.22}$$

where $d_e = \frac{A_e}{a_e}$.

The continuity equation is used to formulate the pressure-correction equation so that corrected velocities satisfy the continuity condition. The continuity equation, when integrated over a scalar control volume, is written as:

$$(\rho U)_e \; A_e - (\rho U)_w \; A_w + (\rho V)_n \; A_n - (\rho V)_s \; A_s = 0 \tag{3.23}$$

If the velocities are now substituted using expressions (3.20) and (3.22), the following discretized equation for p' is obtained:

$$a_P p'_P = \sum_{nb} a_{nb} p'_{nb} + S_u^P \tag{3.24}$$

where

$$S_u^P = (\rho U^*)_w \; A_w - (\rho U^*)_e \; A_e + (\rho V^*)_s \; A_s - (\rho V^*)_n \; A_n.$$

All equations presented hitherto form the basis needed for obtaining the velocity components and pressure field through SIMPLE algorithm.

3.4.1.2 Cell-Face Velocity Interpolation for Co-located Grids

In order to overcome the oscillatory pressure field which may arise from the SIMPLE algorithm for co-located grid, Rhie and Chow (1983) proposed a special interpolation practice for the cell-face velocities. This will be explained on the U-velocity component using notation shown in Fig. 3.5.

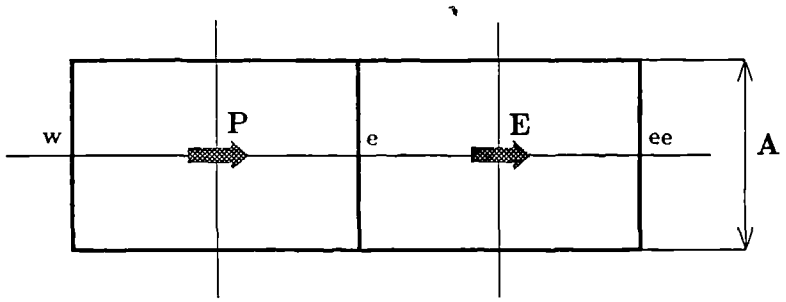

Fig. 3.5 The co-located U-velocity cell

The values of U_P and U_E velocities are extracted from their discretized equations as follows:

$$U_P = \left[\frac{\sum a_{nb}U_{nb} + S_u^- - (p_e - p_w)\,A}{a_P}\right]_P \tag{3.25}$$

$$U_E = \left[\frac{\sum a_{nb}U_{nb} + S_u^- - (p_{ee} - p_e)\,A}{a_P}\right]_E \tag{3.26}$$

The value of the cell-face velocity U_e is now obtained from the U_P and U_E using linear interpolation for all terms on the right hand side of equations

(3.25) and (3.26), except for the pressure differences. This results in:

$$U_e = \overline{\left[\frac{\sum a_{nb} U_{nb}}{a_P}\right]_e} + \overline{\left[\frac{S_{\bar{u}}}{a_P}\right]_e} - \overline{\left[\frac{1}{a_P}\right]_e} (p_E - p_P) A_e \qquad (3.27)$$

where overbars denotes linear interpolation between P and E grid nodes.

The strong coupling between velocity and pressure is clearly seen from equation (3.27) where the cell velocity becomes function only of pressure values from the neighbouring nodes.

3.4.2 Streamwise-Pressure Gradient

The assumption that the flow is elliptic in the cross section and parabolic in the main-flow direction implies a decoupling of cross- and streamwise-pressure gradients. This simplifies the calculation of the latter which is assumed to be uniform over a cross section. The streamwise-pressure gradient for duct flows is calculated so as to satisfy the integral mass-conservation. In open channels, the flow is driven by the channel-bed slope and the integral mass flow is an outcome of the calculations. Consequently, different algorithms are required depending on whether ducts or channels are considered.

3.4.2.1 Duct-Flow Algorithm

The procedure of Patankar and Spalding (1972) is adopted for the calculation of the streamwise-pressure gradient. The starting point is an estimate of $(\partial \overline{p}/\partial z)$ which is denoted as $(\partial \overline{p}/\partial z)^*$. The next step is to use

this estimate to calculate the velocity field W^* which, when integrated over cross section, will not produce the correct mass-flow rate ($\dot{m}$). Thus, the initial pressure gradient and resulting velocity field are corrected using the following equations:

$$\left(\frac{\partial \overline{p}}{\partial z}\right) = \left(\frac{\partial \overline{p}}{\partial z}\right)^* + \left(\frac{\partial \overline{p}}{\partial z}\right)' \tag{3.28}$$

$$W = W^* + d^W \left(\frac{\partial \overline{p}}{\partial z}\right)' \tag{3.29}$$

where $d^W = \left(\frac{\Delta x \, \Delta y}{a_P}\right)$.

To determine the pressure-gradient correction, the following relationship is used:

$$\left(\frac{\partial \overline{p}}{\partial z}\right)' = \frac{\dot{m} - \sum \rho \, W^* \, \Delta x \, \Delta y}{\sum \rho \, d^W \, \Delta x \, \Delta y} \tag{3.30}$$

The iterative procedure is repeated until the mass error becomes negligible resulting in a constant streamwise-pressure gradient.

3.4.2.2 Channel-Flow Algorithm

In open channels, the main flow is driven by the channel-bed slope and hence the pressure gradient in the streamwise momentum equation becomes:

$$\rho \, g \, \sin\theta \tag{3.31}$$

where

g - the earth acceleration

θ - a slope of the channel bed

In contrast to duct flows, where the pressure gradient is forced to satisfy the imposed flow rate, in open channels the mass flow rate will be determined according to the imposed bed slope. In order to introduce term ρ g $\sin\theta$ into the streamwise-momentum equation, two alternative procedures are used in place of the Patankar and Spalding algorithm.

Approach a

The driving force and the retarding shear force become equal when a three-dimensional parabolic flow reaches fully-developed conditions. This can be expressed through the following equation:

$$-\left(\frac{\partial \overline{p}}{\partial z}\right) A_{rea} = \int_P |\tau_w| \, dP \tag{3.32}$$

where

A_{rea} - area of the cross section
P - wetted perimeter
τ_w - the wall-shear-stress

In this approach, all features of duct algorithm are maintained and only the pressure correction is replaced by:

$$\left(\frac{\partial \overline{p}}{\partial z}\right)' = \left(\rho \, g \, \sin\theta - \frac{\int |\tau_w| \, dP}{A_{rea}}\right) \tag{3.33}$$

When convergence is achieved, the following condition is satisfied:

$$\rho \, g \, \sin\theta \; A_{rea} = \int |\tau_w| \, dP \tag{3.34}$$

It is clear from equations (3.32) and (3.34) that by the end of the iterative procedure the streamwise-pressure gradient becomes equal to $\rho g \sin\theta$.

Approach b

The second approach involves the introduction of term ρ g $\sin\theta$ in the streamwise momentum equation without any corrections during the solution procedure.

The two approaches, when applied to the a simple rectangular channel, produced identical results but with different time requirements to achieve converged solutions. The first approach produced somewhat faster convergence for simpler geometries, but, for more complicated geometries (compound channels), produced numerical instabilities. Approach b was therefore preferred.

In the present study, the duct algorithm is replaced with the algorithm for the channel flow only when the mass flow in the open channel is required as an output information and when a reliable value of channel bed slope is provided.

3.5 Boundary Conditions

In the present study, boundary conditions need to be specified at three types of boundaries: the wall, the symmetry plane and the free surface.

3.5.1 Wall-Boundary Conditions

All velocities on the solid boundaries are set to zero. Very close to the wall, viscous effects prevail and hence high Reynolds-number-turbulence models cannot be used there without a special adaptations. In order to avoid the problems associated with this, the near-wall region is usually bridged using the wall-function approach of Launder and Spalding (1974).

The grid node closest to the wall is placed in the zone where the velocity is assumed to follow the logarithmic distribution:

$$\frac{W}{W_\tau} = \frac{1}{\kappa} \ln\left(\frac{E\ W_\tau\ y_w}{\nu}\right) \tag{3.35}$$

where

W_τ - shear velocity in streamwise direction

E - logarithmic law constant

y_w - distance between wall and nearest grid node in the flow

κ - von Karman constant

The wall-shear-stress τ_w is expressed in the following form:

$$\tau_w = -\rho\, W_\tau^2 \tag{3.36}$$

An iterative procedure was used to calculate the shear velocity W_τ , as follows :

$$W_{\tau,new} = \frac{W\,\kappa}{\ln\left(\frac{E\ W_{\tau,old}\ y_w}{\nu}\right)} \ . \tag{3.37}$$

W_τ, is then used to calculate τ_w using expression (3.36).

When using a co-located grid, the wall-shear-stress was calculated using alternative expression:

$$\tau_w = -\frac{\rho\, C_\mu^{1/4}\, k^{1/2}\, W\,\kappa}{\ln\left(\frac{E\ W_\tau\ y_w}{\nu}\right)} \tag{3.38}$$

The local-equilibrium assumption dictates the wall-boundary conditions for k and ϵ. The turbulent kinetic energy in the near-wall region is prescribed as:

$$k_w = \frac{W_\tau^2}{C_\mu^{1/2}} = \frac{|\,\tau_w\,|}{\rho\, C_\mu^{1/2}} \tag{3.39}$$

The boundary condition for the dissipation rate of turbulent kinetic energy is also chosen to obey local-equilibrium assumption, resulting in the

relation:

$$\epsilon_w = \frac{C_\mu^{3/4}}{\kappa} \frac{k^{3/2}}{y_w} \tag{3.40}$$

When the ϵ-transport equation is solved in conjunction with the Reynolds-stress model the value of ϵ near to the wall is specified to be:

$$\epsilon_w = P_k \tag{3.41}$$

The wall boundary conditions for all the turbulent stresses in the Reynolds-stress model is obtained by setting the normal gradients to zero.

3.5.2 Symmetry-Plane and Free-Surface Boundary Conditions

Zero-gradient boundary conditions are adopted at the symmetry plane for all variables except for the shear stresses. The main shear stress $\overline{uw}$ is set to be zero for the vertical symmetry plane while for the horizontal one the zero gradient is applied. Similarly, the $\overline{vw}$ is set to be zero at the horizontal-symmetry plane while for the side one the zero-gradient treatment is used. The shear stress $\overline{uv}$ is set to be zero at all symmetry planes.

The free surface is treated as a symmetry plane for all the variables except for the dissipation of turbulent kinetic energy. Naot and Rodi (1982) suggested that the presence of the free surface reduces the length scale of turbulence resulting in an increased level of dissipation (ϵ). Following Hossain and Rodi (1980), they proposed the dissipation rate at the free surface to be prescribed as:

$$\epsilon_f = \frac{C_\mu^{3/4}}{\kappa} k_f^{3/2} \left(\frac{1}{y'} + \frac{1}{y^*} \right) \tag{3.42}$$

where average distance from the nearest wall (y^*) was added to ensure smooth transition between the wall- and surface-boundary conditions.

The value for y′ was adjusted using some experimental results to the 7 % of the channel depth (y′ = 0.07H).

A similar expression for ϵ at the free surface was proposed by Krishnappan and Lau (1986) as follows:

$$\epsilon_f = \frac{C_f}{\kappa\, C_\mu^{3/4}} \frac{k_f^{3/2}}{y_f} \tag{3.43}$$

where

$C_f = 0.164$ - an empirical constant

y_f - distance between the free surface and the nearest internal grid node.

Summation of all constants in equation (3.43) yields:

$$\epsilon_f = 2.439 \frac{k_f^{3/2}}{y_f} \tag{3.44}$$

Both proposals result in a parabolic distribution of the eddy-viscosity in open channels, as observed by Ueda et al. (1977).

To understand the basis of the proposed ϵ-boundary conditions, the ϵ-transport equation is simplified by neglecting convection and diffusion in the x-direction (consistent with a fully-developed flow in a broad open channel), to obtain:

$$\frac{\partial}{\partial y}\left(\frac{\mu_t}{\sigma_\epsilon}\frac{\partial \epsilon}{\partial y}\right) + \rho \frac{\epsilon}{k}\left(C_{\epsilon 1} P_k - C_{\epsilon 2}\, \epsilon\right) = 0 \tag{3.45}$$

If ϵ is assumed to approach the free surface as $\epsilon = \alpha / y^2$, where α stands for a proportionality coefficient, the first term in equation (3.45) becomes:

$$\frac{\partial}{\partial y}\left(\frac{\mu_t}{\sigma_\epsilon}\frac{\partial \epsilon}{\partial y}\right) = \rho \frac{2C_\mu}{\sigma_\epsilon} \frac{k^2}{y^2} \tag{3.46}$$

Now equation (3.45) can be re-written in a simple algebraic form:

$$\frac{C_{\epsilon 2}}{k}\,\epsilon^2 - \frac{C_{\epsilon 1} P_k}{k}\,\epsilon - \frac{2C_\mu}{\sigma_\epsilon}\,\frac{k^2}{y^2} = 0 \tag{3.47}$$

The production of turbulent kinetic energy (P_k) vanishes at the free surface thus the second term in equation (3.47) can be dropped resulting in the following value of ϵ at the free surface:

$$\epsilon_f = \left(\frac{2C_\mu}{\sigma_\epsilon C_{\epsilon 2}}\right)^{1/2} \frac{k^{3/2}}{y_f} = 0.277\,\frac{k^{3/2}}{y_f} \tag{3.48}$$

It is clear from equation (3.48) that dissipation has again turned out to be a function of $k^{3/2}$ and a relevant distance as in expressions (3.42) and (3.43). However, the magnitude of constants multiplying $k^{3/2}/y_f$ is quite different by factor of ≈ 9.

Proposal (3.42) is used here in conjunction with the free-surface damping function (equation 2.47) in all the reported Reynolds-stress model calculations. Krishnappan and Lau's proposal (3.43) is used as boundary condition for ϵ equation when calculations are carried out using the non-linear k-ϵ model.

3.5.3 Roughness

It is often the case that the flood plains are rough due to vegetation and this has to be accounted for in the model. The velocity distribution in the regions adjacent to the rough walls is no longer best described with the usual log-law. Knight and Hamed (1984,b) conducted a systematic experimental investigation of the influence of rough flood plains on the flow structure including the velocity distribution near rough walls. They presented the velocity distribution near the rough walls as follows:

$$\frac{\tilde{W}}{W_\tau} = 6.06 \log_{10}\left(\frac{H-h}{\chi}\right) \tag{3.49}$$

where

$\tilde{W}$ - depth-averaged mean velocity

H - main channel depth

h - height of flood plains above main channel bed

χ - roughness parameter

In order to compare present predictions with the data of Knight and Hamed, the standard log-law expression for the smooth walls (3.35) is replaced on the rough flood plains by equation (3.49).

3.6 Treatment of the Velocity Gradients near the Wall

The successful implementation of the present turbulence models depends on the accurate calculation of the velocity gradients particularly in the regions adjacent to the solid boundaries where those gradients are greatest. Fig. 3.6 shows the consequences of alternative methods for calculating the gradient of streamwise velocity, W.

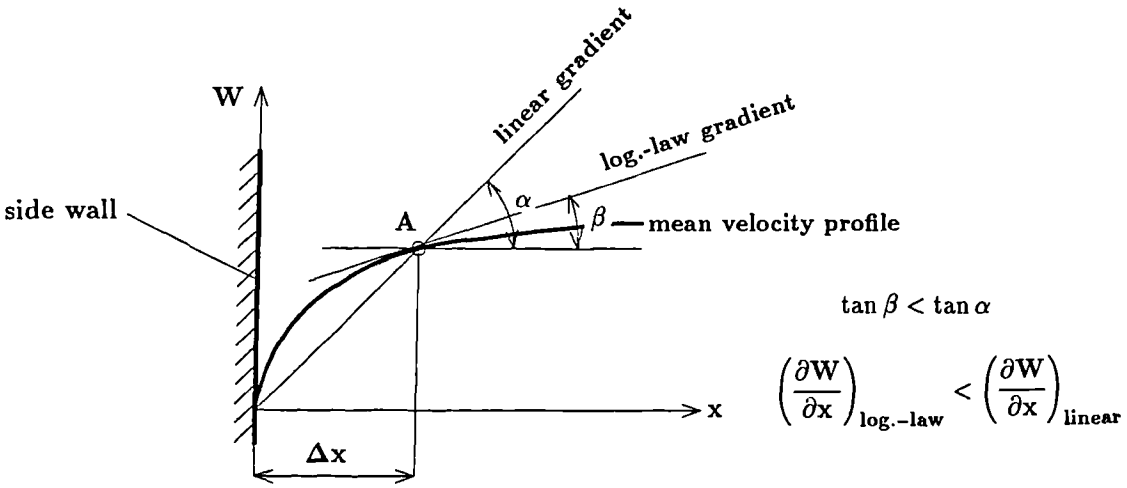

Fig. 3.6 The velocity profile near the side wall

When calculated through log-law the velocity gradient in the A grid node takes form:

$$\left(\frac{\partial W}{\partial x}\right)_{log-law} = \frac{W_\tau}{\kappa\, \Delta x} \tag{3.50}$$

If we replace $\frac{W_\tau}{\kappa}$ using log-law expression (3.35) equation (3.50) becomes:

$$\left(\frac{\partial W}{\partial x}\right)_{log-law} = \frac{W_A}{\Delta x\, \ln(Ex^+)} \tag{3.51}$$

The linear approach yields:

$$\left(\frac{\partial W}{\partial x}\right)_{linear} = \frac{W_A}{\Delta x} \tag{3.52}$$

If the nearest grid node is placed out of the laminar sublayer ($x^+ \geq 11.63$) the $\ln(Ex^+)$ is always greater than unity implying that mean-velocity gradient calculated using the log-law approach is always smaller than its linear counterpart. This is the approach finally adopted here; it is consistent with the use of the log-law in defining the boundary conditions as outlined in the previous sections.

3.7 Computational Aspects

3.7.1 Initial Field

The mean-velocity field is assumed to be uniform throughout the cross section and prescribed at a value appropriate to the reported Reynolds number. The secondary-velocity components are initially prescribed as $U = V = 0.01\, W_{bulk}$. The normal stresses are set to the $\overline{u^2} = \overline{v^2} = \overline{w^2} = 0.01\, W_{bulk}^2$. The turbulent viscosity is usually taken to be $\mu_t = 10\,\mu$ and as such is used to deduce the ϵ initial field through the eddy-viscosity relation. All shear stresses are initialized to zero.

3.7.2 Fully-Developed Conditions

The present study is only concerned with fully-developed flows, a condition usually achieved by marching in physical space until the flow parameters cease to change. Here, fully-developed conditions were assumed in advance and hence all gradients representing change in the streamwise-flow direction were dropped from the governing equations. This made possible the replacement of space-marching with advancement in iteration space.

3.7.3 Solution Sequence

Starting from prescribed initial fields, the U- and V-momentum equations are first solved followed by the pressure correction equation which is then used to correct the velocity and pressure field. The streamwise velocity is then obtained, and then corrected to satisfy overall continuity. The next steps depend on the choice of turbulence model. In the case of the k-ϵ model, transport equations for those variables are solved and obtained results then used to calculate the turbulent viscosity. When the Reynolds-stress model is employed, the ϵ-equation is solved together with equations for the six Reynolds stresses. The above sequence is repeated until a converged solution is attained.

3.7.4 Convergence Criteria

An iterative solution procedure will have converged when the values of the dependent variables do not change with further iterations. This is best checked by calculating the absolute sum of the residuals of each equation solved. The residual of an equation is essentially the difference between the left and right sides of that equation. The residuals are often normalized by an appropriate flux and monitored within the iterative

cycle. Convergence is attained when the normalized residuals fall below 10^{-4}.

Moreover, equation (3.32), which requires equality between the driving force and the retarding shear force, must also be satisfied when a converged solution is attained.

3.7.5 Grid Independence Tests

Table 3.2 below illustrates the type of grid-independence tests performed in the present study (NKE results).

Grid size per quarter of domain	CPU time (in minutes)	Number of iterations	Relative drop of shear stress at centre line [%]
12×12	2.1	220	6.38
22×22	34.	950	7.96
32×32	157.5	2000	7.90

Table 3.2 The computational details for the square-duct flow

The wall-shear-stress distribution for the runs presented in the above table is given in the following figure.

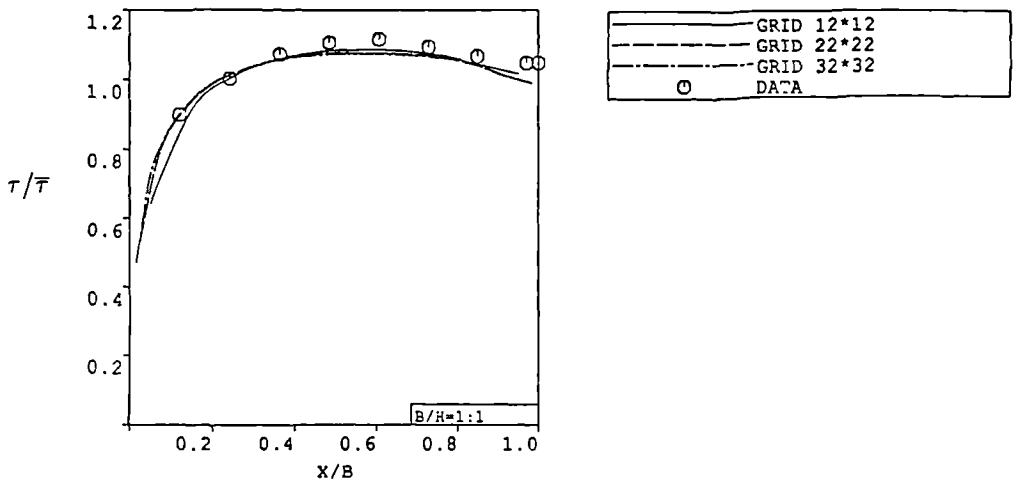

Fig. 3.7 Wall-shear-stress distribution for various grid sizes

It is clear from Fig. 3.7 and Table 3.2 that the solution obtained with 22×22 grid size produces a close agreement with results obtained with 32×32 grid size. Since the calculation using finer grid requires significantly more computational time, it is fully justified to accept the solution obtained with 22×22 grid size as a practical solution to the governing equations.

3.8 Closure to Chapter 3

In this chapter, the methods for the numerical solution of the governing equations presented in Chapter 2 were discussed. Alternative grid arrangements were considered in Section 3.2. Extension of the control-volume approach to the non-orthogonal geometries was presented in Section 3.3. The SIMPLE method was presented in Section 3.4 which also explained the calculation of the streamwise pressure gradient. The boundary conditions were introduced in Sections 3.5 and 3.6 and a summary of various computational aspects was included in Section 3.7.

The application of the solution method to duct flows is presented in the next chapter.

Chapter 4

PREDICTION OF FLOWS IN CLOSED DUCTS

4.1 Introduction

The flows considered in this chapter can generally be classified as part of a wider range of flows which are characterized by the presence of one or more sharp corners. The behaviour of such flows is determined by the precise geometric details. Thus, for example, the flow may be included within the corner, as would occur inside a duct or a channel, or in the junction of an aircraft wing and its body or it may be external to it as, for example, in a compound channel.

The study of the three-dimensional turbulent corner flows is motivated by the frequent occurrence of such flows both in nature and in engineering practice. In nature, those flows are observed in ice-covered rivers and natural streams. In engineering practice, they occur in air-conditioning ducts, in heat exchangers and in the intake ducts of jet engines. Their behaviour is strongly influenced by the region of low wall-shear-stress that exists near the internal corner. This is known to affect the rates of heat transfer to, or from, the wall creating, for example, undesirable 'hot spots'. Low shear stress also has consequences on the rate of sediment transport and, in supersonic flow, on the formation of complex shock-

wave patterns.

From a numerical modelling point of view, the most significant aspect of turbulent corner flows is the presence of Prandtl's second-kind of secondary motion. The origin of that motion has already been discussed in Chapter 1 and need not be repeated here. Suffice it to say that all current closure models found in practical engineering calculation method fail to predict the occurrence, and hence the consequences, of that motion. The purpose of this chapter is to present a detailed assessment of the performance of the present two turbulence models : the non-linear k-ϵ model and the complete Reynolds-stress-transport model. Three typical geometrical situations were chosen for models assessment: rectangular, compound and trapezoidal ducts (see Fig. 4.1). Those comprise all different types of corners (i.e. internal and external) and are all well documented by experiments.

The remainder of this chapter is in five sections. In Section 4.2, a preliminary assessment of the two models is presented. The final results for square, compound and trapezoidal ducts are presented in Sections 4.3 – 4.5, respectively. Conclusions to this chapter are presented in Section 4.6.

4.2 Preliminary Models Assessment

4.2.1 Comparison Between RSM and RSM0

Two variants of the Reynolds-stress-transport model were presented in Chapter 2: the RSM and the RSM0. These differ in the precise way in which the 'rapid' part of the pressure-strain correlation has been modelled. The RSM is given by equation (2.33) while the RSM0, the simplified version, is given by equation (2.34). The purpose of this section is to present the results of each and thus to demonstrate the necessity for

the model development discussed in Chapter 2.

Assessment of the two models was carried out by applying them to the flow in a square duct (AR = 1) with $Re = 2.15 \times 10^5$ where the effects of the turbulence-driven motion were expected to be at their greatest.

The Reynolds-stress model, denoted in the present study as the RSM0, was first to be applied to the flow in a square duct. The distortions of the mean-velocity field, shown in Fig. 4.2 a), are a very weak and the bed-shear-stress (Fig. 4.2 b) incorrectly shows the maximum at the centre line of the duct. This behaviour indicates that the RSM0 produces a weak turbulence anisotropy and consequently a weak secondary flow which is not able to distort a mean-velocity field. The anisotropy in the RSM0 arises only from the $\Phi_{ij,w}$ and can be enhanced by a more rapid decay of the wall-damping function (e.g. $f_x = L_x^2/x^2$). This is clearly seen in Fig. 4.3, where this approach results in a stronger bulging along the corner bisector. Still, this approach results in a mild contour distortions along the wall bisectors. Further anisotropy can be introduced through adoption of the full definition of $\Phi_{ij,2}$ (equation 2.33) instead of simplified one (equation 2.34). This results in a further bulging of the mean-velocity contours along corner- and wall-bisectors, as shown in Fig. 4.4 a). This model, denoted as the RSM (initial), differs from the RSM0 (quadratic f) only in the way in which the $\Phi_{ij,2}$ has been modelled. Unfortunately, the RSM (initial) leads to unexpected discontinuity of the wall-shear-stress near to the corner (Fig. 4.4 b). This can be improved by re-definition of the wall-damping function, using equations (2.41),(2.45) and (2.46) in combination with equation (2.40). This in conjunction with an appropriate boundary condition for the ϵ-equation (equation 3.41) leads to improved model-behaviour in the corner region, as shown in Fig. 4.4 b). An example of the wall-damping function is shown in Fig. 4.5. The Reynolds-stress model, finally adopted, is denoted as the RSM.

Contours of the streamwise velocity (normalized by their maximum value) as predicted with the RSM and the RSM0 are compared in Fig. 4.6 a). The differences are quite significant as can be seen, for example, from the

95% contour where the RSM0 result appears to be largely unaffected by the secondary motion in contrast to the RSM result which correctly reproduces the expected bulging towards the corners. The difference in the mean-velocity field has as a direct consequence a quite different profile of the bed-shear-stress (Fig. 4.6 b). Since the bulging of the mean-velocity contours in non-circular fully-developed duct is entirely attributed to the influence of the secondary motion it is reasonable to expect significant differences in the secondary-velocity field produced by these two models.

To demonstrate those differences, profiles of the U-velocity are compared in Fig. 4.7. Generally, the RSM has produced a stronger secondary motion. A maximum peak in the U-velocity profile obtained by RSM gets closer to the wall with decreasing of x/B indicating the strongest motion along the corner bisector. Furthermore, RSM profiles near wall are significantly stronger comparing with results obtained by RSM0. It is interesting to note that the U-velocity obtained by RSM0 is significant only near the walls but is negligible in the rest of the domain and is therefore incapable of influencing the streamwise velocity there.

Turbulence quantities appear in the U-equation through its diffusion terms and attention is now focused on one of those terms: that involving the normal-stress component $\overline{u^2}$. Contours of this component, averaged by $\overline{W_\tau}^2$, are presented for both models in Fig. 4.8. The difference between the two models is rather significant and in accordance with different secondary- and mean-velocity fields observed in previous figures. The $\overline{u^2}$ contours obtained by RSM are more distorted along corner and side-wall bisector compared with results obtained by RSM0. In order to clarify direct influence of different normal-stress fields the gradient of $\overline{u^2}$ at the position of $x/B = 0.77$ is shown in Fig. 4.9. The gradient is normalized by $\overline{W_\tau}^2/B$. The stress gradient obtained by RSM is stronger in a large portion of the duct implying a larger source inside momentum equation which consequently results in stronger secondary motion there.

The results presented in this section confirm that RSM0 produces a very weak secondary motion compared to RSM; the latter is therefore recom-

mended for further development and testing.

4.2.2 Nonlinear k-ϵ Model Simplification

Inspection of the nonlinear expressions given in equations (2.14) – (2.19) reveals the presence of secondary partial gradients of different velocity components. Consequently when these stresses are incorporated in the momentum equation they give rise to triple velocity gradients which can be sourcesof serious numerical instabilities particularly near the wall where the velocity gradients are the greatest. Therefore, there is benefit to be gained in determining the true significance of those terms. This was done by applying the nonlinear k-ϵ model with and without the secondary gradients for the square-duct flow with Re = $1. \times 10^5$. A calculation domain was covered by the same 32×32 numerical mesh and for both test cases identical under-relaxation was employed (0.5 for velocities and pressure and 0.6 for k and ϵ). The results are summarized in the table below.

Secondary gradients	$-\partial p/\partial z$ [N/m^3]	W_{max} [m/s]	W_{min} [m/s]	$\tau_{w,max}$ [N/m^2]	$\tau_{w,on\ symmetry\ plane}$ [N/m^2]
with	88.4	1.19	0.399	- 2.377	- 2.214
without	88.5	1.19	0.401	- 2.377	- 2.218

Table 4.1 Nonlinear k-ϵ results with and without secondary gradients

From Table 4.1 it is clear that both treatments yield effectively the same result although, when the secondary gradients are retained, convergence of the equations can only be achieved with twice as many iterations as would be required without those terms. For this reason it was decided that the secondary gradients would be dropped from equations (2.14) – (2.19) for all further applications of the nonlinear k-ϵ model.

4.3 Rectangular Ducts

4.3.1 Square-Duct Prediction

The flow in square non-circular ducts is characterized by a secondary motion that is symmetric about the wall and corner bisectors. The predicted secondary-velocity vectors (presented here for a quarter of a square duct), are compared in Fig. 4.10, with the measurements of Brundrett and Baines (1964) for $Re = 8.3 \times 10^4$. It is obvious that the strongest secondary motion occurs along the walls, bringing slow moving fluid from there into the centre of the duct. The returning flow transfers high momentum fluid towards the corners. An idea of how well the present models predict the strength of the secondary-flow streamlines can be gained from Fig. 4.11 which compares the present models with the measurements of Gessner and Jones (1965) for square duct with $Re = 1.5 \times 10^5$. The predictions are in close agreement with measurements for the two external levels. The external RSM contour is mildly extended to the corner in comparison with the contour obtained by NKE and this implies that the influence of the secondary motions obtained by RSM extends deeper into the corner region. None of the models captured the small streamline ($|\Psi \times 10^4| = 12$) in the middle of the vortex.

Fig. 4.12 compares the predicted mean-velocity contours (averaged by W_{max}) with the data of Brundrett and Baines (1964). The extent of mean-velocity bulging toward the corner depends on the strength of the secondary-velocity vectors along the corner bisector. Fig. 4.12 indicates that distortion of profiles obtained by RSM is closer to the measured behaviour than distortion obtained by NKE, especially for the two profiles closest to the wall. Overall, the degree of bulging obtained by NKE slightly underestimates both experimental results and RSM predictions.

Further comparisons were made using the data of Launder and Ying

(1972) for $Re = 2.15 \times 10^5$. Predicted and measured profiles of secondary velocity (normalized by average shear velocity $\overline{W_\tau}$) are shown in Fig. 4.13 for three x/B locations. Also included in that figure are the RSM results of Reece (1977) and algebraic-stress-model (ASM) results of Launder and Ying (1973). Comparisons at first two locations (x/B=0.2 and 0.5) indicate a close agreement between our predictions and Reece's results while his prediction produced stronger secondary flow in the middle portion of the duct at location x/B=0.8. The ASM predictions show the position of maximum velocity to be shifted towards the middle section of the duct. It is interesting to note that the present predictions using the RSM and the NKE are very close for all three profiles and, bearing in mind that the relatively small secondary velocities are very difficult to measure accurately, their agreement with data can be regarded as satisfactory.

Predicted and measured mean-velocity profiles along wall and corner bisector of the square duct are displayed in Fig. 4.14. The data are again those of Brundrett and Baines. Along the wall bisector the agreement between both predictions and experimental results is very good. The same is also true for the corner bisector although NKE profile is slightly underestimated in the near-wall region comparing with the experiment and the RSM results.

The experimental study of Brundrett and Baines (1964) was primarily conducted to determine the magnitude of the terms in the streamwise-vorticity equation. Various turbulence parameters were reported (e.g. the normal stress difference($\overline{u^2} - \overline{v^2}$) and the secondary-velocity shear stress $\overline{uv}$) and those are compared with the present models results in Figs. 4.15 and 4.17 respectively. The measured contours of normal-stress anisotropy, shown in Fig. 4.15, represent approximately straight lines in large part of domain which tend to become normal to the symmetry plane indicating the constant energy level in that region. Such trend is simulated by both models but especially by RSM. The NKE also shows a good agreement with experiment, particularly in the region closer to the corner bisector. In order to additionally test the models'

ability to predict normal-stress anisotropy, attention is focused on the normal-stress difference along wall bisector (Fig. 4.16). The spread of data shown there was taken from Perkins (1970) for the square duct flow with $Re = 1.5 \times 10^5$. Both models appear to produce return to isotropic turbulence with approach to the symmetry plane while some differences between them can be noticed in the near-wall region. In general, the normal-stress anisotropy produced by both models can be regarded as satisfactory especially bearing in mind that the same contours obtained by ASM underestimated experimental results by an order of magnitude (see Nakayama et al. 1983). The shear-stress distributions are presented in Fig. 4.17. The experimental results show an interesting pattern of elliptically enclosed contours along the corner bisector. A similar behaviour is also evident from the predictions though it appears that the NKE-model results show increasing levels of shear stress in the near-corner region contrary to the data and the RSM results.

The present predictions of turbulent-kinetic-energy field are compared with measurements of Brundrett and Baines in Fig. 4.18. The predicted and measured results are similar although predicted levels are found to be lower than those of experiment. Further predictions of the turbulent kinetic energy were obtained for the flow conditions of Gessner and Po (1976) who measured the profiles of this quantity in a square duct with $Re = 1.5 \times 10^5$. The predicted and measured profiles (normalized by $\overline{W_\tau}^2$) are presented in Fig. 4.19. Again both models are in close agreement with each other and, to a lesser extent, with the experimental values which they appear to underestimate in the near-wall region.

The final comparisons presented here relate to the shear-stress component $\overline{vw}$ which is responsible for diffusing the W-velocity in the y-direction. Gessner and Po (1976) measured $\overline{vw}$ profiles and their results together with present predictions are shown in Fig. 4.20. At the location of $x/B = 0.25$ both models closely follow the data while for the $x/B \geq 0.5$ some discrepancies occur in the near wall region.

4.3.2 Production of Vorticity

Present predictions of the turbulence anisotropy and the secondary-shear-stress for the flow in the square duct of Brundrett and Baines (1964) are used here to calculate terms A2 and A3 which comprise the production of the streamwise vorticity (P_{Ω_z}).

$$P_{\Omega_z} = \overbrace{\frac{\partial^2}{\partial x \partial y}(\overline{u^2} - \overline{v^2})}^{A2} - \overbrace{(\frac{\partial^2}{\partial x^2} - \frac{\partial^2}{\partial y^2})\overline{uv}}^{A3}$$

The contours of those terms averaged by $\overline{W_\tau}^2/B^2$ are shown in Fig. 4.21. The term A2 is greater than the term A3 by an order of magnitude only in a narrow region very close to the corner. In the rest of domain both terms are of a similar magnitude and it is therefore apparent that both terms contribute to the vorticity production. This result confirms the experimental considerations about the origin of the secondary motion, presented in Section 1.2.

4.3.3 Effects of Aspect Ratio

The aim of this section is to investigate the influence of the duct aspect-ratio on the flow structure. The experiment of Hoagland [1] (1960) is considered with AR = 3 and Re = $6. \times 10^4$. The predicted and measured secondary-velocity streamlines are plotted in Fig. 4.22 where it can be seen that the secondary-flow structure is significantly altered compared to that in square duct especially in the appearance of a large vortex. Some

[1] Present data concerning Hoagland's experiment was taken from Brundrett and Baines (1964)

similarities between square and rectangular sections have been maintained in the sense that both domains are again covered by two vortices which are of opposite sign whose zone of influence lies approximately along the corner bisector. This is also apparent in the measurements. The overall agreement between predictions and measurement is satisfactory.

Fig. 4.23 shows the data and the predicted contours of mean velocity as compared with the ASM results of Nakayama and Chow (1983). The mean-velocity contours are normalized by W_{max} The data are those of Leutheusser (1963) for $Re = 5.6 \times 10^4$ and $AR = 3$. All contours shown in Fig. 4.23 show the strongest distortion in the region near to the corner along its bisector though they appear to overestimate the measured contours there particularly for the levels of 0.9 and 0.95.

The predicted and measured anisotropy are compared in Fig. 4.24. The data are from Hoagland (1960): the aspect ratio is as before but with $Re = 2. \times 10^4$. As for square ducts, the sign of contours changes as the corner bisector is reached. This confirms a strong division of the secondary flow indicated by the positions of secondary-velocity vortices shown in Fig. 4.22. Agreement between contours obtained by RSM and experimental results is acceptable while the NKE results are accompanied by rather unexpected zero (i.e. isotropic) contour along the horizontal wall bisector though this does not seem to have serious impact on the secondary-flow structure obtained by NKE.

An important consequence of the distortion to the mean-velocity field under influence of secondary motion is the modification to the wall-shear-stress distribution. Detailed measurements of this parameter have been reported by Knight and Patel (1985,a) for eight different aspect ratios and those are used to assess the present models. The comparisons are presented in Fig. 4.25 where it can be seen that the shear-stress maximum does not occur in the centre-plane of the duct (as it would do in strictly two-dimensional flows) but is shifted towards the corner. Thus a region of stress deficit is created in the central portion of duct which is seen to

move towards the duct's corner as the aspect ratio of the duct increases. The NKE model results seems to be more sensitive to the influence of the secondary motion leading to deeper stress deficits. In contrast, the RSM profiles are less sensitive although exhibiting mild discontinuities in the corner regions for two small aspect ratios.

4.4 Compound Ducts

4.4.1 Symmetric Ducts

In contrast to the situation for rectangular ducts, far fewer measurements of flows in compound ducts have been reported in the literature. The most complete sets available are those of Knight and Lai (1985,a) and (1985,b) and those will be used here for models validation.

The predicted secondary-velocity vectors for various values of h^* are presented in Fig. 4.26. It is immediately clear that the external corner appears to generate additional secondary motion which exceeds in strength that produced in other parts of the duct. For the flow situation with $h^* = 0.516$ the main-duct area is almost entirely dominated by the strong secondary motion originating from the external corner. Some of that motion spills over the flood plains. By decreasing of h^* the intensity of the secondary motion steadily decays at the main flow-flood plain interface such that, for the lowest value of h^*, the flow in the main duct becomes very similar to that observed in an isolated rectangular duct. The secondary motion is still present near to the external corner but its influence is confined to a narrow neighbouring region.

The positions of the secondary-flow cells may be clearly seen from Fig. 4.27. The streamlines are closest around the external corners indicating the strongest velocity gradients there. It can be seen that for $h^* = 0.516$ two dominant vortices, one from the main part of the duct and one from

the flood plain come together along the external-corner bisector. The influence of the flood-plain vortices extends almost to the very end of the flood plain. The mutual interaction between these two vortices is strongest for $h^* = 0.516$ while it decays with decreasing h^*. In such manner the main-duct vortex for $h^* = 0.221$ is almost unaffected by the flood-plain vortex.

The data and the present RSM predictions of the mean-velocity contours for all four values of h^* are presented in Fig. 4.28. The mean velocity is normalized by bulk velocity (W_b). The consequence of the strong secondary motion near to the external corner can be clearly seen from this figure where the contours bulge outwards. The distortion to the velocity contours is so strong that for higher h^* it leads to the creation of a local maximum of mean velocity in the flood plain area. The reduction in the distortion of the mean velocity with decreasing h^* is in accordance with the secondary-velocity behaviour observed in Fig. 4.26. Clearly, the RSM reproduces mean-velocity contours which agree closely with measurements as can be seen for duct with $h^* = 0.516$. The agreement for the remaining values of h^* is generally satisfactory. The NKE results are presented in Fig. 4.29. The bulging here is somewhat weaker than with the RSM but nevertheless agreement between data and predictions can be regarded as satisfactory.

The predicted and measured bed-shear-stress profiles ,non-dimensionalized by mean-shear-stress ($\bar{\tau}$), are plotted in Fig. 4.30. The shear stress on the flood plain for the $h^* = 0.516$ shows mild depression around the $x/B = 0.4$ which is slightly better captured by NKE. Both models produce a small drop of shear stress on the flood plain just before the junction with the main duct. The perturbations of the shear-stress distributions on the flood plain are generally very weak and almost disappear for the smallest value of h^*. The shear-stress behaviour in the main duct also varies with decreasing of h^*. For $h^* = 0.516$, the shear-stress maximum occurs at the centre line of the duct while for $h^* = 0.221$, where the effects of the bulging on the main duct-flood plain interface are weakened, the maximum appears to be shifted from the centre line towards the corners.

This is clearly predicted by NKE but not with RSM.

A summary of the predicted and measured average shear-stress values for the geometries considered is provided in Table 4.2.

			$\overline{\tau}$ [N/m^2]				
Re $\times 10^4$	h*	B/b	DATA	NKE	Er. %	RSM	Er. %
8.13	0.516	4.1	0.2388	0.2411	+0.96	0.2214	−7.3
6.82	0.404	4.0	0.3211	0.3031	−5.6	0.3023	−5.8
5.60	0.310	4.0	0.3569	0.3367	−5.6	0.3302	−7.5
4.27	0.221	4.0	0.3293	0.2966	−9.9	0.2919	−11.3

Table 4.2. Average-shear-stress in compound ducts.
Data of Knight and Lai (1985,b)

The 'relative errors' between data and predictions vary with h*: for the NKE it ranges from 0.96% for h* = 0.516 to the −9.9% for h* = 0.221 while, for the RSM, it varies from −7.3% for h* = 0.516 to −11.3% for h* = 0.221.

4.4.2 Asymmetric Ducts

Asymmetric-compound ducts possess all the features of compound ducts mentioned above , only now those are no longer simplified by the presence of a plane of symmetry. Here, the ratio B/b, of the total duct width to that of the main-channel is different between the left and the right banks. The effects of asymmetry are strongest when one part of the duct is rectangular ($(B/b)_l = 1$) while the other is compound ($(B/b)_r > 1$). In this section, the focus is on the data of Knight and Lai (1985,a) for the following parameters: Re $= 8.23 \times 10^4$, $(B/b)_l = 1$, $(B/b)_r = 4.92$ and h* $= 0.514$.

The secondary-velocity vectors obtained with the RSM and the NKE are plotted in Fig. 4.31. Here, as for the symmetric ducts, the strongest secondary motion again appears in the vicinity of the external corners. This motion interacts with secondary motion originating from the main duct but the flow in the flood plain far from the external corner resembles that in a rectangular duct. The impact of the large vortex, which appears in the main duct adjacent to the flood plain, on the rest of the flow domain can be clearly seen from Fig. 4.32. This vortex dominates a large part of the main duct and by its influence suppresses the two remaining vortices. The situation in the flood plain is very similar to that observed in symmetric ducts implying that the effects of asymmetry are primarily confined to the flow in the main duct. The secondary velocity streamlines produced by both models are very similar.

The mean-velocity contours presented in Fig. 4.33 again show the appearance of a local maximum at the flood plain. The strongest bulging occurs near to the external corner and, since this is absent from the left side of duct, the flow inside main duct becomes asymmetric. The asymmetry effects are clearly well predicted by both models. Since, the flow in an asymmetric-compound duct comprises all secondary effects, mentioned so far, it would be interesting to consider the mean-flow contours in the absence of the secondary flow. Thus, the mean-velocity contours obtained with a linear k-ϵ model are also presented in Fig. 4.33. It is apparent that all distortions to the velocity contours, shown for various geometries hitherto, are completely absent.

The modified mean-velocity field in the main duct results in mild bed-shear-stress asymmetry as can be seen from Fig. 4.34. There, the distribution obtained with the RSM slightly underestimates experiments and NKE predictions. The measured bed-shear-stress distribution in the flood plain shows typical wavy behaviour which is satisfactorily reproduced by both models. In the case of absent secondary flow, the shear-stress profiles are undisturbed and differ from the data and the present predictions. The discrepancy is particularly apparent near the corner regions.

To our knowledge, only two experimental investigations of the fully-developed flows in trapezoidal ducts have been reported. The first was by Rodet[2] (1960) who measured the distribution of the mean velocity and the turbulent stresses inside relatively narrow trapezoidal duct (AR = 0.82) having the bottom and top angles of 105° and 75° respectively. The second was for a trapezoidal duct with larger aspect ratio (AR = 3.5) measured by Prinos et al. (1988). The side walls in this case were slightly more inclined, resulting in the corner angles of 116° and 64°. Unfortunately, in none of the above were measurements for the secondary velocities presented.

The predictions reported here were obtained using the NKE model in conjunction with body-fitted coordinates. The computational grid for the Rodet's geometry can be seen in Fig. 4.35 a). The secondary-velocity vectors are presented in Fig. 4.35 b) for Re = 2.4×10^5. The velocity vectors are again directed towards the corners (along their bisectors) and thereafter along the side walls to the central portion of the duct. Note that here, due to the duct asymmetry, the secondary vectors are weaker along the top and bottom walls compared with the motion along the side walls. The present secondary velocity behaviour can be clearly seen from the secondary-velocity streamlines plotted in Fig. 4.35 c): the flow domain is dominated by four vortices in the middle interacting with two pairs of smaller ones along the bottom and top walls.

Fig. 4.36 a) compares the predicted and measured mean-velocity contours for Rodet's trapezoidal duct. The top corner appears to have a stronger impact upon mean-velocity bulging compared to the bottom one. A mild distortion of the profiles near to the side walls appears exactly at the

[2]In the present study results of Rodet's experiment are taken from Brundrett and Baines (1964)

position where the two middle vortices meet each other. The predicted and measured contours show the same behaviour although the extent of the bulging appears to be slightly underpredicted. The turbulence anisotropy is presented in Fig. 4.36 b). The predicted zero contour (corresponding to isotropic turbulence) in the lower part of the duct extends to the symmetry plane in the same manner observed in rectangular ducts (Fig. 4.24). The agreement between measured and predicted results is generally satisfactory.

Fig. 4.37 shows the predicted secondary motion for the flow of Prinos et al. (1988) for which Reynolds number (based on maximum velocity) was $Re = 2.25 \times 10^5$. It can be seen from Fig. 4.37 b) that the strongest motions appear next to the inclined surface, reducing in strength with approach to the duct's center. The secondary motion adjacent to the bottom corner is no longer directed along corner bisector.

The predicted and measured mean-velocity contours (averaged by W_{max}) are presented in Fig. 4.38 a). The measurements show a significant level of distortion near to the duct symmetry plane. Since the mean-velocity behaviour is strongly linked to the strength of the secondary motion it is likely that those distortions are caused by strong secondary motion along the symmetry plane from the upper part of the duct. The predicted secondary-velocity vectors do not show such behaviour and it is unfortunate that Prinos et al. (1988) did not measure the secondary-velocity field as this would have explained the cause of the severe mean-velocity distortion. The predictions show the strongest distortion in the corner regions while the contours approaching the middle portion of the duct are almost unaffected. Such behaviour is consistent with mean-velocity contours presented in Fig. 4.23.

The contours of the turbulent kinetic energy (k/W_{max}^2) plotted in Fig. 4.38 b) confirm that the distortions caused by secondary motion are even more severe for the turbulent quantities. Thus the predicted and measured contours of k indicate a very strong bulging towards the corners. However, the significant mean-velocity distortion in the centre of the duct

suggested by the data does not seem to be accompanied with distortion of the contours of the turbulent kinetic energy at the same place. The predicted and measured main-shear-stress ($\overline{vw}$) contours normalized by W^2_{max} are shown in Fig. 4.38 c). The shape of contours is similar although the positions of predicted contours are displaced compared to the experiment.

The predicted and measured wall-shear-stress distributions ($\tau_w/\overline{\tau}$) are presented in Fig. 4.39. The differences here are closely related to the differences observed in the predicted and measured contours of mean velocity. The predicted shear-stress profiles on the top and bottom walls show mild depression approximately half way between the symmetry plane and the side wall. The measured shear stress is quite uniform on the bottom wall while on the top a slight depression appears near the duct's symmetry plane. The predicted shear stress on the side wall shows significant drop with approach to the top of the duct.

4.6 Closure to Chapter 4

Published data for flows in closed ducts of various cross shapes were used to assess the performance of the nonlinear k-ϵ model and the Reynolds-stress model in predicting of turbulence-driven secondary motion and its consequences on the overall flow structure. Two different models for the difficult pressure-strain term were evaluated. The advantages of the complete $\Phi_{ij,2}$ formulation against the simple one were presented in Section 4.2. It was also shown that neglect of the secondary gradients from the nonlinear stress-strain expressions had no influence on the final results.

The predictions for rectangular ducts obtained with both models were discussed in Section 4.3. Generally, both models were shown to be able to accurately predict most features of the turbulence-driven secondary motion. In many cases the results of the two models were very similar

but there were some differences too. Thus the distortion of mean-velocity contours was better captured by Reynolds-stress model but that was underestimated by nonlinear k-ϵ model. On the other hand, the influence of the secondary motion on the wall-shear-stress distribution was better followed by nonlinear model particularly so in the corner regions where the Reynolds-stress model showed mild discontinuity there for the two smallest aspect ratios.

The present models also proved adequate for flows in compound ducts as was presented in Section 4.4. Generally, the two models were found to be equally suited to the prediction of secondary-motion effects in compound ducts which include the bulging at the main flow-flood plane interface and the local velocity maximum in the flood plane. Although the nonlinear k-ϵ model results were generally satisfactory it is worth noting that some flow characteristics were better reproduced by the Reynolds-stress model, especially concerning the shape of the mean-velocity contours.

Because the two models gave very similar results, it was decided to apply only the nonlinear k-ϵ model to flows in trapezoidal ducts. The predicted results are shown in Section 4.5. It was found that the biggest influence of the changed geometry was on the shape of secondary vortices which then modified the mean-velocity field. The agreement between experiments and predictions was better for the smaller-aspect-ratio duct.

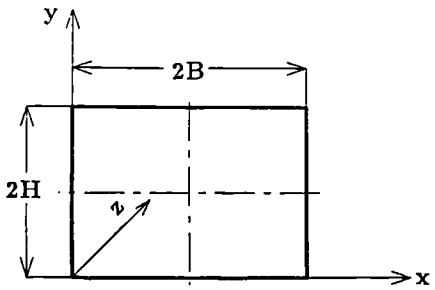

$$AR = \frac{B}{H}$$

a) Rectangular duct

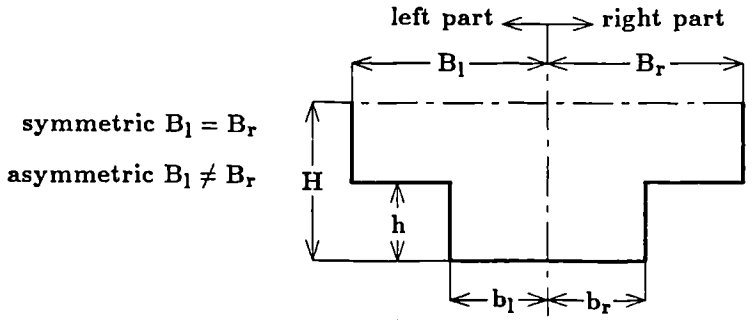

$$h^* = \frac{H - h}{H}$$

$$AR = \frac{(B_l + B_r)}{2H}$$

b) Compound duct

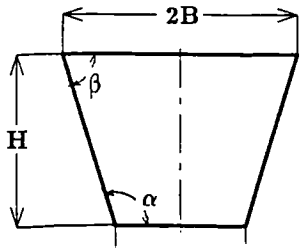

$$AR = \frac{B + b}{H}$$

c) Trapezoidal duct

Fig. 4.1 Duct-flow notation.

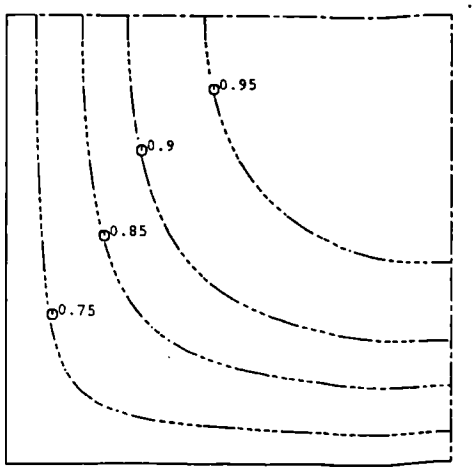

a) Mean-velocity isolines W/W_{max}

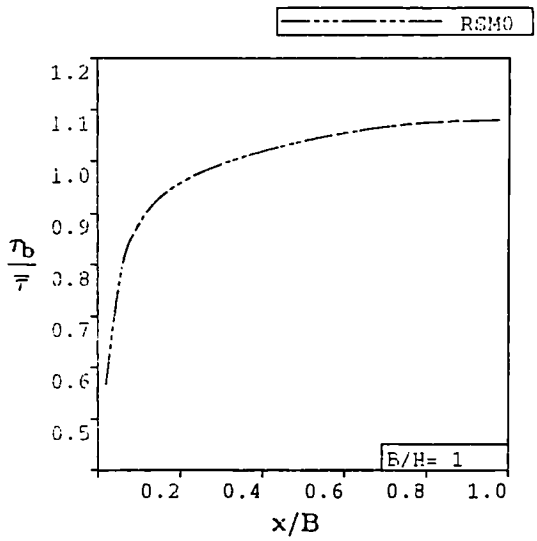

b) Bed-shear-stress

Fig. 4.2 Preliminary Reynolds-stress-model results (RSM0).

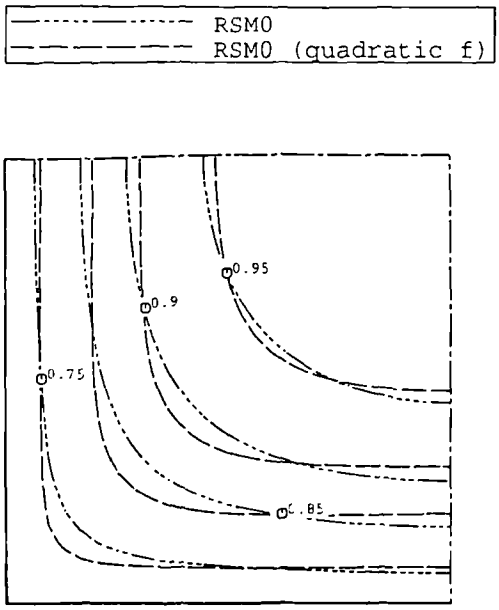

Fig. 4.3 Reynolds-stress-model improvement (step 1).
Mean – velocity isolines W/W_{max}.

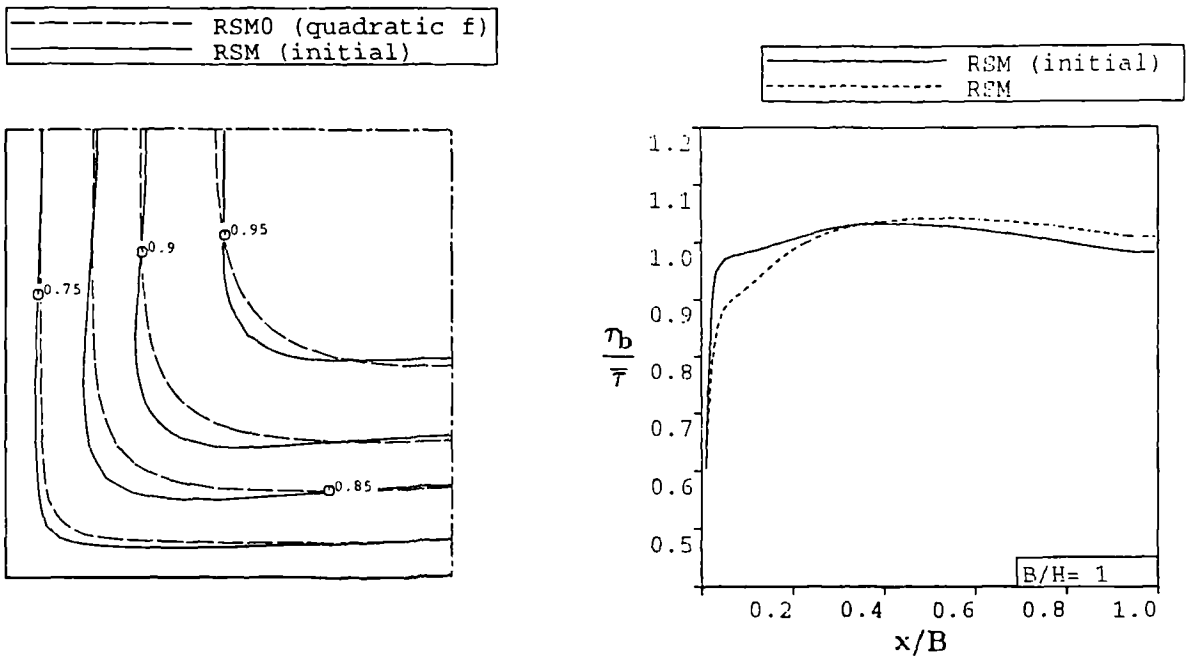

a) Mean-velocity isolines W/W_{max} b) Bed-shear-stress

Fig. 4.4 Reynolds-stress-model improvement (step 2).

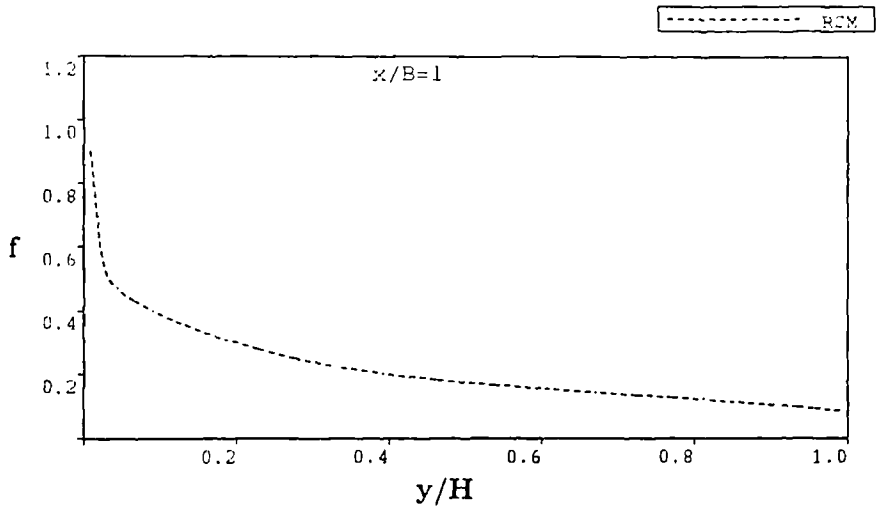

Fig. 4.5 Wall-damping function

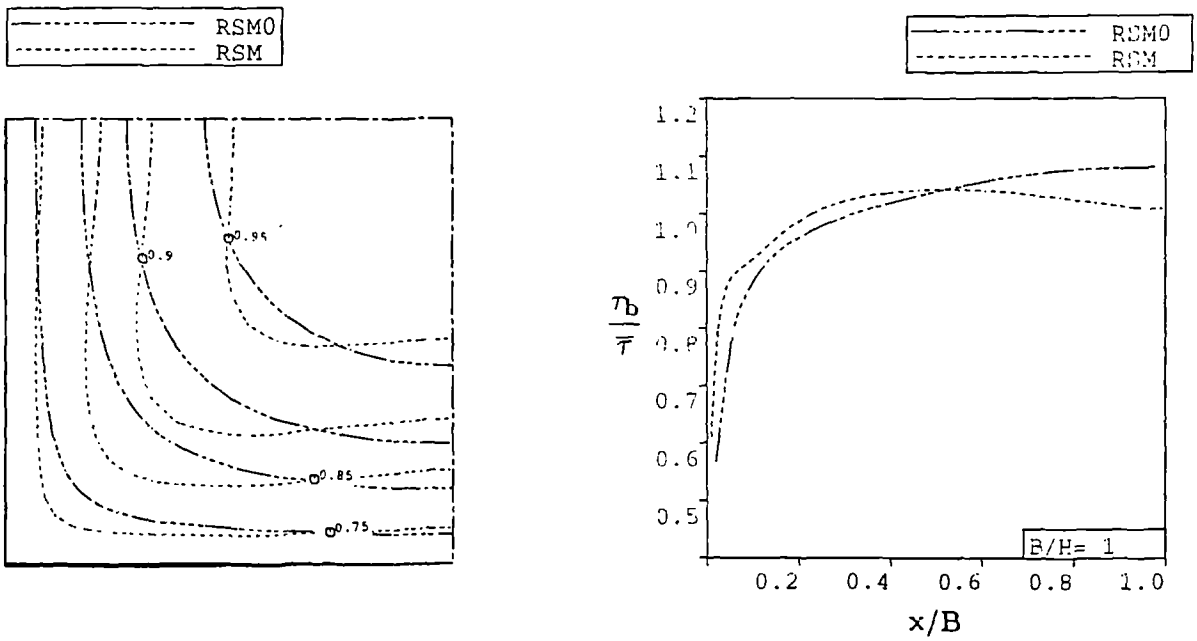

a) Mean-velocity isolines W/W_{max} b) Bed-shear-stress

Fig. 4.6 Comparison between RSM and RSM0.

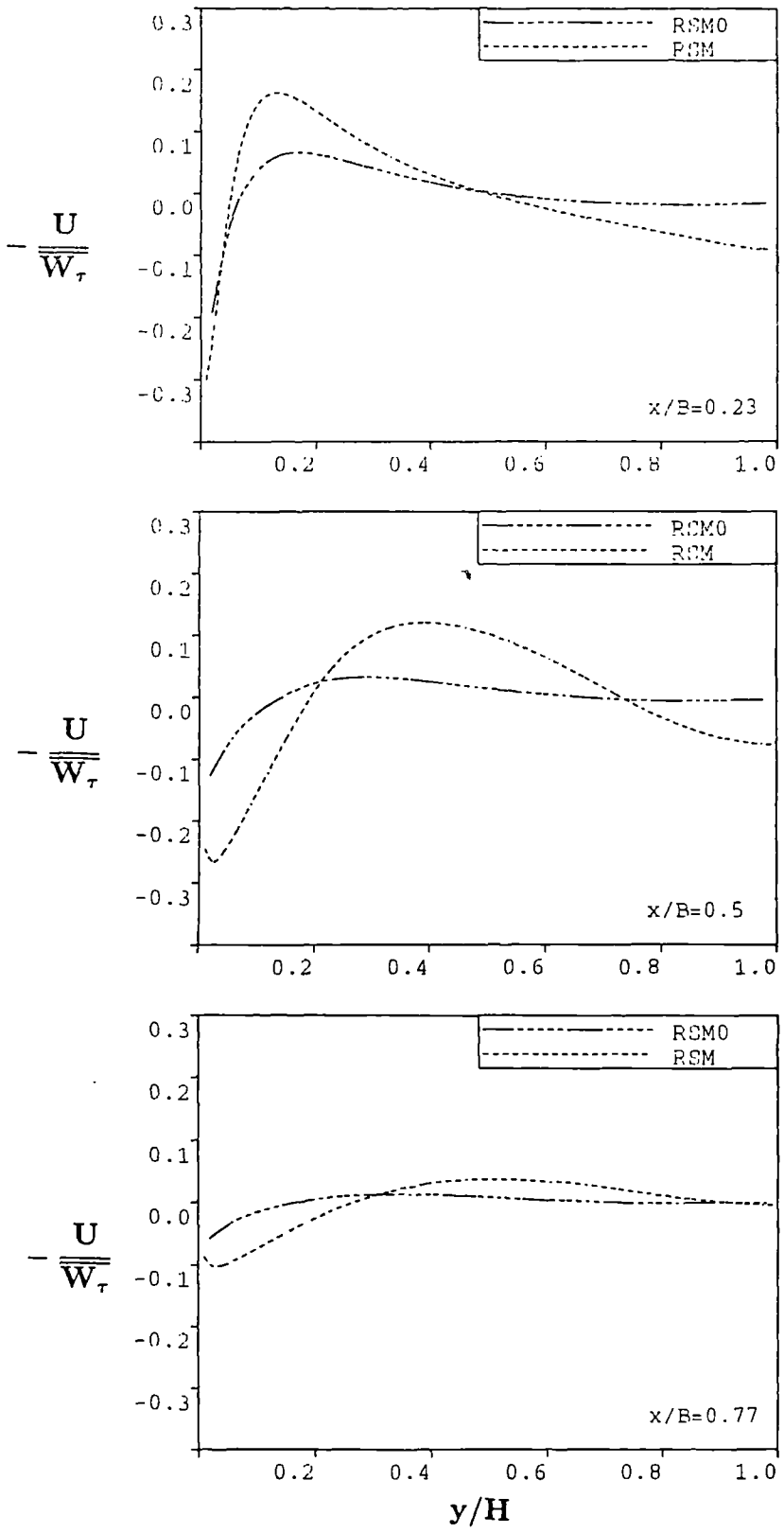

Fig. 4.7 Secondary-velocity profiles.

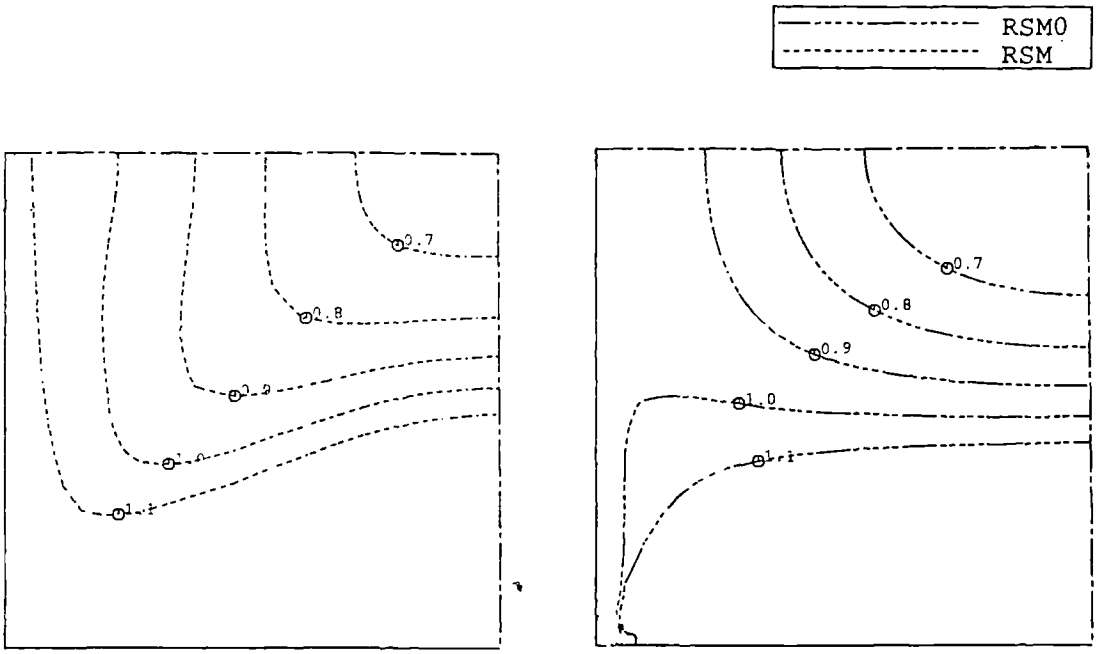

Fig. 4.8 Normal-stress contours $\frac{\overline{u^2}}{\overline{W}_\tau^2}$.

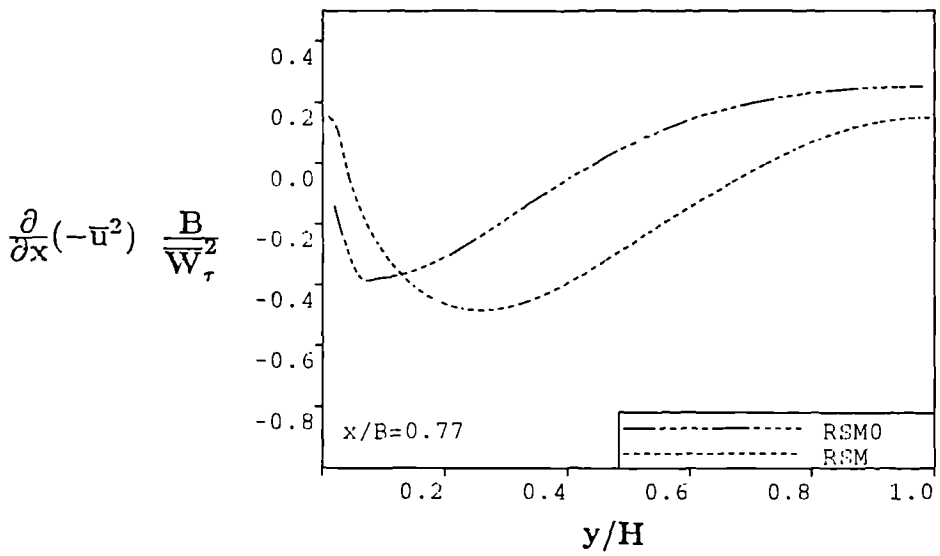

Fig. 4.9 Profile of normal-stress gradient $\frac{\partial}{\partial x}(-\overline{u^2})\ \frac{B}{\overline{W}_\tau^2}$.

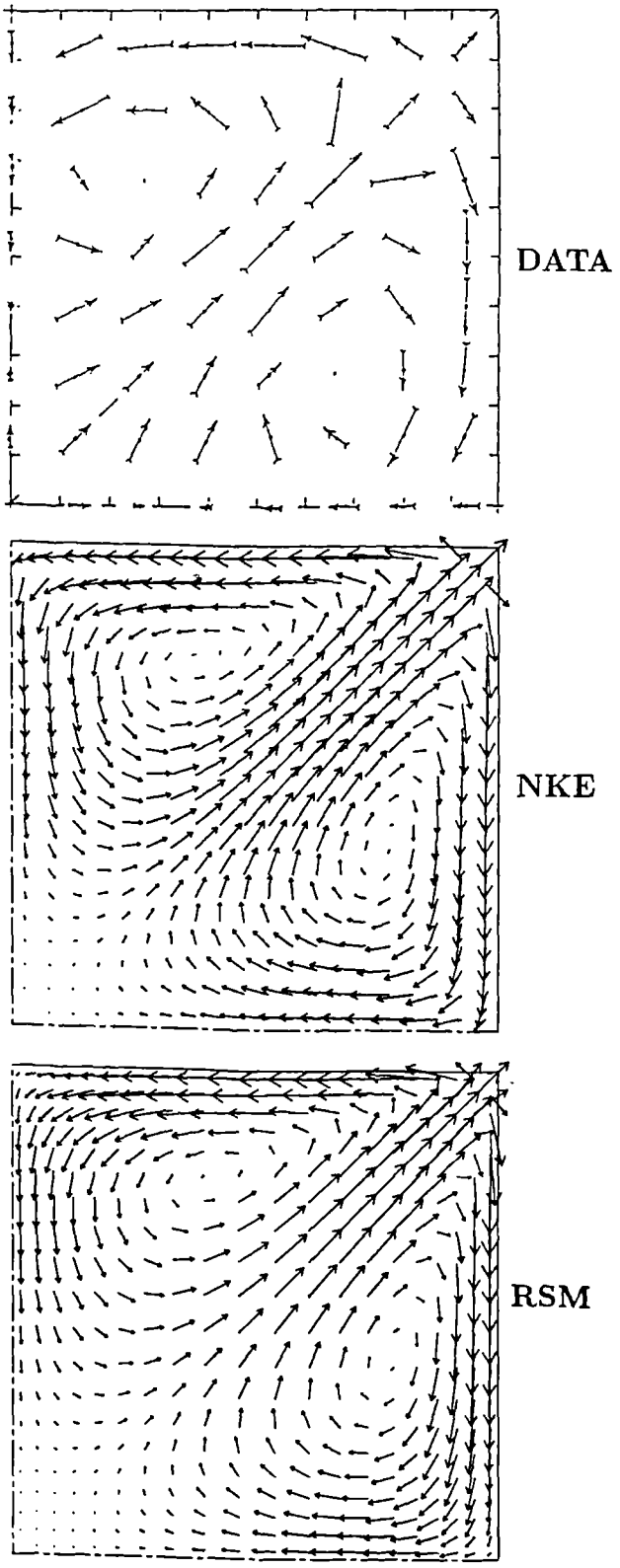

Fig. 4.10 Secondary – velocity vectors.
Data of Brundrett and Baines (1964).

Predictions: NKE / RSM

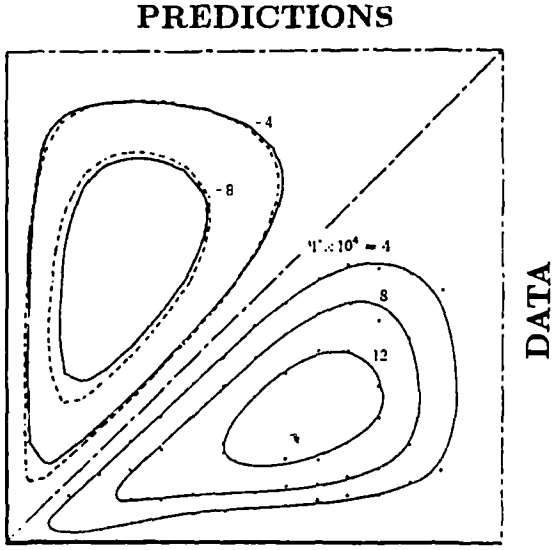

Fig. 4.11 Secondary – flow streamlines $\Psi \times 10^4$.
Data of Gessner and Jones (1965).

Predictions: NKE / RSM

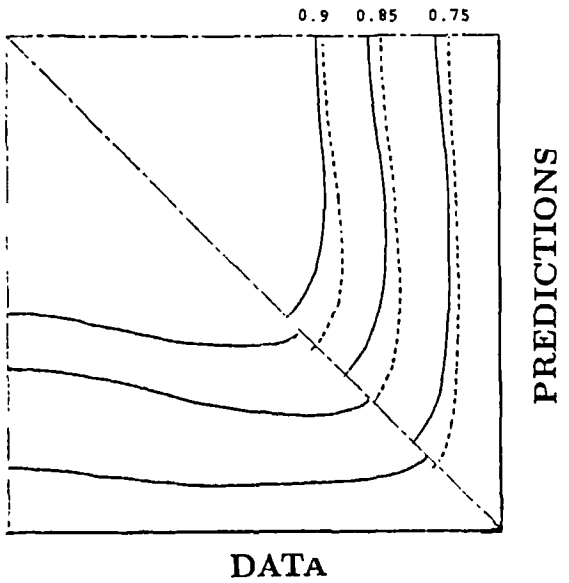

Fig. 4.12 Mean – velocity contours W/W_{max}.
Data of Brundrett and Baines (1964).

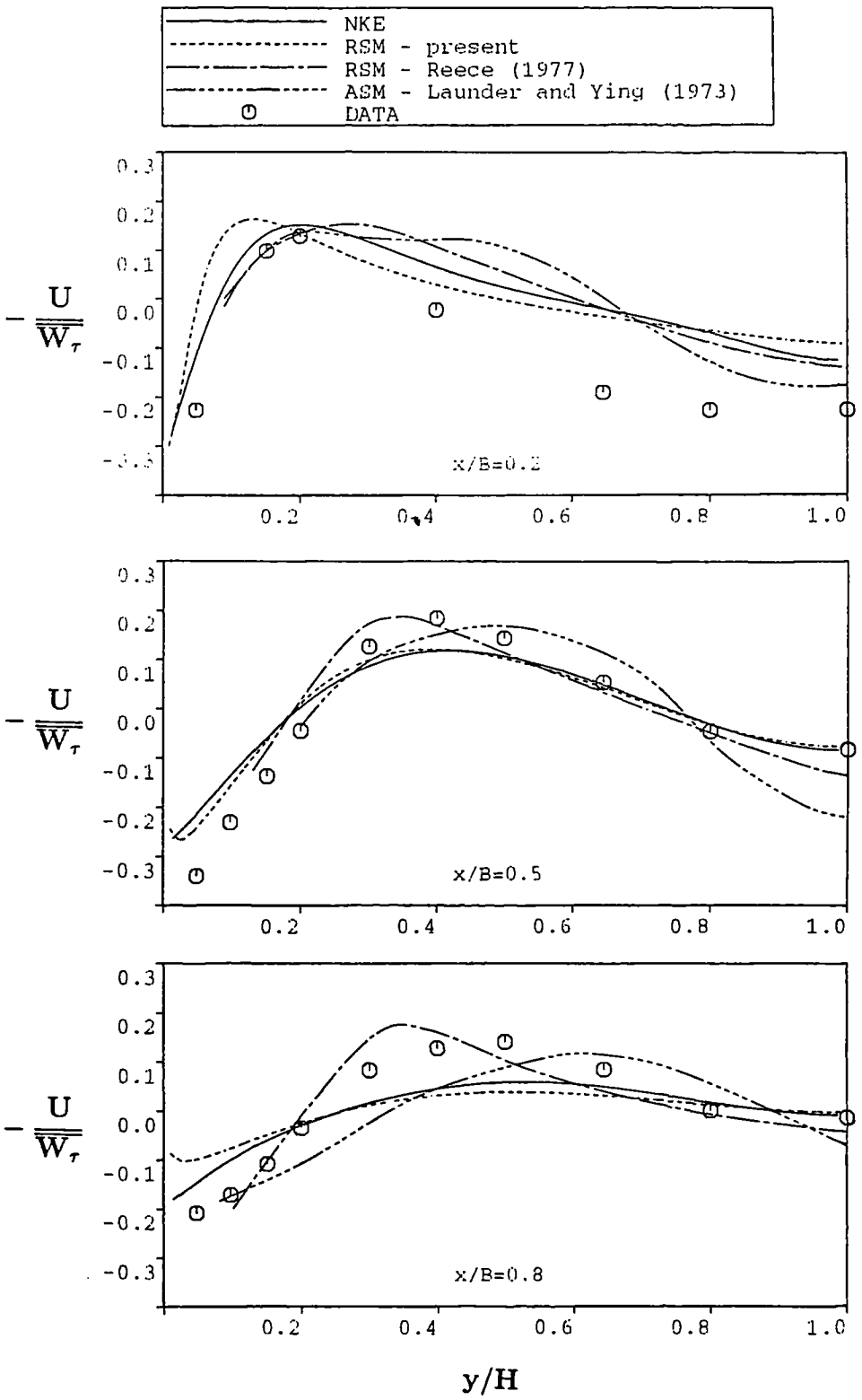

Fig. 4.13 Secondary – velocity profiles.
Data of Launder and Ying (1972).

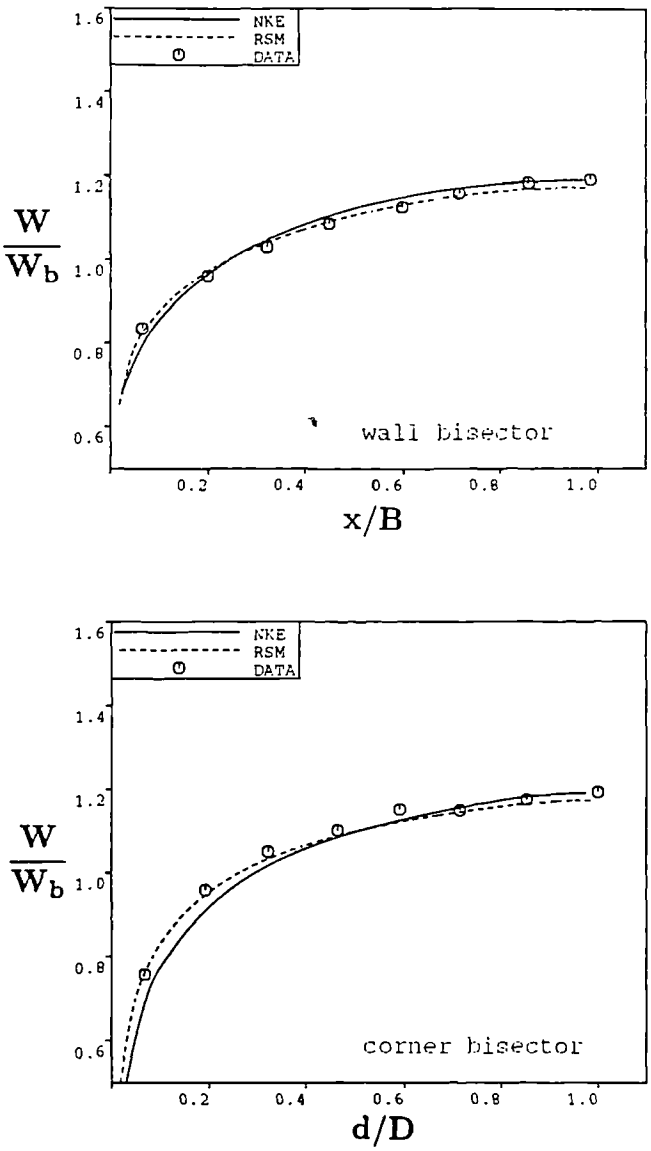

Fig. 4.14 Mean – velocity profiles. Data of Brundrett and Baines (1964).

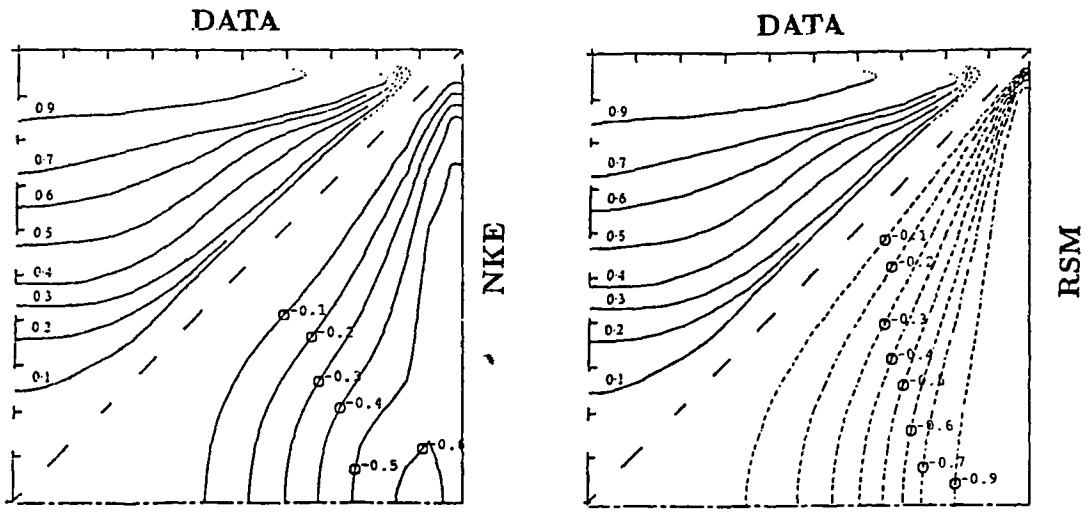

Fig. 4.15 Normal – stress – anisotropy contours $\frac{\overline{u^2}-\overline{v^2}}{\overline{W_\tau}^2}$.
Data of Brundrett and Baines (1964).

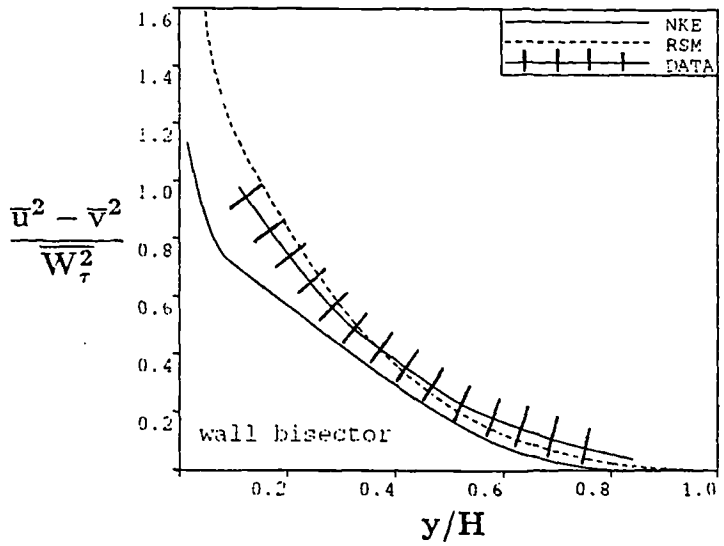

Fig. 4.16 Normal – stress – anisotropy profiles $\frac{\overline{u^2}-\overline{v^2}}{\overline{W_\tau}^2}$.
Data of Perkins (1970).

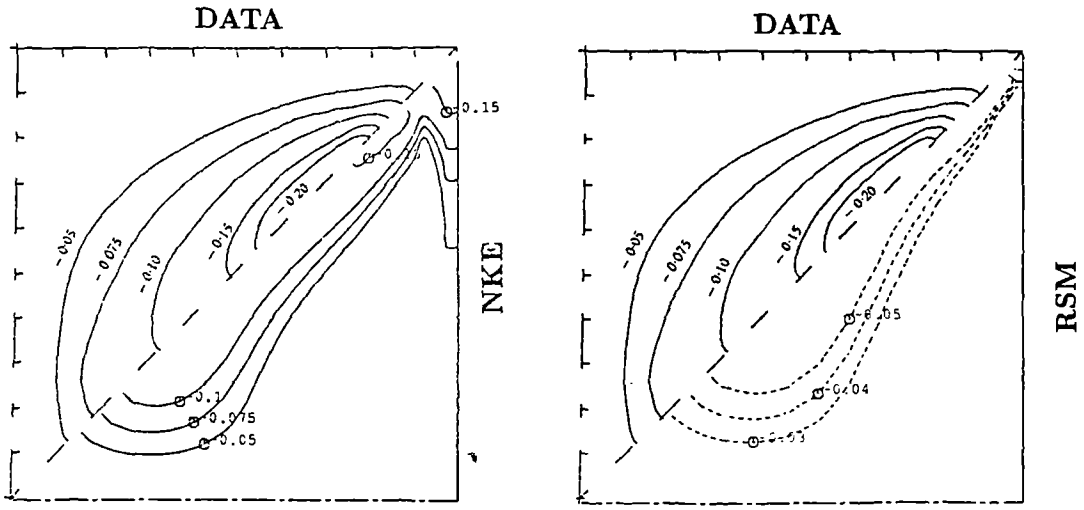

Fig. 4.17 Shear – stress contours $\frac{\overline{uv}}{\overline{W_\tau}^2}$. Data of Brundrett and Baines (1964).

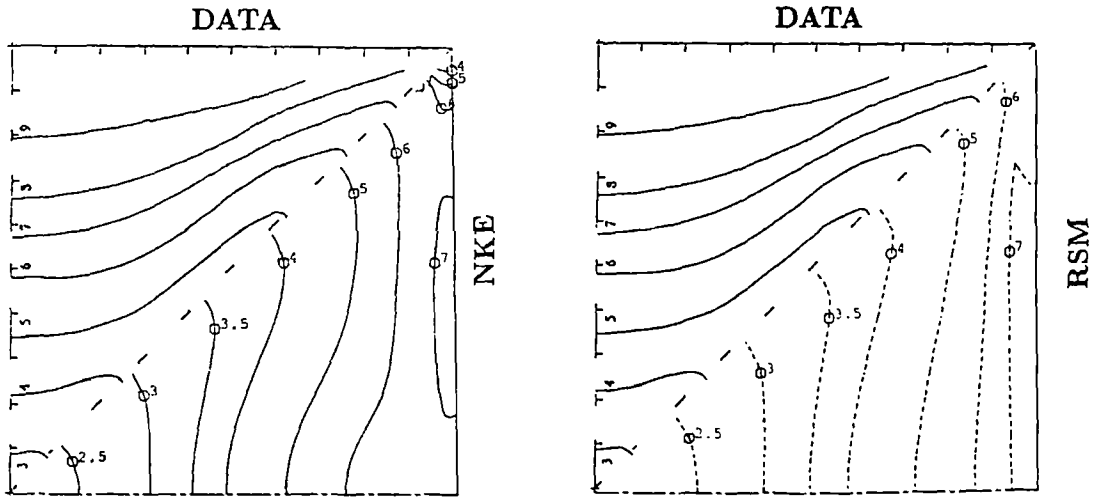

Fig. 4.18 Turbulent – kinetic – energy contours $\frac{2k}{\overline{W_\tau}^2}$. Data of Brundrett and Baines (1964).

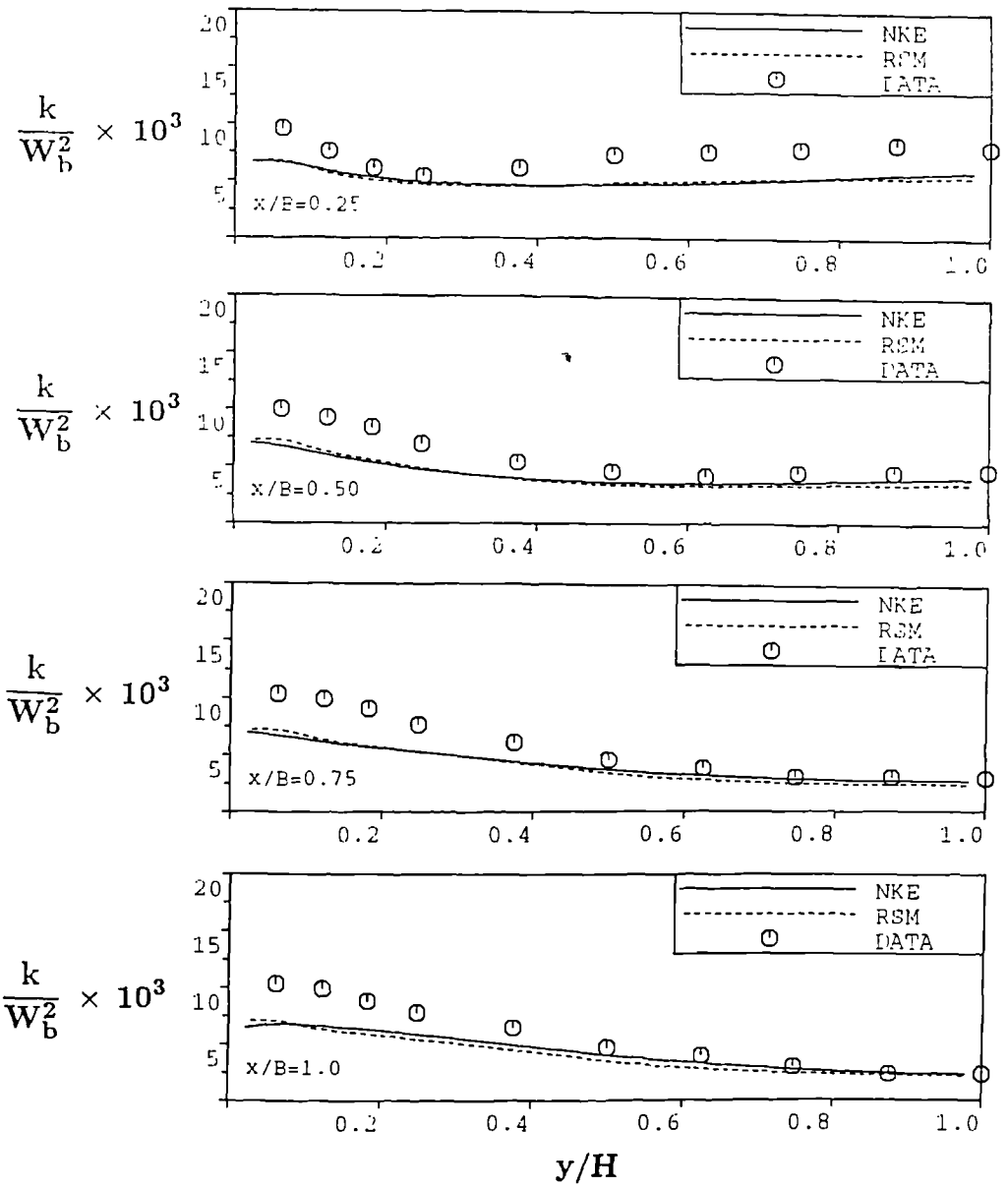

Fig. 4.19 Turbulent – kinetic – energy profiles.
Data of Gessner and Po (1976).

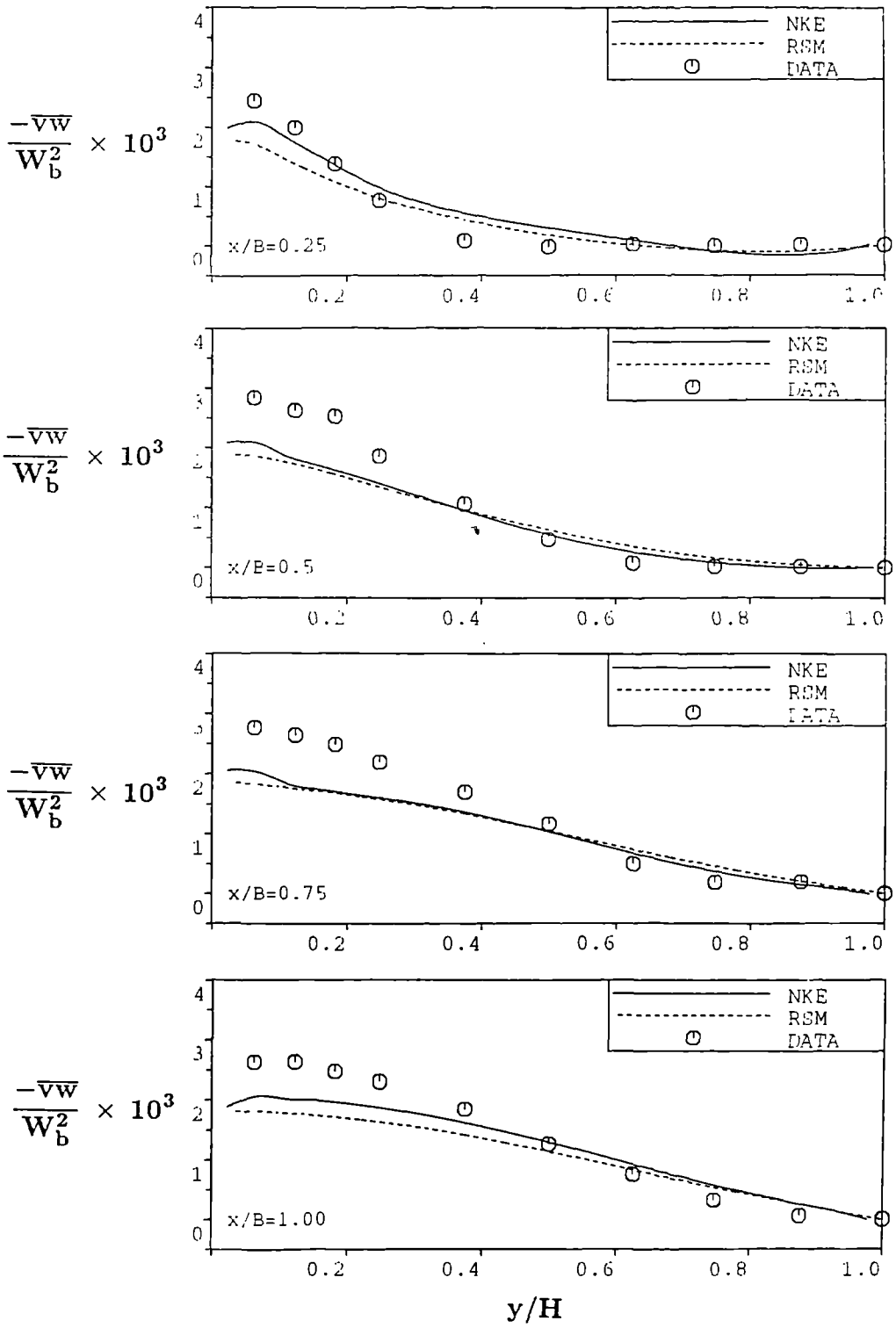

Fig. 4.20 Main – shear – stress profiles.
Data of Gessner and Po (1976).

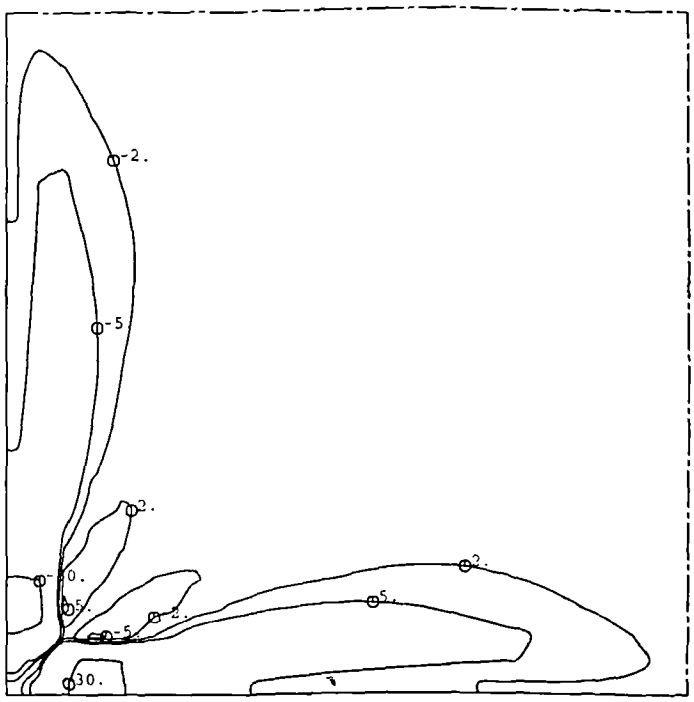

a) Term A2: $\frac{\partial^2}{\partial x \partial y}(\overline{u^2} - \overline{v^2}) \quad \frac{B^2}{\overline{W}_\tau^2}$

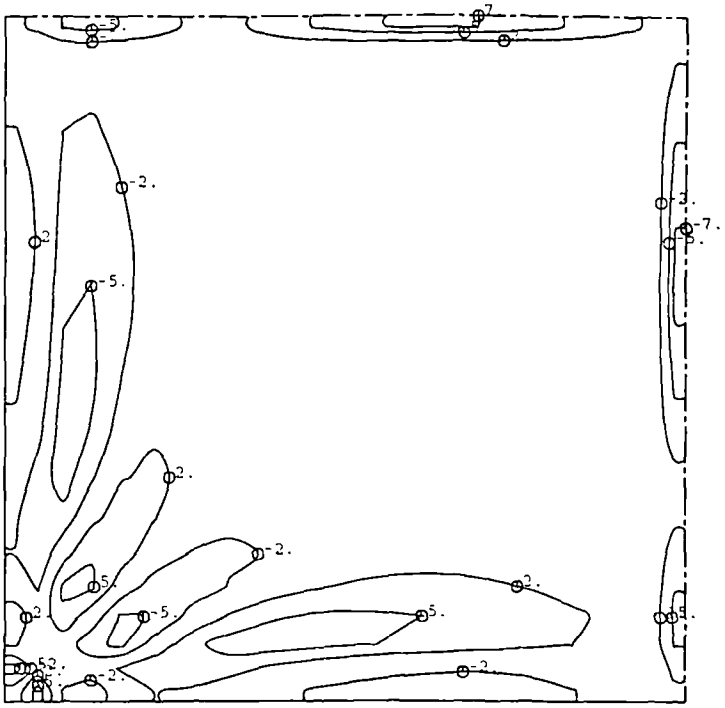

b) Term A3: $(\frac{\partial^2}{\partial x^2} - \frac{\partial^2}{\partial y^2})\overline{uv} \quad \frac{B^2}{\overline{W}_\tau^2}$

Fig. 4.21 Production of vorticity.

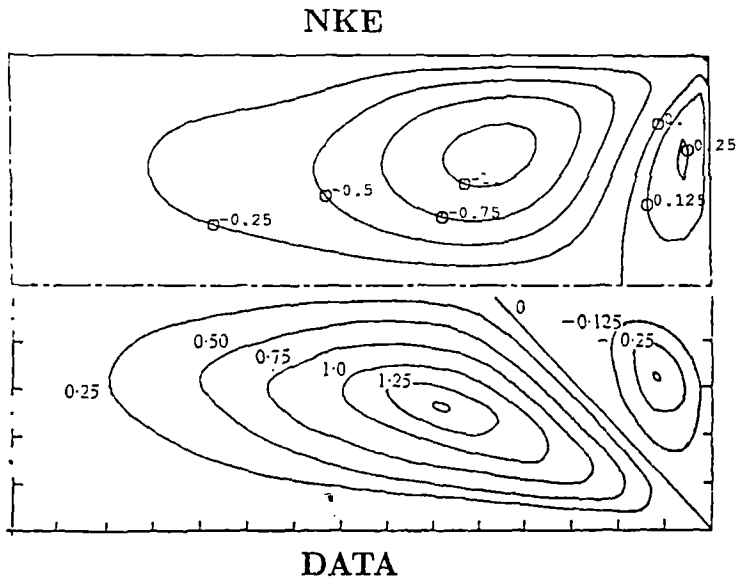

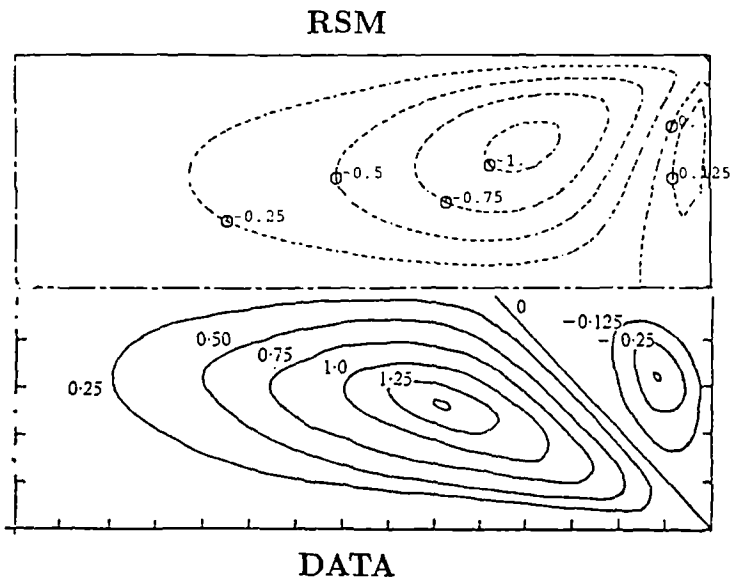

Fig. 4.22 Secondary – velocity streamlines $\Psi \times 10^3$. Data of Hoagland (1960).

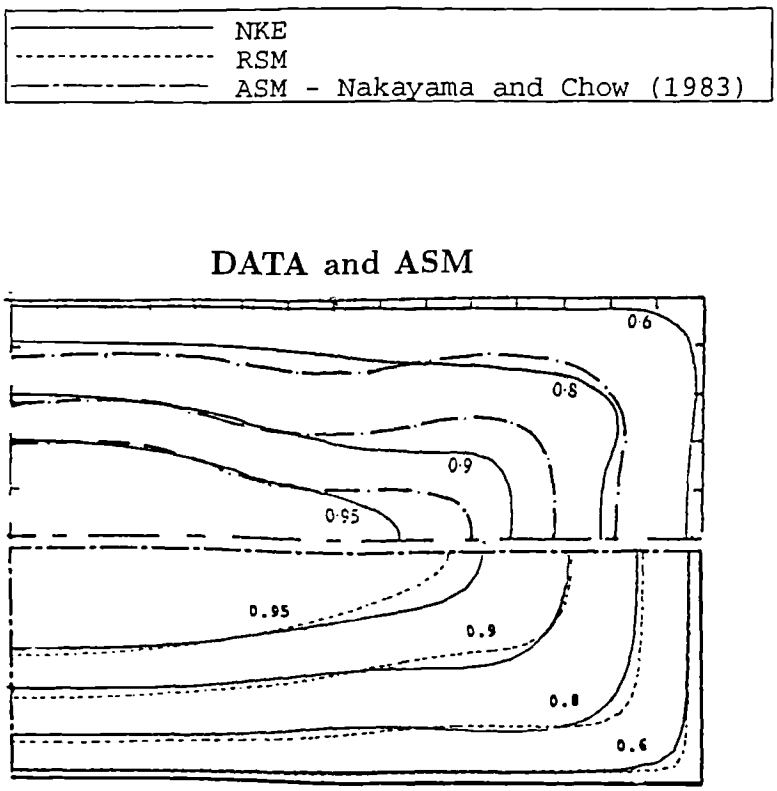

Fig. 4.23 Mean – velocity contours W/W_{max}.
Data of Leutheusser (1963).

NKE

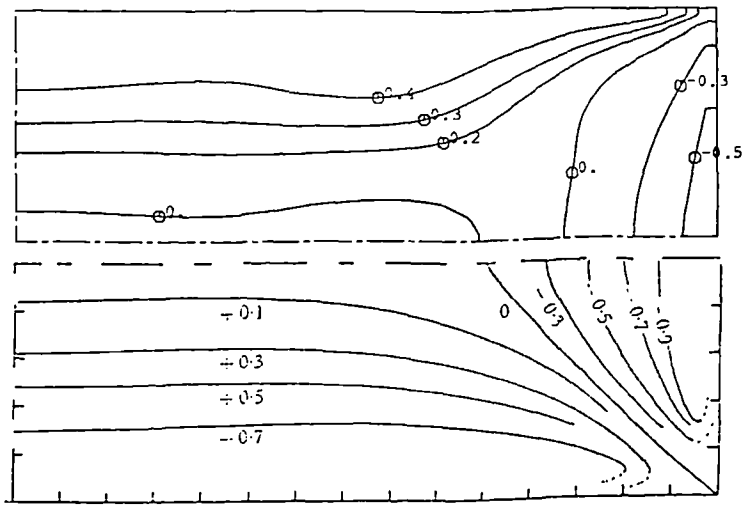

DATA

RSM

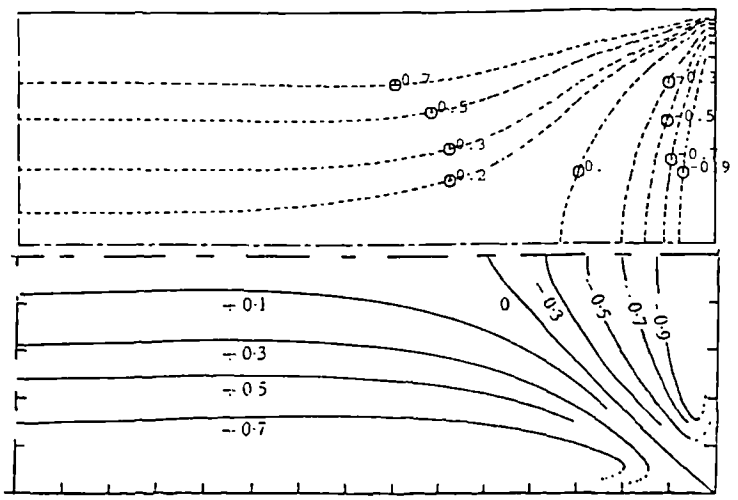

DATA

Fig. 4.24 Normal – stress – anisotropy contours $\frac{\overline{u^2}-\overline{v^2}}{\overline{W}^2_\tau}$.
Data of Hoagland (1960).

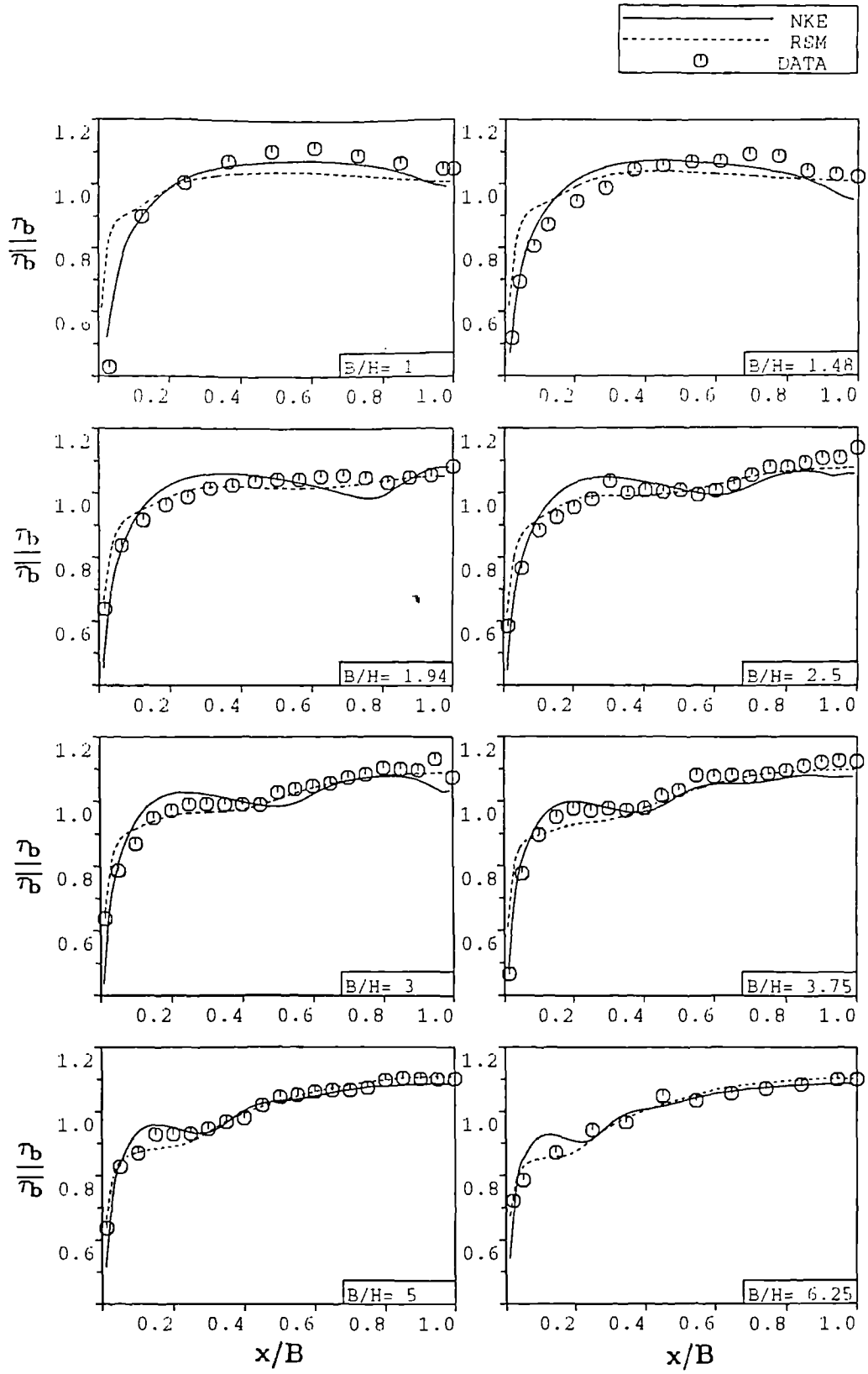

Fig. 4.25 Bed – shear – stress in rectangular ducts. Data of Knight and Patel (1985, a).

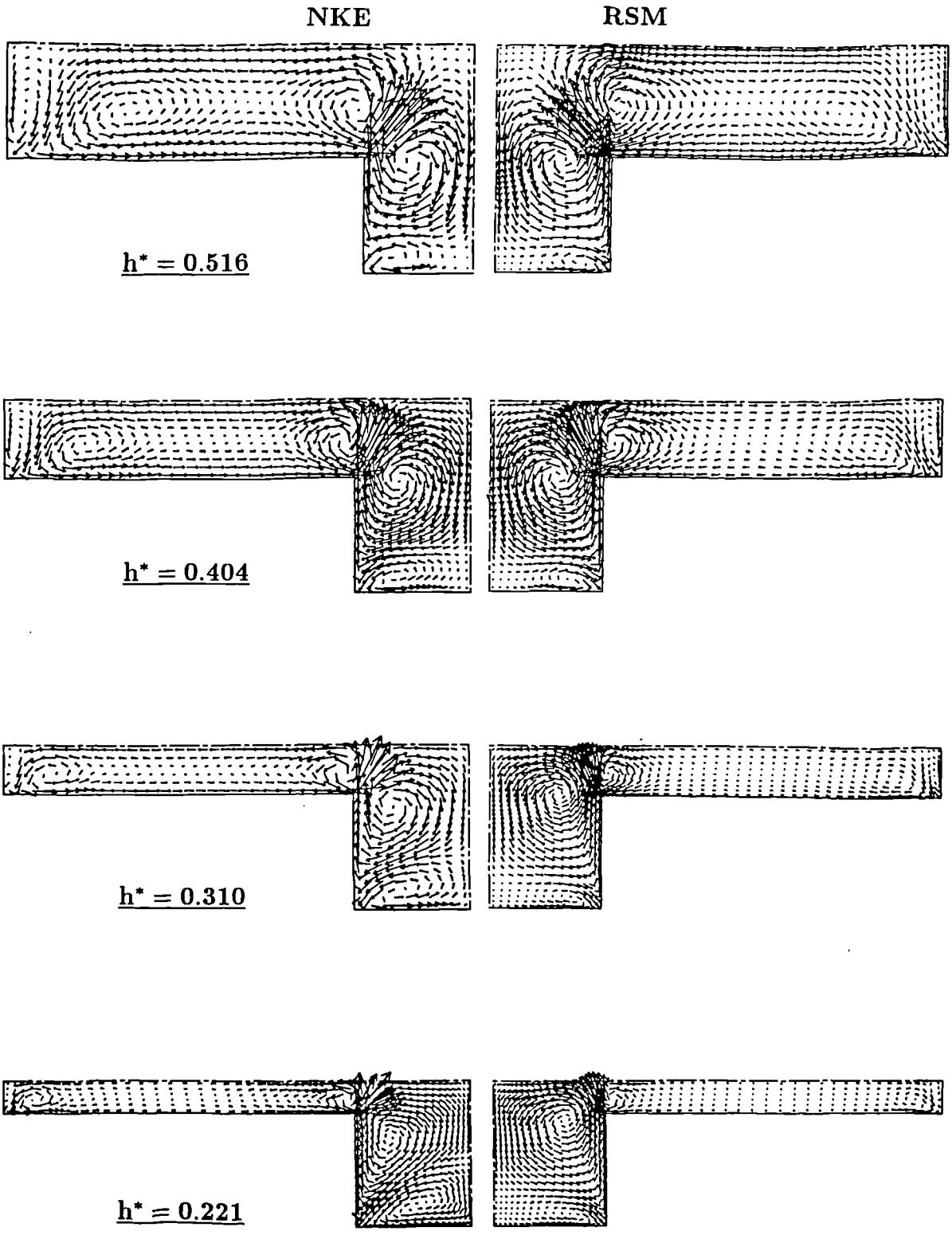

Fig. 4.26 Secondary-velocity vectors in compound-symmetric ducts.

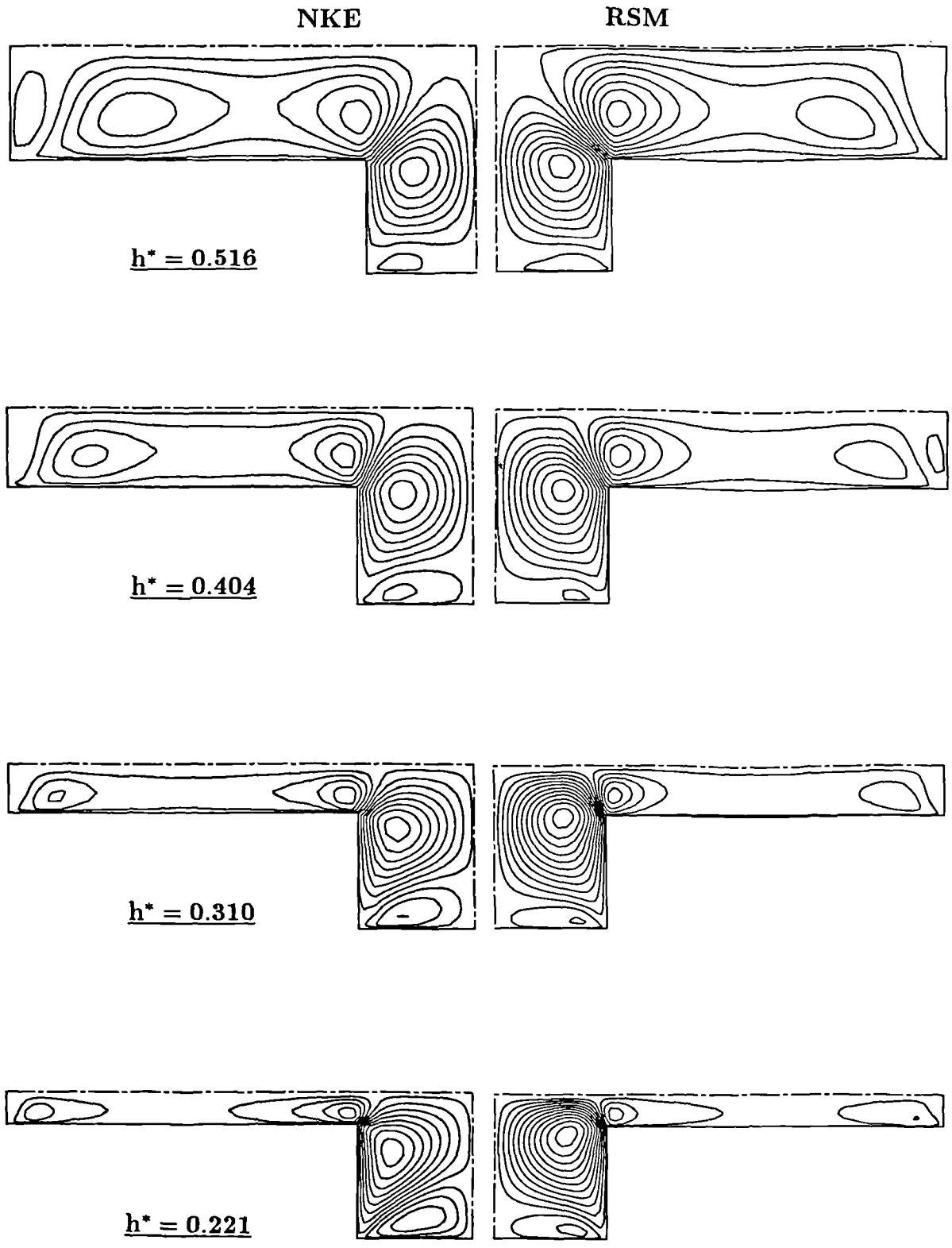

Fig. 4.27 Secondary-velocity streamlines in compound-symmetric ducts.

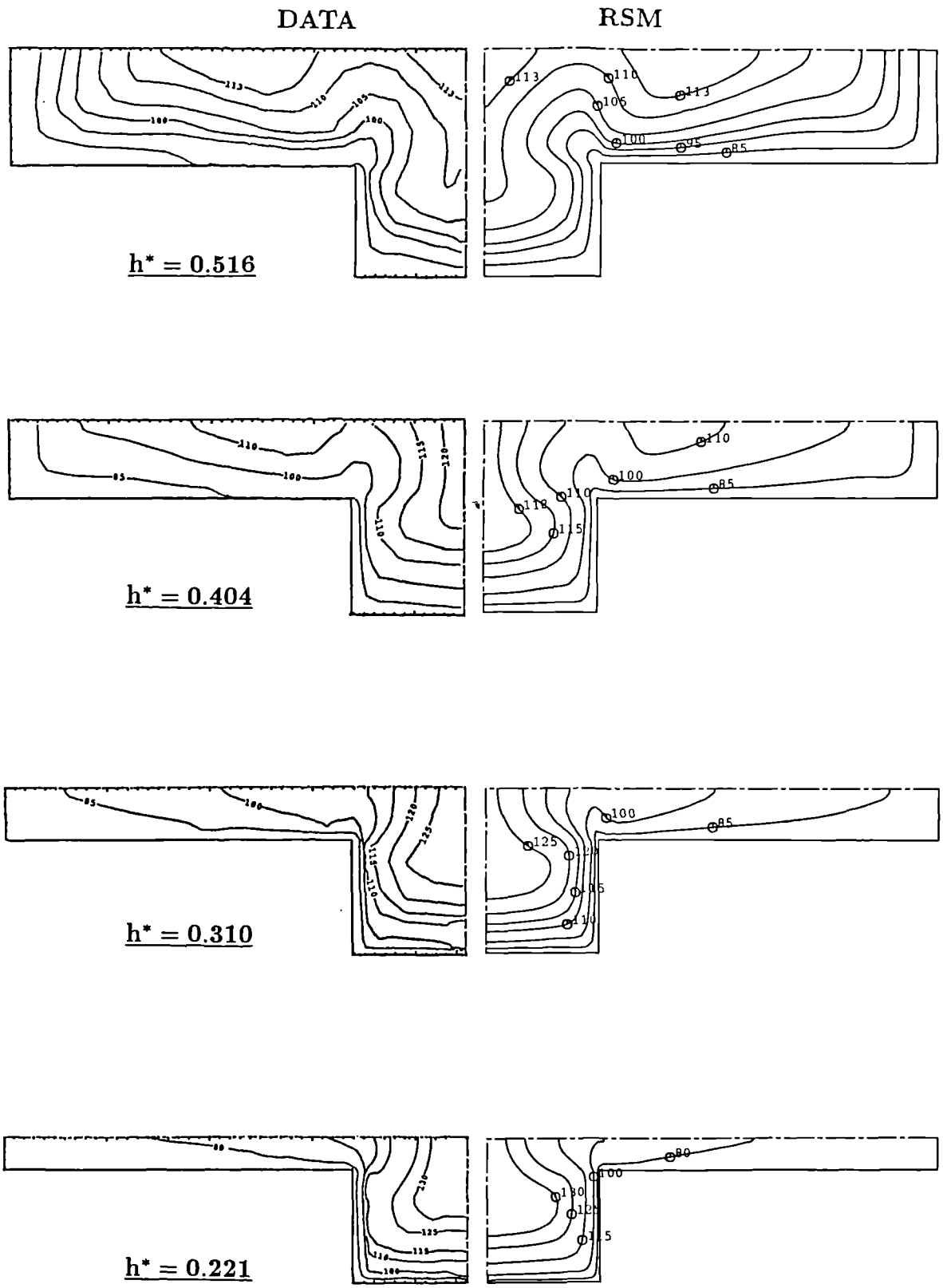

Fig. 4.28 Mean – velocity contours $W/W_b \times 10^2$.
Data of Knight and Lai (1985, a) and (1985, b).

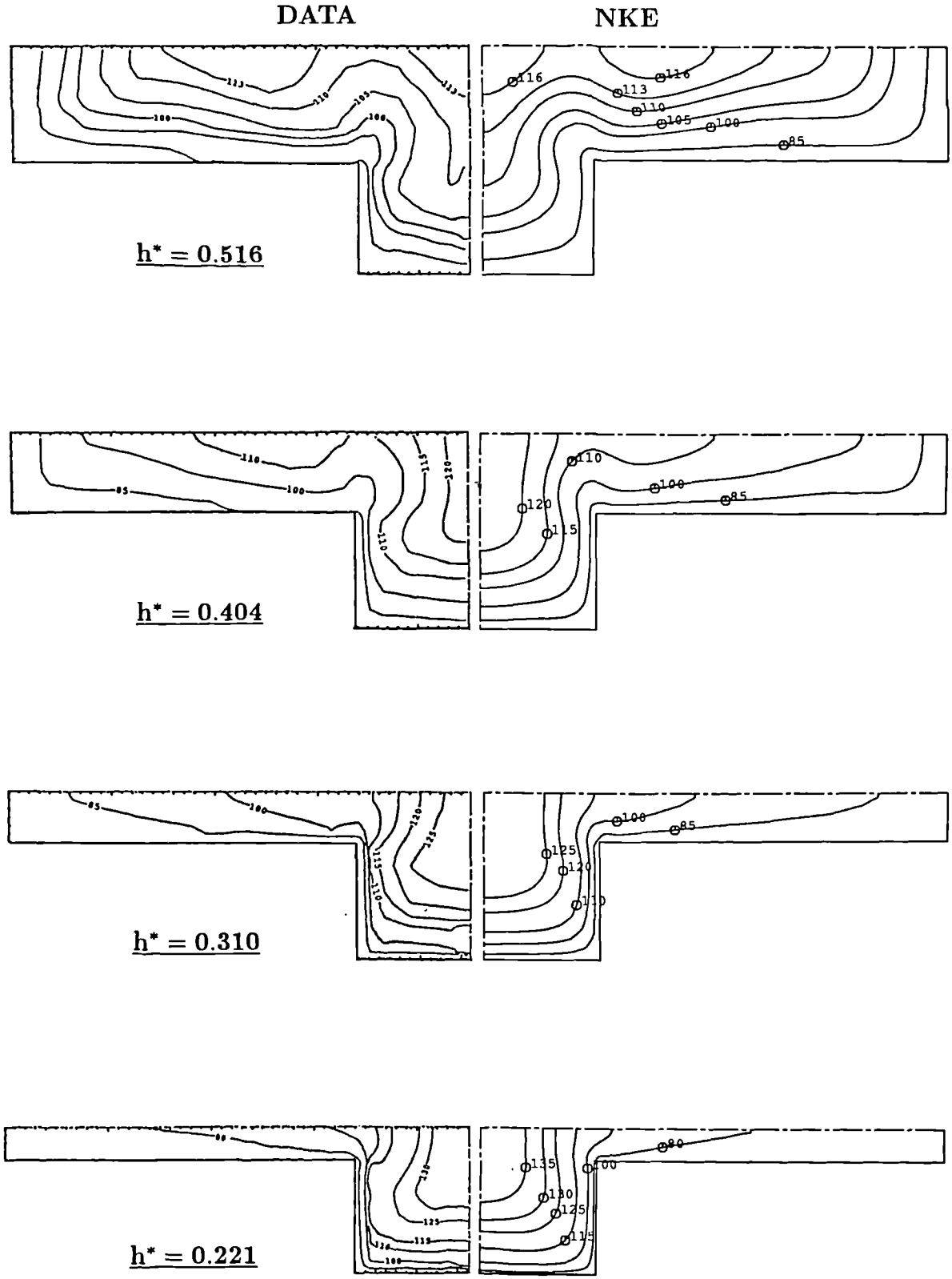

Fig. 4.29 Mean – velocity contours $W/W_b \times 10^2$.
Data of Knight and Lai (1985, a) and (1985, b).

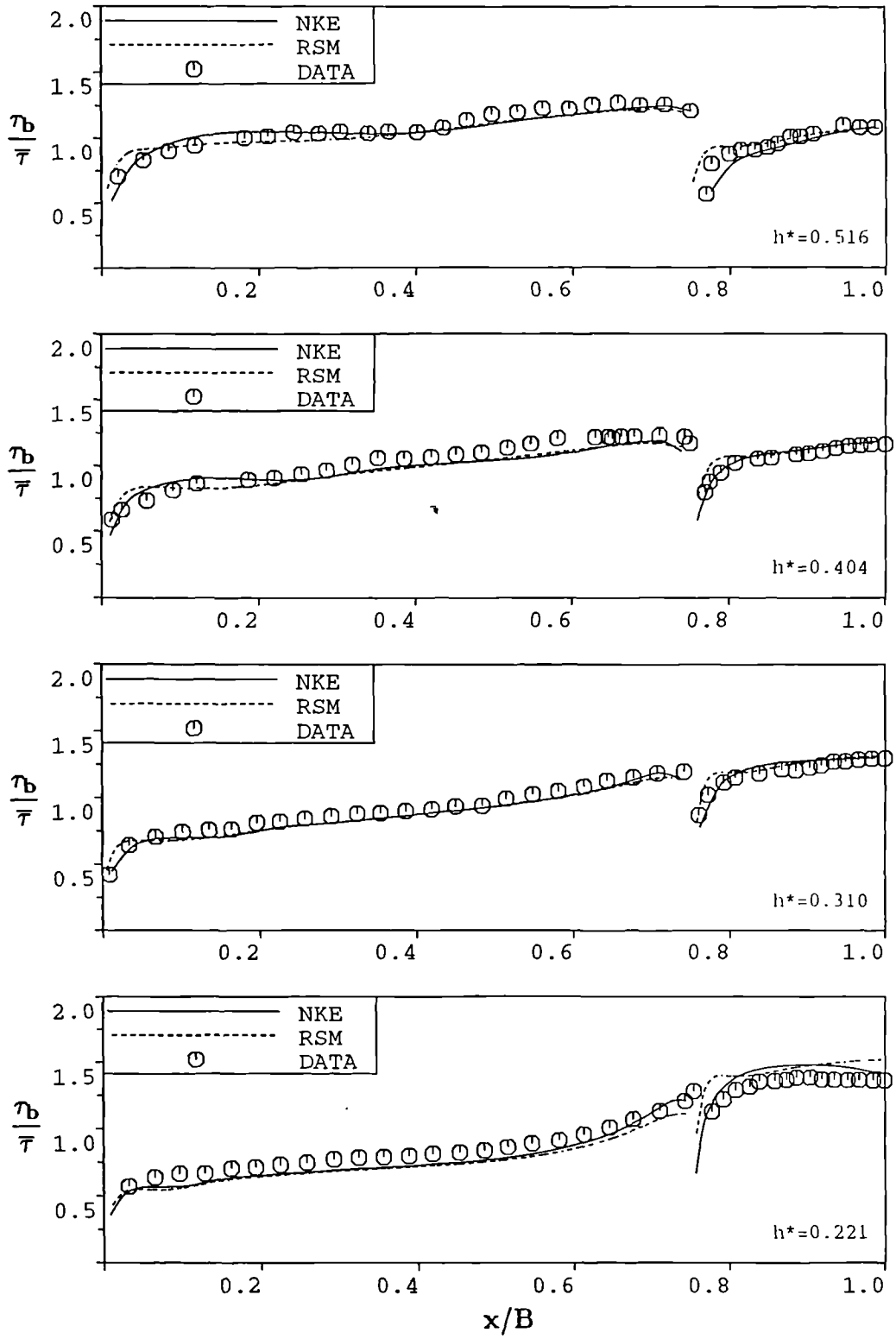

Fig. 4.30 Bed – shear – stress in compound ducts.
Data of Knight and Lai (1985, a) and (1985, b).

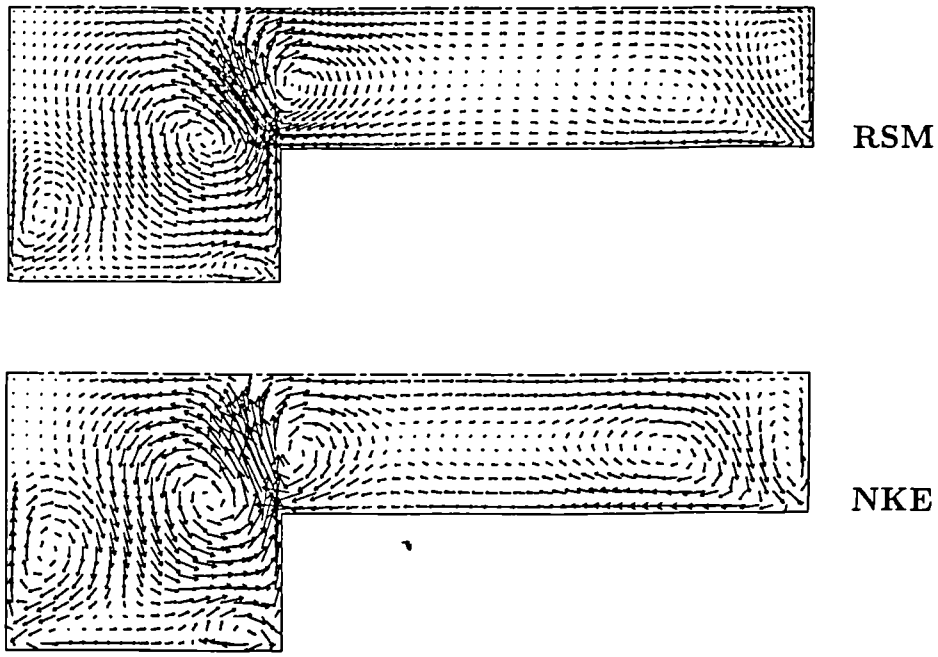

Fig. 4.31 Secondary-velocity vectors in asymmetric-compound duct.

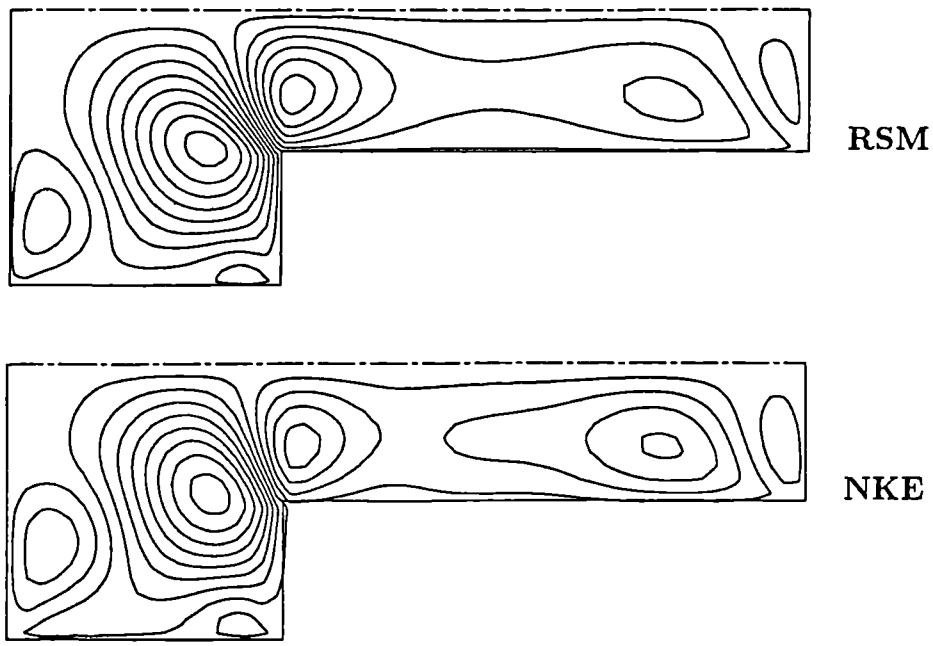

Fig. 4.32 Secondary-velocity streamlines in asymmetric-compound duct.

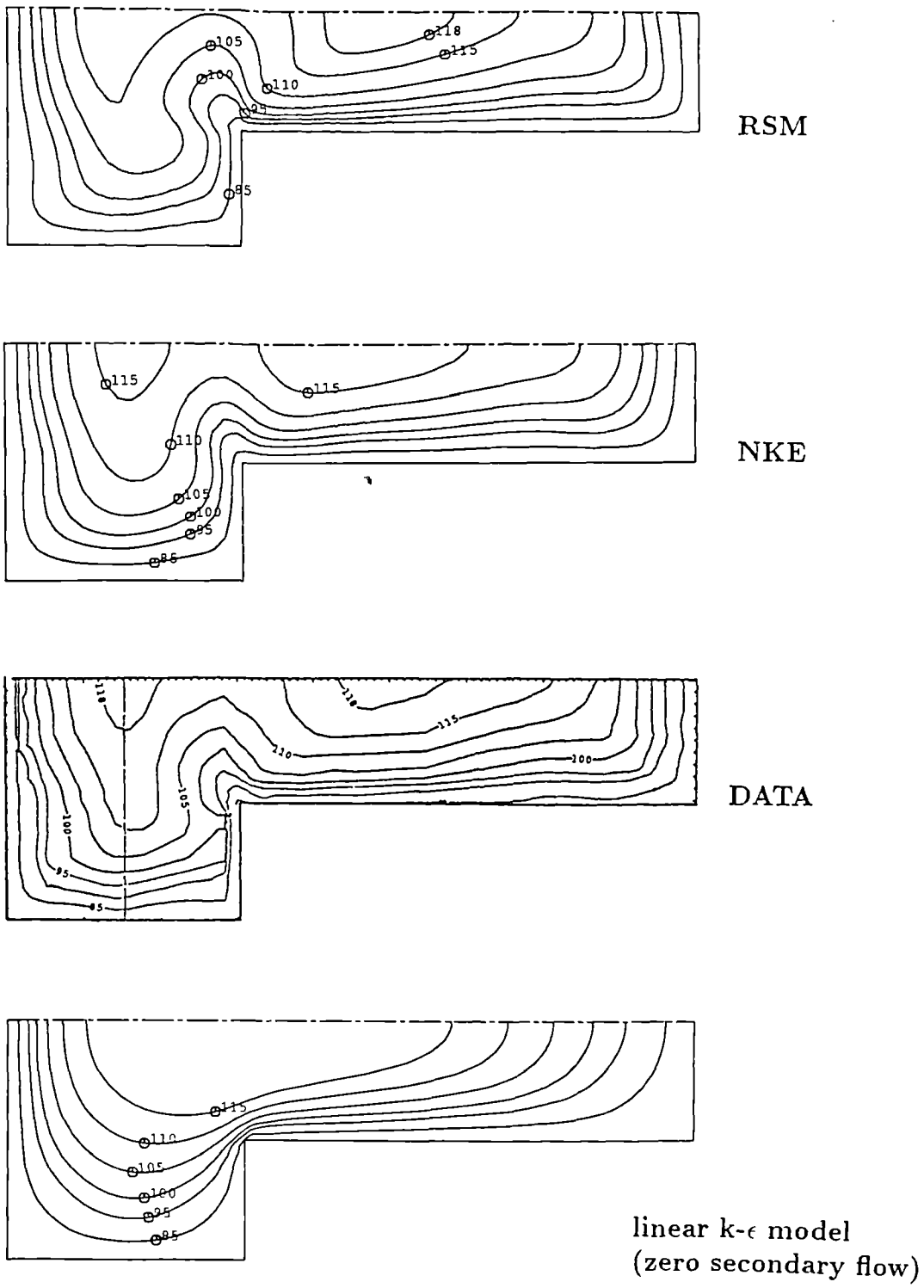

Fig. 4.33 Mean – velocity contours $W/W_b \times 10^2$.
Data of Knight and Lai (1985, a).

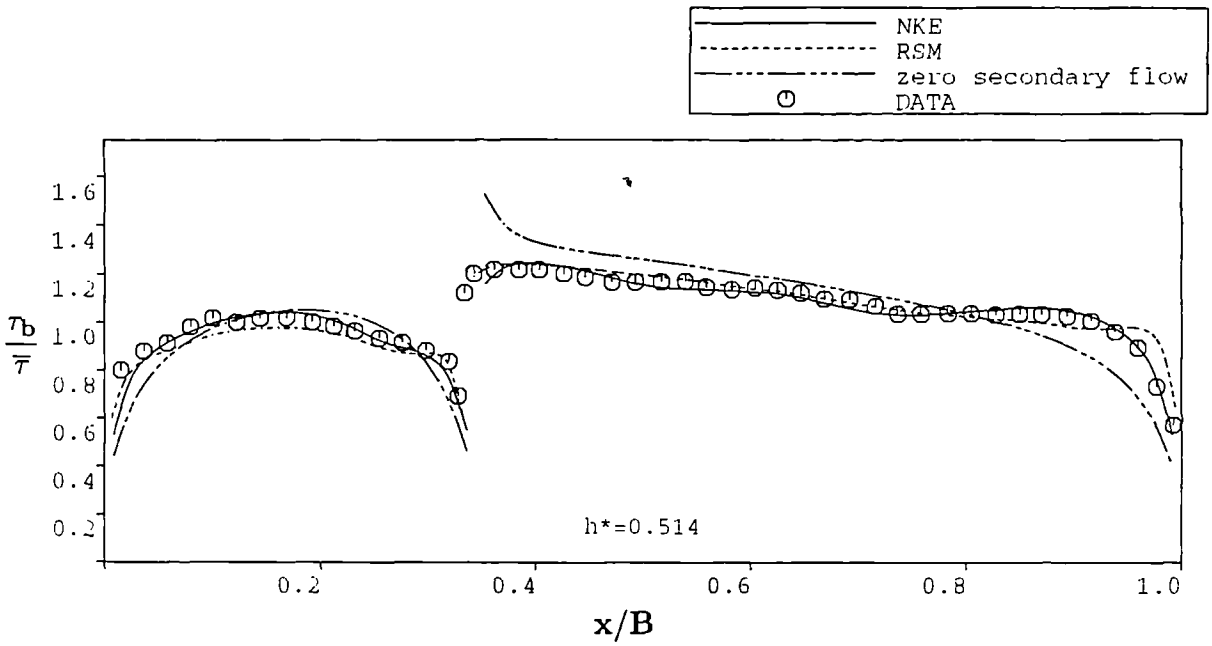

Fig. 4.34 Bed – shear – stress in compound – asymmetric duct. Data of Knight and Lai (1985, a).

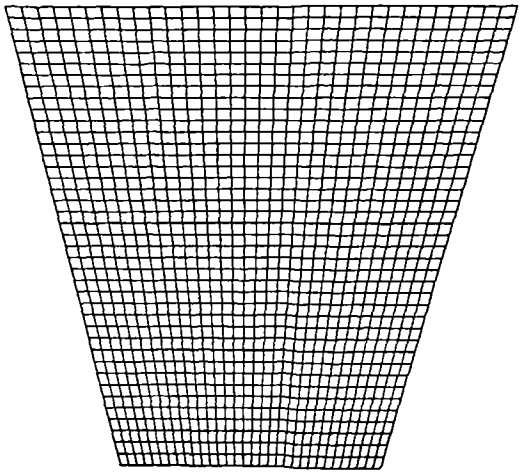

a) Computational grid 34×42

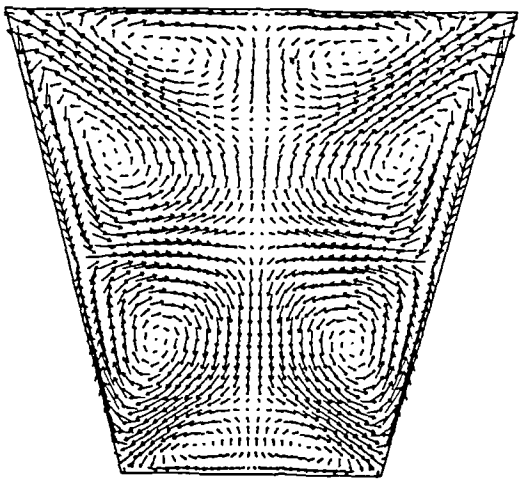

b) Secondary-velocity vectors

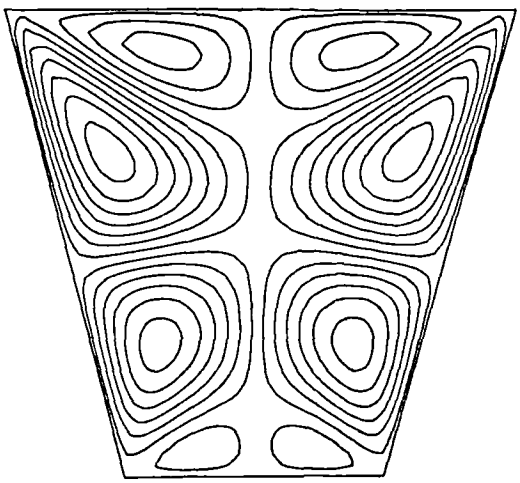

c) Secondary-velocity streamlines

Fig. 4.35 Secondary-motion results obtained by NKE model.

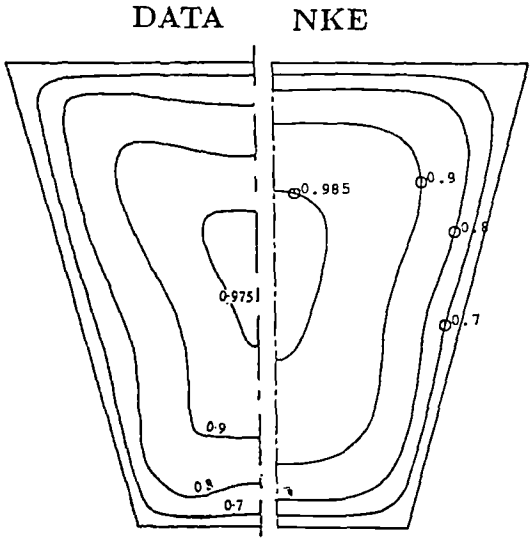

a) Mean-velocity contours W/W_{max}

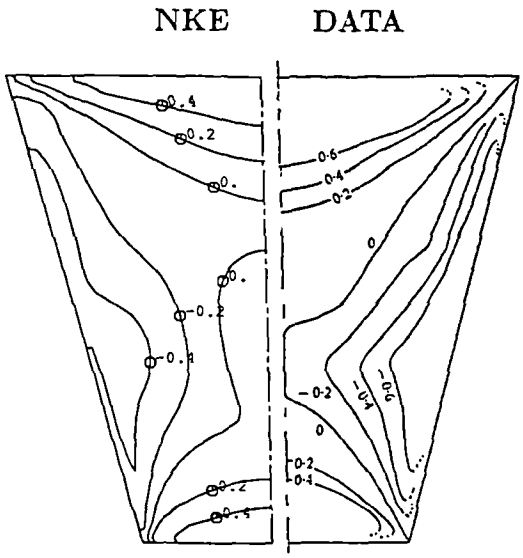

b) Normal-stress anisotropy $\frac{\overline{u^2}-\overline{v^2}}{\overline{W}^2}$

Fig. 4.36 Trapezoidal-duct results.
Data of Rodet (1960).

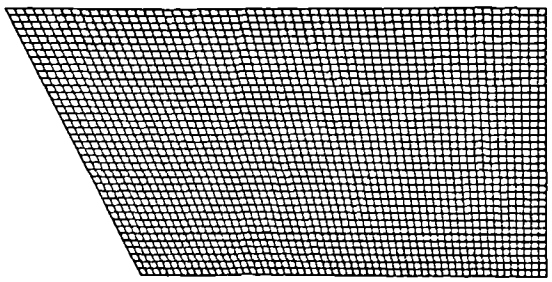

a) Computational grid 61×40

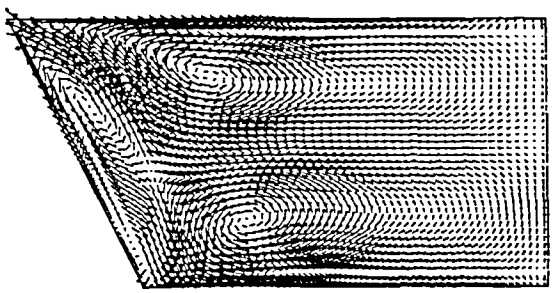

b) Secondary-velocity vectors

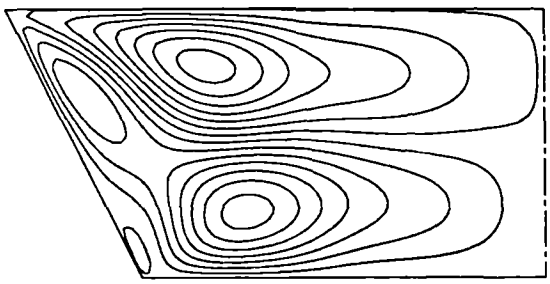

c) Secondary-velocity streamlines

Fig. 4.37 Secondary-motion results obtained by NKE model.

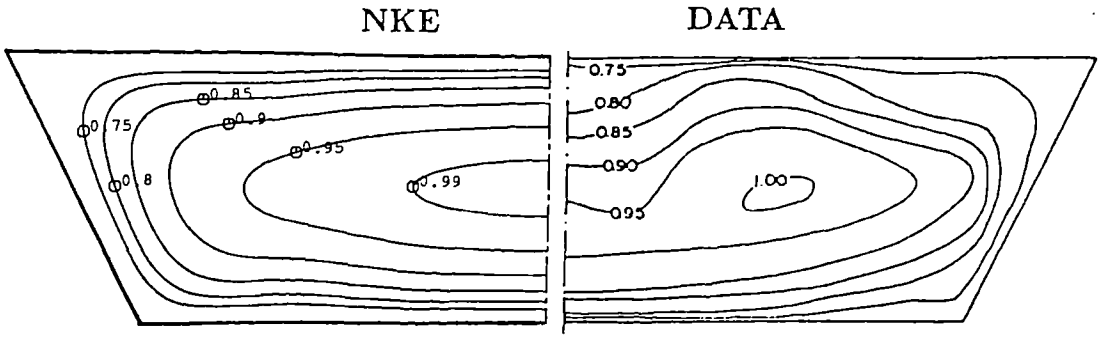

a) Mean-velocity contours W/W_{max}

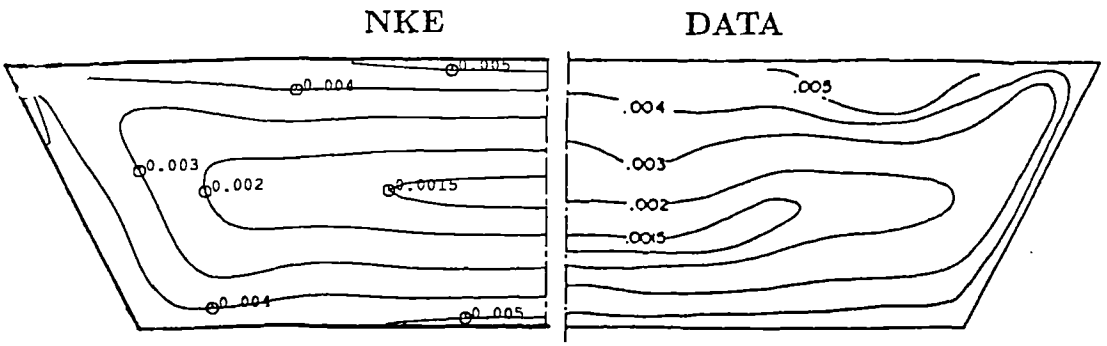

b) Turbulent-kinetic-energy contours k/W^2_{max}

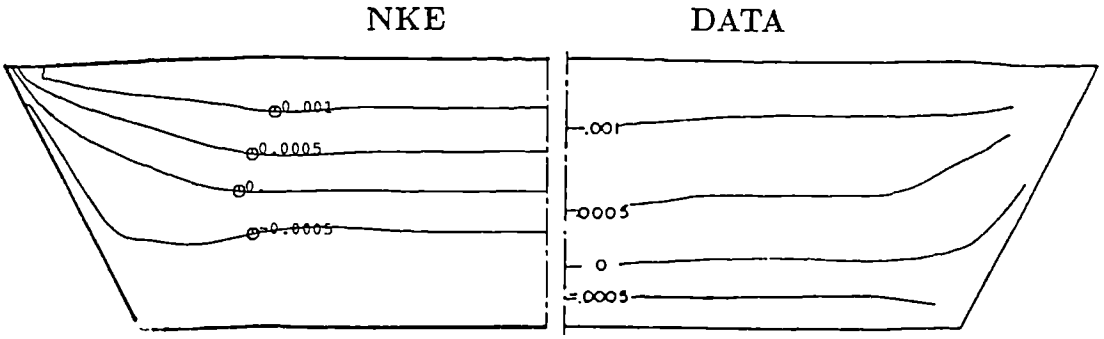

c) Main-shear-stress contours $\overline{vw}/W^2_{max}$

Fig. 4.38 Comparison between prediction and experiment for trapezoidal duct with increased aspect ratio. Data of Prinos et al. (1988)

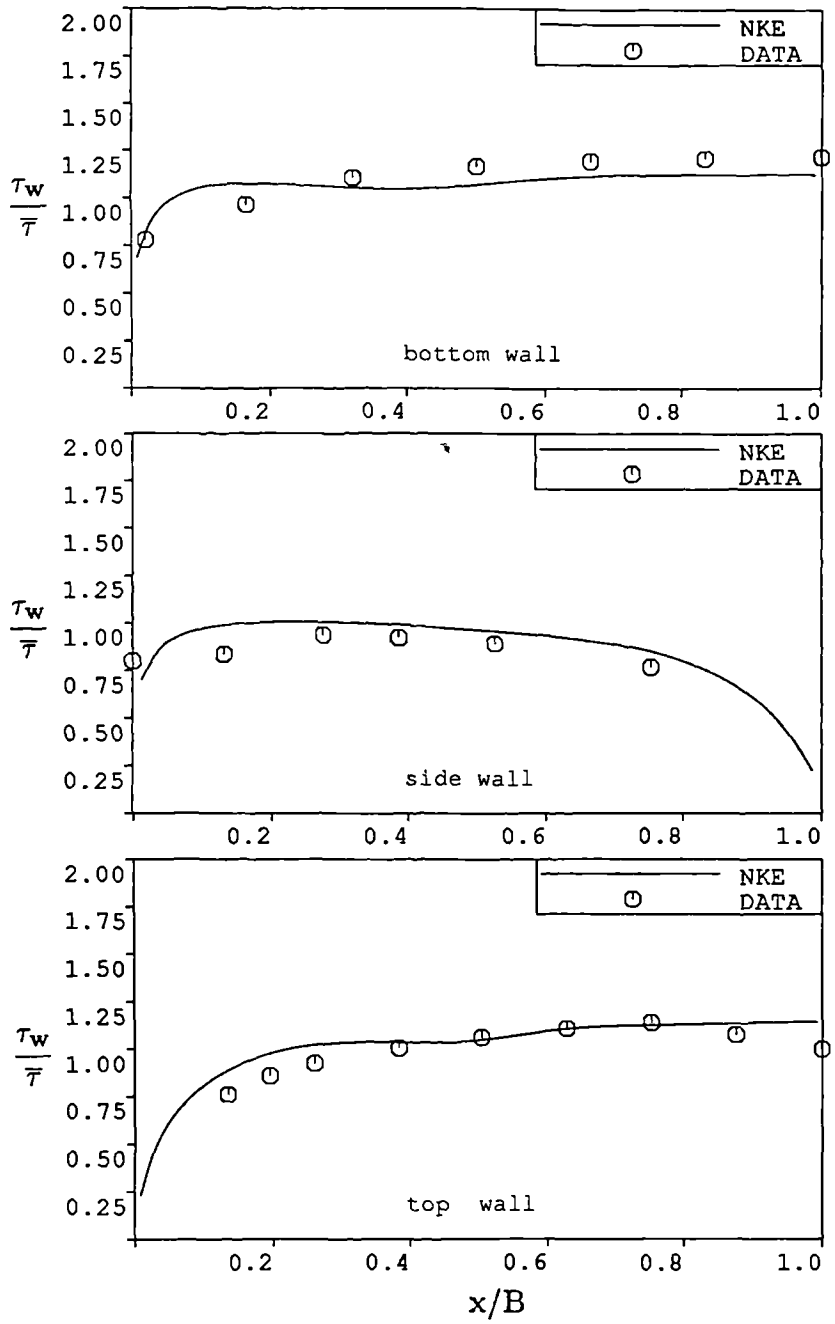

Fig. 4.39 Wall – shear – stress in trapezoidal duct. Data of Prinos et al. (1988).

Chapter 5

PREDICTION OF FLOWS IN OPEN CHANNELS

5.1 Introduction

The focus of this chapter is on turbulent flows in open channels of various cross-sections. The effects of a free surface on the structure of the turbulence in its vicinity have been studied experimentally by many researchers. Briefly, Ueda et al. (1977) and Komori et al. (1982) found that the turbulent fluctuations normal to the free surface are damped and, by virtue of continuity, those fluctuations parallel to it are enhanced. Celik and Rodi (1984) drew analogy between free-surface flows and those adjacent to a moving wall (i.e. where the wall-shear-stress is zero). There, the vertical fluctuations will also be damped and, furthermore, as suggested by the experiments of Thomas and Hancock (1977), the turbulence length scale decreases towards the moving wall. The conclusion drawn was that the dissipation of the turbulent kinetic energy increases next to the free surface and this in turn leads to a reduction in eddy-viscosity there and hence the well-known parabolic eddy-viscosity distribution in fully-developed open-channel flows (see Fig. 5.2).

The need for a predictive procedure for turbulent flows in open channels of non-circular cross-section arises from the frequent occurrence of such flows in hydraulic engineering practice. Examples include open channels, river flood relief schemes, sewers and estuarine flows. In all these flows, the mean-flow structure is significantly affected by the turbulence-driven secondary motion and this in turn alters the overall conveyance of the river system and results in changed wall-shear-stress distribution with implications to the processes of side-bank erosion and bedload sediment transport.

Prediction of open-channel flows are obtained here using the same turbulence models as for flows in closed ducts. The free-surface effects are simulated through specifying the boundary condition for ϵ and, in the case of RSM, by modifying the pressure-strain correlation model through an additional free-surface-damping function (Section 5.2). The ability of the models to predict the secondary-motion effects in open channels is assessed through detailed comparisons with the best available experimental data. Both simple and compound channels are considered (see Fig. 5.1). Flows in rectangular channels have been calculated using both models and the results are presented in Sections 5.3.1 and 5.3.2. Side-wall inclination further modifies the flow structure, the degree of modification being a strong function of the wall inclination angle (θ_c) : the present results for those trapezoidal channels are presented in Section 5.3.3. A compound cross-section, consisting of a deep main channel and shallow flood plains, is an important feature of many rivers and the present results, for both symmetric and asymmetric geometries, may be found in Sections 5.4.1 and 5.4.2. Finally, flows in real compound channels are often affected by inclination of the side walls or by roughness of the flood plains due to vegetation and the influences of those on the total flow structure are presented in Sections 5.4.3 and 5.4.4.

5.2 Free-Surface Modelling

5.2.1 The Nonlinear k-ϵ Model

The main task here is to ensure a damping of the vertical fluctuations near to the free surface. This is expected to lead to enhanced turbulence anisotropy there resulting in a such secondary motion which can create an appearance of mean-velocity maximum to below the free surface. Turbulent stresses in this model are proportional to the eddy-viscosity and thus, if a parabolic distribution of the eddy-viscosity is achieved the damping of vertical fluctuations would be a natural consequence. A parabolic eddy-viscosity distribution can be attained by way of prescribing the ϵ-value at the free surface using either of two proposed models (equations 3.42 and 3.43). The eddy-viscosity distributions for open channel with AR=2.01 and Re = 7.31×10^4 are presented in Fig. 5.3 a) (eddy-viscosity is defined using equation 2.8). The eddy-viscosity profiles show a decay as they approach the free surface. This behaviour is completely different from that of the case without prescribing a value of ϵ at the free surface (symmetry plane). The mean-velocity contours are shown in Fig. 5.3 b). Both proposals show a velocity maximum at the top of flow domain. An explanation for such behaviour will be presented in Section 5.3.1. At this stage it can be concluded that although there is no strong reason to prefer one ϵ-boundary condition against the other, the equation (3.43) ensures a slightly stronger contour-distortions adjacent to the free surface (see level 0.95) and therefore is recommended to be further tested in conjunction with the nonlinear k-ϵ model.

5.2.2 The Reynolds-Stress Model

Here, the damping of the vertical fluctuations near to the free surface

can be achieved by way of supplementing the model with the additional damping function (equation 2.47) to the redistributive term. Unfortunately, this approach by itself leads to unexpectedly increased level of eddy-viscosity adjacent to the free surface, as can be seen in Fig. 5.4 a) (this is the same test case as in previous section). This defect can be resolved by applying one of two proposed ϵ-boundary conditions. Both proposals when applied in conjunction with the free-surface-damping function ensure a steady decay of the eddy-viscosity near to the free surface (eddy-viscosity is again defined using equation 2.8; the k needed in that expression was calculated as half of the summation of the normal stresses). The mean-velocity contours obtained with the Reynolds-stress model are presented in Fig. 5.4 b). The approach which excludes ϵ-boundary condition at the free surface, not only to result in unrealistic eddy-viscosity than, also leads to a contour discontinuities there. When the ϵ-boundary condition (equation 3.43) is added to the free-surface modelling it leads to appearance of two velocity maximums: one below and one at the free surface. The local maximum at the top disappears when the equation (3.42) is used instead of equation (3.43). An explanation for mentioned behaviours can be found in the profiles of the free-surface-damping function, shown in Fig. 5.4 c). It is clear that when equation (3.43) is used the damping function is completely suppressed adjacent to the free surface which results in an unrealistic local-maximum there. Above mentioned discussion can be summarized as follows: In order to ensure expected behaviour of the eddy-viscosity as it approaches the free surface it is necessary to accompany the free-surface-damping function (2.47) with adequate ϵ-boundary condition. The ϵ-boundary condition (equation 3.43) leads to an unrealistic velocity maximum at the free surface and it is therefore necessary to replace it with equation (3.42).

5.3 Simple Channels

5.3.1 Rectangular Channels

The behaviour of flows in rectangular-open channels was investigated by Tominaga et al. (1989) using hot-wire anemometry. Detailed measurements of many important quantities were obtained including the secondary velocities, the mean-velocity field, the turbulence anisotropy and wall-shear-stress distribution. Their data are used here for model validation.

To understand the influence of the free surface it is worth comparing the secondary-flow structure in closed ducts and open channels. Note that if the top symmetry plane for the bottom-left quarter of the square duct (AR=1) is replaced by a free surface, the result would be a channel flow with AR=2. Consider first the channel flow conditions of Tominaga et al. (1989): AR=2.01, Re = 7.31×10^4 (slope not given). The calculated and measured secondary-velocity vectors and streamlines are compared in Fig. 5.5. It is immediately clear that the secondary flow is now completely altered under the influence of the free surface relative to that observed in square duct (Figs. 4.10 and 4.11). The secondary velocity along the corner bisector is significantly reduced and is now confined to a narrow region close to the internal corner. Also, the secondary motion along bed does not reach the middle of the channel while the flow along the side walls reaches the top of the domain. The strongest motion now occurs parallel to the free surface and next to it. This is obtained by both the experiments and the present predictions. The effect of such strong secondary flow is to transport slow-moving fluid from the wall region into the central portion of the channel. The secondary-velocity field is clearly seen from the plot of the flow streamlines presented in the same figure. Two vortices are present, as in the duct flow, but those are no longer symmetric about the corner bisector. The predicted streamlines show one dominant vortex below the free surface and a second, significantly

smaller one, adjacent to the bed in near-corner region. The experiments also show this although there the free-surface vortex is not the dominant one.

The consequence on mean-velocity field can be seen from the mean-velocity contours(W/W_{max}), presented in Fig. 5.6. The slow momentum fluid, brought by the secondary motion from the wall region, significantly distorts the mean-velocity field adjacent to the free surface leading to a shift in the position of maximum velocity to below the free surface. This phenomenon is also apparent from the RSM predictions and the experiments although the precise details are somewhat different. The NKE agrees with the measurements for contours up to 0.95 but the maximum mean velocity remains at the free surface which is in sharp contrast with the RSM predictions which correctly show the displaced maximum. It is worth noting here that the two models agree fairly closely in the details of the contours near the bottom corner.

Since the depression of the mean-velocity maximum below the free surface arises from the turbulence anisotropy, it is interesting to examine the models results for this parameter. The predicted and measured anisotropy field, averaged by W^2_{max}, are compared in Fig. 5.7. Apart from slight overestimation of the anisotropy contours near the free surface, the RSM results agree fairly well with measurements particularly for the position of the 'isotropic-turbulence' contour. The NKE produces less anisotropy adjacent to the free surface especially near the centre line where extensive regions of isotropic turbulence are being predicted.

To gain better understanding of this behaviour, the normal-stress profiles along the channel centre line are plotted in Fig. 5.8 a). So far, we have already emphasized that the free surface is expected to damp only vertical fluctuations. This requirement seems to be achieved by both models, as can be seen from $\overline{v^2}$ profiles shown in Fig. 5.8 a). In the same time, the horizontal fluctuations, as normal stress $\overline{u^2}$, should not be damped by the free surface. This requirement is qualitatively differently described by two adopted models. From the $y/H \leq 0.7$ both models

follow the same trend but beyond that point the discrepancies start to emerge. The NKE profile is again damped while the $\overline{u^2}$ profile obtained by RSM is even slightly enhanced in the free-surface region.

The malprediction of $\overline{u^2}$ by the NKE is due to eddy-viscosity stress-strain relationship (equation 2.11) which connects the stresses and the strains via eddy-viscosity. The eddy-viscosity profiles for this flow are shown in Fig. 5.9. Both models have reproduced well-known parabolic distribution. The eddy-viscosity tends to become zero at the free surface and therefore all quantities proportional to it will assume zero or near-zero value there. In such manner, the proportionality of the Reynolds stresses to the eddy-viscosity (which multiplies the linear part of equation (2.11) directly and nonlinear part through L_1) will result in negligible contribution of non-isotropic part in equation (2.11) in the free-surface region. Thus, not only vertical but also horizontal fluctuations are damped there. Contrary to that, the turbulent stresses in the case of the RSM are obtained by solving their own transport equations and hence they are not directly correlated to the eddy-viscosity. In such manner they can assume the desired level of turbulence anisotropy near to the free surface.

Fig. 5.8 b) shows the vertical distribution of the main-shear stresses at x/B = 0.5 (this position was chosen because $\overline{uw}$ is zero at the centre line). Again, both models produce very similar profiles of $\overline{vw}$ but the real differences appear in $\overline{uw}$ which is predicted by the RSM to be finite at the free surface but is obtained by the NKE as zero there.

5.3.2 Effects of Aspect Ratio

The next test case considered is for a larger aspect-ratio (AR=3.94) channel. The measurements are again Tominaga et al.'s (1989) and correspond to the $Re = 5.07 \times 10^4$ and channel slope (SL) of 0.138×10^{-3}. The calculated and measured secondary velocities are compared in Fig. 5.10. The

increased aspect ratio modifies the secondary-velocity field resulting in the appearance of a third vortex near to the centre line. The secondary flow, predicted by the RSM, is very weak in the central portion of the channel and therefore the third vortex does not appear there. From the other side, the centre line vortex can be clearly seen from the results obtained by NKE and its acting is so strong that unable secondary motion coming along the free surface to reach the central portion of the channel. The bottom corner vortex, predicted by both models, remains essentially unchanged from before.

Fig. 5.11 shows the calculated and measured mean-velocity contours, normalized by W_{max}. The main differences between the RSM and NKE results occur in the central portion of the channel, which is where the greatest differences in secondary velocities were observed. For RSM, the severest distortion to the contours occur near to the free surface but this is insufficient to displace the position of velocity maximum. For the NKE, the velocity maximum is shifted to either side of the centre plane, to a position which coincides with the point where two the vortices meet at the free surface. Furthermore, the strong secondary velocities along the centre line distort the main-flow contours there. Contrary to the predictions, where both models obtain the velocity maximum to occur at the top of domain, the data show that the velocity maximum lies below free surface which suggests that the secondary flow is even stronger than produced with either model.

The largest aspect-ratio channel of Tominaga et al. is considered next. AR is 8.0 and the following flow conditions apply: $Re = 6.37 \times 10^4$ and $SL = 0.937 \times 10^{-3}$. The predicted and measured secondary-velocity vectors and streamlines are presented in Fig. 5.12. The predictions show significantly weaker velocity vectors in the middle of the channel compared to the side walls and the corners. Here, both the predictions and measurements indicate that the strong secondary motion from the side walls along the free surface does not reach the middle of the channel due, in part, to the weak reverse flow from the centre line.

The mean-velocity contours presented in Fig. 5.13 indicate a very similar mean-velocity field produced by two models. In general, agreement between predictions and measurements seems to worsen with increasing aspect ratio and the advantages of the RSM over the NKE, obvious for narrow channels, disappears with higher aspect ratios.

The predicted and measured distribution of bed-shear-stress for rectangular channels are compared in Fig. 5.14 for various aspect ratios. For the smallest aspect ratio, a local minimum is observed at $x/B \approx 0.5$. A region of 'stress deficit' is thus created, analogues to that found in duct flows, and this moves steadily towards the corner with increasing aspect ratio. For the channel with AR=3.94, the local minimum occurs at $x/B \approx 0.3$, while for AR=8.0 the depression is very weak and occurs around $x/B = 0.15$. The NKE also produces two narrow regions of bed-shear-stress deficit for the aspect ratios of 3.94 and 8. Those are attributed to the vortex near the centre line, (predicted by this model for AR=3.94 ; Fig. 5.10), which distorts the mean velocity there (Fig. 5.11) and this in turn leads to the drop in bed-shear-stress. Similarly, for the highest aspect ratio, the NKE produces a strong vortex at $x/B \approx 0.5$ which modifies the bed-shear-stress at that position. Apart from those two narrow regions, the NKE predictions are in better overall agreement with the data. It is also worth noting that, although the NKE and the RSM produced significantly different mean-velocity profiles for AR=2.01, the bed-shear-stress was closely predicted by both models which suggests that the departure of the NKE at the centre line near to the free surface is rather localized without serious consequences for the rest of flow domain.

The side-wall shear stresses for the same flows are presented in Fig. 5.15. Measurements were only available for AR=3.94. The agreement between the data and present predictions is quite satisfactory and it is interesting to note that the wall-shear-stress is largely independent of the aspect ratio resulting in almost identical profiles for all three test cases.

Knight et al. (1984,a) reported on the bulk quantities in open-rectangular channels and those are used next to determine the influence of aspect

ratio on the flow structure in open channels. The bed slope was kept constant at $SL = 9.66 \times 10^{-4}$ which allows for a convenient way to present the changes in mean-bulk parameters (channel discharge, bed and wall average-shear-stress etc.) with increasing aspect ratio. The data and the present predictions for the bulk quantities are presented in Fig. 5.16. The NKE and RSM predictions for discharge are, when plotted, too close to be distinguishable. The agreement with experiment is better for smaller aspect ratios. For $AR > 3$ the predictions slightly overestimate the measured values which is in accordance with the observed deterioration of agreement between measured and predicted mean-velocity contours for high aspect ratios. The predicted average wall-shear-stresses, on the other hand, agree well with the measured values. The same is true for the average bed-shear-stress except for $AR = 6$ where predictions overestimate the measured value.

In conclusion, the inability of the NKE to produce depression of mean velocity maximum to below the free surface in narrow channels does not seem to have a serious impact on the prediction of other important parameters. Both models have produced similar shear-stress distributions along the wetted perimeter and very close values for the bulk quantities. Moreover, for higher aspect ratios, both models have produced a very similar mean-velocity fields. It follows that the influence of side-wall inclination on the flow in open channels can be calculated using the NKE model in conjunction with body-fitted coordinates, as will be shown next.

5.3.3 Effects of Side-Wall Inclination

The flows in open-trapezoidal channels were experimentally investigated by Tominaga et al. (1989). The experiments were conducted for side-wall inclinations (θ_c) of 60°, 44° and 32°.

The predicted and measured secondary-velocity vectors and streamlines,

for all three side-wall inclinations, are plotted in Fig. 5.17. For the case of $\theta_c = 60°$, the flow conditions were: AR = 2.9, Re = 6.48×10^4 and SL = 0.389×10^{-3}. Both experiment and predictions show three dominant vortices though with different centres. The predictions show strong secondary motion along the corner bisector which is only vaguely apparent in the experiments. Note that here the secondary velocities at the centre line are directed towards the free surface, a behaviour apparent in both predictions and measurements.

For the two test cases with 44° and 32°, the aspect ratios were 3.25 and 3.86 and the Reynolds numbers were Re = 8.76×10^4 and Re = 5.34×10^4, respectively. The bed slope was 0.594×10^{-3}. With decrease of wall inclination (θ_c), the middle vortex decays and disappears for $\theta_c = 32°$ while the bottom vortex becomes increasingly dominant. The corner vortex is unaffected by the side-wall inclination. The flow in the middle of the channel is influenced by secondary flow from the bed rather than from the side walls, as was the case in simple channels.

The mean-velocity contours are presented in Fig. 5.18. The shift in the position of velocity maximum is consequence of the strong secondary motion adjacent to the centre line already discussed. The secondary velocities distort the mean-velocity contours all along the centre line and finally result in the displaced velocity maximum. The predicted and measured positions of velocity maximum are quite close except for the channel with $\theta_c = 60°$. The bulging towards the bottom corner evident from the measurements is also captured in the predictions. The mild bulging adjacent to the side wall is a consequence of the secondary flow from the side wall. With decreasing wall inclination (θ_c), the extent of bulging is reduced and finally disappears for $\theta_c = 32°$. This is not easy to see from the measured contours since those show some scatter next to the side wall.

Distributions of side-wall shear stress for the trapezoidal channels are shown in Fig. 5.19 a) as a function of wall inclination. As before, the wall-shear-stress shows a local minimum or depression at a location corre-

sponding with that of maximum mean-velocity distortion (see Fig. 5.18). This deficit is most pronounced for $\theta_c = 60°$, and virtually non-existent for $\theta_c = 32°$. The shear-stress drop near to the free surface is apparent for all three cases. The agreement between the NKE predictions and the data is generally quite satisfactory.

The predicted and measured shear stresses on the channel bed are shown in Fig. 5.19 b). The experiments show a steady drop near the channel's centre line and this becomes more severe with decreasing θ_c. The predictions underestimate the measurements near the centre line for $\theta_c = 60°$ and near the bed-wall junction for $\theta_c = 32°$ but apart from that the agreement is quite reasonable.

5.4 Compound Channels

5.4.1 Symmetric Channels

Tominaga et al. (1988,a) and (1988,b) reported detailed measurements of flows in symmetric-compound channels including secondary-velocity vectors, mean-velocity contours and boundary shear stress. They also measured some turbulence quantities such as the main-shear stresses $\overline{uw}$ and $\overline{vw}$. Two of their data sets were selected for model validation; those are summarized in Table 5.1.

symmetric channel	h*	B/b	AR	Re
experiment 1	0.5	2.07	3.89	5.44×10^4
experiment 2	0.243	2.07	5.9	3.43×10^4

Table 5.1 Flow conditions for symmetric-compound channels

Further details are given in Tominaga et al. (1988,a) though, unfortunately, not the bed slope.

The predicted and measured secondary-velocity vectors for $h^* = 0.5$ are compared in Fig. 5.20. As was the case for compound ducts (Fig. 4.26), the strongest secondary flow occurs near the external corners but here the presence of the free surface further complicates the flow. Thus, the secondary flow generated by the external corner is enhanced near the free surface such that its influence now extends to the centre line of the channel. The flow in the flood plain is also quite different from the flow in closed compound ducts. Here, the flow from the main channel-flood plain junction forms a vortex adjacent to the corner in addition to the two found in the far corners. For the shallow flood plain ($h^* = 0.243$), the secondary flow (Fig. 5.21) is especially strong around the external corner and adjacent to the free surface as can be seen from both data and predictions. Compared to the previous case, the secondary flow in the main channel is now less affected by the flow from the external corner. Fig. 5.22 compares the patterns of secondary-flow streamlines obtained with the NKE and the RSM for the two values of h^*. Some differences are apparent mainly in the size of the vortex on the main-channel bed where the vortex predicted by the RSM is smaller. Contrary to the uniform flow observed in ducts, the split in the flood-plain secondary flow can be seen from the formation of two separate large vortices in that region ($h^* = 0.5$). In contrast, the vortices for $h^* = 0.243$ are very similar to those observed in closed ducts (Fig. 4.27 ; $h^* = 0.221$).

Fig. 5.23 compares the measured mean-velocity contours with the RSM predictions. The external corner and the free surface play an important role in the distortion of the mean-velocity field. The bulging of mean-velocity contours near the external corner is due to the strong secondary motion in that region: it is a strong function of the depth ratio as it disappears for $h^* = 0.243$. The secondary motion also causes a shift in the location of velocity maximum to below the free surface in exactly the same way as already seen in simple channels. In very shallow flood plains, (e.g. for $h^* = 0.243$), the contours of main velocity are uneventful near the external corner. The details of the distorted contours, and the position of velocity maximum, are very well predicted by RSM.

The mean-velocity contours obtained by NKE for the same test cases are presented in Fig. 5.24. The results for $h^* = 0.5$ agree quite well with the data although the positions of some contours are slightly displaced. For the lower h^* value, the agreement is generally satisfactory, particularly away from the free surface. Also, the velocity maximum is predicted to occur at the free surface.

The turbulence field in compound channels was documented by Tominaga et al. (1988,a) by way of contours of main-turbulence shear stresses. The contours of Reynolds stress $-\overline{uw}$ normalized by $\overline{W_\tau}^2$ are presented in Fig. 5.25. The data show the largest value of $-\overline{uw}$ to occur adjacent to the external corner within the main channel and this is reproduced by both models. A zone of negative shear stress divides two regions of positive shear stress within the main channel and flood plain and the size and position of this region are well predicted by both models. It is interesting to note that this negative stress region does not appear for $h^* = 0.243$ as can be seen from Fig. 5.26.

The predicted and measured contours of $-\overline{vw}$ are shown in Fig. 5.27. The region of negative shear stress is again attached to the external corner extending into the main flow. The measurements show that the region of negative shear stress is localized by the corner while the RSM shows it to be much more extensive even reaching the free surface. For the NKE, this region appears to be split into two: a small one very close to the corner and a second one attached to the free surface. Both models and the data also suggest the existence of a second region of negative stress in the left top corner of the flow domain. The shear stress ($-\overline{vw}$) contours for the smaller h^* can be seen in Fig. 5.28. Again, the RSM predictions for the negative shear-stress region agree very closely with the data and the same is true, to a lesser extent, for the NKE.

The predicted and measured shear stress around wetted perimeter are presented in Fig. 5.29 for $h^* = 0.5$. The shear stresses on the flood-plain wall are very well predicted. The shear-stress distribution on the flood-plain bed is characterized by a mild depression around $x/B_1 \approx 0.25$

which is captured by both models. The shear stress on the main-channel bed is similar to that observed in simple-rectangular channels (Fig. 5.14 ; B/H = 2.01) while the profile on the main-channel wall seems to be quite unaffected by the secondary motion. The reduction in h^* leads to quite different wall-shear-stress distribution, as can be seen from Fig. 5.30. The differences are apparent from the wall-shear-stress partition between the flood plains and main channel and from the profile shapes. The difference in magnitude of wall-shear-stress in flood plain and main channel can be seen from Fig. 5.30 for $h^* = 0.243$. In the channel with $h^* = 0.5$, the stress levels on all four sides which comprise the compound section were nearly equal. Here, the lower shear-stress profiles on the flood plains, for $h^* = 0.243$, indicates the presence of the low-momentum fluid in that region.

The data of Knight and Demetriou (1983) are used next to assess the performance of the present models for the flow's bulk quantities. Measurements of channel discharge and of boundary shear-force distribution were presented for various h^*s and B/bs. The slope was 9.66×10^{-4} and the height of the flood plain was fixed as 76 mm in order to give b/h=1 for all tests. The predicted and measured discharge and its partition between main channel and flood plain are shown in Fig. 5.31 for various h^*s and B/bs. Both models accurately predict the total discharge as well as the partitioning between main channel and flood plains. The percentage of total shear force in each section of compound channels with B/b = 2 and 3 are presented in Figs. 5.32 and 5.33, respectively. For B/b=2, a large part of the total shear force occurs in the main channel and agreement between predictions and data is quite reasonable. The predictions slightly underestimate the shear force on the flood plain bed for B/b = 3 and especially for the smallest value of h^*. The loss of shear force there is compensated for by overestimating the shear force on the main-channel bed and wall. Both models predict the shear-force distribution fairly well, with the RSM slightly better overall.

5.4.2 Asymmetric Channels

Data for the mean and turbulent parameters in asymmetric-compound channels have been reported by Tominaga and Nezu (1991). Two different geometries were adopted for models comparison: main-channel depth ($H \approx 80$mm) was kept constant while the rest of the flow conditions are given in Table 5.2.

asymmetric channel	h^*	$(B/b)_l$	$(B/b)_r$	AR	Re
experiment 1	0.5	1.0	3.0	5.0	5.45×10^4
experiment 2	0.25	1.0	3.0	5.0	4.56×10^4

Table 5.2 Flow conditions for asymmetric-compound channels

The channel slope was not quoted in the original study.

The predicted and measured secondary-velocity vectors for the asymmetric channel with $h^* = 0.5$ are presented in Fig. 5.34. The experiments show strong secondary motion adjacent to the external corner and near to the free surface. Positive and negative velocities at the free surface appear to meet at a point in the main channel which is away from its center-line and closer to the flood plain. The position of this point is predicted almost exactly by RSM while the NKE obtains this point closer to the channel's axis. For the shallow flood plain, shown in Fig. 5.35, the asymmetry is now significantly less than before. The measurements do not show any secondary velocities in the flood plain presumably due to limitations in the experimental method used.

Fig. 5.36 compares the calculated and measured mean-velocity contours for the asymmetric channel with $h^* = 0.5$. The asymmetry already noted in the secondary flow behaviour results in asymmetric distortion of mean-velocity contours within the main channel. This is closely reproduced by RSM and to a lesser extent by NKE. This flow geometry comprises all

secondary-flow effects discussed so far in this study. Briefly, a velocity bulging is observed towards the left and right bottom corners, velocity maximum below the free surface, flow asymmetry within the main channel, strong velocity bulging outwards from the external corner and finally the appearance of local velocity maximum within flood plains. All these effects are closely predicted by RSM as can be seen from Fig. 5.36. The NKE results show most of these effects (except velocity maximum below the free surface) but it is apparent that all contour distortions are now significantly weaker compared with the data and the RSM. The mean-velocity field in asymmetric-compound channel with $h^* = 0.25$ is presented in Fig. 5.37. The flow asymmetry within the main channel is very mildly indicated by data and RSM while in the case of the NKE it completely disappears.

Tominaga and Nezu (1991) also presented detailed turbulence measurements but only for $h^* = 0.5$. The predicted and measured turbulence anisotropy are displayed in Fig. 5.38. The greatest anisotropy in the main channel appears at the top and bottom with the lowest values occurring at the half-height location. Also, negative contours appear near the external corner. Apart from mild contour displacement, the RSM results agree fairly well with measurements. The greatest differences between the NKE results and the data appear in the region near the free surface where the experiments show an increase in anisotropy as the free surface is approached while the NKE results show almost complete isotropy.

Fig. 5.39 shows the main-shear stress ($-\overline{uw}$) contours averaged by $\overline{W_\tau}^2$. The two models yield essentially the same profiles throughout most of the flow domain except that the NKE seems to produce lower shear stress near the free surface. Apart from this, the agreement between predictions and experiment within the flow domain is quite reasonable. Since the damping of second main-shear stress by the free surface can be fairly well predicted by both models, the predictions of the ($-\overline{vw}$), shown in Fig. 5.40, are also fairly close.

An insight into the energy distribution in compound-channel flows can be gained from the turbulence-energy contours shown in Fig. 5.41. The experiments show bulging of the contours away from the external corner and, also, towards the internal corner. They also show the appearance of local energy maximum below the free surface. Apart from certain differences between predictions and data in the contour levels, the agreement for the near-corner regions is fairly good though neither model produces the energy depression below the free surface.

The bed-shear-stress distributions for the main channel and the flood plain, normalized by the average shear stress ($\overline{\tau}$), are plotted in Fig. 5.42. The asymmetry of the mean-velocity field within the main part of channel with $h^* = 0.5$ has a direct influence upon the bed-shear-stress distribution: the maximum wall-shear-stress within the main channel appears to be shifted from the centre line to the position of $x/(b_l + b_r) \approx 0.6$. This is obtained by both predictions and by experiment although the predictions overestimate the measurements along large part of channel bed especially for $h^* = 0.25$.

5.4.3 Effects of Roughness

Knight and Hamed (1984,b) investigated the effects of roughness in compound channels. The bed slope was constant at 9.66×10^{-4}. Also, $b = h = 76$mm. Roughness of the flood plains was characterized by the parameter (χ) appearing in equation (3.49). This parameter is a function of strip-roughness height (k_r) and longitudinal spacing between roughness elements (λ). Knight and Hamed presented the values of χ for various range of λ/k_r. The case with maximum flood-plain roughness was adopted for the present comparisons where $\lambda/k_r = 10$ and, according to Knight and Hamed (1984,b), χ is 3.4924.

The predicted and measured mean-velocity distributions in compound

channel with $h^* = 0.505$ and $B/b = 4.013$ are presented in Fig. 5.43. The experiments show the appearance of local velocity maximum below the free surface but this is not reproduced by present predictions. The mean-velocity bulging next to the external corner is towards the centre line of the channel as can be seen from both predictions and measurements. Both models also show local-velocity maximum in the lower part of the main channel. Unlike the results for smooth walls (Figs. 5.23 and 5.24), both models here show almost identical behaviour indicating the prevalence of the influences due to flood-plains roughness over those associated with the free surface. For this reason the performance of the NKE near the free surface has little impact on the velocity field elsewhere.

Since the mean-velocity contours in Fig. 5.43 are averaged with the bulk velocity (W_b), the contour $W/W_b = 1.0$ represents the line which divides the slow and fast moving flows within the compound channel. Clearly, the fast moving flow occurs within the main channel while the slow moving fluid is contained within the flood plains. This is also clear from Fig. 5.44 which shows the variation of depth-mean velocity ($\widetilde{W}$), normalized with mean-bulk velocity (W_b). Clearly, the flood plain roughness has a significant impact upon the discharge redistribution between main channel and flood plain and this is well predicted by both models as can be seen from Fig. 5.44. Attention is turned next to consideration of the total discharge where the present predictions are compared with the data of Knight and Hamed (1984,b) for the same geometry but with varying h^*. The results are displayed in Fig. 5.45 where it can be seen that both models accurately predict this quantity for a wide range of depth ratios.

5.4.4 Effects of Wall Inclination

It is often the case that the walls of open-compound channels are inclined and hence the need to assess the models performance for such cases. The RSM model is used here in conjunction with a stepwise approximation

of the inclined walls (see Fig. 5.46 a, for an example of such grid) while the nonlinear k-ϵ model is used in conjunction with body-fitted grids, as shown in Fig. 5.46 b).

The computational grids presented in Fig. 5.46 are for the geometries of Tominaga et al. (1988,b). Here again the slope is unknown and the experimental conditions, using notation of Fig. 5.1 d), can be summarized as follows: $h^* = 0.5$, AR = 4.0, B/b = 4.08, $\theta_c = 45°$ and $\theta_f = 90°$. The predicted and measured secondary velocity vectors are shown in Fig. 5.47 which shows that a strong up-flow from the external corner is a characteristic of most compound-channel flows. Unlike compound-rectangular channels, here a strong down-flow is observed along the inclined wall but this is missed by both models. The RSM produces a strong vortex within the flood plain, adjacent to the external corner, while the rest of the flow there is typical of rectangular channels. The NKE, in contrast, produces two vortices with no sign of recirculation near the bed corner.

Fig. 5.48 shows the mean-velocity contours averaged by W_{max} for the same flow. The contours adjacent to the external corner are similar to those observed for rectangular channels (see Fig. 5.23) though with less distortion. The measurements show some scatter (see contour 0.975) but it is clear that the RSM results are fairly close. In contrast, the NKE results show a weak corner bulging and no contours distortion adjacent to the free surface.

The flow structure inside compound channels, with both side-walls inclined, was experimentally investigated by Yuen (1989) and Yuen and Knight (1990) for various flow geometries and bed channel slopes. The main features of the tests were as follows: b = h = 0.075 m, B/b = 3.0, and $\theta_c = \theta_f = 45°$. Three geometries were chosen, with h^* values of 0.5, 0.45 and 0.35 and the bed slopes 2.295×10^{-3}, 2.36×10^{-3} and 2.45×10^{-3} respectively.

The predicted secondary velocities are presented in Fig. 5.49. For $h^* = 0.5$, the results of the two models are mostly similar but with some

differences within the flood plain. There, the RSM suggests that the flow is apparently divided between contra-rotating vortices while the NKE obtains one dominant vortex. Furthermore, the models react differently to changes in h^*: the RSM produces almost identical secondary flow regardless of h^* while the NKE obtains profiles that are quite sensitive to changes in h^*. The differences in the two models are quite apparent from contours of secondary-flow streamlines, presented in Fig. 5.50. The RSM results clearly indicate the existence of three vortices which do not change in the shape and position with decreasing h^*. The NKE responds to the decrease of h^* in quite a different manner which is related to the main-channel vortex attached to the inclined wall. For $h^* = 0.5$ this vortex clearly dominates the large part of main channel while the existence of the bed vortex near to the centre line can only be presumed. Only a small decrease in h^* leads to a reduction of the influence of the vortex near to the inclined main-channel wall while the second main-channel vortex clearly appears at the channel bed. Finally, for the $h^* = 0.35$ the main vortex, which dominates for two highest value of h^*, completely disappears.

The measured mean-velocity contours, together with the RSM predictions, are shown in Fig. 5.51. The predicted mean-velocity distortions are related to the secondary-velocity field, presented in Fig. 5.49. The contour distortions in the flood plain near to the free surface are caused by secondary motion which acts along the free surface. The main-channel vortex causes the bulging near the external corner and in the free-surface region. Although the positions of some isolines are displaced, the RSM shows the same behaviour as the experiments. The mean-velocity contours obtained by NKE are shown in Fig. 5.52. The bulging near the external corner is very mild and is absent for the channel with $h^* = 0.35$. The mean-velocity contours are almost unaffected in the vicinity of the free surface.

Table 5.3 gives the total discharge in trapezoidal-compound channels as obtained by the two models.

h*	SLOPE	Q [l/s]				
		DATA	NKE	Er. %	RSM	Er. %
0.5	0.002295	54.80	57.08	+4.16	53.65	−2.09
0.45	0.002360	44.60	47.15	+5.71	43.91	−1.54
0.35	0.002450	31.65	33.11	+4.61	31.26	−1.23

Table 5.3 Discharge in compound-trapezoidal channel. Data of Yuen (1989).

5.5 Closure to Chapter 5

The Reynolds-stress and the nonlinear k-ϵ models of turbulence were used for the prediction of flows in open channels, both simple and compound. Their performance in those flows were assessed through comparisons with the best available data. The test cases selected for models assessment cover a wide range of flow conditions typical of those encountered in engineering practice.

The results for relatively narrow channels demonstrate that the Reynolds-stress model correctly accounts for the free-surface effects which include the displacement of the position of maximum velocity to below the free surface. Although the nonlinear k-ϵ model reproduces the mean-velocity distribution fairly well in a large part of flow domain, this model fails to predict the occurrence of velocity maximum below the free surface. This was attributed to the use of algebraic stress-strain relationship which gave rise to turbulence isotropy near the free surface. Nevertheless, the differences between the two models near the free surface were seen to have little influence on the bed- and side-wall shear stresses. For the higher aspect-ratio cases, the two models gave qualitatively and quantitatively quite similar results and this argues in favour of the use of the nonlinear k-ϵ model for practical-engineering calculations. This is further confirmed from the results for trapezoidal channels where the agreement

between predictions and data was quite satisfactory.

The results obtained with the Reynolds-stress model for flows in open-compound channels are the best available. The closure adopted here has succeeded in reproducing the most important features of those flows which include the various types of mean-velocity distortions within the flow domain and the shear-stress perturbations over wetted perimeter. The differences between the Reynolds-stress and nonlinear k-ϵ models seem to be less for compound channels. Thus the nonlinear k-ϵ model has produced satisfactory results for many flows especially so concerning the wall-shear-stress distribution. The similarities between the two models are particularly obvious for the compound-channel flows with roughen flood plains.

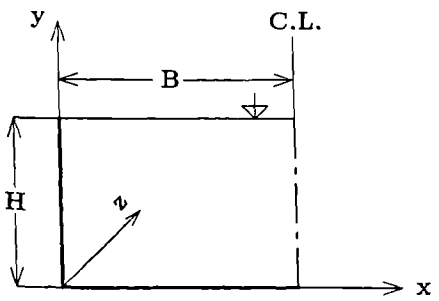

$$AR = \frac{2B}{H}$$

a) Rectangular channel

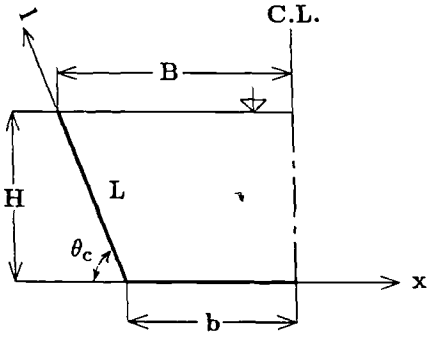

$$AR = \frac{B + b}{H}$$

b) Trapezoidal channel

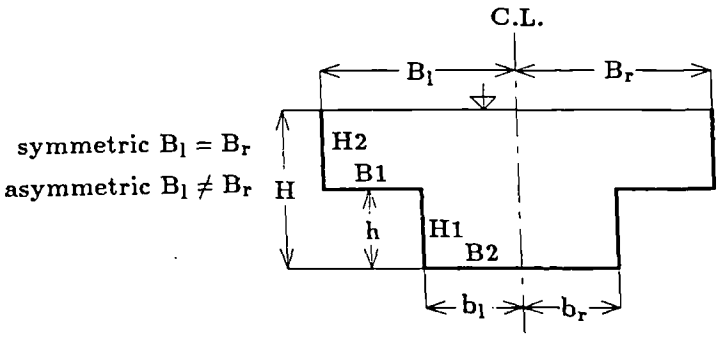

$$h^* = \frac{H - h}{H}$$

$$AR = \frac{(B_l + B_r)}{H}$$

c) Compound channel

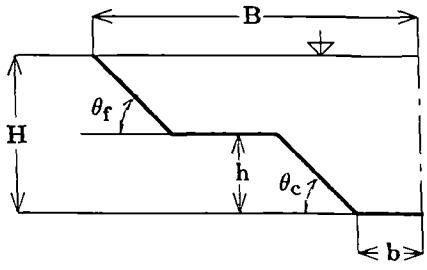

$$h^* = \frac{H - h}{H}$$

$$AR = \frac{2B}{H}$$

d) Compound-symmetric channel with inclined side walls

Fig. 5.1 Channel-flow notation.

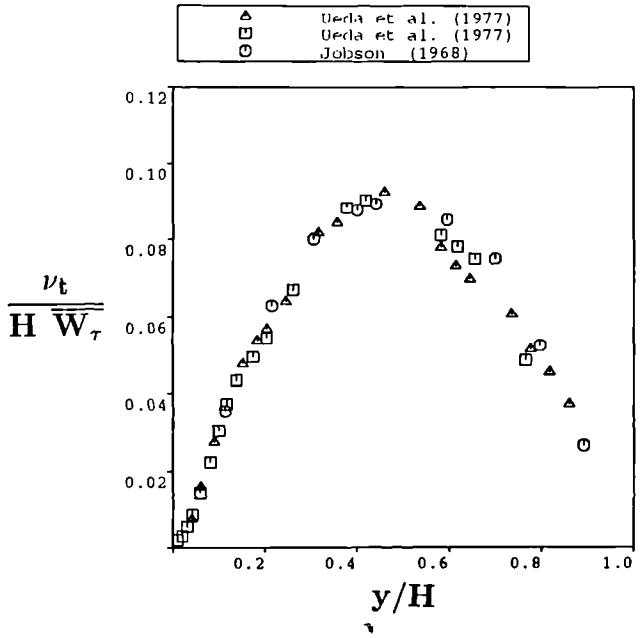

Fig. 5.2 Measured eddy-viscosity distribution in broad open – channel flow.

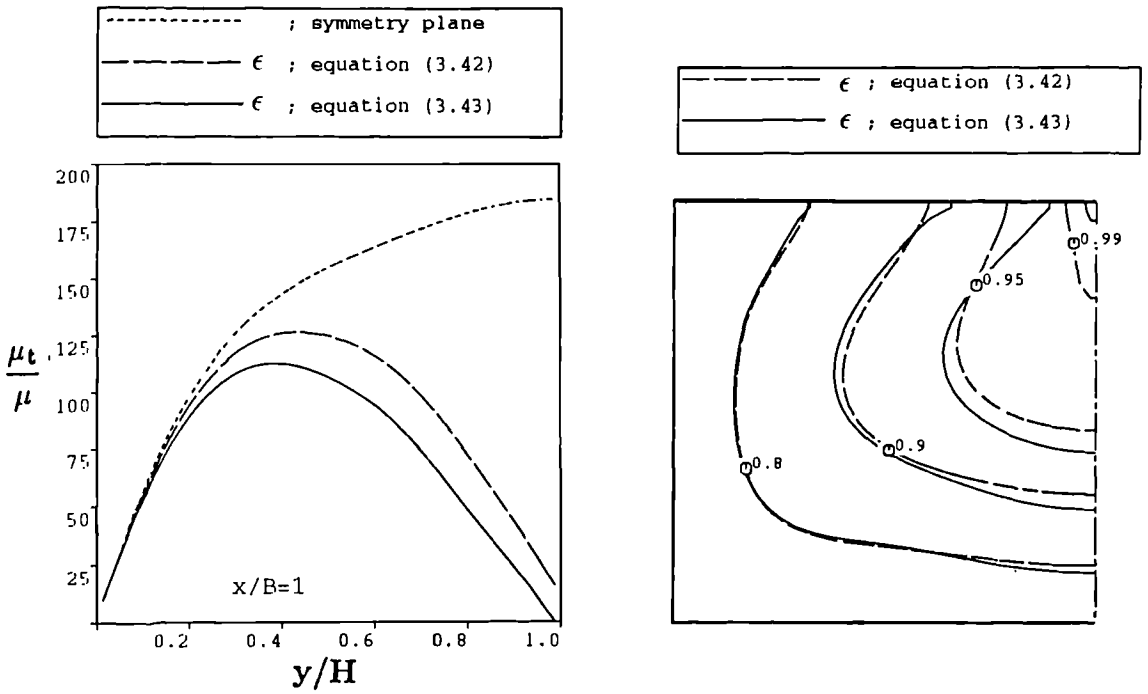

a) Eddy-viscosity profiles b) Mean-velocity contours W/W_{max}

Fig. 5.3 Nonlinear k-ϵ model results. Comparison of predictions for various ϵ – boundary conditions.

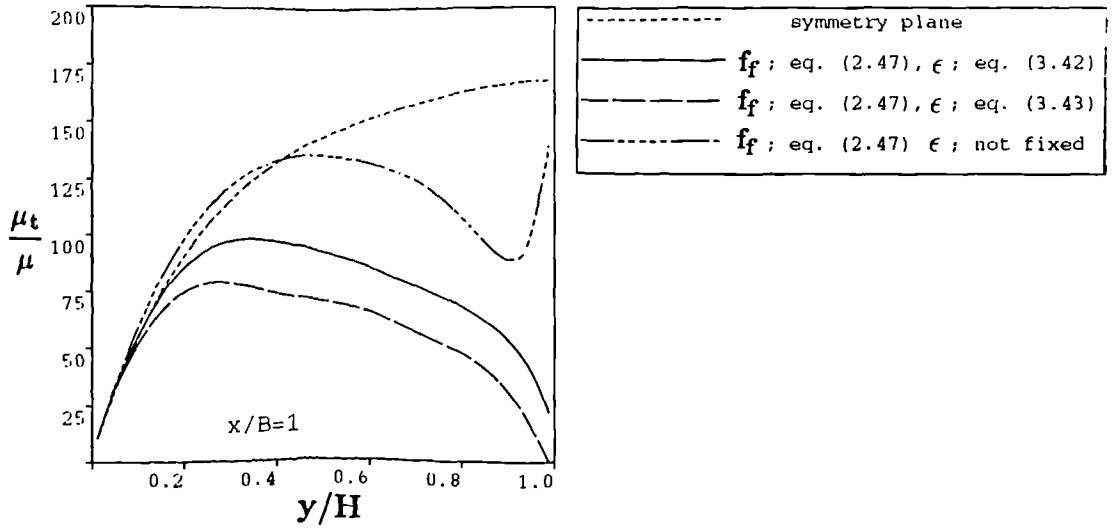

a) Eddy-viscosity profiles

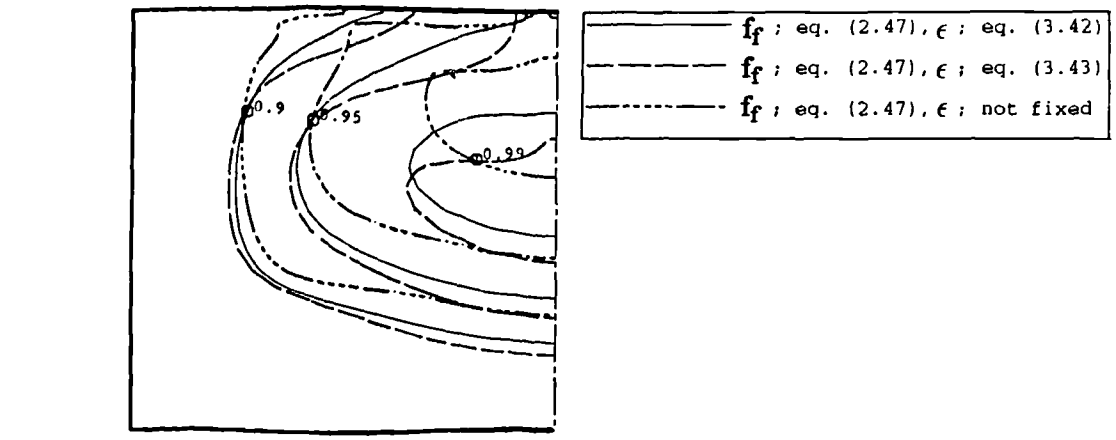

b) Mean-velocity contours W/W_{max}

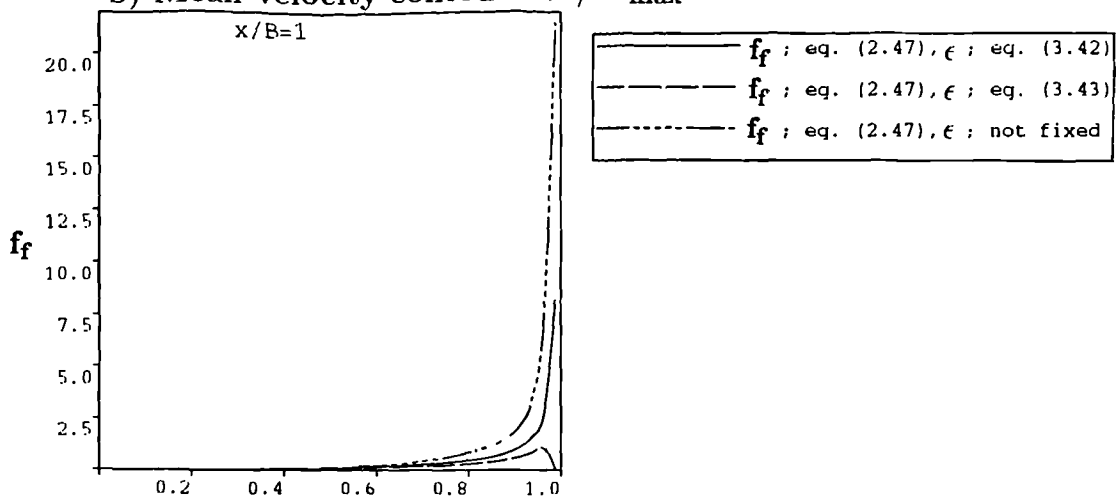

c) Free-surface-damping function

Fig. 5.4 Reynolds-stress model results. Comparison of predictions for various free – surface modellings.

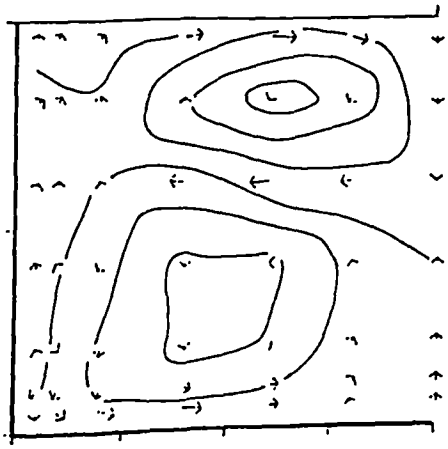

DATA

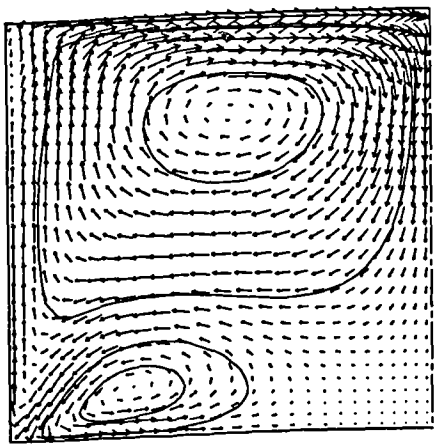

RSM

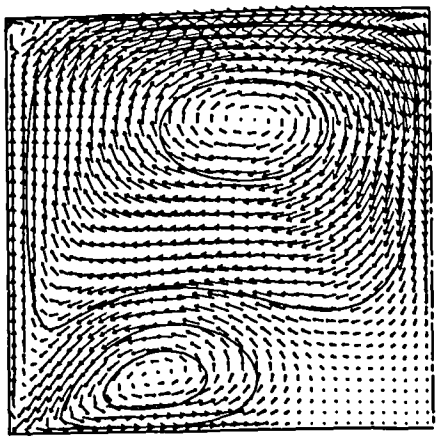

NKE

Fig. 5.5 Secondary – velocity flow.
Data of Tominaga et al. (1989).

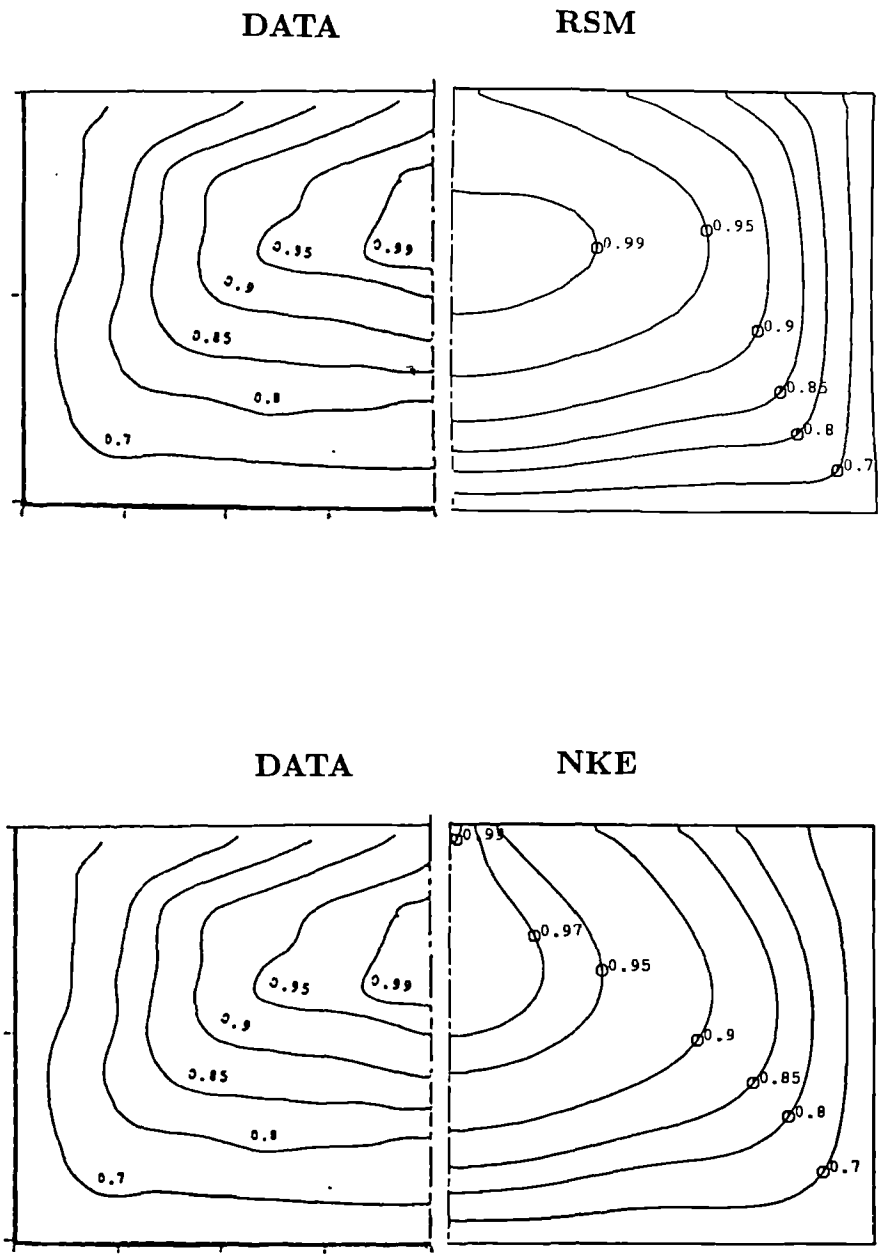

Fig. 5.6 Mean – velocity contours W/W_{max}.
Data of Tominaga et al. (1989).

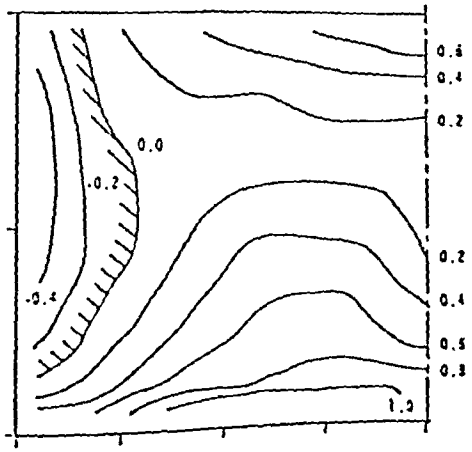

DATA

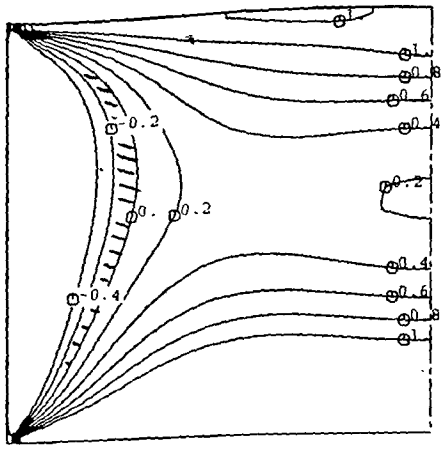

RSM

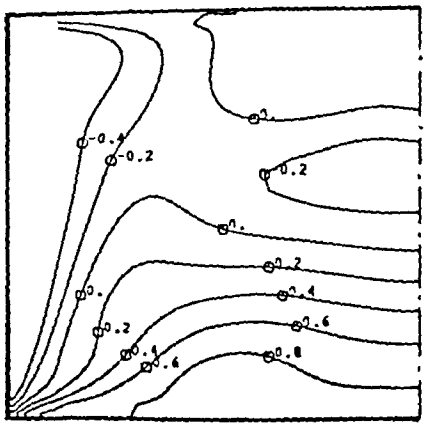

NKE

Fig. 5.7 Normal – stress anisotropy $\frac{\overline{u^2}-\overline{v^2}}{W^2_{max}} \times 10^3$.
Data of Tominaga et al. (1989).

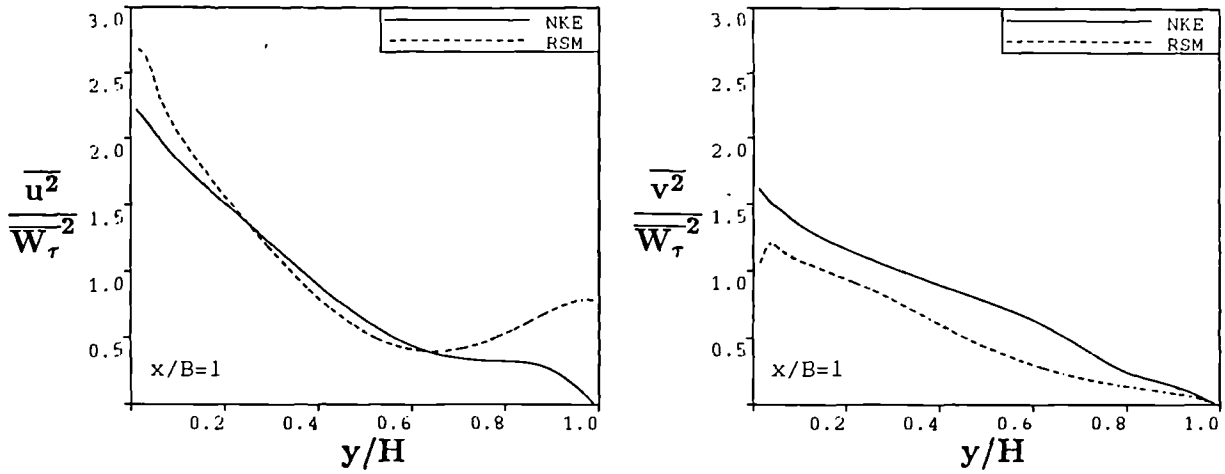

a) Normal-stress profiles

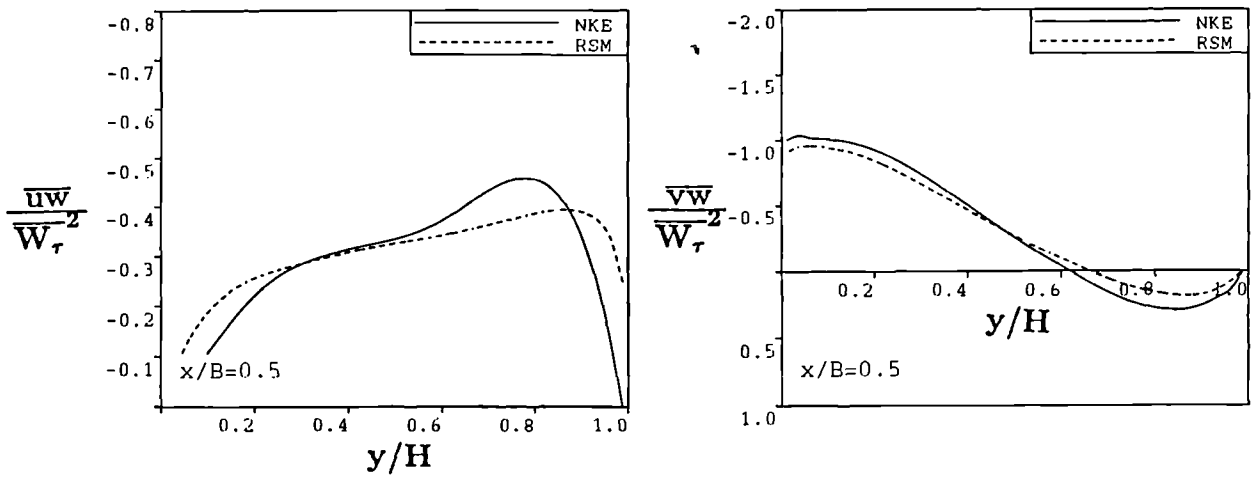

b) Shear-stress profiles

Fig. 5.8 Turbulent stresses in open channel.

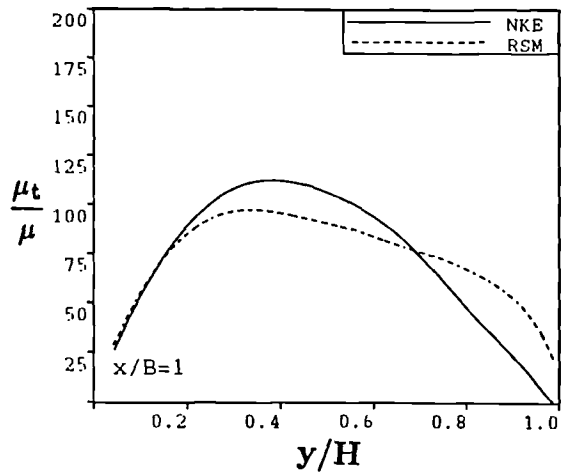

Fig. 5.9 Eddy-viscosity distribution in open-rectangular channel.

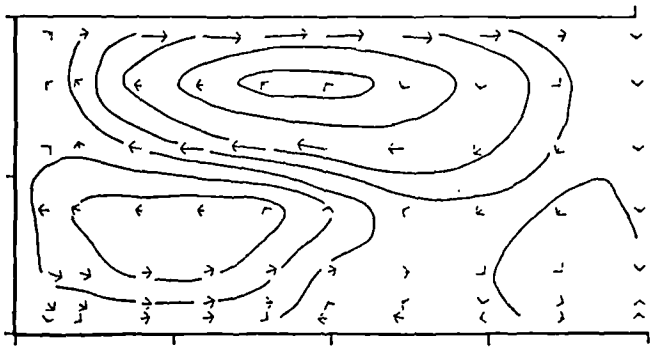

DATA

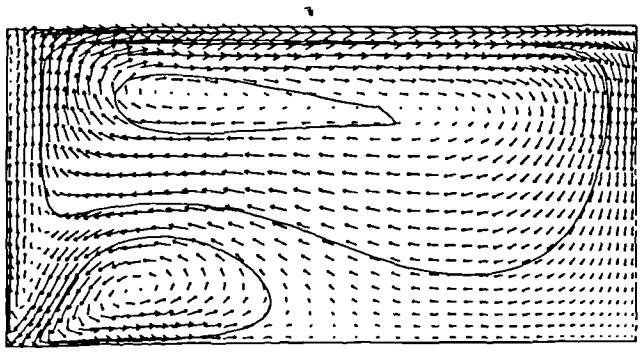

RSM

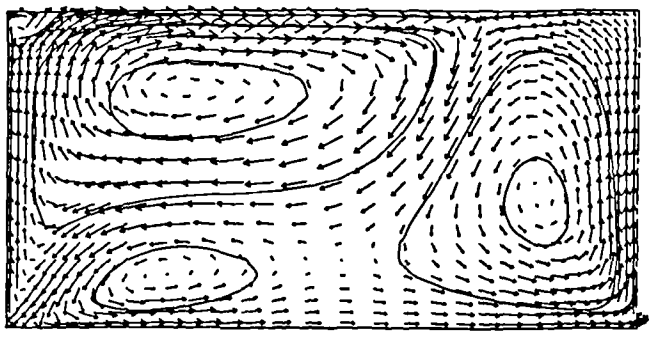

NKE

Fig. 5.10 Secondary – velocity flow.
Data of Tominaga et al. (1989).

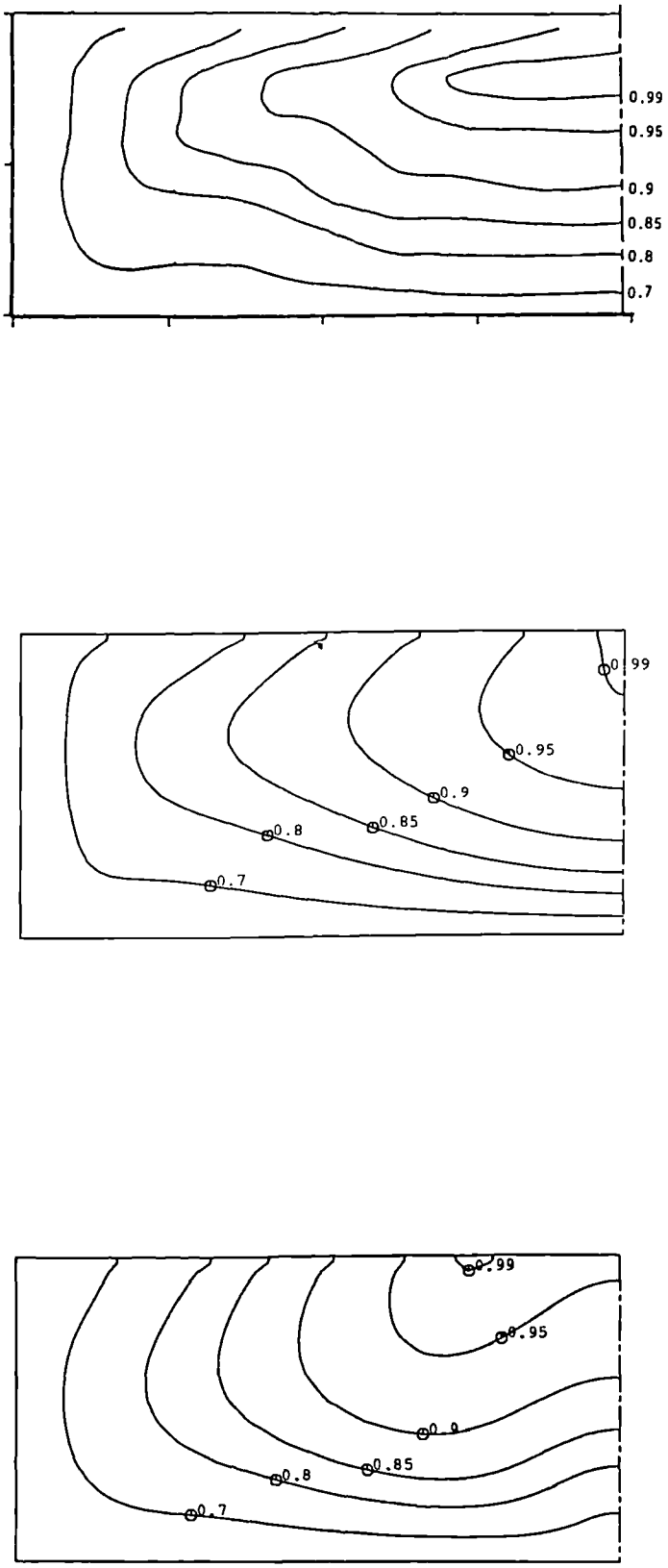

Fig. 5.11 Mean – velocity contours W/W_{max}.
Data of Tominaga et al. (1989).

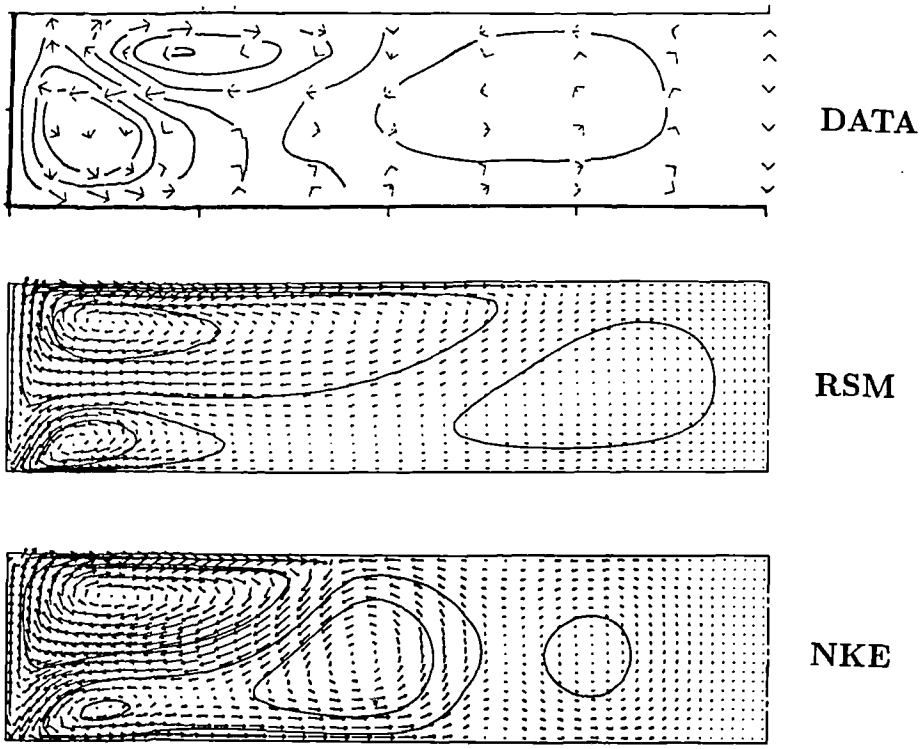

Fig. 5.12 Secondary – velocity flow.
Data of Tominaga et al. (1989).

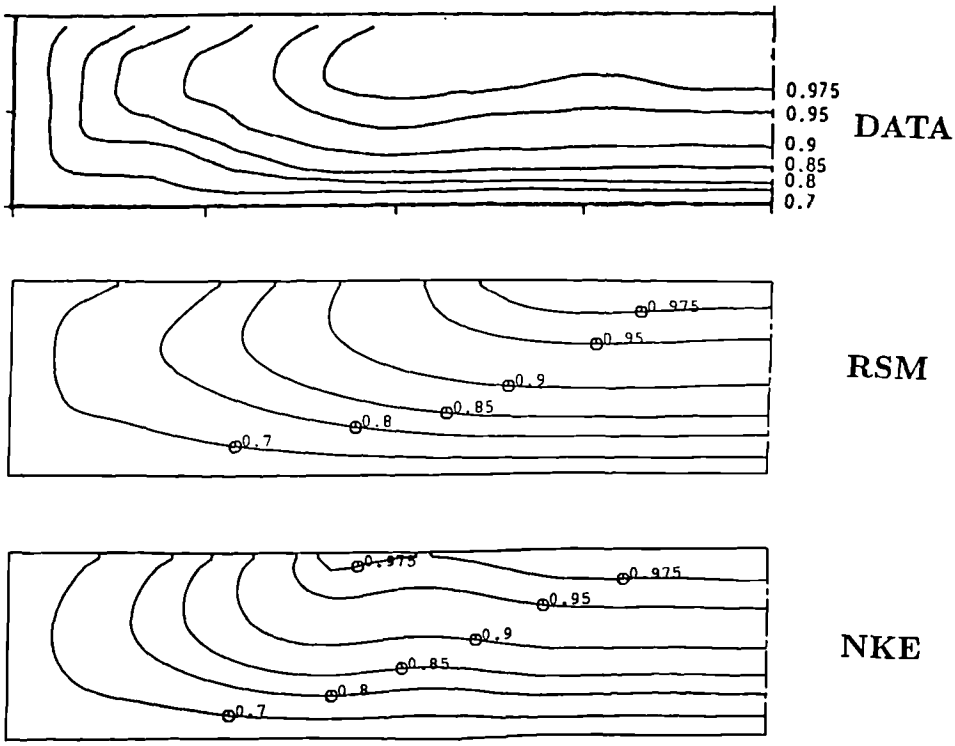

Fig. 5.13 Mean – velocity contours W/W_{max}.
Data of Tominaga et al. (1989).

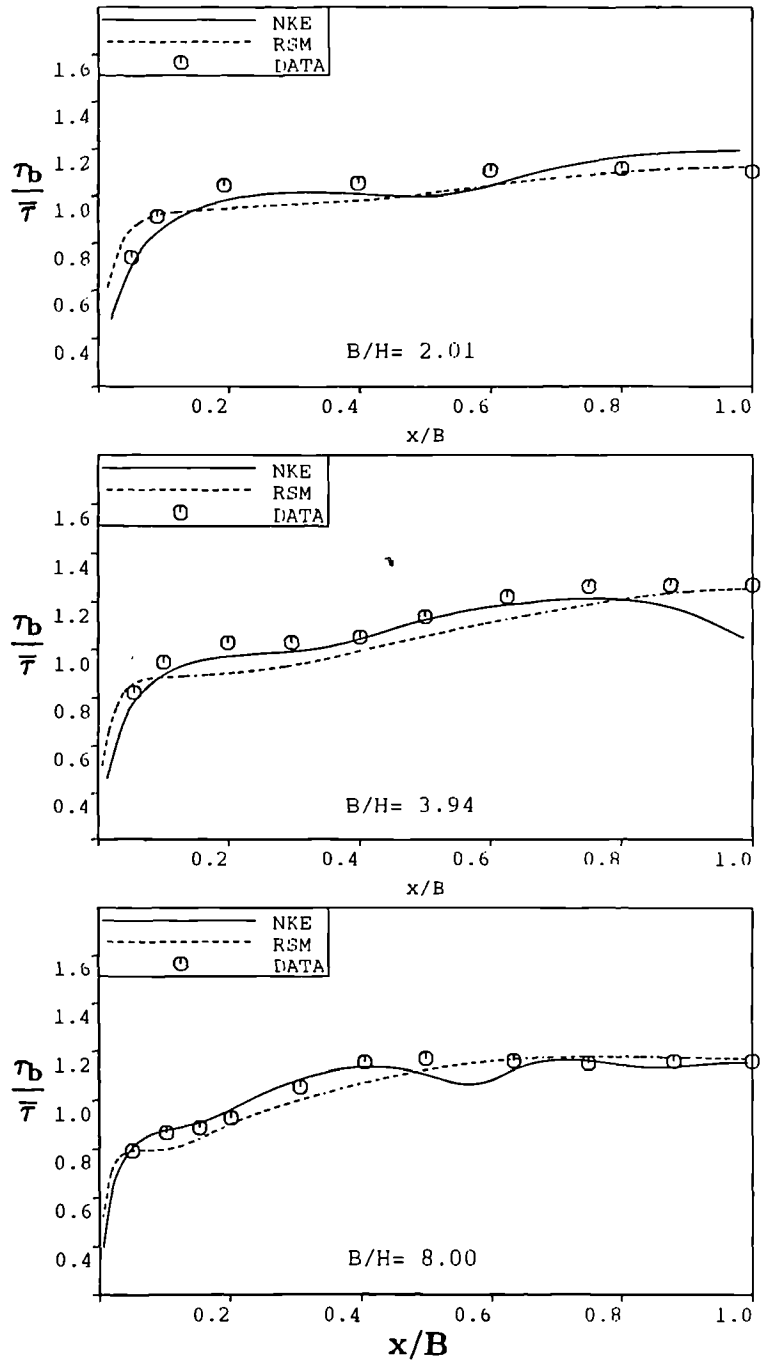

Fig. 5.14 Bed – shear – stress in rectangular – open channels. Data of Tominaga et al. (1989).

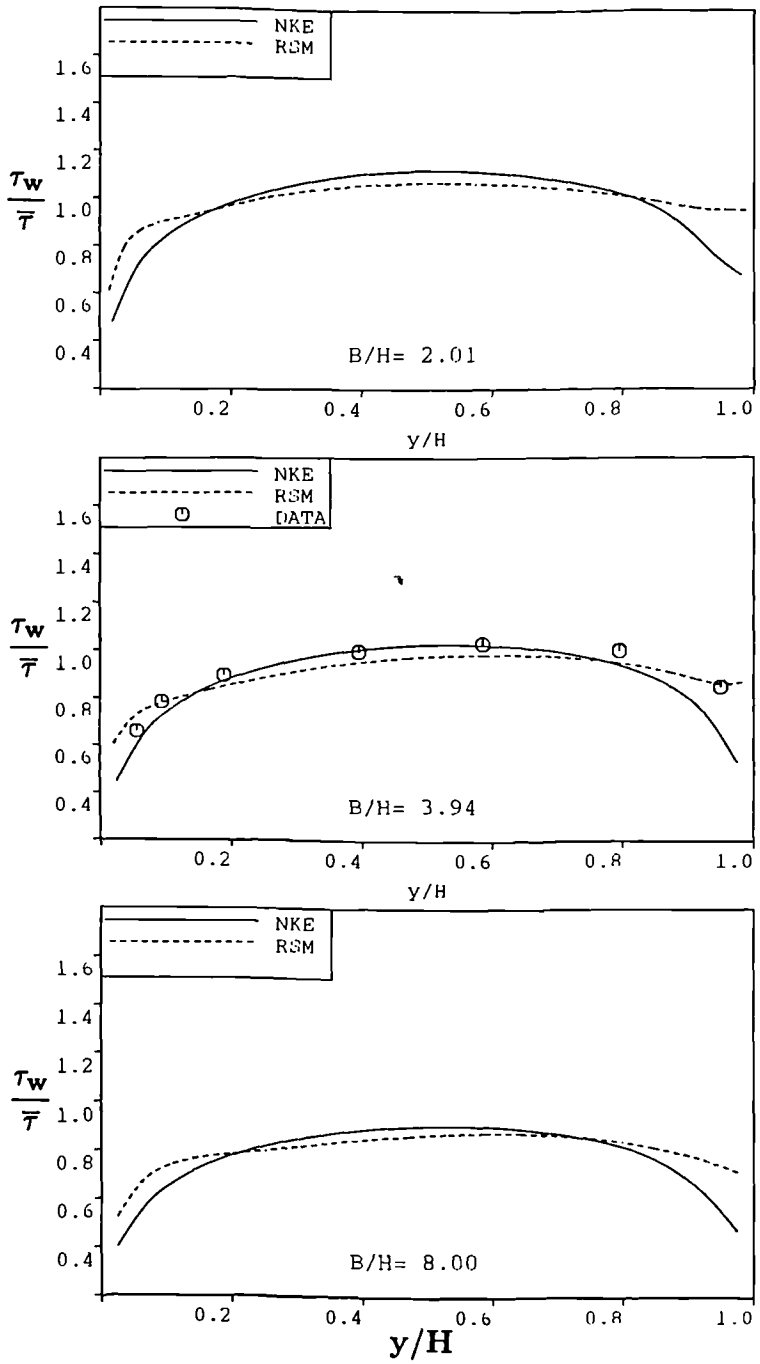

Fig. 5.15 Wall – shear – stress in rectangular – open channels. Data of Tominaga et al. (1989).

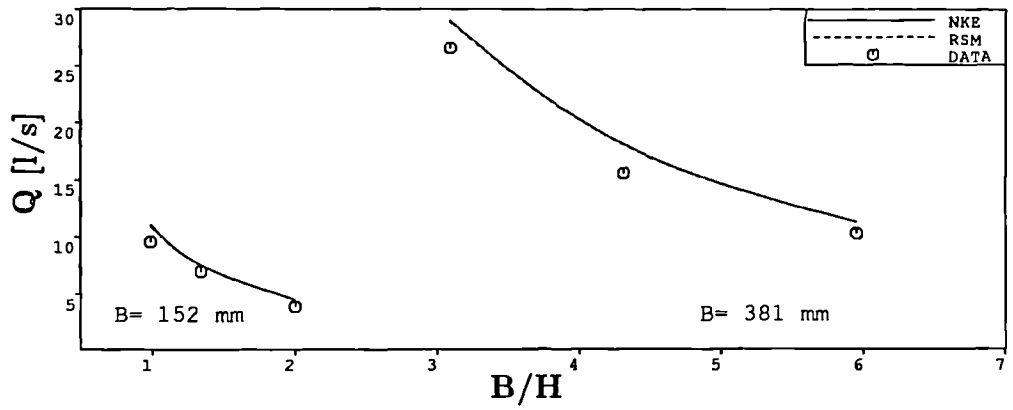

a) Discharge

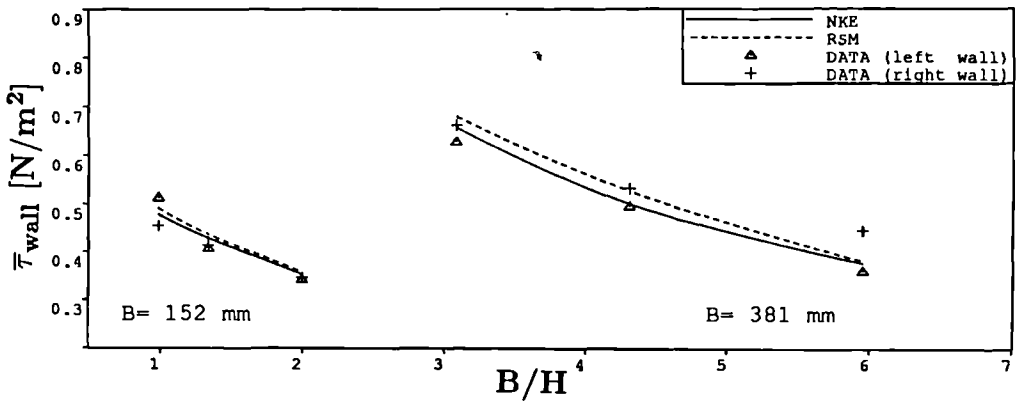

b) Average shear-stress on the wall

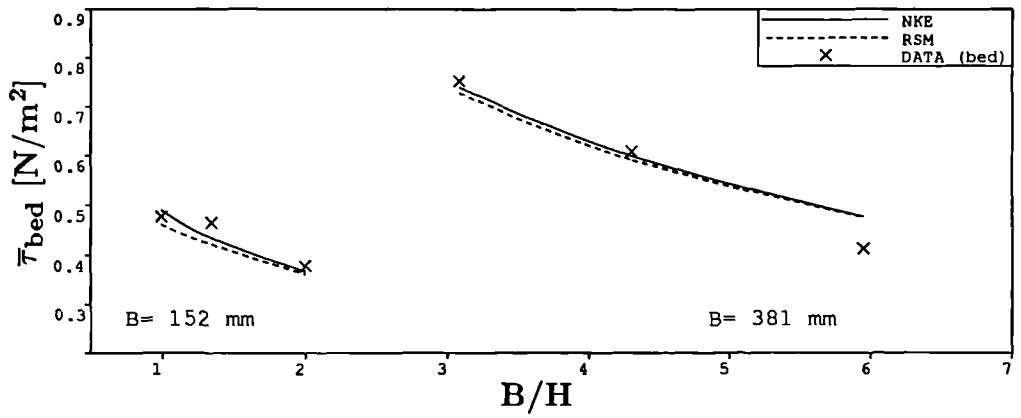

c) Average shear-stress on the bed

Fig. 5.16 Bulk quantities in rectangular – open channels. Data of Knight et al. (1984, a).

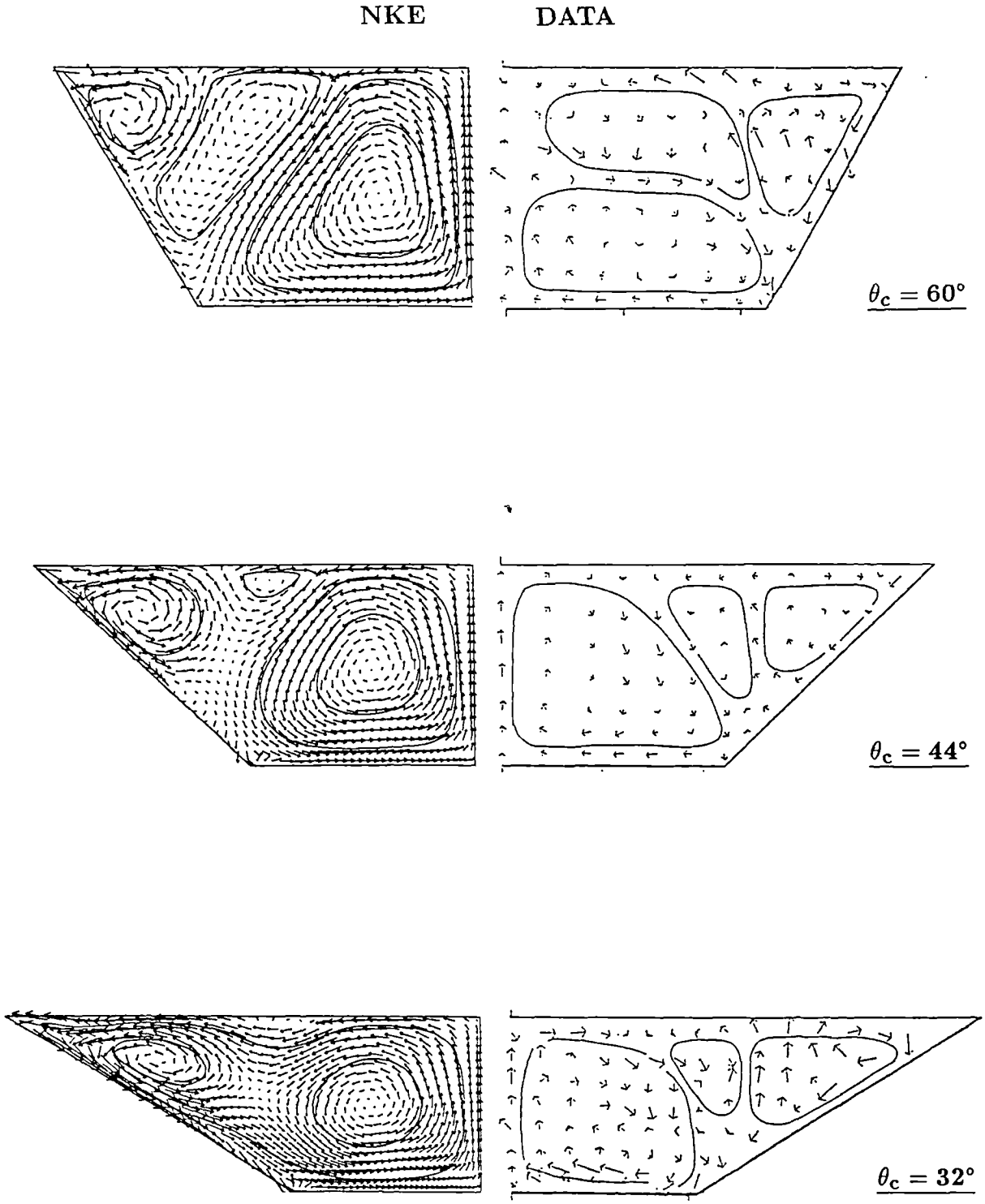

Fig. 5.17 Secondary flow in trapezoidal channels.
Data of Tominaga et al. (1989).

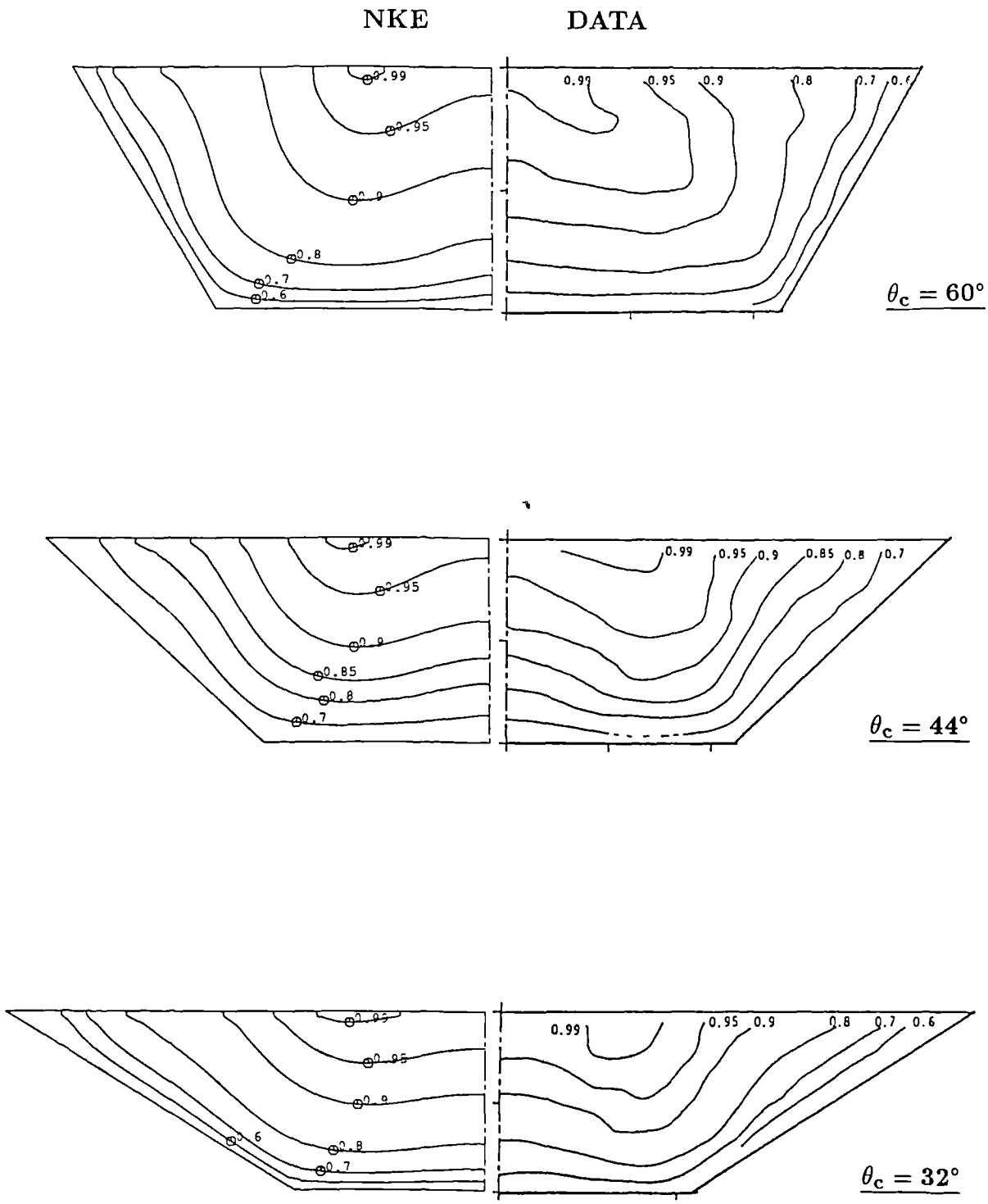

Fig. 5.18 Mean – velocity contours in trapezoidal channels W/W_{max}. Data of Tominaga et al. (1989).

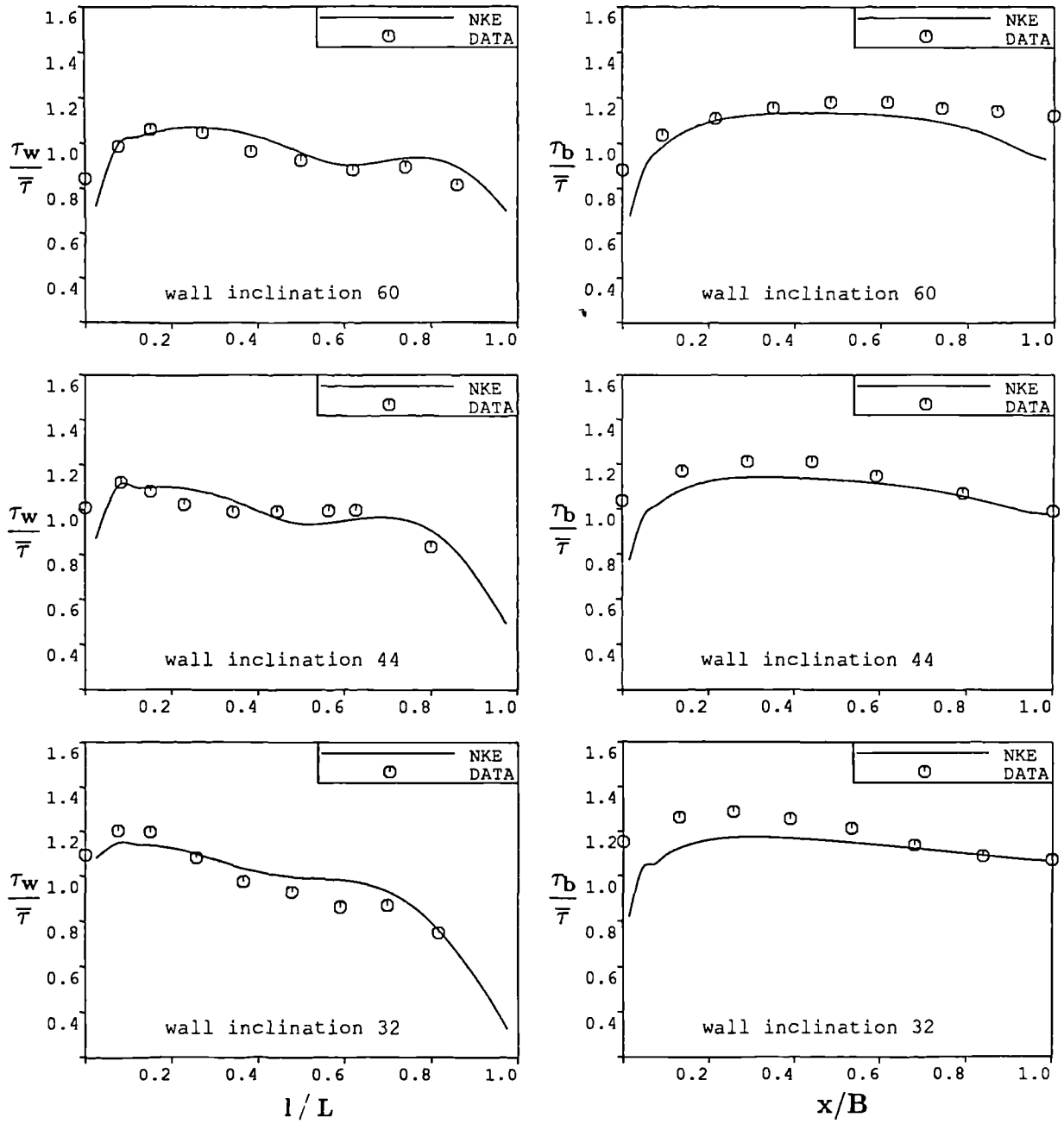

a) Wall-shear-stress

b) Bed-shear-stress

Fig. 5.19 Shear – stress over wetted perimeter in trapezoidal channels. Data of Tominaga et al. (1989).

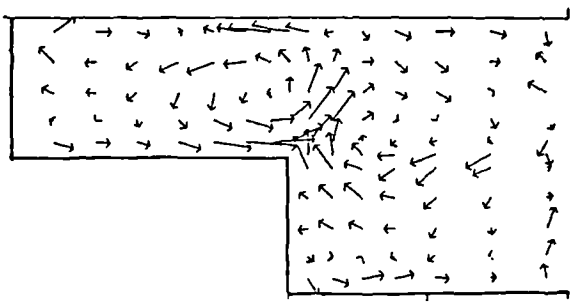

DATA

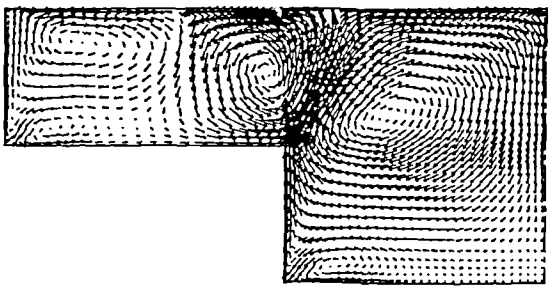

RSM

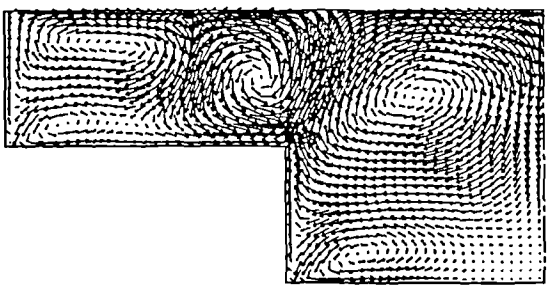

NKE

Fig. 5.20 Secondary – velocity vectors in symmetric compound channel with $h^* = 0.5$.
Data of Tominaga et al. (1988, a).

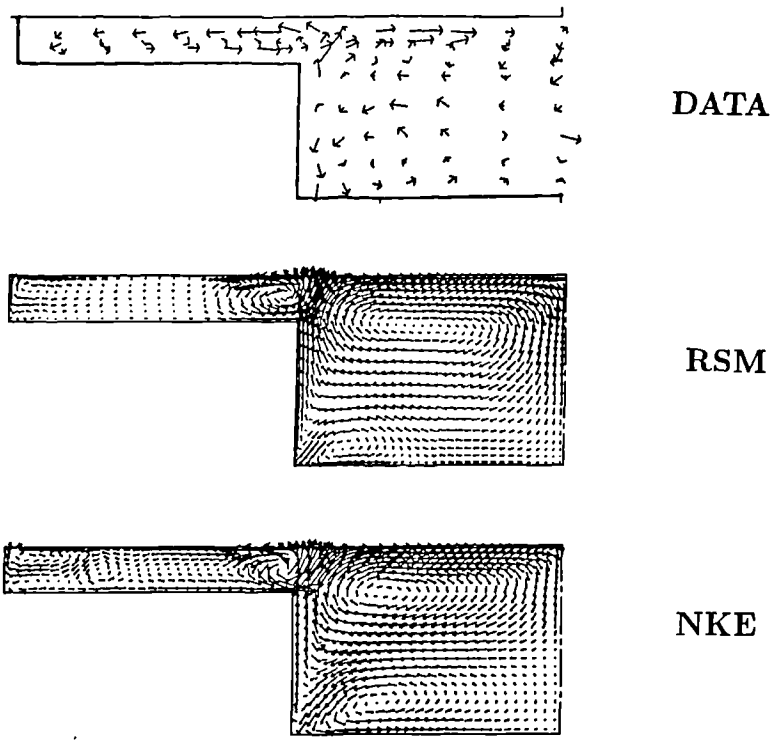

Fig. 5.21 Secondary – velocity vectors in symmetric compound channel with $h^* = 0.243$. Data of Tominaga et al. (1988, a).

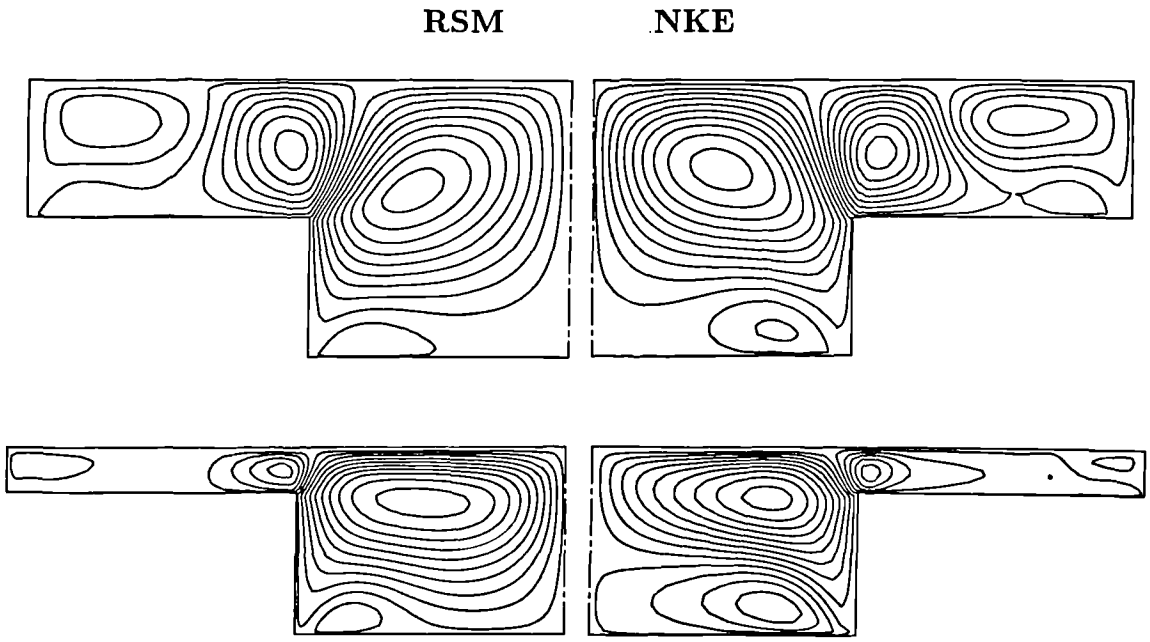

Fig. 5.22 Predicted secondary – velocity streamlines in symmetric – compound channels.

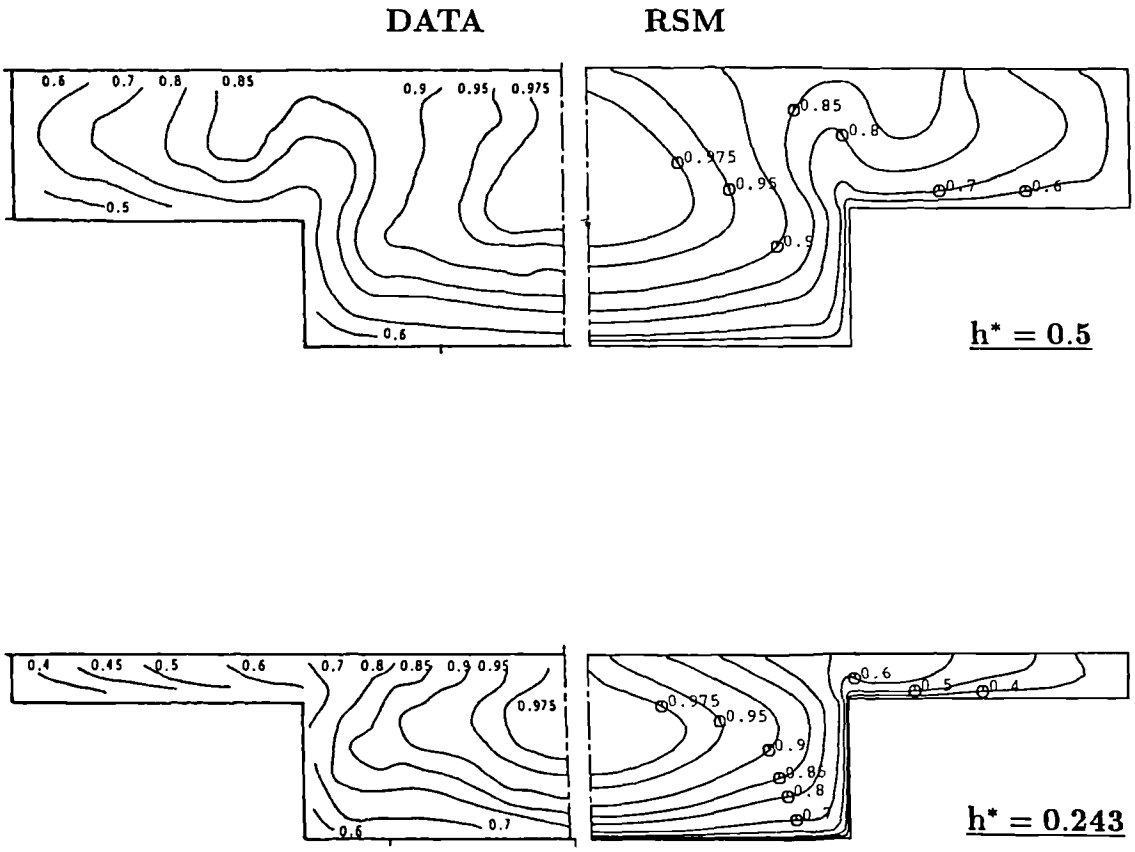

Fig. 5.23 Mean – velocity contours W/W_{max}.
Data of Tominaga et al. (1988, a).

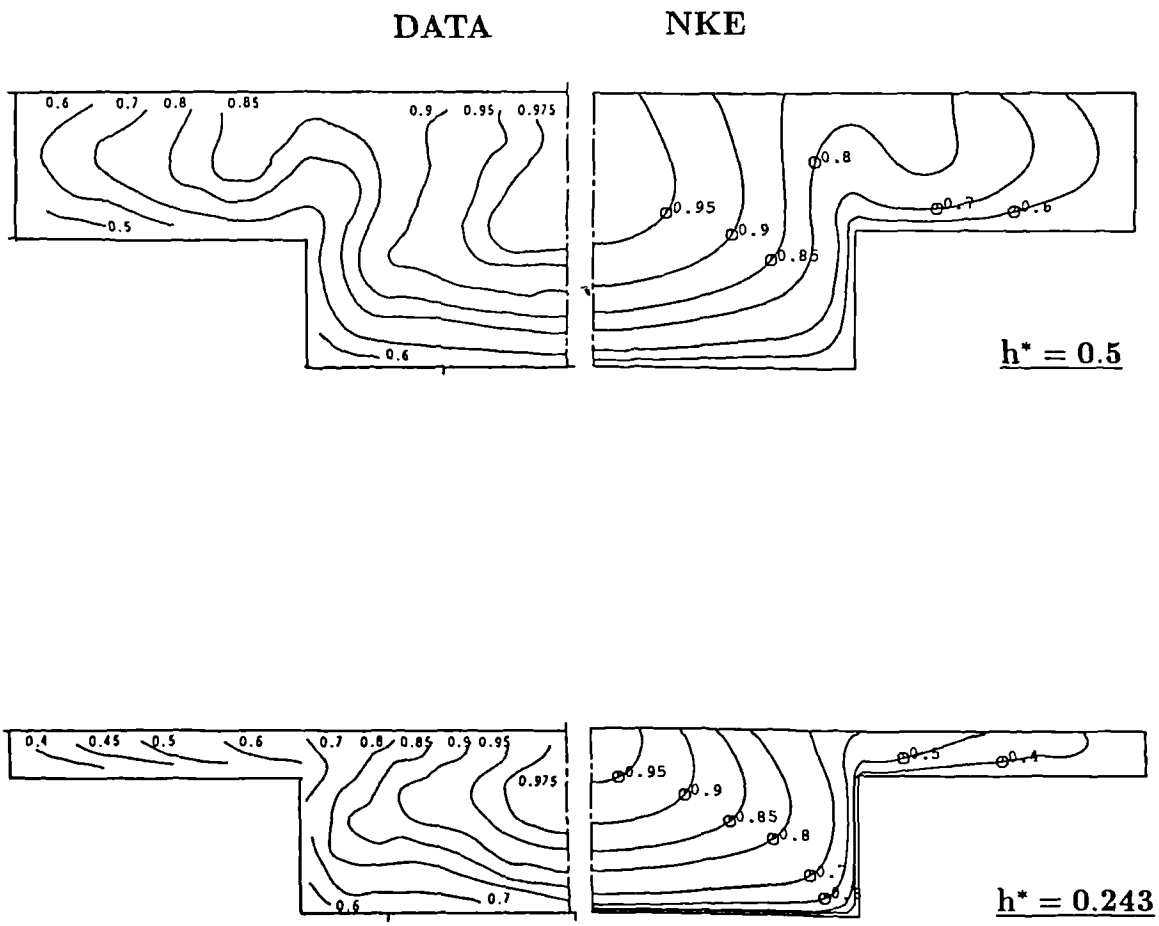

Fig. 5.24 Mean – velocity contours W/W_{max}.
Data of Tominaga et al. (1988, a).

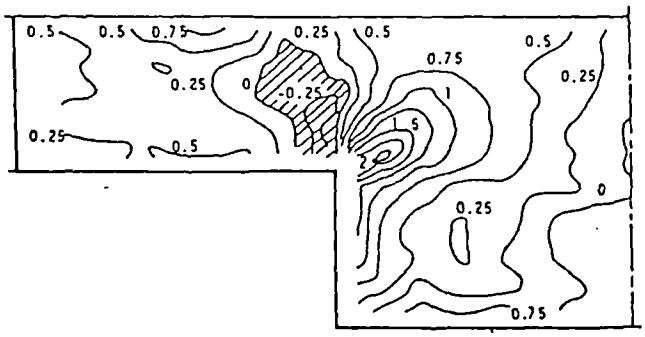

DATA

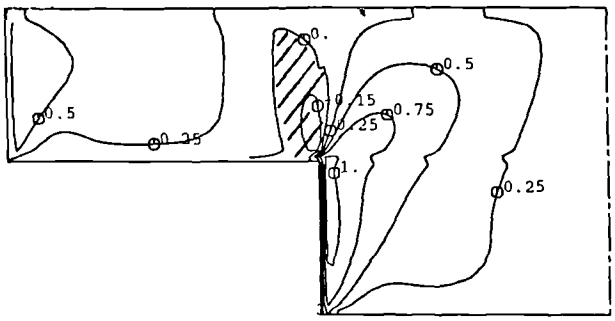

RSM

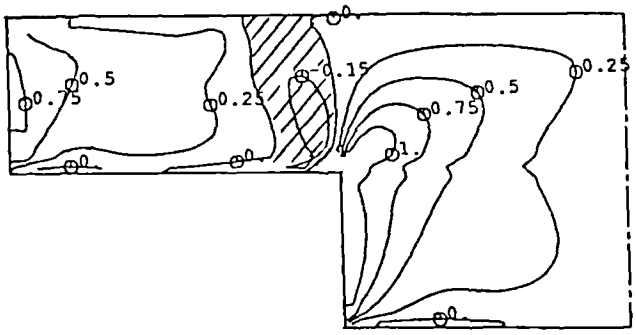

NKE

Fig. 5.25 Main – shear – stress contours $\frac{-\overline{uw}}{\overline{W_\tau}^2}$.
Data of Tominaga et al. (1988, a).

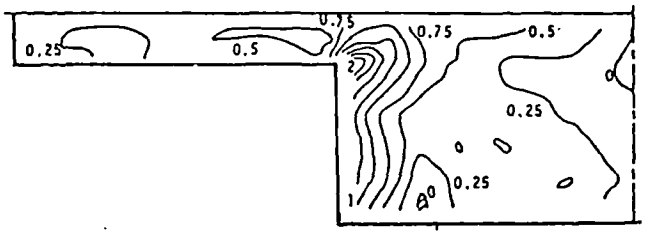

DATA

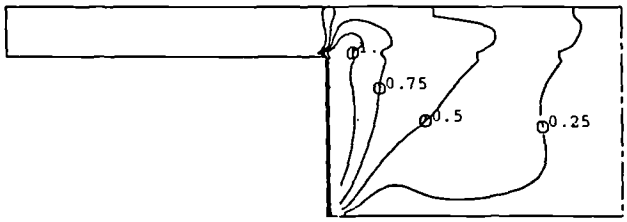

RSM

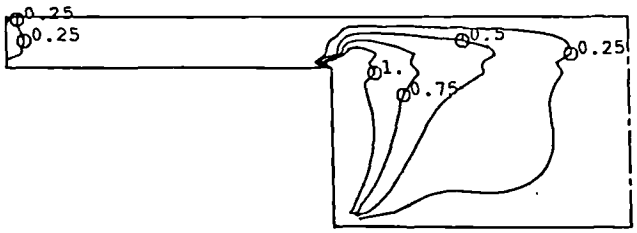

NKE

Fig. 5.26 Main – shear – stress contours $\frac{-\overline{uw}}{\overline{W_\tau}^2}$.
Data of Tominaga et al. (1988, a).

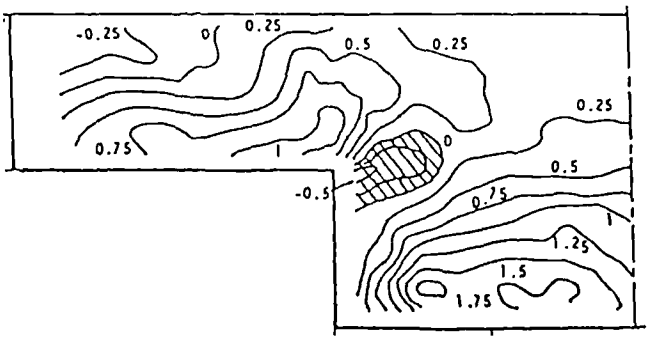

DATA

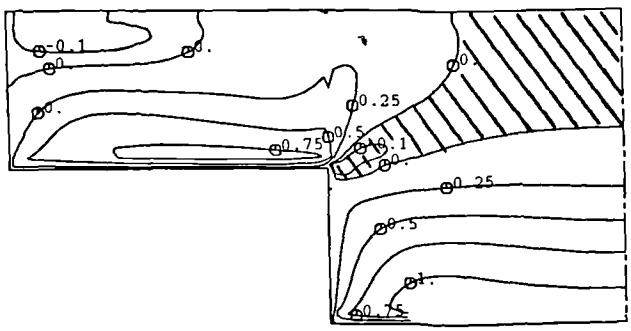

RSM

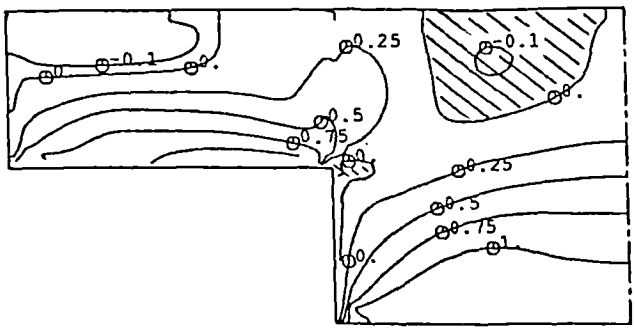

NKE

Fig. 5.27 Main – shear – stress contours $\frac{-\overline{VW}}{\overline{W_\tau}^2}$.
Data of Tominaga et al. (1988, a).

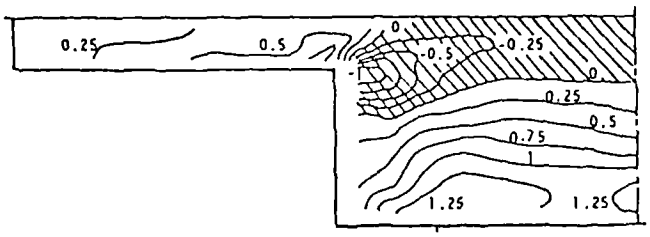

DATA

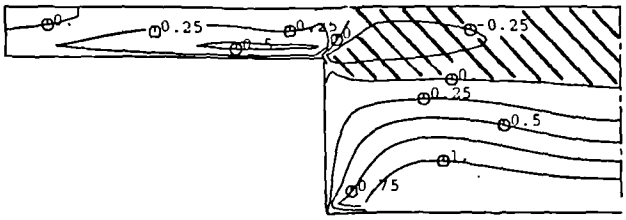

RSM

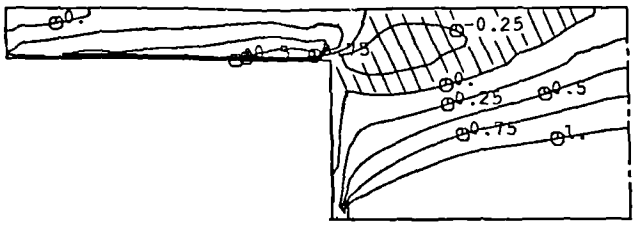

NKE

Fig. 5.28 Main – shear – stress contours $\frac{-\overline{VW}}{\overline{W_\tau}^2}$.
Data of Tominaga et al. (1988, a).

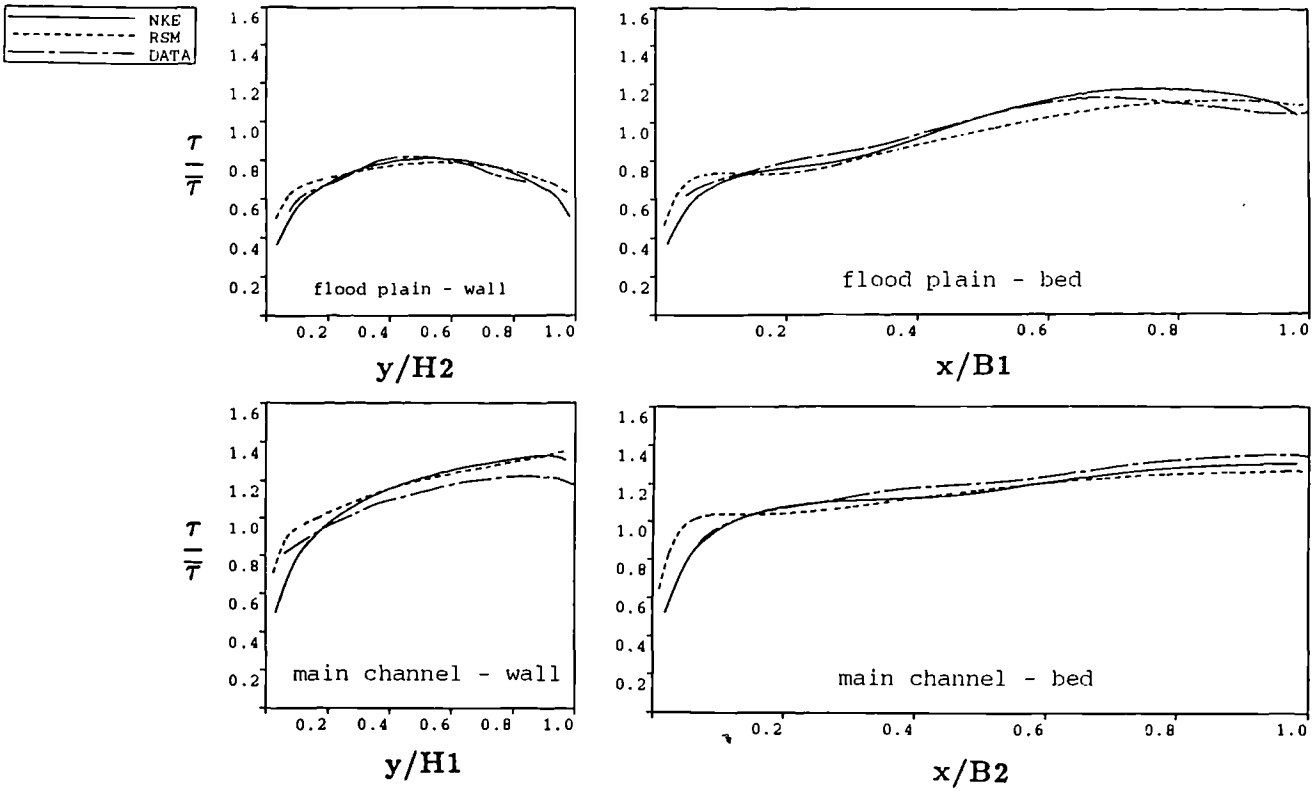

Fig. 5.29 Wall – shear – stress distribution in compound symmetric channel with $h^* = 0.5$.
Data of Tominaga et al. (1988, b).

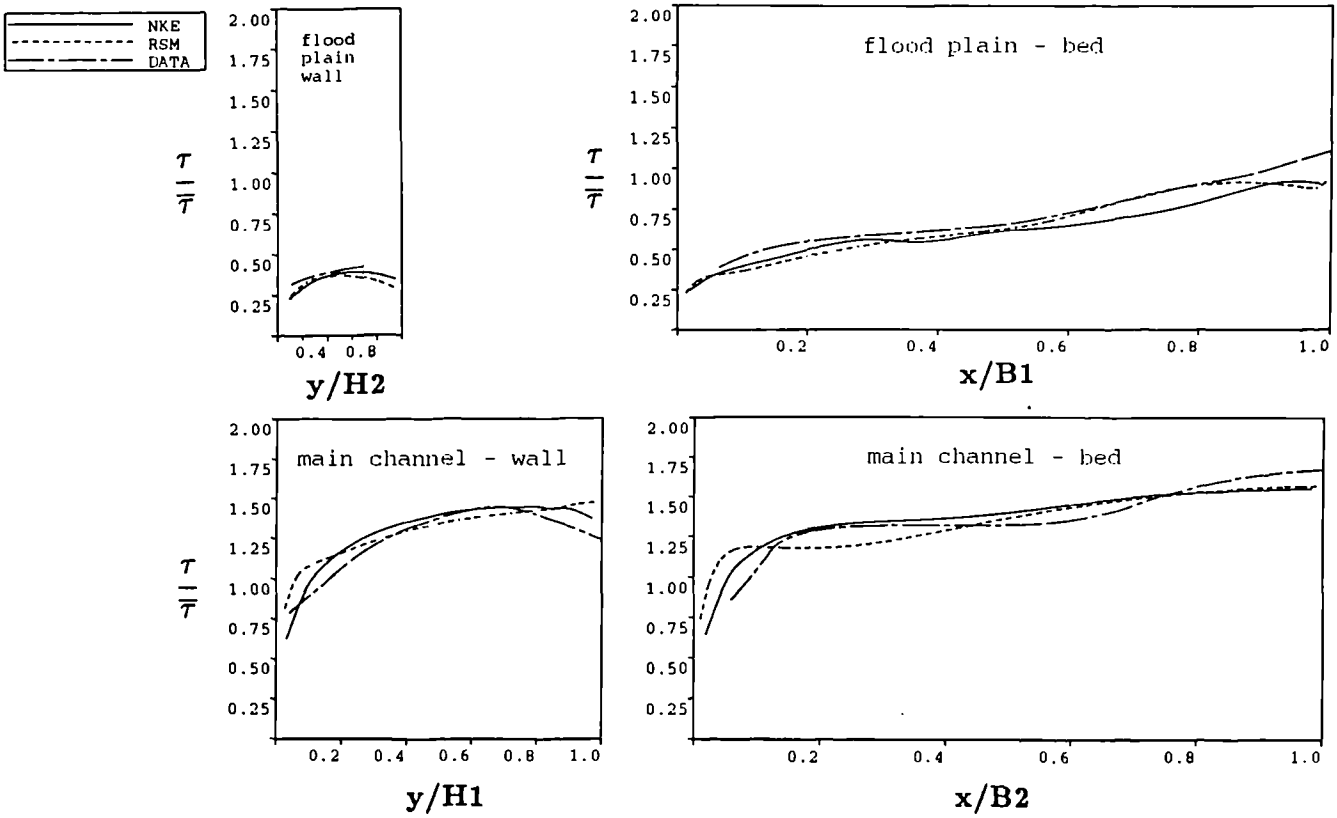

Fig. 5.30 Wall – shear – stress distribution in compound symmetric channel with $h^* = 0.243$.
Data of Tominaga et al. (1988, a).

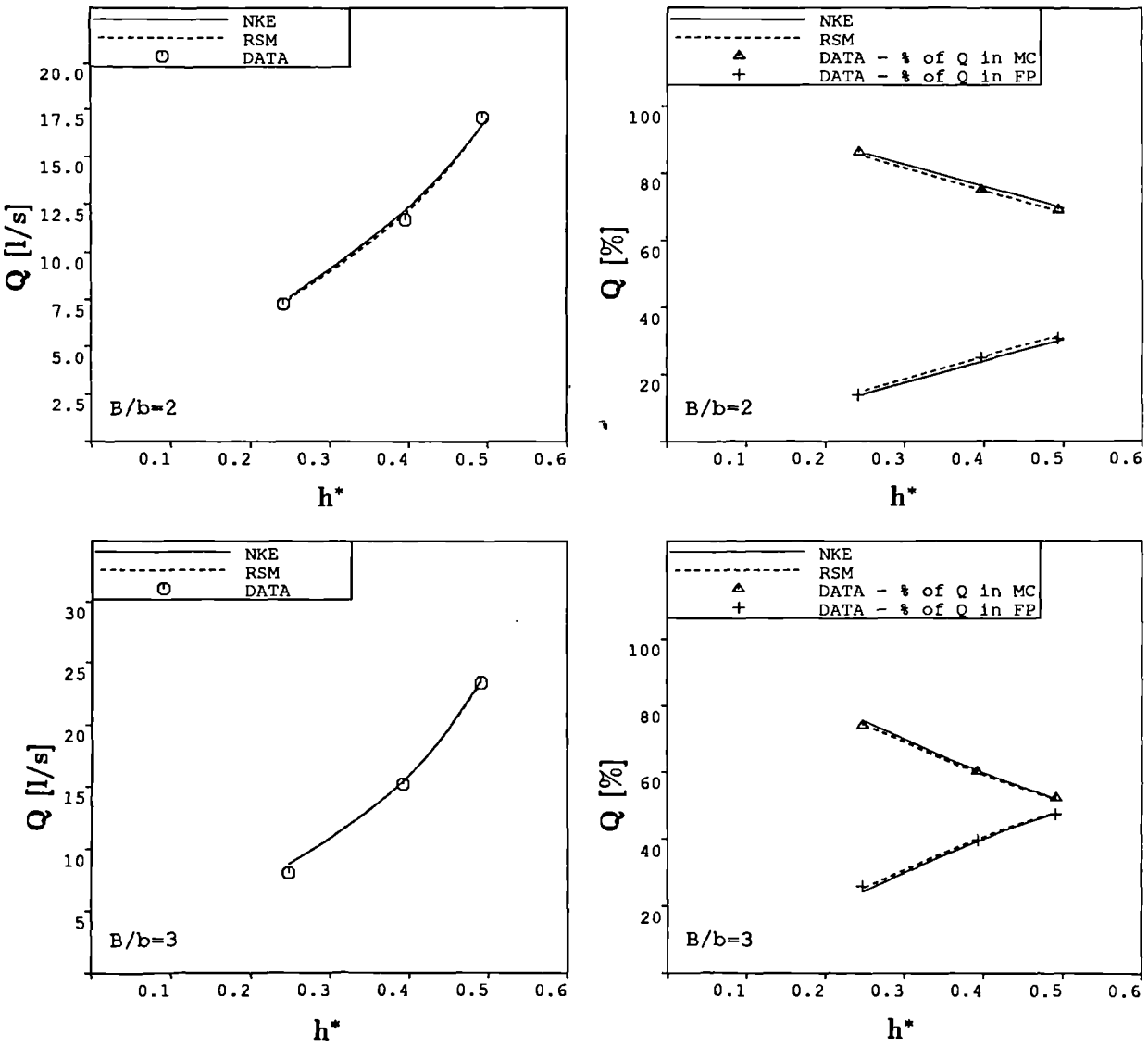

Fig. 5.31 Discharge in compound – symmetric channels.
Data of Knight and Demetriou (1983).

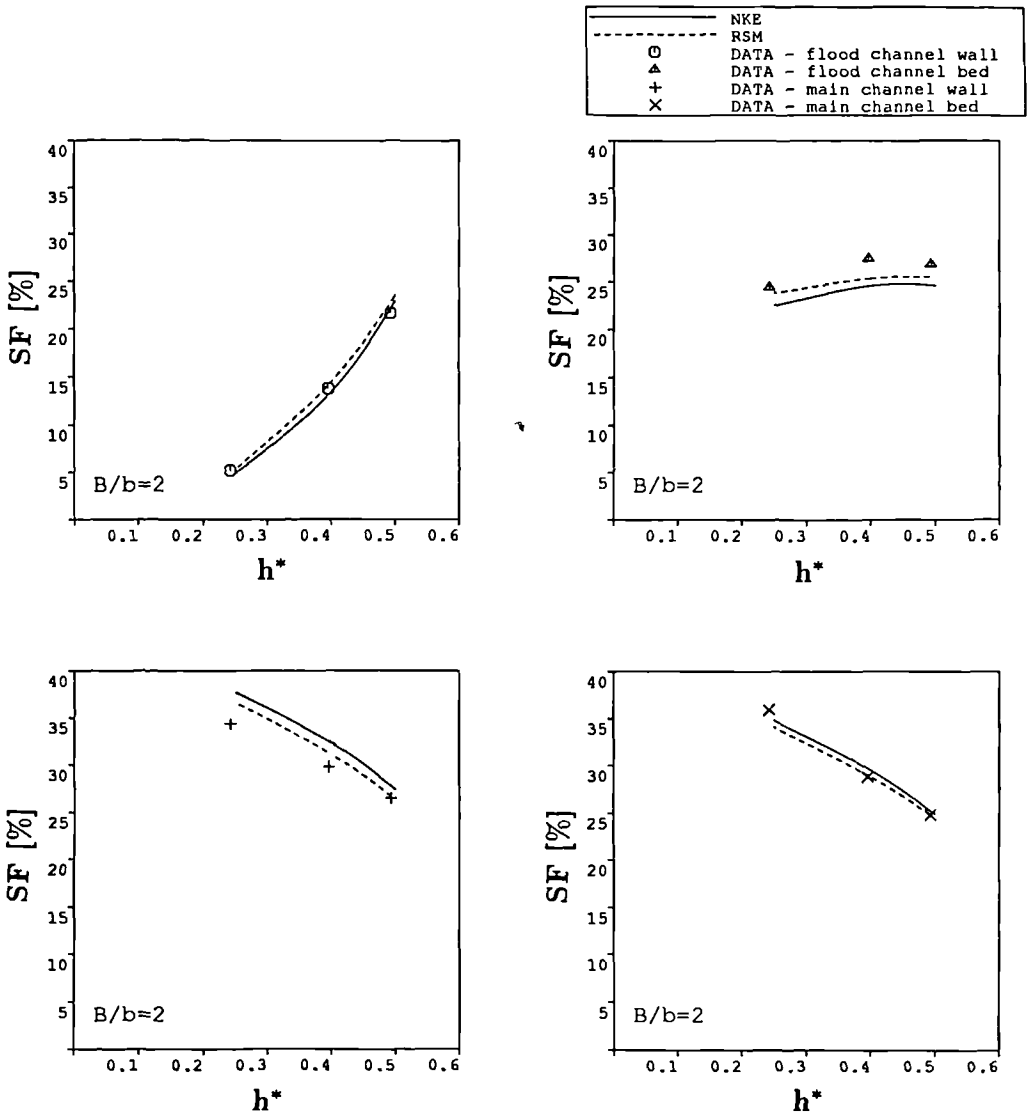

Fig. 5.32 Average shear – force in compound symmetric channel with B/b = 2. Data of Knight and Demetriou (1983).

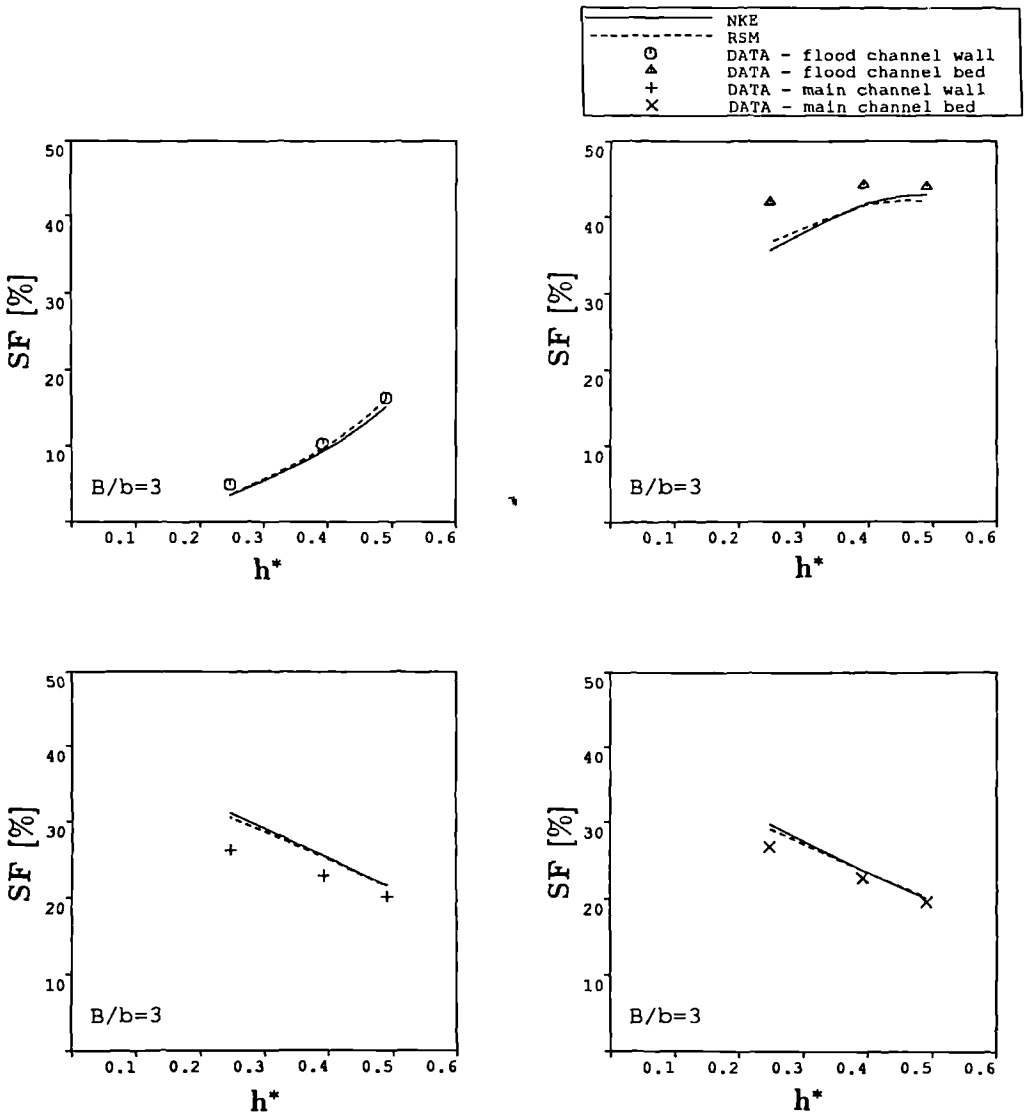

Fig. 5.33 Average shear – force in compound symmetric channel with B/b = 3. Data of Knight and Demetriou (1983).

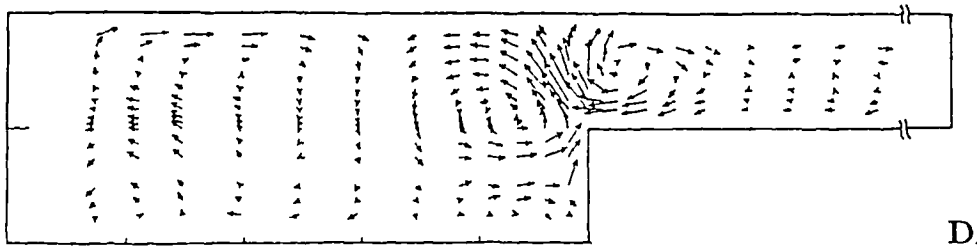

DATA

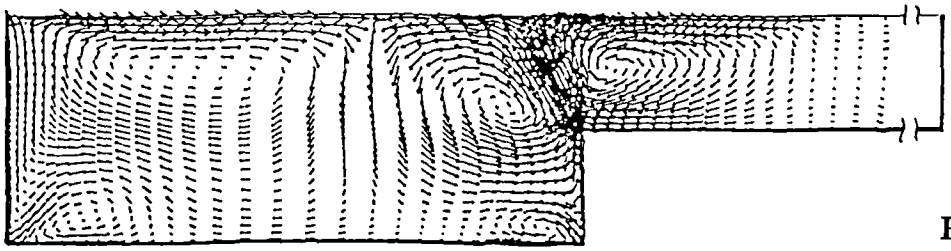

RSM

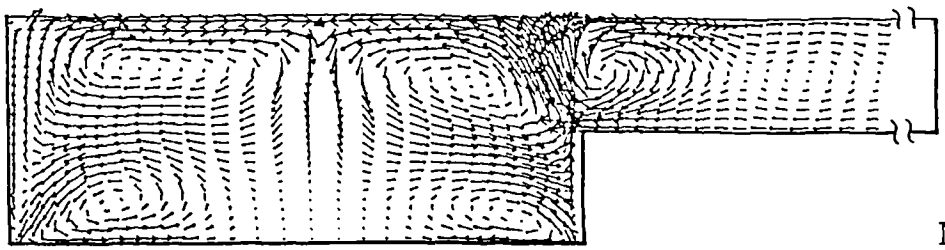

NKE

Fig. 5.34 Secondary – velocity vectors in asymmetric compound channel with $h^* = 0.5$.
Data of Tominaga and Nezu (1991).

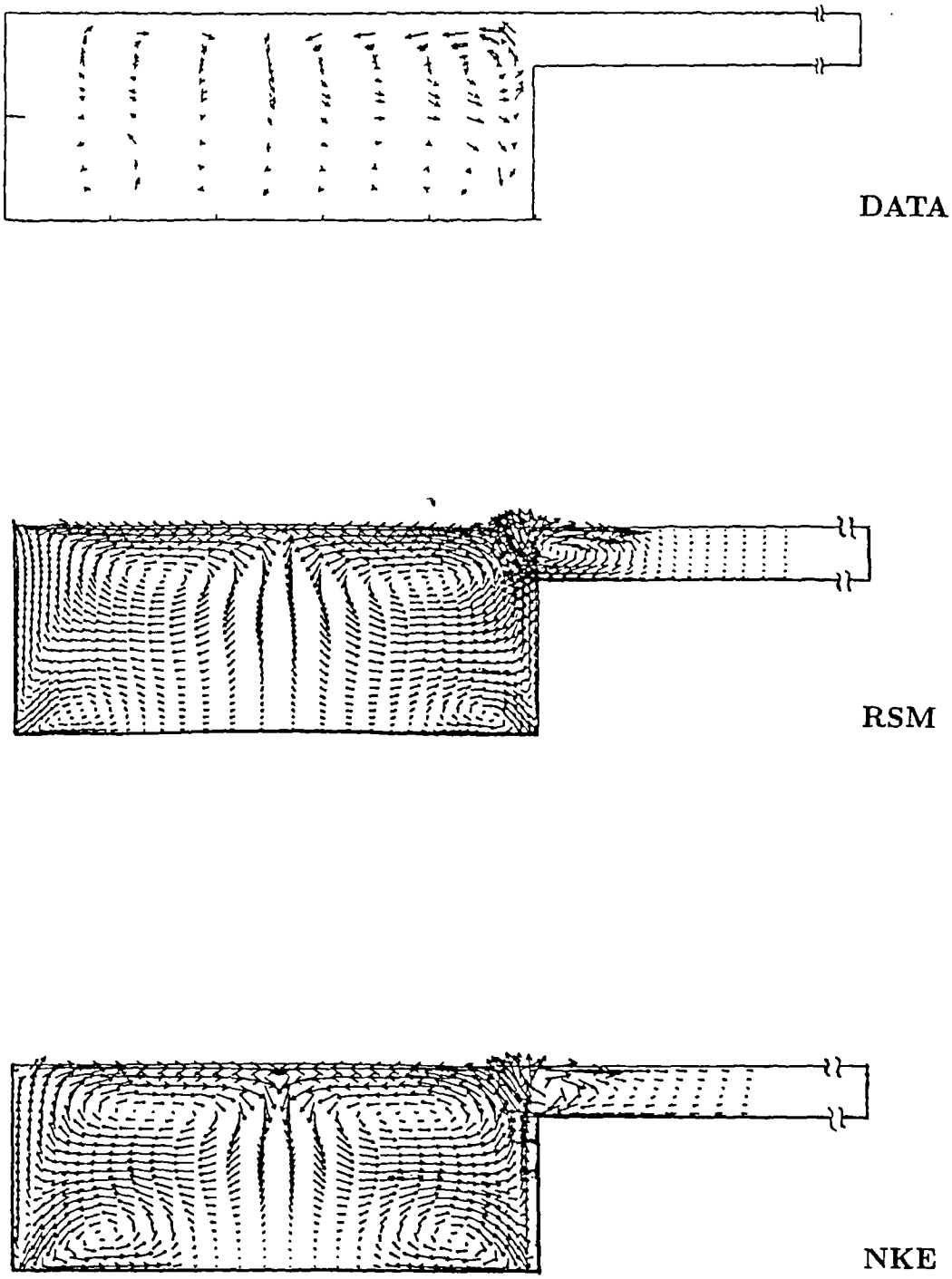

Fig. 5.35 Secondary – velocity vectors in asymmetric compound channel with $h^* = 0.254$.
Data of Tominaga and Nezu (1991).

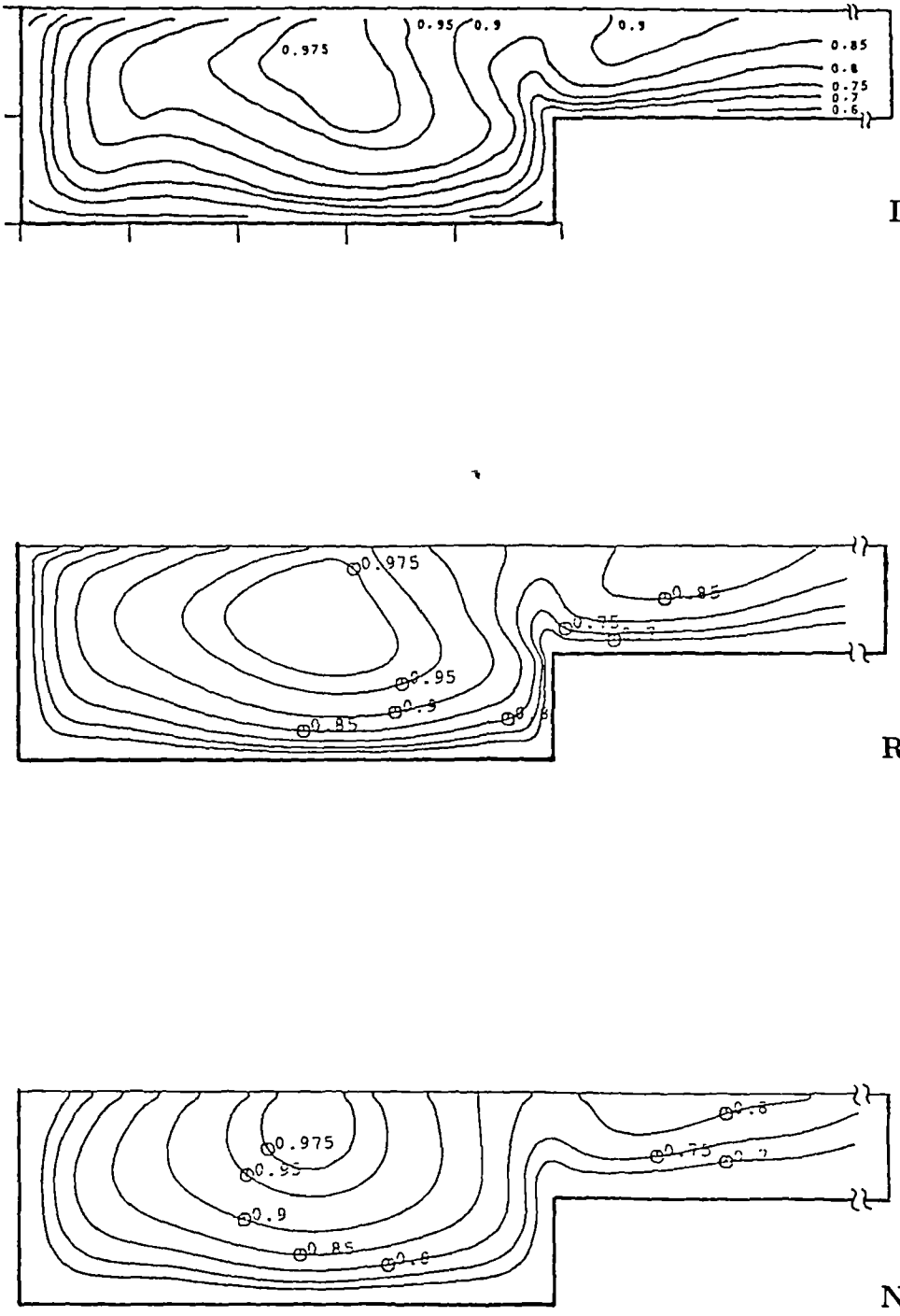

Fig. 5.36 Mean – velocity contours (W/W_{max}) in asymmetric compound channel with $h^* = 0.5$.
Data of Tominaga and Nezu (1991).

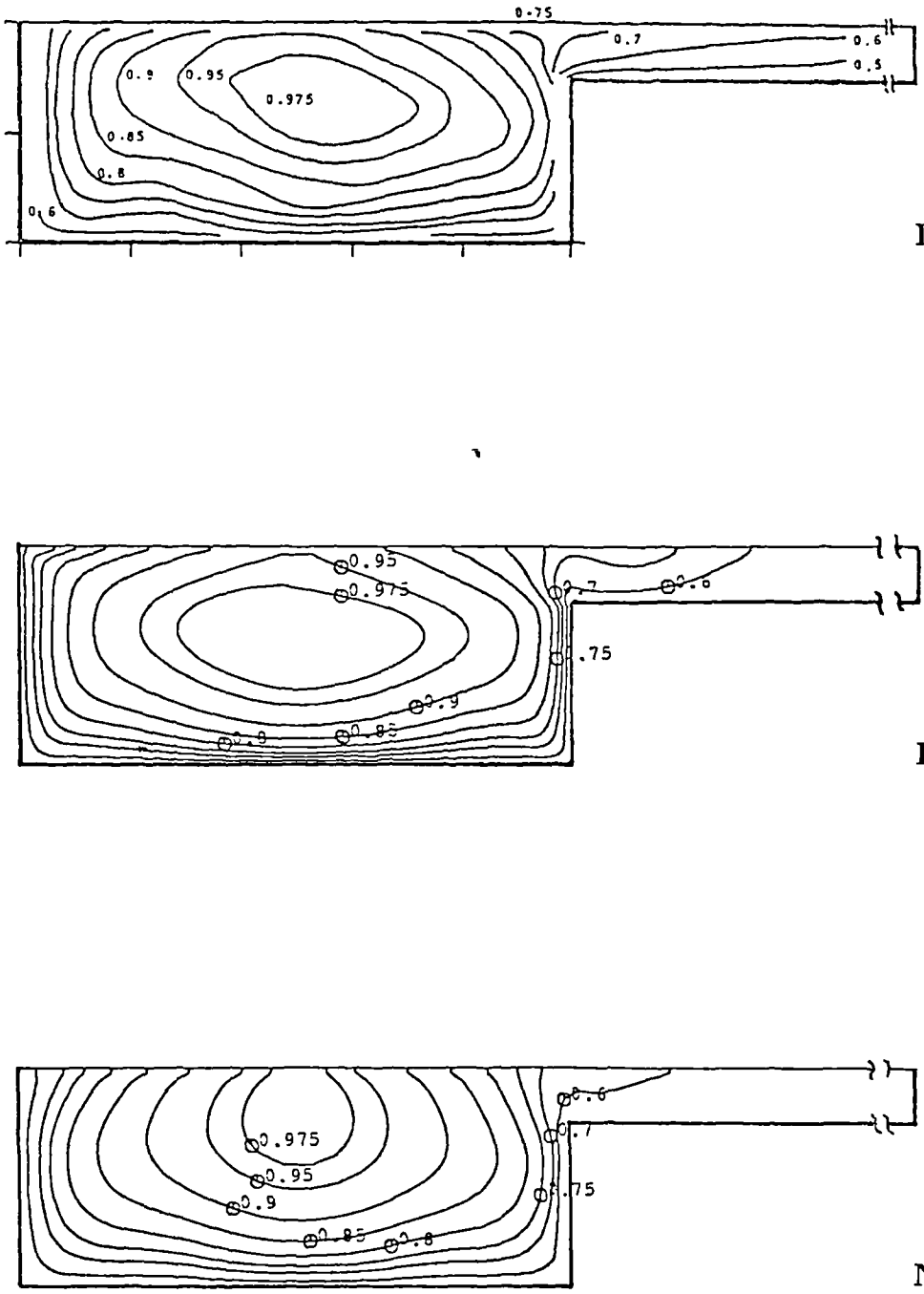

Fig. 5.37 Mean – velocity contours (W/W_{max}) in asymmetric compound channel with $h^* = 0.254$.
Data of Tominaga and Nezu (1991).

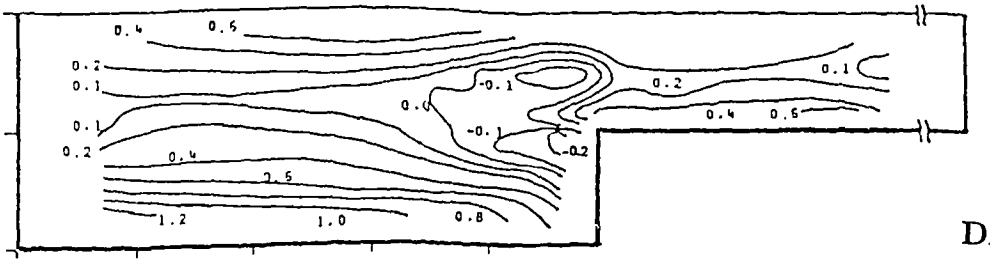

DATA

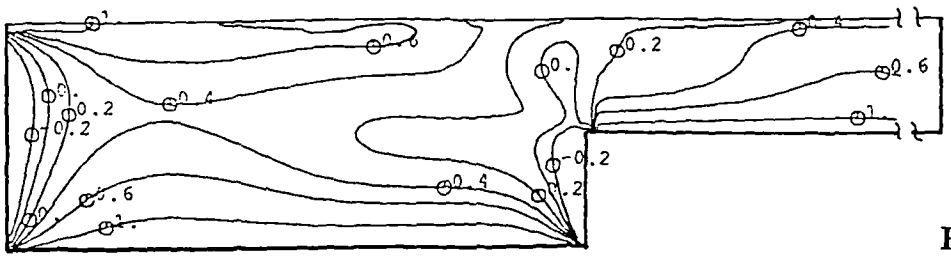

RSM

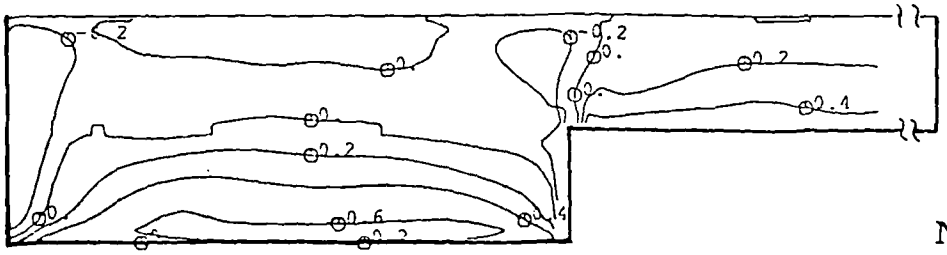

NKE

Fig. 5.38 Normal – stress anisotropy $\frac{\overline{u^2}-\overline{v^2}}{\overline{W_\tau}^2}$.
Data of Tominaga and Nezu (1991).

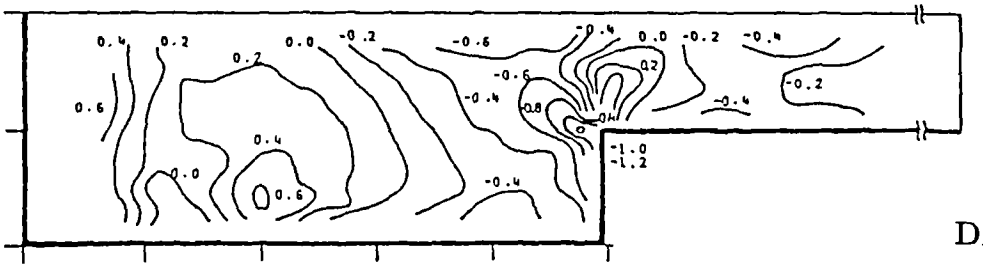

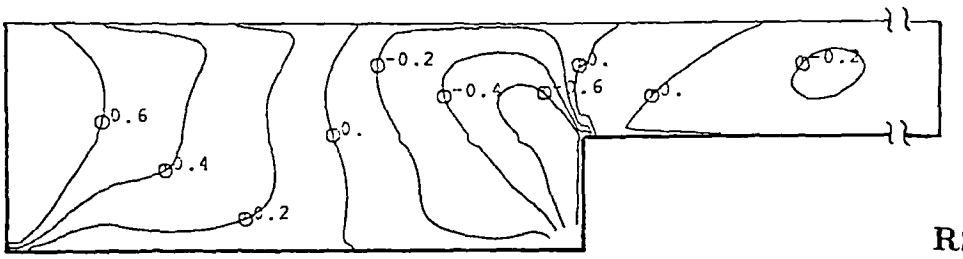

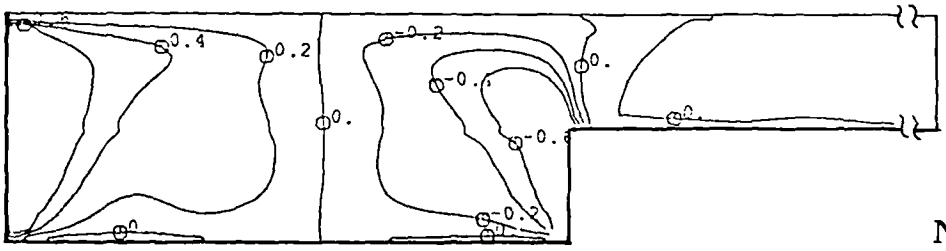

Fig. 5.39 Main – shear – stress contours $\frac{-\overline{uw}}{\overline{W_\tau}^2}$.
Data of Tominaga and Nezu (1991).

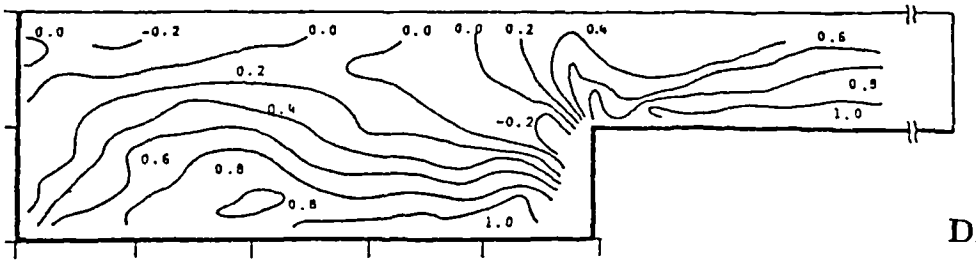

DATA

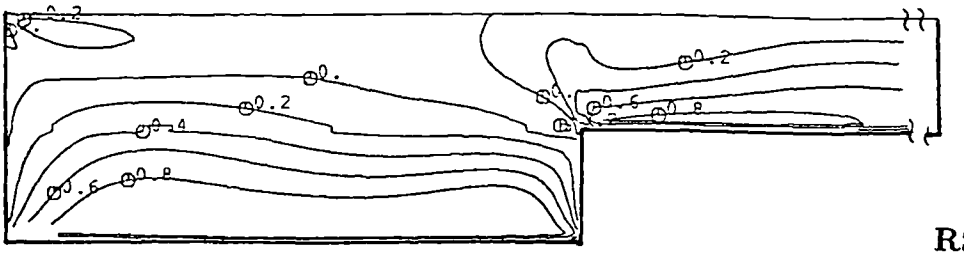

RSM

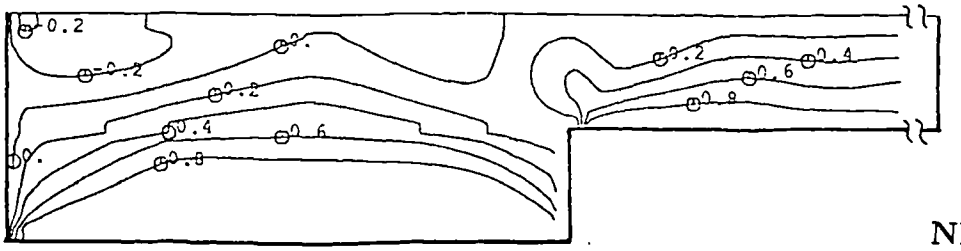

NKE

Fig. 5.40 Main – shear – stress contours $\frac{-\overline{vw}}{\overline{W}_\tau^2}$.
Data of Tominaga and Nezu (1991).

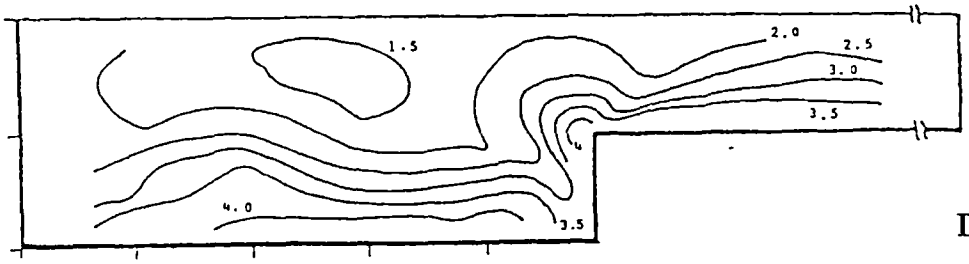

DATA

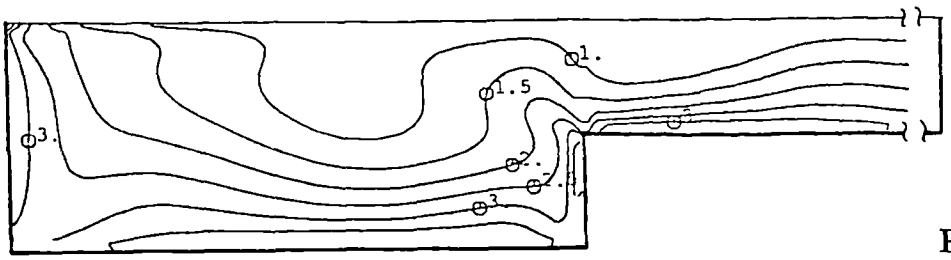

RSM

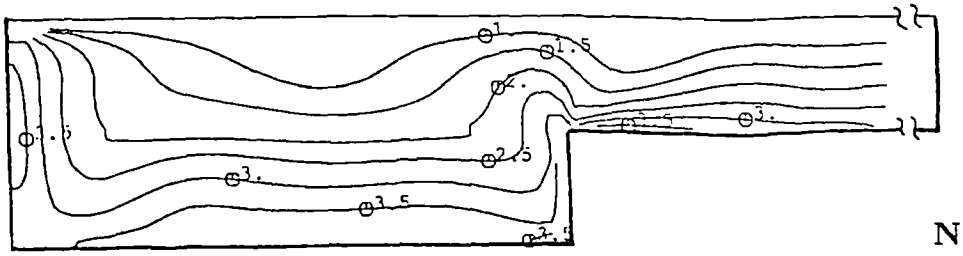

NKE

Fig. 5.41 Turbulent – kinetic – energy contours $\frac{k}{\overline{W_\tau}^2}$.
Data of Tominaga and Nezu (1991).

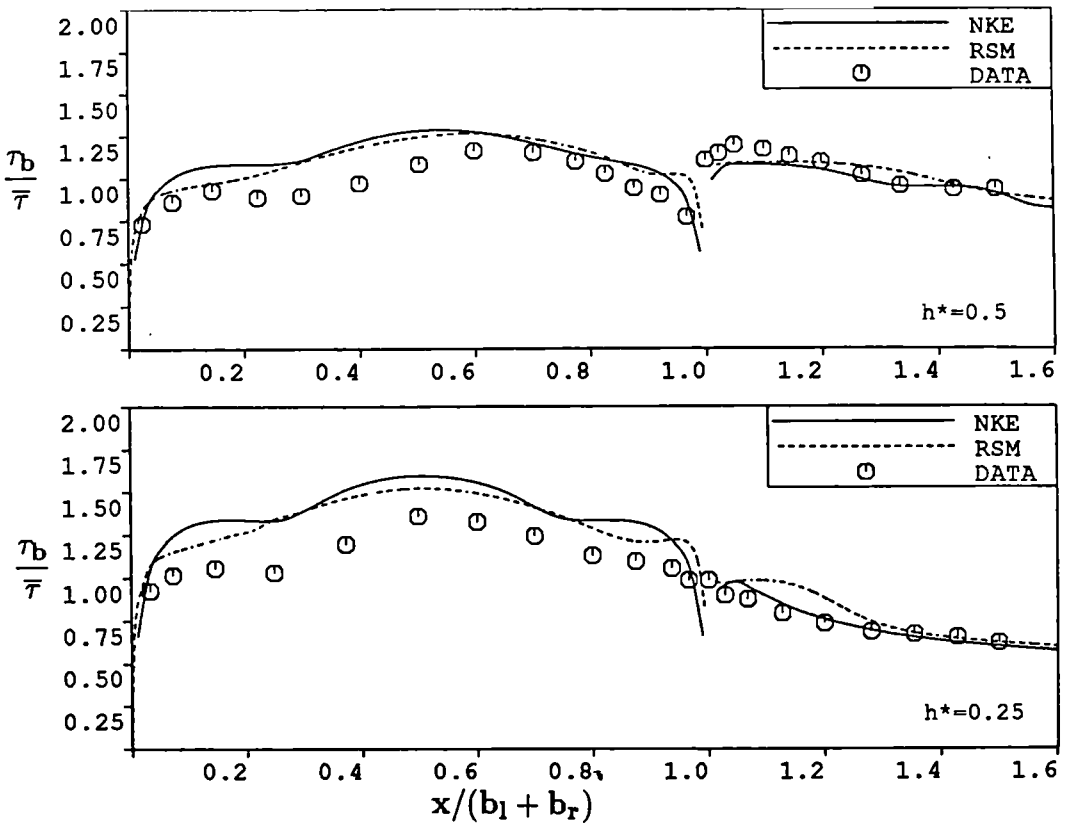

Fig. 5.42 Bed – shear – stress distribution in compound asymmetric channel.
Data of Tominaga and Nezu (1991).

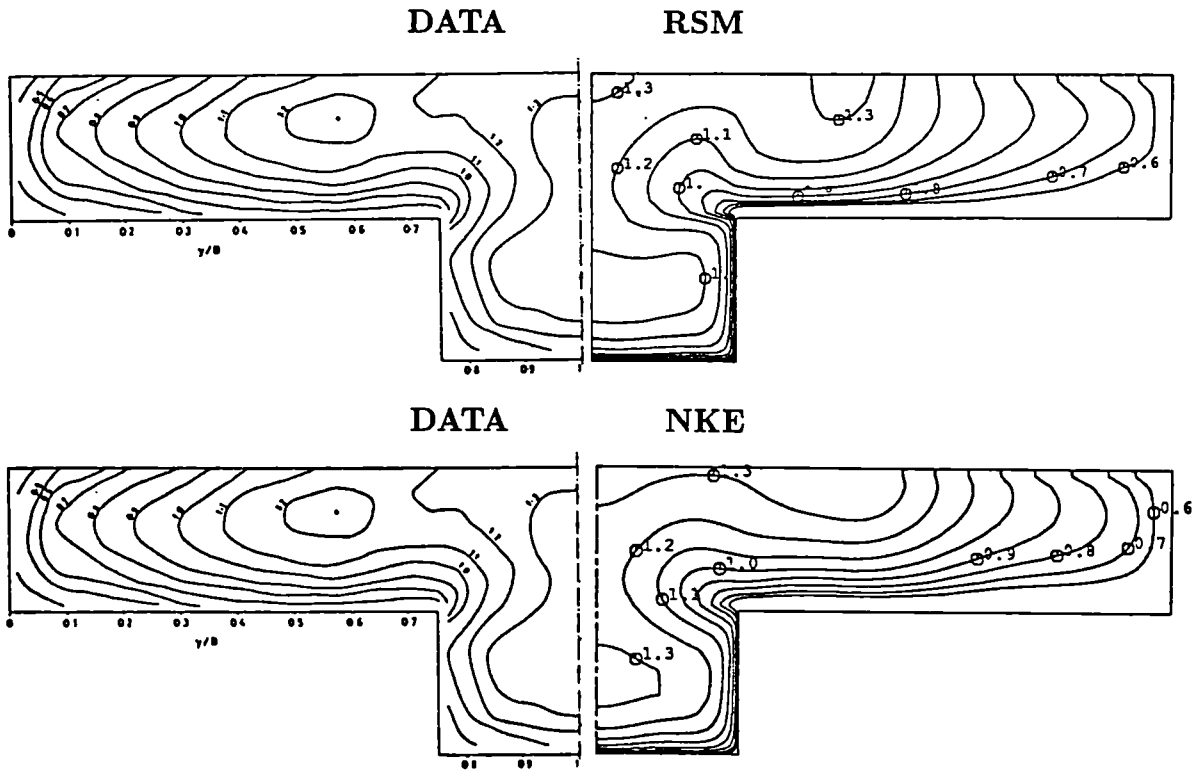

Fig. 5.43 Mean – velocity contours (W/W_{max}) in symmetric compound channel with roughen flood plains.
Data of Knight and Hamed (1984, b).

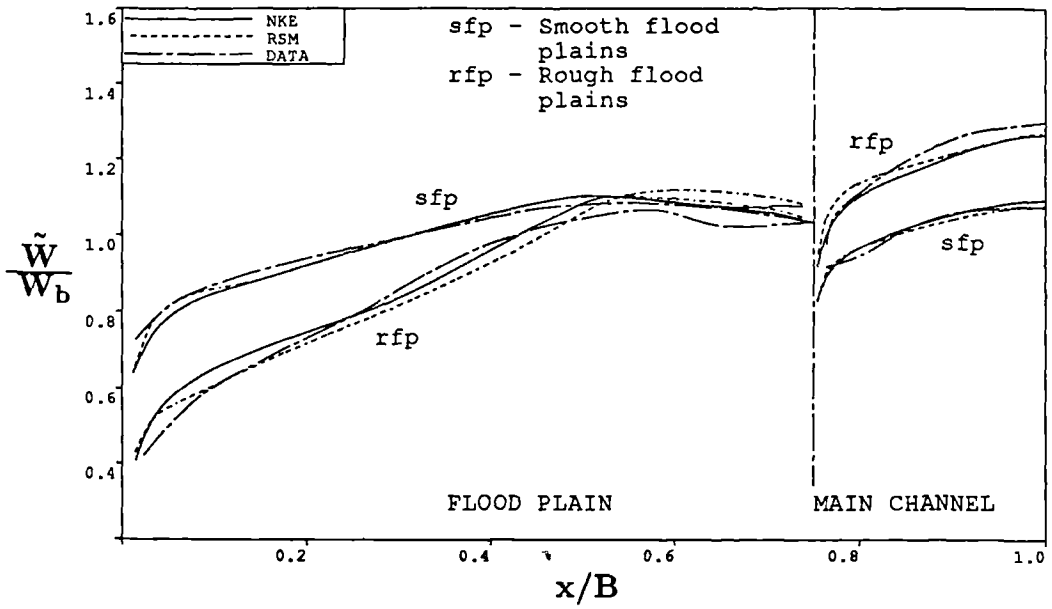

Fig. 5.44 Variation of depth-mean velocity.
Data of Knight and Hamed (1984, b).

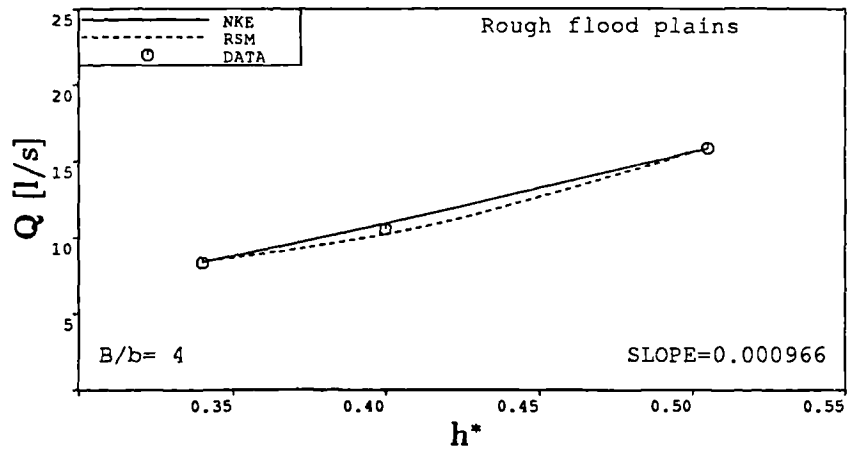

Fig. 5.45 Channel discharge.
Data of Knight and Hamed (1984, b).

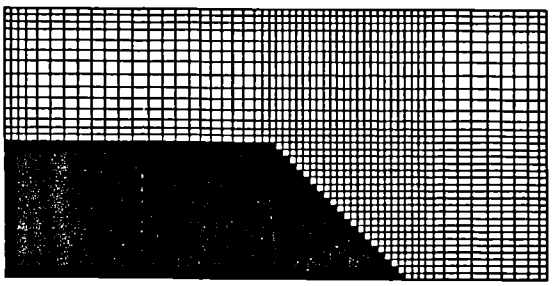

a) Stepwise approximation of inclined wall. Grid 58×36.

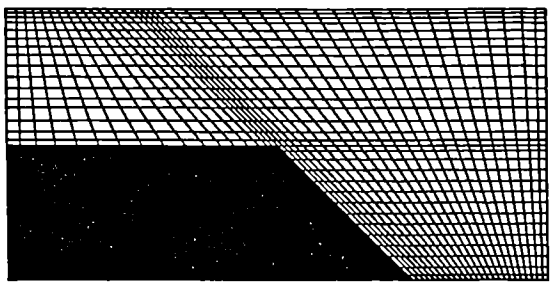

b) Non-orthogonal grid 44×32.

Fig. 5.46 Computational grids for compound channel with trapezoidal main channel.

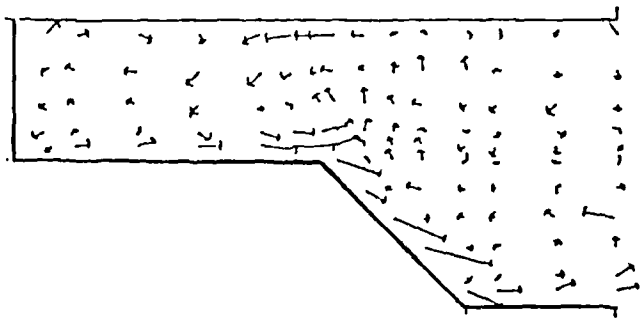

DATA

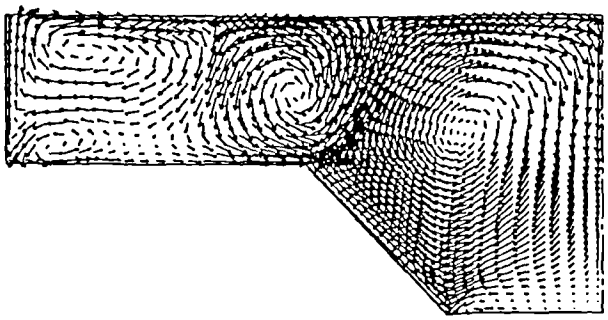

RSM

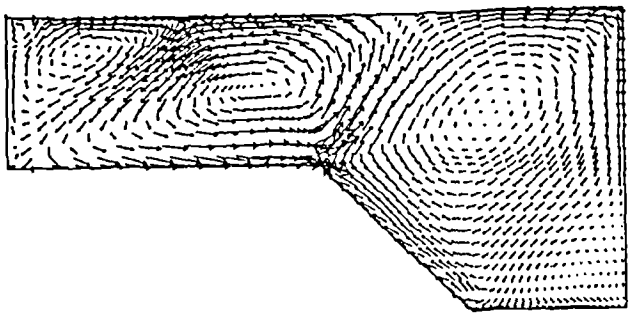

NKE

Fig. 5.47 Secondary – velocity vectors in compound trapezoidal channel with $h^* = 0.5$. Data of Tominaga et al. (1988, b).

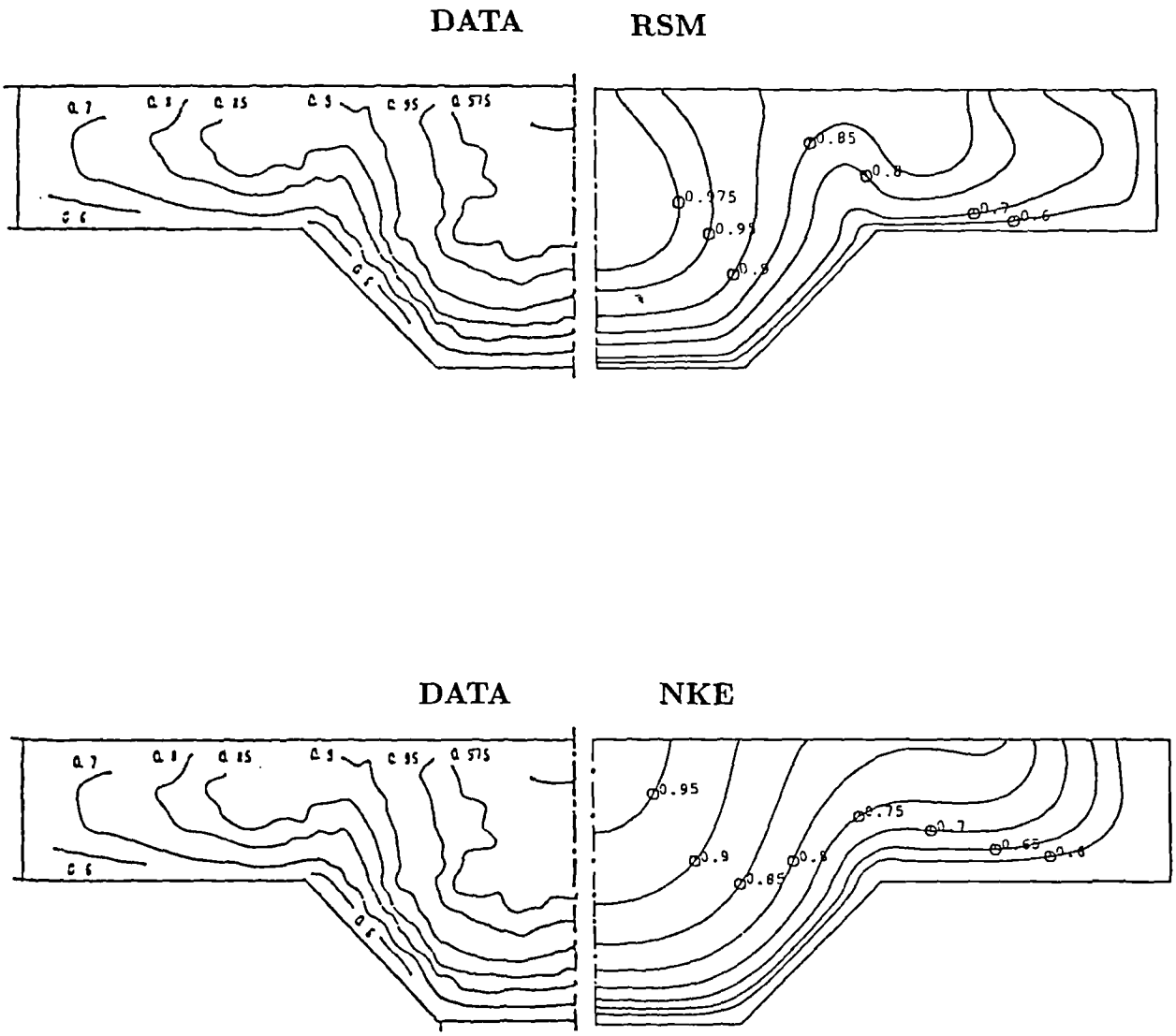

Fig. 5.48 Mean – velocity contours W/W_{max}.
Data of Tominaga et al. (1988, b).

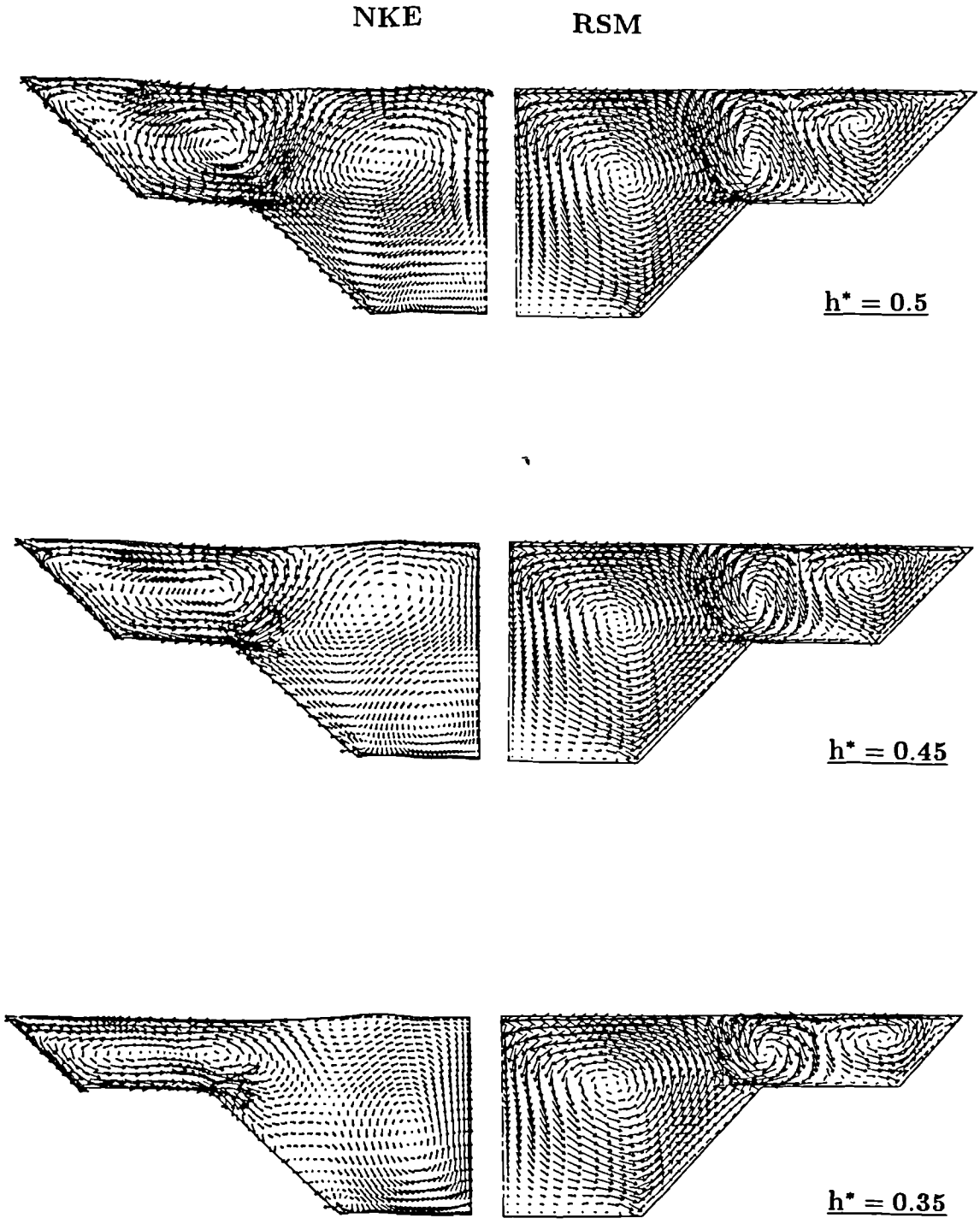

Fig. 5.49 Predicted secondary – velocity vectors in symmetric – compound – trapezoidal channels.

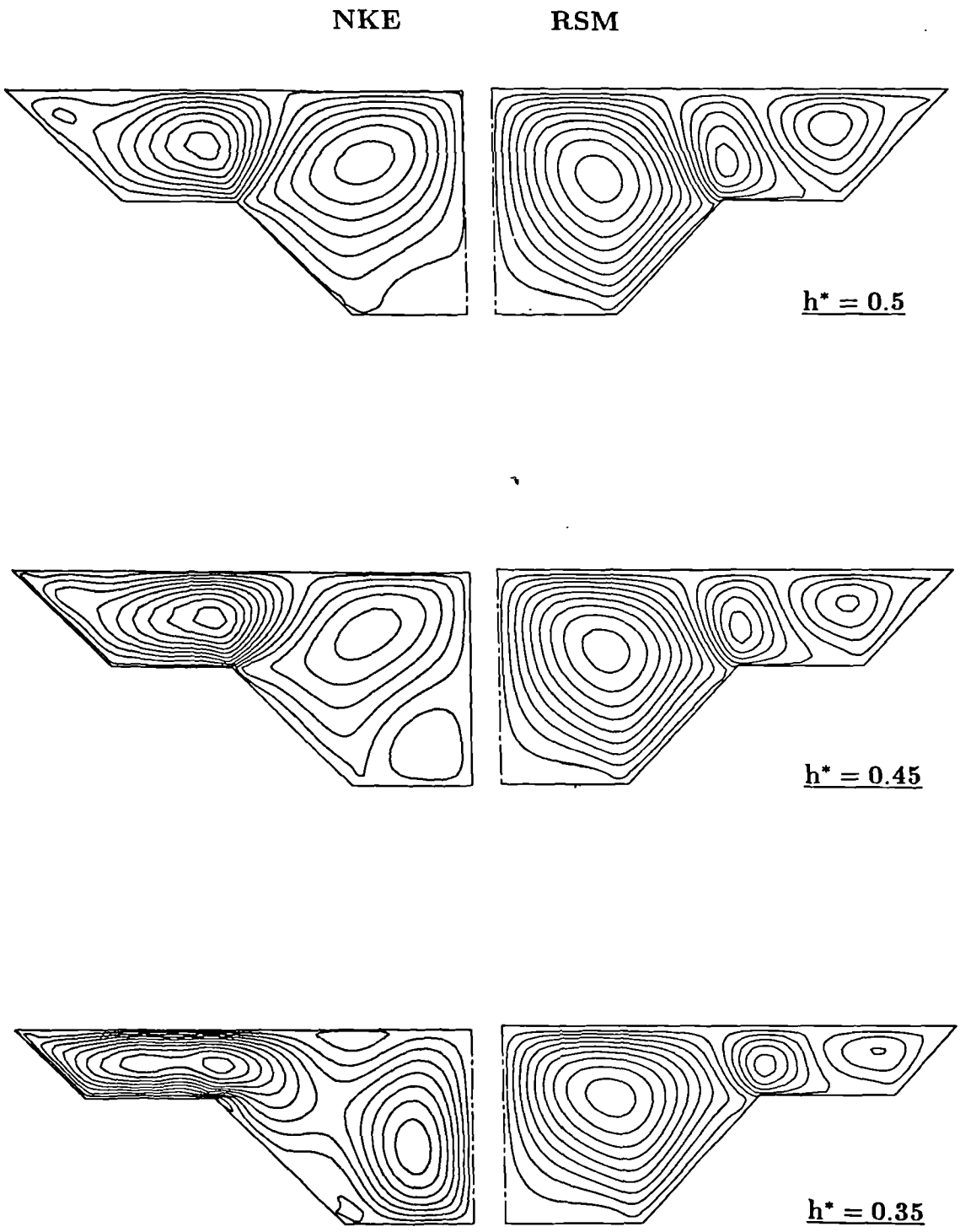

Fig. 5.50 Predicted secondary – velocity streamlines in symmetric – compound – trapezoidal channels.

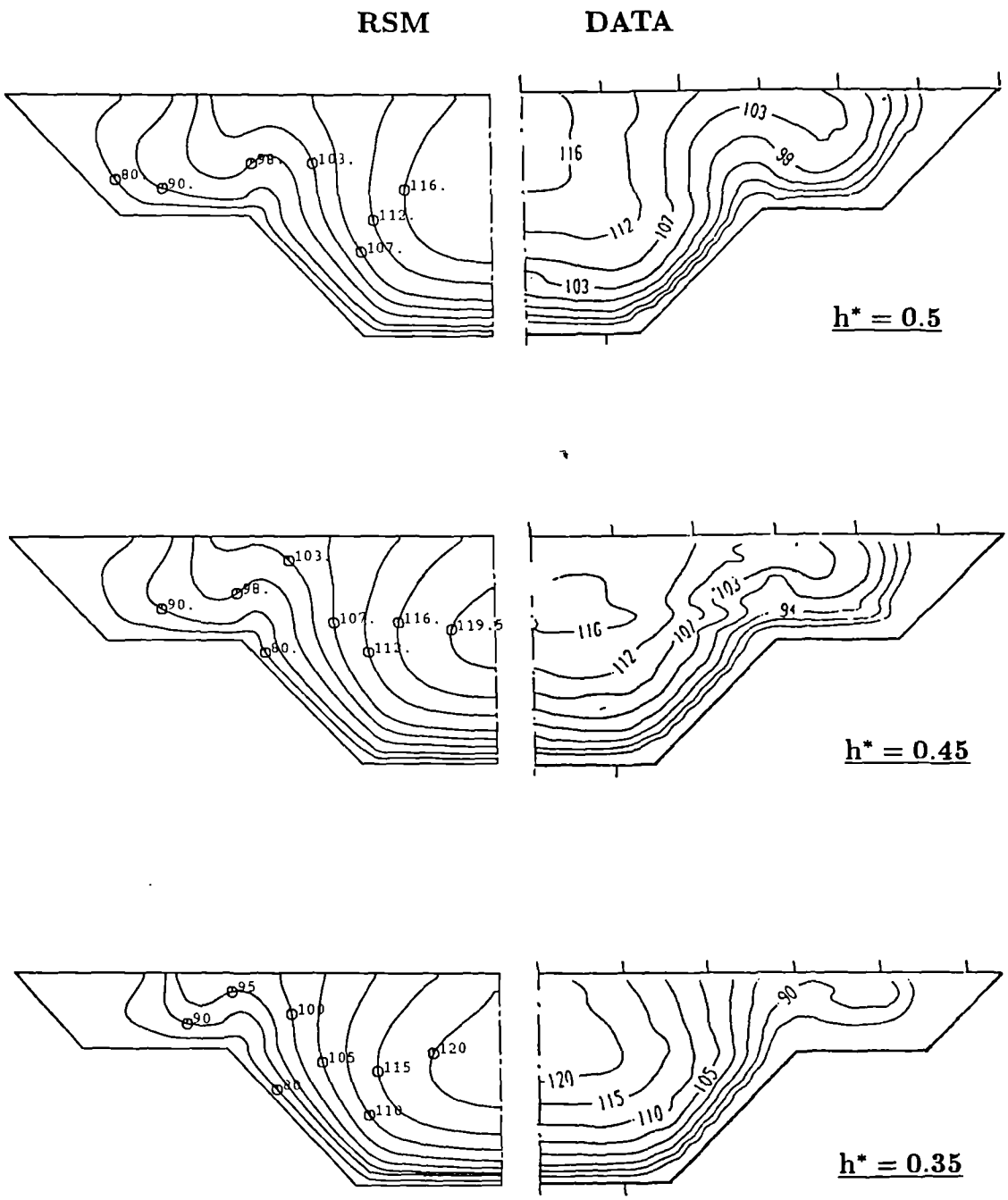

Fig. 5.51 Mean – velocity contours ($W/W_b * 10^2$) in symmetric compound – trapezoidal channels.
Data of Yuen and Knight (1990).

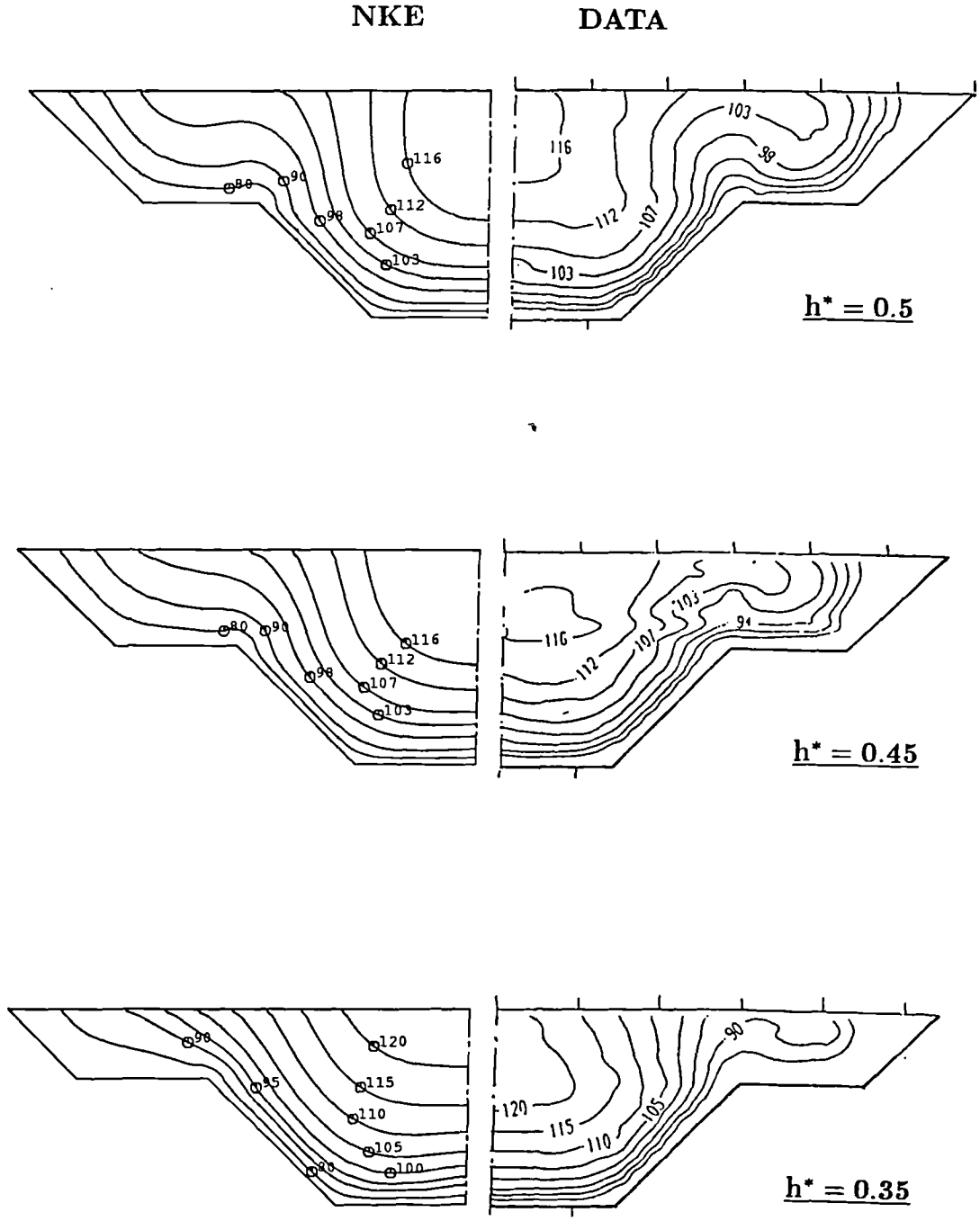

Fig. 5.52 Mean – velocity contours ($W/W_b * 10^2$) in symmetric *compound – trapezoidal channels.*
Data of Yuen and Knight (1990).

Chapter 6

CLOSURE

The present study was motivated by the need for a predictive procedure for a three-dimensional fluid flows in which turbulence-driven secondary motion plays an important role. Two very different closure methods were proposed: a complete Reynolds-stress model (Section 2.3) and a k-ϵ model (Section 2.2) used in conjunction with the nonlinear stress-strain relationship (Section 2.2.1). The extent to which the objectives of this study have or have not been fulfilled is discussed in Section 6.1. Suggestions for future work are proposed in Section 6.2.

6.1 Fulfillment of Objectives

The first objective was to formulate a second-order closure method from existing proposals for closing the Reynolds-stress equations. In Section 2.3 proposals for modelling the turbulent diffusion, dissipation and pressure-strain correlation were presented and assessed on the basis of their past performance in simple shear flows. This resulted in the Reynolds-stress model (denoted as the RSM0) which was the first to

be tested in the present study.

The development of the numerical procedure for solving the momentum and the turbulence-model equations was the second objective of the present study. The main points concerning this objective are as follows:

- The algorithm of Patankar and Spalding (1972) was used for the calculation of the streamwise-pressure gradient. In order to calculate open-channel flows, two relatively straightforward approaches were proposed and tested (Section 3.4.2.2).

- The pressure field in the cross-section was calculated using the well-known SIMPLE algorithm.

- In order to ensure the correct behaviour of both models adjacent to the solid boundaries, the velocity gradients were calculated using log-law expressions (Section 3.6).

- The wall-boundary condition for the dissipation of the turbulent kinetic energy was dictated by the local-equilibrium assumption. Equation (3.40) was used in conjunction with the nonlinear model while it was found that equation (3.41) was more appropriate when the ϵ-equation was being solved in conjunction with the Reynolds-stress model.

- Since the present study was only concerned with fully-developed flows, the terms representing changes in streamwise-flow direction were dropped from the beginning and thus the usual practice of forward marching in physical space was replaced by advance through the iteration space.

- A numerical procedure was also adapted for solving the governing equations on body-fitted coordinates. This was done in conjunction with the nonlinear k-ϵ model. This was considered to be the optimum approach for predicting flows in arbitrary domains.

The third objective was to conduct a preliminary models assessment through their application to flow in a square duct. The most important

findings are summarized as follows:

- It was found that the RSM0 produced very weak secondary motion which in a turn led to negligible influence on the mean-velocity field and hence a very weak mean-velocity distortions.

- It was found that the mean-velocity distortions are slightly better captured with this model when more rapid decay of the wall-damping function (quadratic) was applied. Since the turbulence anisotropy in this model arises only from $\Phi_{ij,w}$, this mechanism was examined in some details in order to improve the model's performance.

- The outcome of this examination showed that the simple form of $\Phi_{ij,2}$ (equation 2.34) was not suited for the present applications and has to be replaced by the more complicated model given by (equation 2.33). The combination of this model with that for $\Phi_{ij,w}$ (equation 2.39) has not been previously tested for the flow situations considered in the present work. This model required re-optimization of the model constants to satisfy some well-known experimental measurements for near-wall turbulence in local equilibrium.

- Unfortunately, this model produced an unexpected wall-shear-stress discontinuity in the corner region. Attention was then turned to the question of how to improve the model's behaviour near the wall. The distance from the wall, which appears within the wall-damping functions (equation 2.40), was calculated using expression (2.41) while the turbulent length scales were calculated using some novel definitions (equations 2.45 and 2.46). It was found that this re-definition of the wall-damping function led to improved model behaviour in the corner region. This Reynolds-stress model version was denoted as RSM.

- The nonlinear k-ϵ model was applied in the same form as was originally proposed by Speziale (1987) except for the omission of the second-order gradients which were found not to influence the performance of this model.

The fourth objective of the present study was to verify the predictive procedures by detailed comparisons with the data from three-dimensional flows in non-circular ducts. The predictions of the flows in closed ducts were conducted for a wide range of geometries, namely for rectangular, compound and trapezoidal ducts. The most significant findings regarding the models performance can be summarized as follows:

- The present closure models proved capable of reproducing the correct turbulence field. In particular, the turbulence anisotropy was well predicted.

- The closure models correctly reproduced the secondary-velocity field with only marginal differences between the two models.

- Both of the present models were capable of capturing the mean-velocity distortions caused by secondary motion. Both models produced satisfactory distortion of the mean-velocity contours with the Reynolds-stress results appearing to be in a better agreement with experiment (especially for the flow along the corner bisector for the square duct and adjacent to the external corners of compound ducts).

- The present models also proved to be adequate for the accurate prediction of the wall-shear-stress distribution in closed ducts. It was shown that the present treatment of the near-wall region enabled both models to produce wall-shear-stress distributions which were in good agreement with experiment.

- Despite some differences between the two models when applied to rectangular and compound ducts it can be concluded that both are very suited for the prediction of turbulence-driven secondary motion. The nonlinear model was then extended to the non-orthogonal geometries and the results obtained for trapezoidal ducts showed that this model is to be recommended for the prediction of three-dimensional flows in ducts of arbitrary cross-section.

The fifth objective was to identify the physical processes that are dominant in the region adjacent to the free surface, and their implications to

turbulence modelling there. The main points concerning this objective are as follows:

- Previous experimental research (Section 5.1) revealed that the free surface influences the turbulence field in two ways:

  1. The free surface damps the fluctuations in the vertical direction.
  2. The dissipation of turbulent kinetic energy increases next to the free surface which in a turn leads to the experimentally observed parabolic eddy-viscosity distribution in the open channels.

- In order to predict the effects of the free surface, the Reynolds-stress model was modified there by way of an additional damping function applied to the redistributive term (Section 2.3.5).

- The free surface was treated as a symmetry plane for all variables except for a dissipation of turbulent kinetic energy which was prescribed there (Section 3.5.2).

The sixth objective was to assess the validity of the present models for the prediction of the various open-channel flows. The most important findings to emerge were as follows:

- The prediction of the flow in rectangular channel with AR = 2.01 demonstrated the capability of the Reynolds-stress model to produce the secondary-velocity field which results in the displacement of the mean-velocity maximum to below the free surface. Although the nonlinear k-ϵ model predicts satisfactory mean-velocity distortions in large part of flow domain, this model does not produce the above mentioned displacement mainly because it does not predict the correct level of turbulence anisotropy there. This is due to the use of an algebraic relation to connect the stresses and the strains via a turbulent viscosity. Thus, contrary to expectations and, also, to the Reynolds stress predictions, the nonlinear model damps both the vertical as well as the horizontal fluctuations adjacent to the free surface.

- The differences between the two models predictions of the mean-velocity field narrowed for the rectangular channels with higher aspect-ratios.

- Regardless of channel aspect-ratio, both models predicted very similar wall-shear-stress distributions. This indicates that the nonlinear model can predict quite accurately the wall-shear-stress in open-channel flows. This was also confirmed through the prediction of the flows in trapezoidal channels where the nonlinear model produced very satisfactory agreement with measurements.

- The second-order closure correctly described the secondary-velocity flow and the turbulence field inside practically important compound-channel geometries. Consequently, the influence of the turbulence-driven secondary motion upon the mean-velocity field and the wall-shear-stresses were accurately reproduced. The nonlinear model generally predicted a weaker secondary-motion effects even though many important characteristics of compound-channel flows were satisfactory described. It was particularly so for the predictions of the wall-shear-stress and bulk-flow parameters.

- The mean-velocity field for compound channels with rough flood plains was almost identically predicted by both models.

- It can be finally concluded that Reynolds-stress model appears to be very suitable for the prediction of three-dimensional fully-developed flows in open channels of various shapes. Although the nonlinear model is obviously less accurate for the prediction of the open channel flows this model seems to be an acceptable approximation to the Reynolds-stress model for prediction of many important parameters in open-channel flows.

6.2 Recommendations for Future Work

The present study has shown that a Reynolds-stress transport model of turbulence can accurately predict three-dimensional free-surface flows, albeit in simplified geometries. There is, however, a need for a numerical

procedure for general free-surface flows in complex geometries utilizing both the Reynolds stress model and body-fitted coordinates. The obvious application of such a method will be to flows in meandering and skewed two-stage channels. These flows are very common in practice and their accurate prediction will contribute to their safe and economic design. Another aspect which requires attention is the mathematical modelling of suspended sediment taking into account the effects of the turbulence- driven secondary motions on the transport of suspended matter. The boundary conditions for such simulations, essentially the rate of bed-load transport, can be deduced from the predictions for bed shear-stress arising from the present calculations. The complete process of momentum-sediment transport is, of course, a coupled one but this can be handled quite conveniently with a procedure like the one developed in the course of this work.

References

AMANO, R.S. and GOEL, P. (1984), "A numerical study of a separating and reattaching flow by using Reynolds-stress turbulence closure", *Numerical Heat Transfer*, 7, p. 343.

BOUSSINESQ, J. (1877), "Theorie de l'ecoulement tourbillant", *Mem. Pre. Par. Div. Sav.*, 23, Paris.

BRADSHAW, P. (1987), "Turbulent secondary flows", *Ann. Rev. Fluid Mech.*, 19, p. 53.

BRUNDRETT, E. and BAINES, W.D. (1964), "The production and diffusion of vorticity in duct flow",*J. Fluid Mech.*, 19, p. 375.

BULEEV, N.I. (1963), "Theoretical model of the mechanism of turbulent exchange in fluid flows", AERE transl., p. 957.

CELIK, I. and RODI, W. (1984), "Simulation of free-surface effects in turbulent channel flows", *Physico Chemical Hydrodynamics*, 5, p. 217.

CHOU, P.Y. (1945), "On velocity correlations and solutions of the equations of turbulent fluctuations", *Quart. Appl. Math.*, 3, p. 38.

DALY, B.J. and HARLOW, F.H. (1970), "Transport equations in turbulence", *Phys. Fluids*, 13, p. 2634.

DEMIRDZIC, I. (1982), "A finite volume method for computation of fluid flow in complex geometries", Ph.D. Thesis, Imperial College, University of London.

DEMIRDZIC, I. and PERIC, M. (1990), "Finite volume method for prediction of fluid flow in arbitrarily shaped domains with moving boundaries", *Int. J. for Numerical Methods in Fluids*, 10, p. 771.

DEMUREN, A.O. and RODI, W., (1984), "Calculation of turbulence driven secondary motion in non-circular ducts", *J. Fluid Mech.*, 140, p. 189.

FUJITA, H., YOKOSAWA, H. and HIROTA, M. (1989), "Secondary Flow of the Second Kind in Rectangular Ducts with One Rough Wall", *Experimental and Fluid Science*, 2, p. 72.

GESSNER, F.B. (1973), "The origin of secondary flow in turbulent flow along a corner", *J. Fluid Mech.*, 58, p. 1.

GESSNER, F.B. and EMERY, A.F. (1976), "A Reynolds Stress Model for Turbulent Corner Flows - Part 1: Development of the Model", *J. of Fluids Eng.*, p. 261.

GESSNER, F.B. and EMERY, A.F. (1977), "A Length-Scale Model For Developing Turbulent Flow in a Rectangular Duct", *J. of Fluids Eng.*, p. 347.

GESSNER, F.B. and EMERY, A.F. (1981), "The Numerical Prediction of Developing Turbulent Flow in Rectangular Ducts", *J. of Fluids Eng.*, p. 445.

GESSNER, F.B. and EPPICH, H.M. (1981), "A near-wall pressure-strain model for turbulent corner flows", Proc. 3rd Symposium on Turbulent Shear Flows, Davis - California.

GESSNER, F.B. and JONES, J.B. (1965), "On some aspects of fully developed turbulent flow in rectangular channels", *J. Fluid Mech.*, 23, p.689.

GESSNER, F.B. and PO, J.K. (1976), "A Reynolds Stress Model for Turbulent Corner Flows - Part 2: Comparisons Between Theory and Experiment", *J. of Fluids Eng.*, p. 269.

GIBSON, M.M, JONES, W.P. and YOUNIS, B.A. (1981), "Calculation of turbulent boundary layers on curved surfaces", *Phys. Fluids*, 24, p. 386.

GIBSON, M.M. and LAUNDER, B.E. (1978), "Ground effects on pressure fluctuations in the atmospheric boundary layer", *J. Fluid Mech.*, 86, pp. 491.

GIBSON, M.M. and RODI, W. (1989), "Simulation of free surface effects on turbulence with a Reynolds stress model", *J. of Hydraul. Research*, 27, p. 233.

GIBSON, M.M and YOUNIS, B.A. (1982), "Modelling the Curved Turbulent Wall Jet", *AIAA Journal*, 20, p. 1707.

GIBSON, M.M and YOUNIS, B.A. (1986), "Calculation of Boundary Layers With Sudden Transverse Strain", *J. of Fluids Eng.*, 108, p. 470.

GIBSON, M.M and YOUNIS, B.A. (1986), "Calculation of swirling jets with a Reynolds stress closure", *Phys. Fluids*, 29, p. 38.

GOSMAN, A.D. and RAPLEY, C.W. (1980), "Fully developed flow in passages of arbitrary cross-section", Recent Advances in Numerical Methods in Fluids, Vol. 1 (ed. C. Taylor and K. Morgan), p. 335, Pineridge.

HANJALIC, K. (1970), "Two-dimensional asymmetric turbulent flow in ducts", Ph.D. Thesis, University of London.

HANJALIC, K. (1984), "Modelling of turbulence transport processes - recent advances and further research trends", Academy of Science and Art of Bosnia and Herzegovina, p. 1., Sarajevo, Bosnia and Herzegovina.

HANJALIC, K. and LAUNDER, B.E. (1972,a), "Fully developed asymmetric flow in a plane channel", *J. Fluid Mech.*, 51, p. 301.

HANJALIC, K. and LAUNDER, B.E. (1972,b), "A Reynolds stress model of turbulence and its application to thin shear flows", *J. Fluid Mech.*, 52, p. 609.

HINZE, J.O. (1959), "Turbulence", McGraw-Hill Book Co., Inc., New York.

HOAGLAND, L.C. (1960), "Fully developed turbulent flow in straight rectangular ducts", Ph.D. thesis, Dept. of Mech. Eng., M.I.T.

HOLDEN, A.P. and JAMES, C.S. (1989), "Boundary shear distribution on flood plains", *J. of Hydraul. Research*, 27, p. 75.

HOSSAIN, M.S. and RODI, W. (1980), "Mathematical Modelling of Vertical Mixing in Stratified Channel Flow", Proc. of 2nd Symposium on Stratified

Flows, Trondheim, Norway,

HUR, N., THANGAM, S. and SPEZIALE, C.G. (1989), "Numerical study of turbulent secondary flows in curved ducts", Contract No. NAS1-18605, NASA Langley Research Center, Hampton, Virginia 23665, USA.

IMAMOTO, H. and ISHIGAKI, T. (1988), "Mean and Turbulence Structure Near the Inclined Side-wall in An Open Channel Flow", Proc. of the Third Int. Symp. on Refined Flow Modelling and Turbulence Measurements, p. 545, 26–28 July, Tokio, Japan.

IMAMOTO, H. and ISHIGAKI, T. (1990), "Flow visualization in a cross section of an open channel flow", Engineering Turbulence Modelling and Experiments (Editors Rodi and Ganic), Elsevier Science Publishing Co., p. 335.

IRWIN, H.P.A.H. (1973), "Measurements in a self-preserving plane wall jet in a positive pressure gradient", *J. Fluid Mech.*, 61, p. 33.

IRWIN, H.P.A.H. and SMITH, P.A. (1975), "Prediction of the effects of streamline curvature on turbulence", *Phys. Fluids* , 18, p. 624.

JOBSON, H.E. (1968), "Vertical mass transfer in open channel flow", U.S. Geological Survey, Open-File Report, Fort Collins, Colorado.

KACKER, S.C. (1973), "Discussion of 'prediction of flow and heat transfer in ducts of square cross-section' , Proc. Inst. Mech. Eng., 187, p. D147.

KEBEDE, W., LAUNDER, B.E. and YOUNIS, B.A. (1985), "Large-amplitude periodic pipe flow: a second-moment closure study", Proc. of 5^{th} Turbulent Shear Flows, Cornell, 7-9 August.

KELLER, R.J. and RODI, W. (1988), "Prediction of flow characteristics in main channel / flood plain flows", *J. of Hydraul. Research*, 26, p. 425.

KNIGHT, D.W., DEMETRIOU, J.D. and HAMED, M.E. (1984,a), "Boundary Shear in Smooth Rectangular Channels", *J. of Hydraul. Eng.* , ASCE, 110, p. 405.

KNIGHT, D.W. and DEMETRIOU, J.D. (1983), "Flood Plain and Main Channel Flow Interaction", *J. of Hydraul. Eng.* , ASCE, 109, p. 1073.

KNIGHT, D.W. and HAMED, M.E. (1984,b), "Boundary Shear in Symmetrical Compound Channels", *J. of Hydraul. Eng.* , ASCE, 110, p. 1412.

KNIGHT, D.W. and LAI, C.J. (1985,a), "Turbulent flow in compound channels and ducts", Int. Symp. on Refined Flow Modelling and Turbulence Measurements, Iowa, USA.

KNIGHT, D.W. and LAI, C.J. (1985,b), "Compound duct flow data", Summary of Experimental Results, Dept. of Civil Eng., University of Birmingham, U.K.

KNIGHT, D.W. and PATEL, H.S. (1985,a), "Boundary shear in smooth rectangular ducts ", *J. of Hydraul. Eng.* , ASCE, 111, p. 29.

KNIGHT, D.W. and PATEL, H.S. (1985,b), "Boundary shear stress distributions in rectangular duct flow", Proc. Int. Symposium on Refined Flow Modelling and Turbulence Measurements, Iowa, USA.

KOMORI, S., UEDA, H., OGINO, F. and MIZUSHINA, T. (1982), "Turbulence structure and transport mechanism at the free surface in an open channel flow", *Int. J. Heat Mass Transfer*, 25, p. 513.

KRISHNAPPAN, B.G. (1984), "Laboratory Verification of Turbulent Flow Model", *J. of Hydraul. Eng.* , ASCE, 110, p. 500.

KRISHNAPPAN, B.G. and LAU, Y.L. (1986), "Turbulence Modelling of Flood Plain Flows", *J. of Hydraul. Eng.* , ASCE, 112, p. 251.

LAI, C.J. and KNIGHT, D.W. (1988), "Distributions of Streamwise Velocity and Boundary Shear Stress in Compound Ducts", Proc. of the Third Int. Symp. on Refined Flow Modelling and Turbulence Measurements, p. 527, 26-28 July, Tokyo, Japan.

LAU, Y.L. and KRISHNAPPAN, B.G. (1981), "Ice Cover Effects on Stream Flows and Mixing", *J. Hydraul. Div.*, ASCE, 107 (HY10), p. 1225.

LAUNDER, B.E. (1975), "On the effects of a gravitational field on the turbulent transport of heat and momentum", *J. Fluid Mech.*, 67, p. 569.

LAUNDER, B.E. and MORSE, A. (1977), "Numerical prediction of axisymmetric free shear flows with a Reynolds stress closure", Proc. 1st Symposium on Turbulent Shear Flows, Pennsylvania State University.

LAUNDER, B.E., REECE, G.J. and RODI, W. (1975), "Progress in the development of a Reynolds stress turbulence closure", *J. Fluid Mech.*, 68, p. 537.

LAUNDER, B.E. and SPALDING, D.B. (1974), "The numerical computation of turbulent flows", *Computer Methods in Applied Mech. and Eng.* , 3, p.269.

LAUNDER, B.E., TSELEPIDAKIS, D.P. and YOUNIS, B.A. (1987), "A second-moment closure study of rotating channel flow", *J. Fluid Mech.*, 183, p. 63.

LAUNDER, B.E. and YING, W.M. (1972), "Secondary flows in ducts of square cross-section",*J. Fluid Mech.*, 54, p. 289.

LAUNDER, B.E. and YING, W.M. (1973), "Prediction of flow and heat transfer in ducts of square cross-section", Proc. Institution of Mech. Eng., 187, p. 455.

LATIMER, B.R. and POLLARD, A. (1985), "Comparison of pressure-velocity coupling solution algorithms", *Numerical Heat Transfer*, 8, p. 635.

LAWN, C.J. (1971), "The determination of the rate of dissipation in turbulent pipe flow", *J. Fluid Mech.*, 48, p. 477.

LEUTHEUSSER, H.J. (1963), "Turbulent flow in rectangular ducts", *J. Hydraul. Div.*, ASCE, 89 (HY3), p. 1.

LUMLEY, J.L. (1970), "Toward a turbulent constitutive relation", *J. Fluid Mech.*, 41, p. 413.

LUMLEY, J.L. (1975), "Pressure-strain correlation", *Phys. Fluids*, 18, p. 750.

LUMLEY, J.L. and KHAJEH-NOURI, B.J. (1974), "Computational modelling of turbulent transport", *Adv. Geophys.*, A 18, p. 169.

LUMLEY, J.L. and NEWMAN, G. (1977), "The return to isotropy of homogeneous turbulence", *J. Fluid Mech.*, 82, p. 161.

MADABHUSHI, R.K. and VANKA, S.P. (1991), "Large eddy simulation of turbulence-driven secondary flow in a square duct", *Phys. Fluids*, 3, p. 2734.

MALIN, M.R. and YOUNIS, B.A. (1990), "Calculation of turbulent buoyant plumes with a Reynolds stress and heat flux transport closure", *Int. J. Heat Mass Transfer*, 33, p. 2247.

MELLING, A. and WHITELAW, J.H. (1976), "Turbulent flow in a rectangular duct", *J. Fluid Mech.*, 78, p. 289.

MYERS, W.R.C. and BRENNAN, E.K. (1990), "Flow resistance in compound channels", *J. of Hydraul. Research*, 28, p. 141.

NAKAYAMA, A., CHOW, W.L. and SHARMA, D. (1983), "Calculation of fully developed turbulent flows in ducts of arbitrary cross-section", *J. Fluid Mech.*, 128, p. 199.

NAKAYAMA, A. and KOYAMA, H. (1986), "Numerical Prediction of Turbulent Flow and Heat Transfer Within Ducts of Cross-Shaped Cross Section", *Int. J. Heat Transfer*, 108, p. 841.

NAOT, D. and RODI, W. (1981), "Numerical simulation of secondary currents in open channel flow with an algebraic stress turbulence model", Report SFB 80/T/187, February, University of Karlsruhe, Germany.

NAOT, D. and RODI, W. (1982), "Calculation of secondary currents in channel flow", *J. Hydraul. Div.*, ASCE, 108 (HY8), p. 948.

NAOT, D., SHAVIT, A. and WOLFSHTEIN, M. (1972), "Fully developed turbulent flow in a square channel", TECHNION-FLUID MECHANICS GROUP, Haifa, Israel.

NEZU, I., NAKAGAWA, H. and TOMINAGA, A. (1985), "Secondary Currents in a Straight Channel Flow and the Relation to its Aspect Ratio", Turbulent Shear Flows, Springer-Verlag, 4, p. 246.

NIKURADSE, J. (1926), "Untersuchungen uber die Geschwindigteitsverteilung in turbulenten stromungen", Thesis, Gottingen, V.D.I. - Forsch. 281.

OBI, S., PERIC, M. and SCHEURER, G. (1989), "A finite-volume calculation procedure for turbulent flows with second-order closure and colocated variable arrangement", 7th Symposium on Turbulent Shear Flows, Stanford University, USA.

PATANKAR, S.V. (1980), "Numerical Heat Transfer and Fluid Flow", McGrow-Hill.

PATANKAR, S.V. and SPALDING, D.B. (1972) "A calculation procedure for heat, mass and momentum transfer in three-dimensional parabolic flows", *Int. J. Heat Mass Transfer*, 15, p. 1787.

PERIC, M. (1985), "A finite volume method for the prediction of three dimensional fluid flow in complex ducts", Ph.D. Thesis, Imperial College, University of London.

PERIC, M., KESSLER, R. and SCHEUERER, G. (1988), "Comparison of finite-volume numerical methods with staggered and colocated grids", *Computers and Fluids*, 16, p. 389.

PERKINS, H.J. (1970), "The formation of streamwise vorticity in turbulent flow", *J. Fluid Mech.*, 44, p. 721.

PRANDTL, L. (1925), "Bericht uber Untersuchungen zur ausgebildeten Turbulenz", ZAMM, 5, p. 136.

PRANDTL, L. (1926), "Uber die ausgebildete Turbulenz", Verh. 2nd, Int. Kong. fur Tech. Mech. Zurich (Trans. N.A.C.A. Tech. Memo. no. 435.), p. 62.

PRINOS, P., TAVOULARIS, S. and TOWNSEND, R. (1988), "Turbulence Measurements In Smooth and Rough-Walled Trapezoidal Ducts", *J. of Hydraul. Eng.* , ASCE, 114, January, p. 43.

RASTOGI, A.K. and RODI, W. (1978), "Predictions of Heat and Mass Transfer in Open Channels", *J. Hydraul. Div.*, ASCE, 104(HY3), p. 397.

REECE, G.J. (1977), "A Generalized Reynolds-stress Model of Turbulence", Ph.D. thesis, Imperial College, University of London.

REYNOLDS, O. (1895), "On the dynamical theory of incompressible viscous fluids and the determination of the criterion ", Philosophical Transactions of the Royal Society of London, Series A, 186, p. 123.

RHIE, C.M. and CHOW, W.L. (1983), "Numerical Study of the Turbulent Flow Past an Airfoil with Trailing Edge Separation", *AIAA Journal*, Paper 82-0998, 21, p. 1525.

RIVLIN, R.S. (1957), "The Relation Between the Flow of Non-Newtonian Fluids and Turbulent Newtonian Fluids", *Quart. Appl. Math.*, 15, p. 212.

RODET, E. (1960), "Etude de l'ecoulement d'un fluide dans un tunnel prismatique de section trapezoidale", Publ. Sci. et Tech. du Min. de l'Air, no. 369.

ROTTA, J.C. (1951), "Statistische Theorie nichthomogener Turbulenz" *Z. Phys.*, 129, p.547.

SAMARAWEERA, D.S.A. (1978), "Turbulent heat transport in two- and three-dimensional temperature field", Ph.D. Thesis, University of London.

SHIONO, K. and KNIGHT, D.W. (1991), "Turbulent open-channel flows with variable depth across the channel", *J. Fluid Mech.*, 222, p. 617.

SHIR, C.C. (1973), "A preliminary study of atmospheric turbulent flows in the idealized planetary boundary layer", *J. Atmos. Sci.* , 30, p. 1327.

SOKOLNIKOFF, I.S. (1964), "Tensor Analysis", 2^{nd} Ed., J. Wiley and Sons, Inc., New York.

SPEZIALE, C.G. (1987), "On nonlinear k-l and k-ϵ models of turbulence", *J. Fluid Mech.*, 178, p. 459.

SPEZIALE, C.G. (1991), "Analytical methods for the development of Reynolds-stress closures in turbulence", Ann. Rev. Fluid Mech., 23, p. 107.

STEGER, J.L. (1978), "Implicit Finite-Difference Simulation of Flow about Arbitrary Two-Dimensional Geometries", *AIAA Journal*, 16, p. 679.

TATCHELL, D.G. (1975), "Convection Processes in Confined Three-dimensional Boundary Layers", Ph.D. Thesis, University of London.

THOMAS, N.H. and HANCOCK, P.E. (1977), "Grid turbulence near a moving wall", *J. Fluid Mech.*, 82, p. 481.

TOMINAGA, A. and EZAKI, K. (1988,a), "Hydraulic Characteristics of Compound Channel Flow", 6^{th} Congress Asian and Pacific Regional Division, International Association for Hydraulic Research, 20-22 July, Kyoto, Japan.

TOMINAGA, A., EZAKI, K. and NEZU, I. (1988,b), "Turbulent structure in compound channel flows with rectangular and trapezoidal main channel", Proc. of the Third Int. Symp. on Refined Flow Modelling and Turbulence Measurements, 26-28 July, Tokyo, Japan.

TOMINAGA, A. and NEZU, I. (1991), "Turbulent Structure in Compound Open-Channel Flows", *J. of Hydraul. Eng.* , ASCE, 117, p. 21.

TOMINAGA, A., NEZU, I., EZAKI, K. and NAKAGAWA, H. (1989), "Three-dimensional turbulent structure in straight open channel flows", *J. of Hydraul. Research*, 27, p. 149.

UEDA, H., MOLLER, R., KOMORI, S. and MIZUSHINA, T. (1977), "Eddy Diffusivity Near the Free Surface of Open Channel Flow", *J. Heat Mass Transfer*, 20, p. 1127.

VASIC, S. (1982), "Application of first- and second-order models of turbulence for prediction of homogeneous fluid flows", M.Sc. Thesis, Mechanical Faculty, Belgrade, Yugoslavia.

YOUNIS, B.A. (1982), "Boundary layer calculations with Reynolds stress turbulence models", Internal report, Imperial College, Mech. Eng. Depth., London.

YOUNIS, B.A. (1984), "On Modelling the Effects of Streamline Curvature on Turbulent Shear Flows", Ph.D. Thesis. Imperial College, University of London.

YOUNIS, B.A. and ABDELLATIF, O.E. (1989), "Modelling of sediment transport in rectangular ducts with a two-equation model of turbulence", Proc. Int. Symp. on Sediment Transport Modelling, ASCE, New Orleans, August, p. 197.

YUEN, K.W.H. (1989), "A study of boundary shear stress, flow resistance and momentum transfer in open channels with simple and compound trapezoidal cross section", Ph.D. Thesis, Depth. of Civil Eng., University of Birmingham, England.

YUEN, K.W.H. and KNIGHT, D.W. (1990), "Critical flow in a two stage channel", Int. Conf. on River Flood Hydraulics, Hydraulics Research Limited, Published by John Wiley and Sons Ltd., Paper G4, p. 267.